Simulation of Multi Pulse EPR Signals for Distance Measurement in Biological Systems by Exploitation of COSY, DQ, DQM, DQC, and DEER Signals; Relaxation Due to Fluctuation of Spin-Hamiltonian Parameters of Echo ELDOR Signal; and Effect of Instantaneous Diffusion and Many Body Interaction in a Frozen Malonic Acid Crystal on a SECSY Signal

Hamidreza Salahi

A Thesis

In the Department

of

Physics

Presented in Partial Fulfillment of the Requirements

For the Degree of

Doctor of Philosophy (Physics) at

Concordia University

Montreal, Quebec, Canada

August 2022

CONCORDIA UNIVERSITY

SCHOOL OF GRADUATE STUDIES

This is to certify that the thesis prepared

By: Hamidreza Salahi

Entitled: Simulation of Multi Pulse EPR Signals for Distance Measurement in Biological Systems by Exploitation of COSY, DQ, DQM, DQC, and DEER Signals; Relaxation Due to Fluctuation of Spin-Hamiltonian Parameters of Echo ELDOR Signal; and Effect of Instantaneous Diffusion and Many Body Interaction in a Frozen Malonic Acid Crystal on a SECSY Signal

and submitted in partial fulfillment of the requirements for the degree of

DOCTOR OF PHILOSOPHY (Physics)

complies with the regulations of the University and meets the accepted standards with respect to originality and quality.

        Signed by the final examining committee:

_____ Chair
        Yogendra P. Chaubey

_____ External Examiner
        René T. Boeré

_____ Examiner
        Mariana Frank

_____ Examiner
        Calvin Kalman

_____ Examiner
        Saurabh Maiti

_____ Supervisor
        Sushil K. Misra

        Approved by_____

        Pablo Bianucci
        Graduate Program Director

August 09, 2022   _____

        Pascale Sicotte, Dean
        Faculty of Art & Science

Abstract

Simulation of Multi Pulse EPR Signals for Distance Measurement in Biological Systems by Exploitation of COSY, DQ, DQM, DQC, and DEER Signals; Relaxation Due to Fluctuation of Spin-Hamiltonian Parameters of Echo ELDOR Signal; and Effect of Instantaneous Diffusion and Many Body Interaction in a Frozen Malonic Acid Crystal on a SECSY Signal

Hamidreza Salahi, Ph.D.

Concordia University, 2022

This dissertation is devoted to three main subjects:

In the first part, an algorithm to calculate the multi-pulse EPR signals including COSY (Correlation Spectroscopy), two-pulse DQ (Double Quantum), five-pulse DQM (Double Quantum Modulation), four-, five-, six-pulse DQC (Double Quantum Coherence) is developed. The applicability of each of these pulse sequences is further studied.

In addition, a novel method based on doubly rotating frames (DRF) has been exploited to calculate three- and four-pulse DEER (Double Electron-Electron Resonance) signals for a system of two dipolar-coupled nitroxides on a sample of bis-nitroxide nanowire, P1, in deuterated ortho-terphenyl solvent with 5% BnPy (d14-oTP/BnPy) as well as two coupled Gd^{3+} ions in Gd ruler 1_5 in D_2O/glycerol-d_8 (7/3 volume ratio). The technique is then used to calculate the basis kernel signals accurately by numerical techniques to obtain the probabilities of distance distribution, $P(r)$, using Tikhonov regularization and *DeerAnalysis* software.

In the second part, two models, namely cylindrical and conical models of fluctuation, are presented wherein one considers the random fluctuations in the $\tilde{g}$ and $\tilde{A}$ matrices of the spin Hamiltonian due to thermal motion of malonic acid molecule. Accordingly, the relaxation matrix is calculated in Liouville space for the four-level coupled electron-nuclear spin system, using the formalism outlined by (Lee, Patyal and Freed 1993). The obtained relaxation matrix is then used to calculate the time-dependent echo-ELDOR signal by solving the relevant Liouville-von Neumann (LVN) equation.

In the third part, the relaxation during free evolution and many-body effects in a SECSY signal, including instantaneous and spectral diffusions, which are due to the dipolar interaction between an electron with other electrons in a γ-irradiated malonic acid crystal are investigated.

Acknowledgements

Contribution of the authors

The original research study is presented in chapters 3-6 and the list of the publications can be found in Appendix G. Professor Sushil K. Misra conceived of the presented ideas and prepared a Fortran code, which was further converted into a Matlab code by Hamidreza Salahi, who performed the computations. The theory was developed through daily discussions between the supervisor and the student, both of whom discussed the results and prepared the final manuscripts together.

Table of Contents

List of Figures

xiii

List of Tables

List of Abbreviations

EPR - Electron Paramagnetic Resonance

ESR - Electron Spin Resonance

LVN – Liouville-von Neumann

COSY (Correlation Spectroscopy)

DQ (Double Quantum)

DQM (Double Quantum Modulation)

DQC (Double Quantum Coherence)

DEER - Double Electron-Electron Resonance

Echo-ELDOR - Echo Electron-electron Double Resonance

SECSY - Spin Echo Correlation Spectroscopy

FID - Free Induction Decay

FT - Fourier Transform

HF – Hyperfine

NMR - Nuclear Magnetic Resonance

PELDOR - Pulse Electron Double Resonance

RIDME - Relaxation-Induced Dipolar Modulation Enhancement

TR- Tikhonov Regularization

SHP - Spin-Hamiltonian Parameters

Chapter 1

1. Introduction to Electron Paramagnetic Resonance

Electron Paramagnetic Resonance (EPR) spectroscopy is a very powerful technique in that it can be exploited to reveal the electronic and geometric structures of the environment around paramagnetic centers. Even weak interactions between electron spins, as well as those between electron and nuclear spins not resolved by continuous wave (CW) EPR, can be distinguished by pulsed EPR (Misra, Multifrequency electron paramagnetic resonance: theory and applications 2011).

The EPR spectroscopy can be understood using the concept of the magnetic moment of electron spin. The electron spin, a quantum mechanical property, has an intrinsic angular momentum characterized by a quantum number $s = 1/2$. In accordance with the quantum theory, it exists in two states: spin-up state with $m_s = +1/2$, and a spin-down state with $m_s = -1/2$. As an electron has a charge, there is a magnetic moment associated with the spin angular momentum:

$$\mu = -g\frac{e\hbar}{2m_e}S = -g\beta_e S \tag{1.1)}$$

where β_e is the Bohr magneton, S is the spin angular momentum, and the factor g can be obtained in accordance with Dirac's relativistic quantum mechanics. The free electron g-value is $g_e = 2.00231930436153(53)$.

In the presence of an external magnetic field with the strength B_0 the electron's magnetic moment aligns itself either antiparallel ($m_s = -1/2$) or parallel ($m_s = +1/2$), to the field. Each alignment has a specific energy due to the Zeeman effect, which is $E = -g\beta_e\,m_s B_0$. Therefore, the separation between the lower and the upper state is $\Delta E = g\beta_e B_0$ for unpaired free electrons. This equation implies that the splitting of the energy levels is directly proportional to the strength of the magnetic field, as shown in Figure 1.1.

An unpaired electron can change its electron spin by either absorbing or emitting a photon of energy $h\nu$, such that the resonance condition, $h\nu = \Delta E$, is obeyed. Experimentally, this equation permits a large combination of frequency and magnetic field values, but the great majority of EPR measurements are made with the microwaves in the 9000–10000 MHz (9–10 GHz) range, with fields corresponding to about 3500 G (0.35 T). A collection of paramagnetic centers, such as free radicals, is exposed to microwaves at a fixed frequency. At this point the unpaired electrons can move between their two spin states. Since, there are typically more electrons in the lower state, due to the Maxwell–Boltzmann distribution, there is a net absorption of energy, and it is this absorption that is monitored and converted into a spectrum.
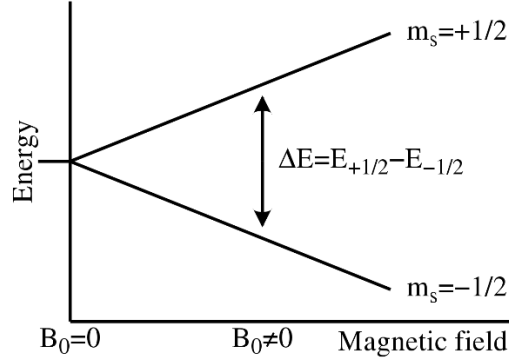
Figure 1.1. External magnetic field B_0 causes a splitting of the energy levels of the spin system. When the resonance condition $\Delta E = h\nu$ is met, spin transitions between the energy levels $m_s = -1/2$ and $m_s = +1/2$ can be detected as energy absorption. The figure is taken from *Electron Paramagnetic Resonance,* "Wikipedia", 2022, https://en.wikipedia.org/wiki/Electron_ _paramagnetic_resonance

1.1 Spin Hamiltonian

The interactions between unpaired electron and nuclei spins in a magnetic field are characterized by two interactions: (i) between the magnetic moments of electron or nucleus and the external magnetic field and (ii) by the electron-nuclear spin interactions. The Hamiltonian describing such a system is referred to as spin Hamiltonian.

The spin Hamiltonian, H_0, for the system of an effective electron spin S interacting with N nuclei with spins I consists of electron Zeeman (H_Z), nuclear Zeeman (H_{nZ}), hyperfine (H_{hf}) and zero-field splitting (H_{ZFS}) has the following form (Schweiger and Jeschke 2001):

$$H_0 = H_Z + H_{nZ} + H_{hf} + H_{ZFS}$$
$$= \frac{\beta_e}{h} B_0 g\, S - \beta_n \sum_{k=1}^{N} \frac{g_{nk}}{h} B_0 I_k + \sum_{k=1}^{N} S\, A_k I_k + SDS \qquad 1.2)$$

where S and I_k are the electron and nuclear spin operators, respectively, B_0 is the external magnetic field, A_k and D are the hyperfine matrix and zero-field splitting matrix, respectively. Each type of interactions can be described by a matrix (g, D and A_k in Eq. *1.2*) above), which is diagonal in an appropriate coordinate system (also known as molecular frame or principal axis system). In this system the interaction can be described by three principal components of the matrix. The different types of interactions are as follows.

i) Electron Zeeman interaction

2

The Electron Zeeman interaction defines the interaction between the electron spin magnetic moment S and external magnetic field B_0, and the corresponding spin Hamiltonian term is:

$$H_Z = \frac{\beta_e}{h} B_0 g\, S \qquad \text{1.3)}$$

As was mentioned before, in a principal axis system g-matrix can be diagonalized, and the interaction can be defined by three principal g-values: g_{xx}, g_{yy} and g_{zz} and three Euler angles defining the orientation of the matrix in the molecular frame.

In the case of a liquid solution the electron Zeeman interaction is typically averaged to a single isotropic value, $g_{iso} = 1/3\,(g_{xx} + g_{yy} + g_{zz})$. In frozen solution and powder states, the principal components of the g-matrix can be identified from the turning points of the EPR spectrum. The lineshape of an EPR spectrum is dominated by electron Zeeman interaction, and there are three limiting symmetries of the lineshape: cubic ($g_{xx} = g_{yy} = g_{zz}$), axial ($g_{xx} = g_{yy} = g_\perp$, $g_{zz} = g_\parallel$) and orthorhombic ($g_{xx} \neq g_{yy} \neq g_{zz}$).

ii) Nuclear Zeeman interaction

The nuclear Zeeman interaction of a spin I with an external magnetic field B_0 can be described in a similar way:

$$H_{nZ} = \frac{\beta_n}{h} B_0 g_n I \qquad \text{1.4)}$$

where the spin quantum number I and the nuclear g_n factor depend on the nucleus type. Nuclear Zeeman interaction does not generally contribute to the EPR spectrum, because the nuclear magneton is three orders of magnitude smaller than the Bohr magneton. However, it plays a role in hyperfine techniques.

iii) Hyperfine interaction

The interaction between the electron spin and coupled nuclei of spin I is called the hyperfine interaction, and can be defined by an effective spin Hamiltonian as following:

$$H_{hf} = \text{SAI} = a_{iso}\text{SI} + \text{STI} \qquad \text{1.5)}$$

There are two different contributions in the isotropic hyperfine interaction: the isotropic part a_{iso} and the anisotropic part described by tensor T.

The isotropic hyperfine coupling constant a_{iso} is defined as the following:

$$a_{iso} = \frac{2\mu_0}{3\hbar} g_e \beta_e g_n \beta_n |\psi_0(0)|^2 \qquad 1.6)$$

It originates from the finite electron spin density at the nucleus $|\psi_0(0)|^2$.

The anisotropic hyperfine interaction can be described in terms of the classic dipole-dipole interaction and the elements of the symmetric tensor, T, which can be expressed as follows:

$$T_{ij} = \frac{\mu_0}{4\pi\hbar} g_e \beta_e g_n \beta_n < \psi_0 | \frac{r_i r_j - \delta_{ij} r^2}{r^5} | \psi_0 > \qquad 1.7)$$

where ψ_0 is the ground-state electronic wave-function and r is the distance between the nuclear and electron spins (Schweiger and Jeschke 2001).

The hyperfine interaction causes splitting of the EPR line. The isotropic hyperfine coupling can be determined from the distance between peaks of the hyperfine structure for solution EPR spectrum when hyperfine anomaly is less than 1% (Schweiger and Jeschke 2001). The splitting pattern depends on the number and type ($I = 1/2, I = 1$, etc.) of coupled nuclei, and is used for the characterisation of molecular structures. In the case of interaction between electron spin and N nuclei with spin I, there occurs a splitting into $2 \times N \times I + 1$ lines with separations determined by the relevant isotropic hyperfine coupling and relative intensities that can be predicted by Pascal's triangles (Perrin 2018).

In frozen solutions and powders the anisotropic parts of the hyperfine couplings also contribute to the EPR spectrum and this makes spectrum analysis more complicated. Pulse techniques such as Electron Spin Echo Envelope Modulation (ESEEM) are used when the hyperfine interactions are not too strong to be resolved by CW EPR.

iv) Zero-Field splitting interaction

In systems with electron spin $S > 1/2$, there exist a dipolar interaction between electron spins which removes the degeneracy of the different m_s levels even in the absence of an external magnetic field. This interaction is called zero-field splitting (ZFS). This interaction is represented by the following spin Hamiltonian term:

$$H_{ZFS} = SDS \qquad 1.8)$$

where D is the symmetric, traceless zero-field splitting interaction tensor. The ZFS interactions are due to the spin-spin dipolar interaction (mostly dominant in the case of organic molecules) and spin-orbit interaction (mostly dominates in case of transition metal ions) (Schweiger and Jeschke 2001).

v) Electron-Electron Dipole interaction

In the case of a two-spin system, spin 1 and spin 2 denoted as S_1 and S_2, respectively, the spin Hamiltonian consists of the Hamiltonians for the single spins that could include all the previously-described interactions, from **i)** – **iv)**, and dipolar coupling Hamiltonian between the two spins:

$$H(S_1, S_2) = H(S_1) + H(S_2) + H_{dd} \qquad 1.9)$$

where $H(S_i); i = 1,2$ is the static spin Hamiltonian for the system of an effective electron spin S_i interacting with N nuclei with spins I which, in general, consists of electron Zeeman, nuclear Zeeman , hyperfine, and zero-field splitting as given in Eq. (2.1). In the high-field approximation, the dipolar part of the Hamiltonian could be rewritten in pseudo-secular approximation as follows:

$$H_{dd} = \omega_{dd}[A + B]$$

$$\omega_{dd} = \frac{\mu_0}{4\pi\hbar} \frac{g_1 g_2 \beta_e^2}{r_{12}^3} \qquad 1.10)$$

$$A = S_{z_1} S_{z_2}(3\cos^2\theta - 1); \; B = -\frac{1}{4}\left(S_{+_1}S_{-_2} + S_{-_1}S_{+_2}\right)(3\cos^2\theta - 1)$$

where θ is an angle between the magnetic field B_0 and the vector $\boldsymbol{r_{12}}$ connecting the two spins and ω_{dd} is called dipolar coupling constant which is inversely proportional to the distance between the two spins. The dipolar coupling leads to a splitting of the EPR signal or to a broadening of the EPR spectra, depending on the size of the interaction compared to other interactions in the spin system.

1.2 Continuous wave EPR and pulsed EPR

There are two common conventional methods, namely continuous wave (CW) EPR and pulsed EPR. EPR spectra can be recorded at different frequencies: L-band ($\approx$1-2 GHz), S-band (2-4 GHz), X-band (8-10 GHz), Q-band ($\approx$ 35 GHz) and W-band ($\approx$ 90 GHz). The choice of frequency band depends on the specific type of interactions of interest that contributes to the system spin Hamiltonian discussed later.

There are limitations of spectral resolution in CW EPR. However, some EPR applications still make use of CW methods as the recording and interpretation of pulsed EPR spectra requires sophisticated technical equipment. A limitation of pulsed EPR is the low measuring temperatures required because of the short relaxation times of the transverse magnetization involved in pulse experiments, especially for transition metal ions. CW EPR spectra, on the other hand, can be recorded at room temperature for a large number of spin systems, including radicals and transition metal ions. The additional information about weakly coupled nuclei and relaxation properties of the spin system that can be obtained by manipulating the spins with sequences of MW pulses justifies the efforts put into the development of new pulse methods. The enhancement of forbidden transitions or establishing of correlations via 2D spectroscopy are examples of such manipulations. Nevertheless, CW and pulse EPR are complementary and only the exploitation of the two gives a reliable picture of the spin system.

1.2.1 Continuous wave EPR

In the case of continuous wave (CW) EPR the sample is continuously irradiated by microwaves at a fixed frequency, while an external magnetic field B_0 is swept. B_0 causes a splitting of the energy levels of the spin system. In case of spin 1/2 system such as electrons (Figure 1.1), the system is characterized by two quantum mechanical states, one with its magnetic moment parallel to B_0 and one antiparallel. The parallel state has lower energy and at thermal equilibrium, there is a surplus of electron spins in the parallel state according to the Boltzmann distribution. Therefore, there is a net magnetization parallel to the z axis. A microwave radiation source creates a standing wave inside the resonator. The resonators are designed to ensure that the magnetic field component is maximum in the center, while the electric field component is to be minimized there. The magnetic component of the microwave radiation B_1 is perpendicular to the external magnetic field B_0. When the resonance condition ΔE = $h\nu$ is satisfied, B_1 causes spin transition between the energy levels, which is detected as energy absorption, constituting an EPR signal.

1.2.2 Pulsed EPR

Due to the limitations of spectral resolution, CW EPR cannot always be used as an EPR spectroscopy method. Pulsed EPR provides better resolution separating different interactions from each other. Different pulse sequences such as hyperfine splitting, relaxation times, dipolar couplings, etc., were developed for investigating different properties of the spin system.

In pulsed EPR, the microwave radiation is in the form of a pulse, consisting of different frequencies. The circuity that generates the pulse consists of attenuators and phase shifters to adjust the length and phase of the pulses and also to apply phase cycling to eliminate unwanted echoes. The generated pulses are of an order of nanoseconds. The pulse rotates the magnetization vector toward the x-y plane. The angle by which the net magnetization vector is rotated is commonly called the tip angle and it is equal to

$$\beta = \gamma B_1 t_p \qquad \text{1.11)}$$

where γ is the gyromagnetic ration of electron, B_1 is the amplitude of the pulse and t_p is the duration of the pulse. Pulses are often labeled by their tip angle, i.e., a $\pi/2$ pulse corresponds to a rotation of magnetisation vector by $\pi/2$. The most commonly used tip angles are $\pi/2$ and π (90 and 180 degrees). The tip angle depends on both the amplitude of B_1 and the duration of the pulse. For instance, a pulse with amplitude B_1 of 10 Gauss and the duration of approximately 9 ns results in a $\pi/2$ pulse. The pulse Hamiltonian in the rotating frame, which is described in next chapter, can be expressed as

$$H_p = \frac{\gamma B_1}{2} \left(e^{-i\phi} S_+ + e^{i\phi} S_- \right) \qquad \text{1.12)}$$

where ϕ is the phase of the pulse and S_+, S_- are the raising and lowering spin operators.

It is important to note that in pulsed ERP spectroscopy, there is usually a time, known as deadtime, after a microwave pulse during which no measurements can be performed due to the ringing of high frequency pulses in the resonator. This issue can be overcome via over-coupling of the resonator and reducing its quality factor Q, which leads to reduced sensitivity and increased excitation bandwidth.

1.3 Pulsed dipolar spectroscopy

Weak interactions between two and more electron spins can be measured via dipolar spectroscopy. The object of the measurements is a distance distribution between the spins of interest. The data on distance distribution between different paramagnetic centers at different points of the macromolecule of interest can be utilized for structural studies. Depending on the length of the distances measured, different techniques can be used. For shorter distances in the range of $1 - 1.7$ nm CW EPR can be used, and the distances can be extracted from the line broadening of the spectrum. The double quantum coherence (DQC) spectroscopy is used to determine distances in the range of 1-5 nm. For longer distances in the range of $8 - 12$ nm, Double Electron-Electron Resonance (DEER), also called Pulsed Electron Double Resonance (PELDOR) (El Mkami 2015), can be employed.

For structural studies of biological systems, EPR dipolar spectroscopy has an advantage over the well-established X-ray crystallography and solution-state NMR methods, because it allows to study complexes that cannot be crystallised or are too large for efficient NMR investigation. EPR can also provide information about longer distance constraints than NMR, which is typically limited to a range of around 0.5 nm.

Most often, nitroxide spin labels are used for dipolar EPR spectroscopy (Misra *et. al.* 2009). Other spin labels such as gadolinium spin labels, Gd^{3+}, a cryptand ligand that, as a unit, replaces the organic nitroxide, (Dalaloyan *et. al.* 2015), (Raitsimring *et. al* 2007) are extensively used in various studies.

1.3.1 The Pake pattern and distance measurements

When two spins are distant from each other more than 1.5 nm, the exchange spin-spin interaction can be neglected. In this case, the spin Hamiltonian of two weakly coupled electron spins with $S_A = S_B = 1/2$ can be written as follows:

$$H(S_A, S_B) = \frac{\beta_e}{\hbar} B_0 g_A S_A + \frac{\beta_e}{\hbar} B_0 g_B S_B + H_{dd} \qquad 1.13)$$

where H_{dd} is given by Eq. (1.10). If the difference in resonance frequency of two spins is larger than a dipolar frequency ω_{dd}, the regime is called a weak-coupling regime. In this regime the splitting between most obvious peaks in the Pake pattern corresponds to ω_{dd}. In the case of strong coupling, the pseudo-secular terms of the spin Hamiltonian i.e., the B term in Eq. (1.10), which will lead to different eigenstates and eigenvalues, have to be considered.

In isotropic frozen solution all orientations of the spin system relative to the magnetic field exist and contribute to the Pake pattern shown in Figure 1.2. (a) Schematic representation of a two-electron system and definition of the angle ϑ between the magnetic field $\boldsymbol{B_0}$ and the distance vector $\boldsymbol{r_{12}}$. (b) The DEER (double electron-electron resonance) signal for two spins obtained by a weighted sum of the differences between the two pairs of EPR transition frequencies over all values of ϑ in the weak-coupling regime. The position of the turning points in the spectrum (shown with arrows in Figure 1.2) defines the inter-spin distance r_{12} ($\omega_{dd} = \frac{\mu_0}{4\pi\hbar} \frac{g_1 g_2 \beta_e^2}{r_{12}^3}$). For short distances, the dipolar interaction is sufficiently large to cause broadening of the EPR spectrum, corresponding to a convolution of the EPR spectrum of the isolated spins with the Pake pattern due to the dipolar interaction between the spins. DEER can, therefore, be used for determination of long distances.
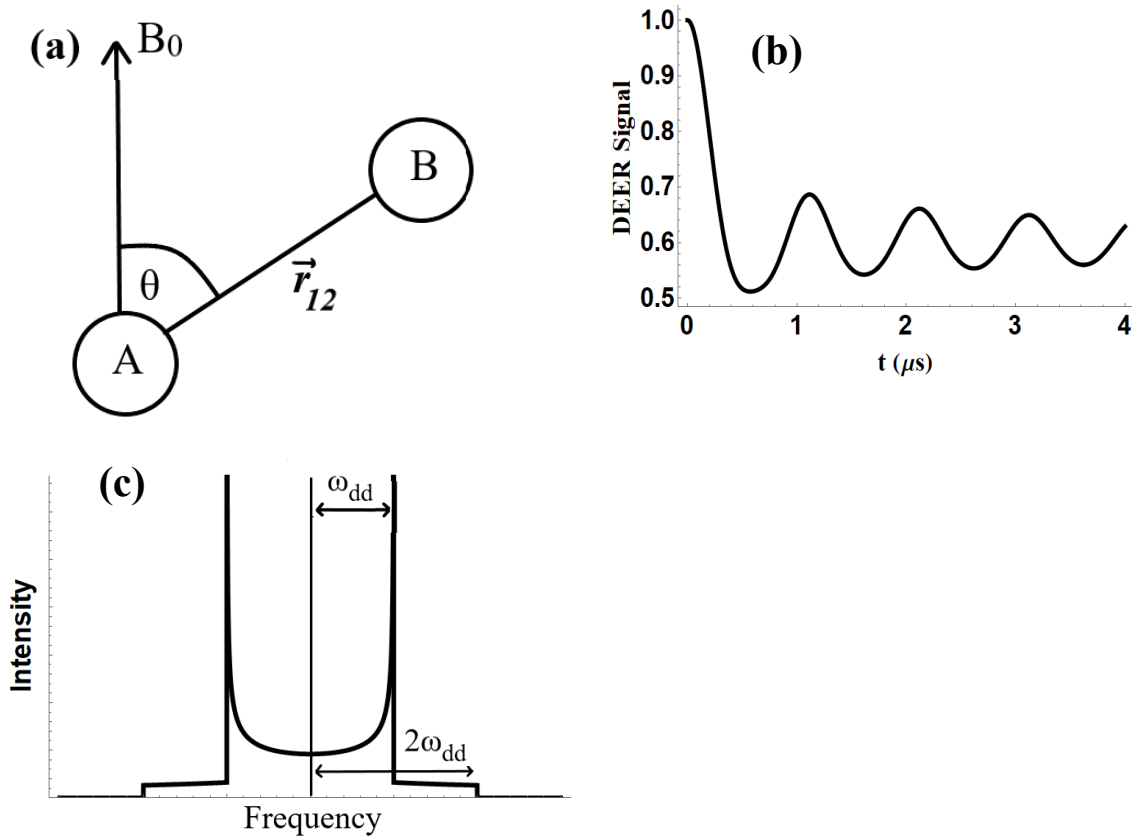
Figure 1.2. (a) Schematic representation of a two-electron system and definition of the angle θ between the magnetic field $\boldsymbol{B_0}$ and the distance vector $\boldsymbol{r_{12}}$. (b) The DEER (double electron-electron resonance) signal for two spins obtained by a weighted sum of the differences between the two pairs of EPR transition frequencies over all values of θ in the weak-coupling regime. (c) The Fourier transform of DEER signal shown in (b), known as the Pake pattern or Pake doublet.

1.4 Relaxation

In an EPR experiments the spin system is perturbed by either oscillating microwave field or microwave pulses and then returns to its state of equilibrium, which is called relaxation.

8

Relaxation defines a linewidth in CW EPR. In pulsed EPR, the relaxation time determines the length of the pulse sequence used and its repetition time.

Depending on a particular spin system, different processes can be involved in relaxation. Typically, two types of processes occur: spin-lattice relaxation, and spin-spin relaxation. Both types of relaxation are briefly discussed below, but more details can be found in (Misra 2011).

1.4.1 Spin-lattice relaxation

The spin-lattice relaxation is characterised by relaxation time T_1. Due to dynamic interactions and energy exchange between electron spins and the surrounding environment (solution, powder or crystal lattice), electron spins flip, and the magnetisation vector returns to the state of their equilibrium position along the direction of $\boldsymbol{B_0}$ (z-axis).

Different processes can cause the spin-lattice relaxation process: molecular motion causing anisotropic interactions like hyperfine, exchange or electron dipole-dipole interaction which perturbs a local field of the electron spin and causes its flip. Collisions with other molecules like oxygen or metal ions cause longitudinal relaxation as well. In solid state spin-lattice -relaxation can be caused by molecular vibrations which is due to the interaction between the lattice and spins.

1.4.2 Spin-spin relaxation

Spin flips can occur with no energy exchange with the surroundings and can cause a loss of phase coherence in the plane perpendicular to B_0 direction (x-y plane). Phase coherence can be lost due to two processes: (i) spin-lattice relaxation and (ii) spin flip-flop. The term phase memory time T_m, as used in EPR experiments, includes any processes that cause the loss of phase coherence, including spin-spin relaxation (Schweiger and Jeschke 2001). If we consider two spin systems, one of those (spin system A) is excited and the other one (spin system B) is not. The magnetic field of spins A is influenced by dipolar coupling to spins B. If spins B experience spin-spin or spin-lattice relaxation, that process will contribute to T_m of spins A that is inversely proportional to the concentration of spins B. If spins B are nuclear spins, the process is called nuclear spin diffusion. This process is typically the main contributor to T_m and can be reduced via sample deuteration (El Mkami, Ward, et al. 2014). If spins B are electronic spins, the process is called spectral diffusion

When the spin magnetization is shifted to a different region of the EPR spectrum, the resonance frequency of the spin changes, which contributes to T_m. An example of such a contribution is spectral diffusion. Spectral diffusion happens when only part of the spins is excited because of limited bandwidth of the resonator. When magnetisation of spins A changes under the influence of spins B as discussed earlier, the resonance frequency of spins A can change to fall outside of the resonator bandwidth. The magnetization of spins B can also change due to the same process, and the resonance frequency for spins B can change to fall within the detection window, replacing spins A and contributing to relaxation.

The local magnetic field around each spin changes due to dipolar interaction during a pulse, depending on the position of the neighbor spins. This process is called instantaneous diffusion.

1.4.3 Relaxation, as treated in Liouville space

Hilbert-space formulation cannot be directly used to calculate relaxation effects rigorously, because the matrix elements of the relaxation superoperator require a pair of double indices, based on the eigenbasis of the Hamiltonian operator, which are not amenable to use in Hilbert space formulations, see e.g., Stoll (2009). Misra *et al*, (2009). Misra (2011), Misra and Freed (2011), Schwartz *et al*, (1982), Gamliel and Levanon (1995), Håkansson *et al*, (2013), Franck *et al*, (2015). Accordingly, one needs to perform numerical simulation technique for calculating pulsed EPR experiments by treating the Liouville-von Neumann (LVN) equation as a matrix differential equation in Liouville space to take into account the relaxation effects rigorously. The LVN equation is an exact quantum-mechanical equation of motion for the density matrix. This equation is valid even for relatively fast random processes, and is therefore especially suitable for EPR, where the natural time scale is so short that the random processes are not usually fast on this time scale (Lee, Patyal and Freed 1993).

1.5 Organization of the thesis

The organization of this thesis is as follows. The procedure for solution of the LVN equation to calculate the pulsed EPR signal is developed in Chapter 2. Thereafter, the details of the calculation of Correlation Spectroscopy (COSY), two-pulse Double Quantum (DQ), five-pulse Double Quantum Modulation (DQM) and four-, five-, six-pulse Double Quantum Coherence (DQC) signals, along with a detailed study of their applicability for distance measurements are given in Chapter 3. The technique of doubly rotating frame to calculate DEER signal and its application to estimate distance distribution for the system of two coupled nitroxides and two coupled Gd^{3+} ions are presented in Chapter 4. Chapter 5 deals with cylindrical and conical models of thermal fluctuation of spin-Hamiltonian parameters which leads to rigorous calculation of relaxation matrix elements in Liouville space. The electron spin-echo decay of SECSY signal induced by dipole-dipole interaction between the electrons in a malonic acid crystal, modulated simultaneously by the spectral diffusion and instantaneous diffusion mechanisms is analyzed in Chapter 6. The concluding remarks and future perspectives are included in Chapter 7.

Chapter 2

2. Calculation of pulsed EPR signal

A pulsed EPR experiment consists of a series of N microwave pulses separated by $N-1$ periods of free evolutions of length t_i. The EPR echo signal from a paramagnetic sample is detected after a delay of length t_N To describe the time evolution of the density matrix, Liouville-von Neumann equation is used.

2.1 Liouville-von Neumann equation

The time evolution of the density matrix is described by the LVN equation which gives an exact quantum-mechanical description of motion for the density matrix. This equation is valid even for relatively fast random processes, and is therefore especially suitable for EPR, where the natural time scale is so short that the random processes are not usually fast on this time scale (Gamliel and Levanon 1995).

The LVN equation which governs the time evolution of the density matrix during free evolution, i.e., in the absence of a pulse is expressed as (Abragam (1961), Jeener (1982), Redfield (1957), Gamliel and Levanon (1995), Slichter (2013)):

$$\frac{d}{dt}\chi(t) = -i[\hat{H}_0, \chi(t)] + \widehat{\hat{\Gamma}}\chi(t) \qquad (2.1)$$

where $\chi = \rho - \rho_0$ is the reduced density matrix with $\rho_0 \propto \exp(-\hat{H}_0/kT)$ being the initial density matrix and discussed in the next Chapter in Sec 3.1.2, and H_0 is the static spin-Hamiltonian. In Eq. (2.1), $\widehat{\hat{\Gamma}}$ is the relaxation superoperator in Liouville space whose elements are usually determined phenomenologically. Equation (2.1) is a matrix differential equation which cannot be solved in Hilbert space, since the relaxation superoperator $\widehat{\hat{\Gamma}}$, is a four-index tensor which connects two elements of the density matrix, which are characterized by two indices each. The procedure to solve Eq. (2.1) is given in Misra and Li (2018) in details. The solution of Eq. (2.1) after time t in Liouville space is given as

$$\hat{\chi}(t) = e^{-(t-t_0)\hat{\hat{L}}}\hat{\chi}(t_0) \qquad (2.2)$$

where $\hat{\chi}$ is the column vector of dimension $n^2 \times 1$ i.e., $\hat{\chi} = Col(\chi)$, (Magnus and Neudecker 2019), (Misra and Li 2018) and the Liouville superoperator, $\hat{\hat{L}}$, is defined as

$$\hat{\hat{L}} = i\hat{\hat{H}} + \widehat{\hat{\Gamma}} = (I_n \otimes \hat{H} - \hat{H} \otimes I_n) + \widehat{\hat{\Gamma}} \qquad (2.3)$$

In Eq. (2.3), I_n is unit matrix of dimension $n \times n$ and $\otimes$ stands for the direct product.
The spin relaxation is usually neglected during the application of a pulse as it has negligible effect since the duration of the pulses ($\sim$5-10 ns) are much smaller than the relaxation time (500-1000 ns). Then, the evolution of the density matrix due to the pulse can described in Hilbert space, as follows:

$$\frac{d}{dt}\rho(t) = -i[(\hat{H}_0 + \hat{H}_p), \rho(t)], \qquad (2.4)$$

where H_p is the pulse Hamiltonian expressed by Eq. 1.12).

The density matrix is transformed by the application of a pulse of duration t_p. The solution of Eq. (2.4), neglecting relaxation during the pulse, is given as (Saxena and Freed 1997), (Misra *et. al* 2009):

$$\rho(t_0 + t_p) = e^{-i(H_0 + H_p)t_p} \rho(t_0) \, e^{i(H_0 + H_p)t_p} \tag{2.5}$$

2.2 Coherence pathways and phase cycling

The selection of well-defined coherence transfer pathways is an essential feature in COSY, SECSY, echo-ELDOR, two-pulse DQ, five-pulse DQM, four-, five-, six- pulse DQC experiments. Multi-pulse sequences produce a series of free induction decays (FIDs) and echos. Among these, only one is of actual interest. All the others distort the measurement but can be removed by phase cycling (Bodenhausen *et. al.* 1984, Gemperle *et. al* 1990).

Phase cycling is based on the concept of coherence order (Bodenhausen *et. al.* 1984, Gemperle *et. al* 1990). For a paramagnetic sample containing one electron with spin $S = 1/2$ each, there are three possible coherence orders, p. Coherence order $p = 0$ corresponds to longitudinal magnetization and is due to spins parallel or antiparallel to the external magnetic field direction. Coherence orders $p = +1$ and $p = -1$ represent transverse magnetization and corresponds to spins rotating in a plane perpendicular to the external magnetic field. Coherences with order $0, +1$ and -1 correspond to the S_z, S_+ and S_- components of the density operator, respectively. Higher coherence orders such as $p = \pm 2$ are achieved in the systems with two coupled electrons.

The path describing the progress of a coherence order in a pulse sequence is called a coherence transfer pathway. It is possible to change the coherence level by applying a pulse. On the other hand, during the time interval between the applications of the pulses the coherence level does not change.

All the multi-pulse experiments start with zero order coherence (z-magnetization) and should end with a coherence order of -1, which is by convention the one that is detected by the quadrature detector. Without quadrature detection the +1 coherences would be equally detectable, all higher orders are not correlated with observable magnetization.

The pulse scheme and the coherence pathway of a simple two-pulse EPR experiment is shown in Figure 2.1. Pulse scheme and the relevant coherence pathway for a two-pulse EPR experiment. The pulses are shown with P1 and P2. The coherence order changes after the application of each pulse. The pathways shown with S_c- and S_c+ produce echo and free induction decay due to the first pulse, respectively.
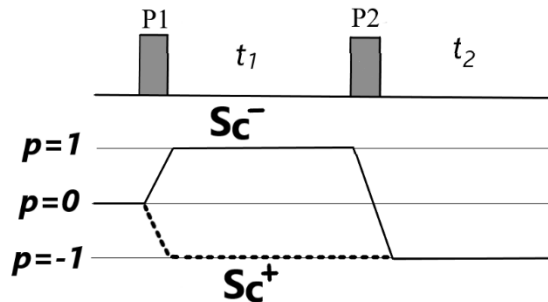
Figure 2.1. Pulse scheme and the relevant coherence pathway for a two-pulse EPR experiment.

In the numerical simulations, the density matrix is projected onto the coherence pathways of interest after the application of a pulse by taking the *Hadamard* product, $\rho^{(k)} = P_k \circ \rho$, of the projection operator matrix, P_k, with the density matrix, ρ, resulting from the application of a pulse. The Hadamard product retains only the relevant elements of the density matrix which correspond to the coherence pathways of interest, putting all the other elements equal to zero.

2.3 Finite and infinite pulses

When the amplitude of the microwave pulse is much larger than the static spin Hamiltonian, one can assume that the microwave pulses are perfect π or $\pi/2$ pulses which is called as the infinite pulse (also known as non-selective pulse, ideal pulse, perfect pulse) approximation (Misra *et. al.* 2009). An ideal $\pi/2$ pulse starting from coherence pathway $p = 0$ generates exclusively coherence orders $p = \pm 1$ and an ideal π pulse inverts the coherence order i.e., $p = 0 \rightarrow p = 0$ and $p = \pm 1 \rightarrow \mp 1$ (Borbat and Freed 1999).

2.4 Final density matrix and EPR signal

The final density matrix for relevant coherence pathway(s) from a sequence of pulses can be obtained. To this end, one can use Eq. (2.5) for the evolution of the density matrix under the application of a pulse followed by free evolution of the density matrix using Eq. (2.2). Having the final density matrix, ρ_f, the complex EPR echo signal corresponding to S_{c^-} pathway can be calculated as (Saxena and Freed 1997)

$$Signal(t) = Tr(S_+\rho_f) \tag{2.6}$$

where Tr stands for trace and S_+ is the raising operator.

2.5 Rotating frame

The magnetization vector in a sample can often undergo very complicated motions. A useful technique, widely used in EPR, is to go to a rotating coordinate system, referred to as the rotating frame. From this alternative point of view, much of the mathematics is simplified and an intuitive understanding of the complicated motion can be gained. The classical picture of the rotating frame is often clearer and more productive than the quantum mechanical picture. Even though the phenomenon on a microscopic scale is best described by quantum mechanics, a bulk property of the sample, namely magnetization, is measured in EPR which is nicely described from a classical point of view (Schweiger and Jeschke 2001).

In order to describe the rotating frame, one needs to first establish a fixed axis system of reference frame. The most common fixed frame is the lab frame which consist of three stationary mutually perpendicular axes. The z-axis is considered parallel to the external magnetic field, B_0, the x-axis is parallel to the microwave field, B_1 and the y-axis is orthogonal to the x and z axes.

When an electron spin is placed in a magnetic field, a torque is exerted on the electron spin, causing its magnetic moment to precess about the magnetic field. The angular frequency of the precession is called Larmor frequency and it is related to the magnetic field by

$$\omega_L = -\gamma B_0 \qquad (2.7)$$

where γ is the gyromagnetic ratio of the electron. The effect of B_1 on the magnetization is very difficult to envision when the magnetization vector is rotating about the z axis. Alternatively, one can observe what is happening from a rotating coordinate system. For simplicity, first we assume a system which is on resonance i.e., the frequency of the microwave pulse matches the Larmor frequency

$$\omega_L = \omega_0 \qquad (2.8)$$

where ω_0 is the microwave frequency. By rotating the coordinate system at an angular velocity of ω_0, one can make the magnetization components precessing at the Larmor frequency to appear stationary. Three very interesting features about the system in the rotating frame should be noted: (A. a. Schweiger 2001)

1) The effect of the static magnetic field B_0 disappears. In the rotating frame the precession of the magnetization vector (and that of its component individual spins) around B_0 is no longer occurring.
2) The microwave field is no longer rotating but appears static.

3) The magnetization vector appears to begin a new precession around B_1. Since B_0 no longer exists in this frame of reference, the only magnetic field acting on the magnetization is the now stationary B_1 field. As a result, the magnetization vector will precess around B_1 with frequency $\omega_1 = \gamma B_1$.

EPR spectra contain different frequencies so not all parts of the EPR spectrum can be exactly on-resonance simultaneously. Therefore, one has to consider off-resonance effects as well. When the part of EPR spectrum under study is not on resonance i.e., $\omega \neq \omega_0$, the magnetization vector appears to rotate in the x-y plane with a rate equal to the frequency differences $\Delta\omega = \omega - \omega_0$. In the case of $\Delta\omega = 0$, the rotation rate is zero which means that the system is exactly on resonance. For off-resonance case, the magnetization rotates counter-clockwise ($\Delta\omega > 0$) or clockwise ($\Delta\omega < 0$). As a consequence, the microwave magnetic field B_1 tips the magnetization into x-y plane differently because $B_0 = \frac{\Delta\omega}{\gamma}$ does not disappear completely. In other words, the magnetization is not tipped by only B_1 but by the vector sum of B_1 and B_0 which is called effective magnetic field, B_{eff}. The magnetization is then tipped about B_{eff} at a faster effective rate ω_{eff}

$$\omega_{eff} = \sqrt{\omega_1^2 + \Delta\omega^2} \qquad (2.9)$$

As shown in Figure 2.2, B_{eff} does not lie in the x-y plane as B_1 does. As a result, the magnetization does not move in an arc as it does on-resonance, but instead its motion is described by a cone.
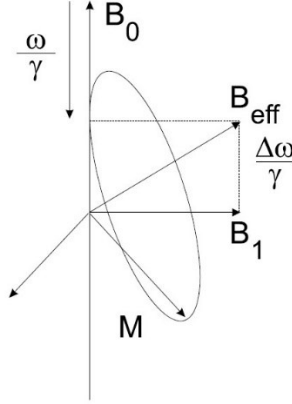
Figure 2.2. The effective microwave magnetic field in the rotating frame

2.6 Polycrystalline averaging

The sample under study in an EPR experiment can be a polycrystalline (powder) material. The pulsed EPR signal for a polycrystalline sample without any dipolar interaction is obtained by averaging the signal given by Eq. (2.6), over the Euler angles $\eta = (\theta, \phi)$ which are defined by the relative orientation of the principal axes-in which the g-matrix is diagonal-with respect to the lab axes. For isotropic distribution of spins there exists a symmetry in the calculated EPR signal with respect to the different quadrants of the unit sphere. Therefore, the EPR signal for a polycrystalline sample is obtained by integrating the signal over (θ, ϕ), considering the spins included in a quarter of the unit sphere (Misra $et.$ $al.$ 2009). It is given as

$$Signal_{powder}(t) = \frac{4}{(4\pi)} \int_0^\pi d\phi \int_0^{\pi/2} S(t) \, d(\cos \theta) \qquad (2.10)$$

The multiplicative factor of 4 appearing in Eq, (2.10) takes into account the signal over the entire unit sphere, whereas the division by 4π is made to take into account the isotropic distribution of spins (Misra $et.$ $al.$ 2009).

Chapter 3

3. Applicability of multi-pulse EPR sequences for distance measurements

In this chapter, multi-pulse EPR signals in biological systems using nitroxide biradicals are calculated and their feasibility for distance measurements is investigated. For the numerical calculations of the pulsed-EPR signals for a polycrystalline sample and its Monte-Carlo average over the various orientations of the two nitroxide dipole moments, the procedure presented in Chapter 2 is used. The signals are first calculated in the absence of relaxation and are extended to calculate the signal in the presence of relaxation using a stretched exponential (Stein *et.al.* 2019, Pfenninger *et.al* 1995).

3.1 Numerical procedure

3.1.1 Spin Hamiltonian of coupled nitroxide system

The spin Hamiltonian for the coupled nitroxides system in the frozen state is expressed in the rigid limit as (Saxena and Freed 1997, Misra $et.al.$ 2009, Borbat and Freed 2009)

$$H_0 = H_{01} + H_{02} + H_{12} \tag{3.1}$$

Here, the static Hamiltonian of the two nitroxide radicals are denoted by H_{0k}; $k = 1,2$, which includes the Zeeman and hyperfine interactions. Assuming the respective g and hyperfine (HF) matrices of each nitroxide to have coincident principal-axis systems, the effective H_{0k} in the high-field approximation (Saxena and Freed 1997) is expressed as:

$$H_{0k} = C_k S_{z_k} + A_k S_{z_k} I_{z_k} + \frac{1}{2} B_k \, S_{z_k} I_{+k} + \frac{1}{2} B_k^* S_{z_k} I_{-k}; \quad k = 1,2 \tag{3.2}$$

where the expressions for the coefficients C, A and B are provided in Appendix A and S_{z_k}, I_{z_k}, I_{+k} and I_{-k} are the spin operators for the two nitroxides. In Eq. (3.1), H_{12} includes the dipolar and exchange couplings between the two nitroxide radicals, expressed as

$$H_{12} = \frac{D}{2}(3cos^2\theta - 1)(S_z^2 - \boldsymbol{S}^2/3) + J\left(\frac{1}{2} - 2\,\boldsymbol{S_1}.\boldsymbol{S_2}\right) \tag{3.3}$$

where J is the exchange-interaction constant between the two electrons, θ is the polar angle of the orientation of the static magnetic field with respect to the dipolar axis that connects the magnetic dipoles of the two nitroxides, as shown in Figure 3.1, $\boldsymbol{S} = \boldsymbol{S_1} + \boldsymbol{S_2}$ is the total electron spin and D denotes the dipolar interaction constant, expressed in terms of r, the distance between nitroxides, as (Saxena and Freed 1997, Misra $et.al.$ 2009)

$$D = \frac{3\gamma_e^2\hbar}{2r^3} \tag{3.4}$$
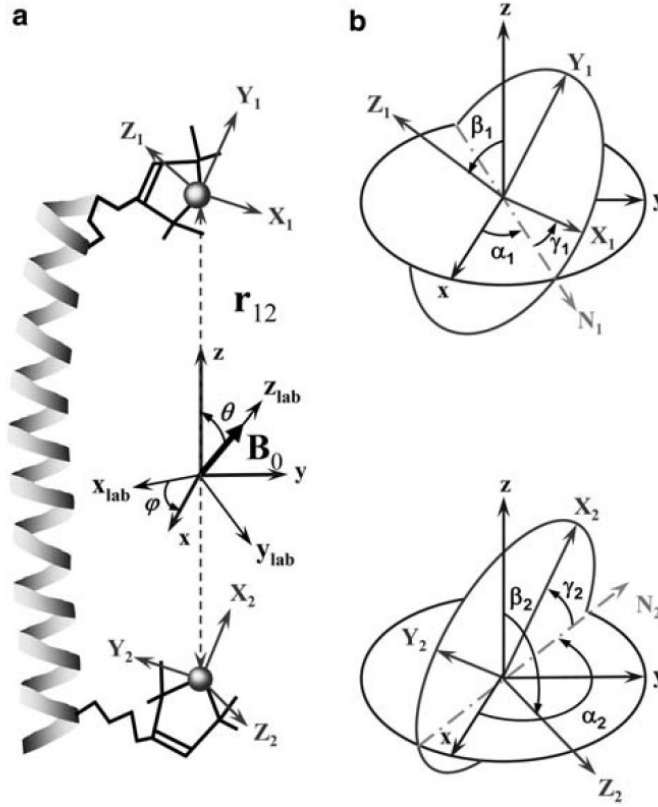
Figure 3.1. (a) The configuration of the two nitroxides in the biradical as shown in the dipolar frame of reference. The z-axis of the dipolar frame is chosen to be along the vector $\boldsymbol{r}$ connecting the magnetic dipoles of the nitroxides. The relative orientation of the laboratory frame, along with its z_{lab} axis parallel to the external magnetic field, B_0; the dipolar frame is defined by the Euler angles $\eta = (0, \theta, \phi)$ with respect to the lab frame; (b) The set of Euler angles $\lambda_k = (\alpha_k, \beta_k, \gamma_k)$, $(k = 1, 2)$, defining the orientations of the principal axes of the hyperfine and g-matrices for the nitroxides 1 and 2 in the dipolar frame with respect to molecular frame of reference, as denoted by X_k, Y_k, Z_k, $k = 1,2$; here N_1 and N_2 indicate the lines of nodes for the frames of the two nitroxides. For the present numerical calculations, the x axis of the magnetic frame of the first nitroxide is chosen to be along the line of nodes of the first nitroxide, N_1, so the value of α_1 becomes zero. (This figure is reproduced from Misra *et. al.* 2009 by permission.)

In Eq. (3.4) γ_e is the gyromagnetic ratio of the electron and $\hbar = h/2\,\pi$ is the reduced Planck's constant. *In the present work, the constant $d = 2/3\,D$ is used and will be referred to as the "dipolar constant" hereafter.*

The Hamiltonian of a pulse with amplitude, B_1, of radiation microwave magnetic field is given as (Saxena and Freed 1997, Misra *et. al.* 2009)

$$H_p = \frac{\omega_1}{2}\left(e^{-i\phi}S_+ + e^{i\phi}S_-\right) \tag{3.5}$$

17

where $\omega_1 = B_1\gamma_e$, ϕ is the phase of the pulse and $S_\pm$ are the raising/lowering operators of the total electronic spin of the coupled nitroxide system in the 36×36 Hilbert-space, defined as

$$S_\pm = S_{\pm S_1} \otimes \mathbb{1}_{S_2} \otimes \mathbb{1}_{I_1} \otimes \mathbb{1}_{I_2} + \mathbb{1}_{S_1} \otimes S_{\pm S_2} \otimes \mathbb{1}_{I_1} \otimes \mathbb{1}_{I_2} \qquad (3.6)$$

where $S_{\pm S_k}; k = 1,2$ are expressed in terms of the Pauli matrices σ_x and σ_y as $S_{\pm S_k} = \frac{1}{2}(\sigma_{x_k} \pm i\sigma_{y_k})$; $\mathbb{1}_{S_k}$ and $\mathbb{1}_{I_k}$; $k = 1,2$, are identity matrices in the electronic 2×2 and nuclear 3×3 spaces, respectively, of each nitroxide, and $\otimes$ stands for the direct product.

In the numerical calculations performed here, the magnetic basis with the basis vectors $|M_{S_1}, M_{S_2}, m_{I_1}, m_{I_2}\rangle$ is used to calculate the matrix elements. Here $M_{S_1}, M_{S_2}, m_{I_1}, m_{I_2}$ are the two electronic and the two nuclear magnetic quantum numbers, respectively, for the two nitroxides. In this basis, the static Hamiltonian H_0 is not diagonal. The eigenvalues of H_0 are obtained by diagonalizing it as $U^\dagger H_0 U = E$, where † denotes the Hermitian adjoint of a matrix and E is the diagonal matrix, whose diagonal elements are the eigenvalues, whereas the columns of the matrix U are the corresponding eigenvectors.

3.1.2 Initial density matrix

The initial density matrix, ρ_0, required to calculate the signal for a multi-pulse sequence, is governed by the Boltzmann distribution for the two electrons in thermal equilibrium, each with spin $\frac{1}{2}$. The initial density matrix in the high-temperature approximation, neglecting the hyperfine interaction, which is much less than the electronic Zeeman interaction, is:

$$\rho_0 = \frac{\exp(-\hat{H}_0/k_B T)}{Tr[\exp(-\hat{H}_0/k_B T)]} \propto (\mathbb{1} - \frac{\hbar\omega_0}{k_B T} S_z + \cdots), \qquad (3.7)$$

where H_0 is given by Eq.(3.1); k_B is Boltzmann constant; T is the temperature; S_z is the z-component of the total electronic spin $S = S_1 + S_2$; and $\hbar\omega_0$ is the Zeeman splitting of the total electron spin. During the evolution of the initial density matrix, ρ_0, to the final density matrix, ρ_f, the term $\mathbb{1}$ in Eq. (3.7) remains invariant. Thus, it does not contribute to the signal $\{= Tr(S_+ \rho_f)\}$, since $Tr(S_+ \mathbb{1}) = 0$. For the calculation of the (unnormalized) signal, one can then replace ρ_0, as follows:

$$\rho_0 \rightarrow S_Z = S_{z_1} + S_{z_2} = (\frac{\sigma_{z_1}}{2}) \otimes \mathbb{1}_{S_2} \otimes \mathbb{1}_{I_1} \otimes \mathbb{1}_{I_2} + \mathbb{1}_{S_1} \otimes (\frac{\sigma_{z_2}}{2}) \otimes \mathbb{1}_{I_1} \otimes \mathbb{1}_{I_2} \qquad (3.8)$$

where $\sigma_{z_i}; i = 1,2$ are the Pauli spin matrices for the two electron spins.

3.1.3 Relaxation matrix elements

Following (Saxena and Freed 1997), the following relaxation superoperator in Liouville space is considered for the numerical calculations of this chapter:

$$\hat{\bar{\Gamma}}_{ij,kl} = -\delta_{ij}\delta_{kl}\frac{1}{(T_1)_{ik}} - \delta_{ik}\delta_{jl}(1-\delta_{ij})\frac{1}{T_2^{S,D}} \qquad (3.9)$$

where $(T_1)_{ik}$ are the spin-lattice relaxation times between the populations ii to kk, which are operative on the coherence pathway $p = 0$, and $T_2^{S,D}$ are the spin-spin relaxation times operative over the $p = \pm 1$ and $p = \pm 2$ pathway, respectively. The indices in Eq. (3.9) are the spin quantum numbers that represent the eigenstate of spin Hamiltonian expressed by Eq. (3.1). It is noted that, in general, different transitions will have different spin-spin relaxation times, $(T_2^{S,D})_{ij}$. However, as shown in (Misra and Salahi 2021), these relaxation times are only slightly different from each other. Thus, they are here approximated by an average spin-spin relaxation time $T_2^{S,D}$ in Eq. (3.9).

3.1.4 Calculation of polycrystalline signal and Pake doublets in the absence of relaxation

The multi-pulse EPR signals for a polycrystalline sample is obtained by averaging the signal for chosen orientations of the two nitroxide dipoles with respect to the dipolar axis, oriented at an angle $\eta = (\theta, \phi)$ with respect to the lab axes, over the unit sphere. The EPR signal for a polycrystalline sample, for isotropic distribution of spins, is obtained by integrating the signal over (θ, ϕ), considering the spins included in a quarter of the unit sphere due to the symmetry of the signal, as confirmed numerically by also integrating the signal over the hemisphere and the full sphere for some cases considered here. It is given as

$$Signal(t) = \frac{4}{(4\pi)} \sum_{\lambda_1,\lambda_2} \int_0^\pi d\phi \int_0^{\pi/2} S(\eta, \lambda_1, \lambda_2) \, d(\cos\theta) \qquad (3.10)$$

In Eq. (3.10) the Euler angles $(\alpha_1 = 0, \beta_1, \gamma_1); (\alpha_2, \beta_2, \gamma_2)$ are denoted as $\lambda_j; j = 1,2$, respectively. The multiplicative factor of 4 appearing in Eq, (3.10) takes into account the signal over the entire unit sphere, whereas the division by 4π is made to take into account the isotropic distribution of spins.

The Pake doublets are calculated by averaging the signal for polycrystalline sample over the five independent Euler angles $(0, \beta_1, \gamma_1, \alpha_2, \beta_2, \gamma_2)$, keeping $\alpha_1 = 0$, which is arbitrary and considering no correlation between the orientations of the two nitroxides. This is achieved by Monte Carlo averaging over random sets of the Euler angles λ_1, λ_2, wherein the varied five independent Euler angles are chosen using random numbers. A set of twenty such simulations seemed to be sufficient as our simulations show. Thus, a total of 180 θ-values and 180 ϕ-values were used over a quarter of a unit sphere, as indicated by the limits of integrations in Eq. (3.10), along with 20 sets of five randomly chosen Euler angles (λ_1, λ_2). This amounts to an average over $180 \times 180 \times 20 = 6.48 \times 10^5$ simulations. (Simulation over a quarter of the unit sphere is sufficient as the other quarters yield the same values as verified by independent simulations.)

3.1.5 Gaussian inhomogeneous broadening

Different spins in a sample (liquid or solid) have slightly different resonant frequencies because they are in slightly different local environments. This results in the inhomogeneous

broadening of the observed signal. The observed broadening of the spectrum arises from a superposition of a large number of slightly different spectra. In order to consider the inhomogeneous broadening effect, the final signal is multiplied by a Gaussian factor $e^{-2\pi^2\Delta_G^2(t_2-t_1)^2}$ where Δ_G is the Gaussian inhomogeneous broadening parameter and t_1, t_2 are the times after the first $\pi/2$ and the last pulse in a pulse sequence, respectively.

3.2 Two-pulse COSY at Ku-band (17.3 GHz)

The pulse sequence for a S_c- COSY experiment is shown in Figure 3.2, which consists of two $\pi/2$ pulses. After the application of the first pulse, the system evolves freely over time t_1 on the coherence pathway $p = +1$ by phase cycling before the application of the second pulse, after which the system evolves freely on the coherence pathway $p = -1$ by phase cycling. Thereafter, the signal is measured after time t_2. The echo occurs at the time $t_2 = t_1$, which is measured in the one-dimensional COSY sequence. In the experiment the time t_1 is stepped by $\Delta t = t_{max}/n$, where n is the number of data points for which the signal is measured, e.g., $n = 100$, and t_{max} is the maximum time of free evolution after the first pulse.
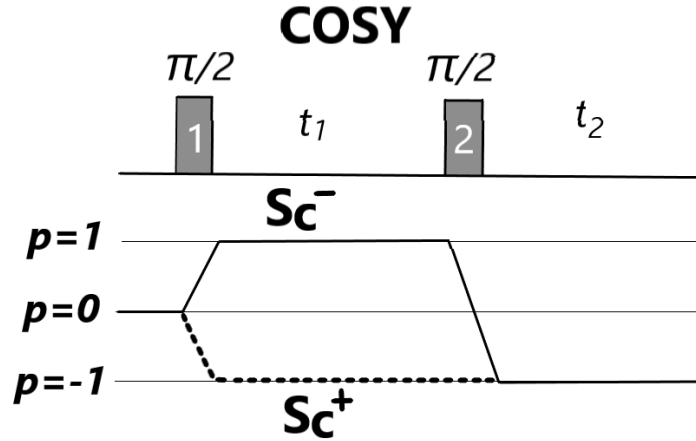
Figure 3.2. The pulse scheme and the relevant coherence pathway for two-pulse COSY showing S_c^- and S_c^+ pathways. Here, p is the coherence order, which represents transverse magnetization, corresponding to spins rotating in a plane perpendicular to the external field.

In the two-pulse COSY sequence as shown in Figure 3.2, the pathway $p = 0$ is not used. Therefore, the relaxation times $(T_1)_{ik}$, which appear in Eq. (3.9), affecting the populations, have no effect on the COSY signal, since the populations appear only on the $p = 0$ pathway. As for the other coherence pathways $p = \pm 1$, which do participate in the two-pulse COSY sequence considered here, only the second term on the right-hand side of Eq. (3.9) which corresponds to the $i \neq j$ elements of the reduced density matrix, affects the relaxation of the two-pulse COSY signal. In that case, the solution of LVN equation after time t, expressing the modification of reduced density matrix, χ_{ij} due to the relaxation along the $p = \pm 1$ pathways, is given as

$$\chi(t_0 + t) = e^{-t/T_2^S} e^{-iH_0 t} \chi(t_0) e^{iH_0 t} \qquad (3.11)$$

The spin relaxation will here be neglected during the application of a pulse as it has negligible effect since the duration of the pulses are much smaller than the relaxation time. Then, the evolution of the density matrix due to the pulse is described in Hilbert space, as follows:

$$\rho(t_0 + t_p) = e^{-i(H_0 + H_p)t_p}\rho(t_0)\,e^{i(H_0 + H_p)t_p} \tag{3.12}$$

where H_p is given by Eq. (3.5). After the application of a pulse, the density matrix is projected onto the coherence pathways of interest, which are: $p = 1, -1$ as shown in Figure 3.2. This is achieved, in the numerical simulation, by taking the *Hadamard* product, $\rho^{(k)} = P_k \circ \rho$, of the projection operator matrix, P_k, for the coherence pathways $p = 1, -1$ for $k = 1, 2$, respectively, with the density matrix, ρ, resulting from the application of a pulse. This Hadamard product retains only the relevant elements of the density matrix which correspond to the coherence pathways, $p = 1, -1$, putting all the other elements equal to zero. Specifically, the projection operator matrices, P_k, for the various coherence pathways are listed in Appendix B.

The two-pulse COSY signal for a single orientation of the dipolar axis (θ, ϕ) and *chosen* orientations $(\alpha_1, \beta_1, \gamma_1, \alpha_2, \beta_2, \gamma_2)$ of the two nitroxide dipoles of the biradical for the pathway S_c^- is calculated, in the absence of relaxation, using the following steps. (i) Transform the initial density matrix by the first pulse using Eq.(3.12); (ii) Apply the coherence pathway projection operator for $p = +1$ given in Appendix B to the density matrix transformed in step (i) by Hadamard product. (iii) Calculate the density matrix after free evolution of the density matrix obtained in step (ii) over the duration t_1 between the first and the second pulses using Eq. (3.11); (iv) Transform the density matrix obtained in step (iii) by the second pulse using Eq. (3.12); (v) Apply the coherence pathway projection operator for the coherence pathway $p = -1$ to the density matrix obtained in step (iv); (v) the final density matrix $\rho_f(t_1, t_2)$ is obtained after free evolution of the density matrix obtained in step (iv) over the time interval $t_2 (= t_1)$. (vi) The complex signal is obtained from the final density matrix using Eq. (2.6). (vii) The 2D COSY signal, which is a function of t_1 and t_2 is reduced to one-dimensional signal by substituting $t_2 = t_1$. It is noted that the Gaussian inhomogeneous broadening factor, $e^{-2\pi^2\Delta_G^2(t_2-t_1)^2}$, vanishes at $t_2 = t_1$. The values of the parameters used in the simulations of this chapter are listed in Table 3.1. The Flow chart for the calculation of multi-pulse EPR signal, including COSY, is given in Appendix C.

The simulations of the COSY signal considered here are those carried out over the range of dipolar coupling constants 0.5 MHz $\leq d \leq 10$ MHz, because for $d < 0.5$ MHz, one does not have enough cycles of dipolar modulation of the signal within the time period of $t_{max} \sim 7000$ ns, the maximum time over which the signal is measured. On the other hand, for $d > 10$ MHz, the modulation depth cannot be measured as discussed in Sec.3.2.3.

3.2.1 Calculation of polycrystalline signal and Pake doublets in the absence of relaxation

The two-pulse COSY signal for a polycrystalline sample is calculated with Monte-Carlo averaging over the orientations of the two nitroxide dipoles in the absence of relaxation following the procedure in Sec. 3.1.4.

3.2.2 Relaxation in polycrystalline sample

To consider the effect of the relaxation for a powder average, the stretched exponential approach is used, following (Stein *et.al.* 2019, Pfenninger *et.al* 1995), which considers the effect of different relaxation times for different orientations of the magnetic field with respect to the crystal axes, on average, by a stretched exponential with an exponent β. This is considered as follows.

Parameter	value
Static magnetic field (B_0)	6186 G (Ku-band) 3300 G (X-band)
Microwave frequency	17.3 GHz (Ku-band) 9.3 GHz (X-band)
Exchange constant (*J*)	*0* MHz
Time on the double quantum coherence pathway ($p = \pm 2$) ($t_{DQ}^{(DQM)} = t_{DQ}^{(4)} = t_{DQ}^{(5)} = t_{DQ}^{(6)}$)	26.5 ns
Relaxation time on Single-quantum coherence pathway (T_2^S)	500 ns
Relaxation time on Double-quantum coherence pathway (T_2^D)	300 ns
Dead time (T_d)	25 ns (Ku-band) 35 ns (X-band)
Stretched exponential parameter (β)	0.8
g-matrix $\widetilde{g} = (g_{xx}, g_{yy}, g_{zz})$	(2.0086,2.0066,2.0032)
Hyperfine matrix $\widetilde{A} = (A_{xx}, A_{yy}, A_{zz})$	(6.0 G,6.0 G,35.0 G)

Table 3.1. The values of the parameters used in the simulations of the multi-pulse EPR signals for the nitroxide bilabel.

Averaging over relaxation time T_2^S. According to Eq. (3.11), the effect of the relaxation for a chosen orientation of the external magnetic field with respect to the dipolar axes and the five independent Euler angles after time t is described by multiplying the calculated signal by an exponential factor $exp(-t/T_2^S(\eta, \lambda_1, \lambda_2))$, for the coherence pathway $p = \pm 1$, with the time constants $T_2^S(\eta, \lambda_1, \lambda_2)$, appropriate for that orientation. Then the cumulative effect of the relaxation, considering the two coherence pathways involved in the COSY sequence as shown in Figure 3.2, is tantamount to a multiplication of two decaying exponential functions multiplied by the calculated signal for the single orientation of the magnetic field with respect to the crystal axes as calculated in the absence of any relaxation. For a polycrystalline sample, the COSY signal is averaged over different values of (θ, ϕ), characterized by relaxation time $T_2^S(\eta, \lambda_1, \lambda_2)$, the effect of the relaxation at the top of the echo can be expressed as

$$Signal(t_1)_{Avg} = \sum_{\eta, \lambda_1, \lambda_2} Signal_0(t_1, \eta, \lambda_1, \lambda_2) \, exp(-2t_1/T_2^S(\eta, \lambda_1, \lambda_2)) \qquad (3.13)$$

where $Signal_0(t_1, \eta, \lambda_1, \lambda_2)$ is the EPR signal calculated in the absence of any relaxation. Using the same reasoning as in (Stein *et.al.* 2019, Pfenninger *et.al* 1995), considering

the variation of $T_2^S(\eta, \lambda_1, \lambda_2)$ over $(\eta, \lambda_1, \lambda_2)$ the polycrystalline average, Eq. (3.2), becomes modified, as follows (Stein *et.al.* 2019, Pfenninger *et.al* 1995),

$$Signal_{Avg}(t_1) = Signal_{0\,Avg}(t_1)\,exp\left(-[2t_1/T_{2str}^S]^\beta\right) \tag{3.14}$$

where, $Signal_{0\,Avg}(t_1)$ is the average of $Signal_0(t_1, \eta, \lambda_1, \lambda_2)$ over all orientations $(\eta, \lambda_1, \lambda_2)$ without considering the relaxation:

$$S_{0\,Avg}(t_1) = \sum_{\eta, \lambda_1, \lambda_2} S_0(t_1, \eta, \lambda_1, \lambda_2) \tag{3.15}$$

and $T_{2\,str}^S$ is the stretched relaxation times over single ($p = \pm1$ pathway) quantum states. In Eq. (3.14), β is the stretching parameter that ranges between zero and one (Stein *et.al.* 2019, Pfenninger *et.al* 1995). In the limiting case when $\beta \rightarrow 1$, Eq. (3.14) reduces to a system with orientation independent relaxation times. For the calculations of the present section, the illustrative value of $\beta = 0.8$ is used. It suffices to first calculate the COSY signal, averaged over the polycrystalline sample without any relaxation, and then multiplying it by the stretched exponential factor as in Eq. (3.14), finding the value of β by fitting the experimental data to the simulation.

3.2.3. Effect of dead time on COSY signal

Recording the signal immediately after the second pulse is not possible during the *dead-time,* denoted as t_d hereafter, of the spectrometer. The best values of the deadtime as reported in (Borbat and Freed 2002) at Ku-band is $t_d = 25\,ns$, which will be considered here. This means that the signal up to the dead-time after the second pulse will not be considered in the calculation following the procedure given in Sec. 3.1 Numerical procedure. The time-domain signals at two different B_1 values calculated with and without dead-time are shown in Figure 3.3 and Figure 3.4. The dead-time effect is shown by hatching the initial time interval t_d of the signal. The Fourier transforms of the COSY signals taken with repsect to both time variables t_1 and $t_1 - t_d$ are plotted, which show that the intensity of the Fourier transforms are reduced by including the dead-time. However, the Pake doublets still occur at $\pm d$, although diminished in their intensities and widths.
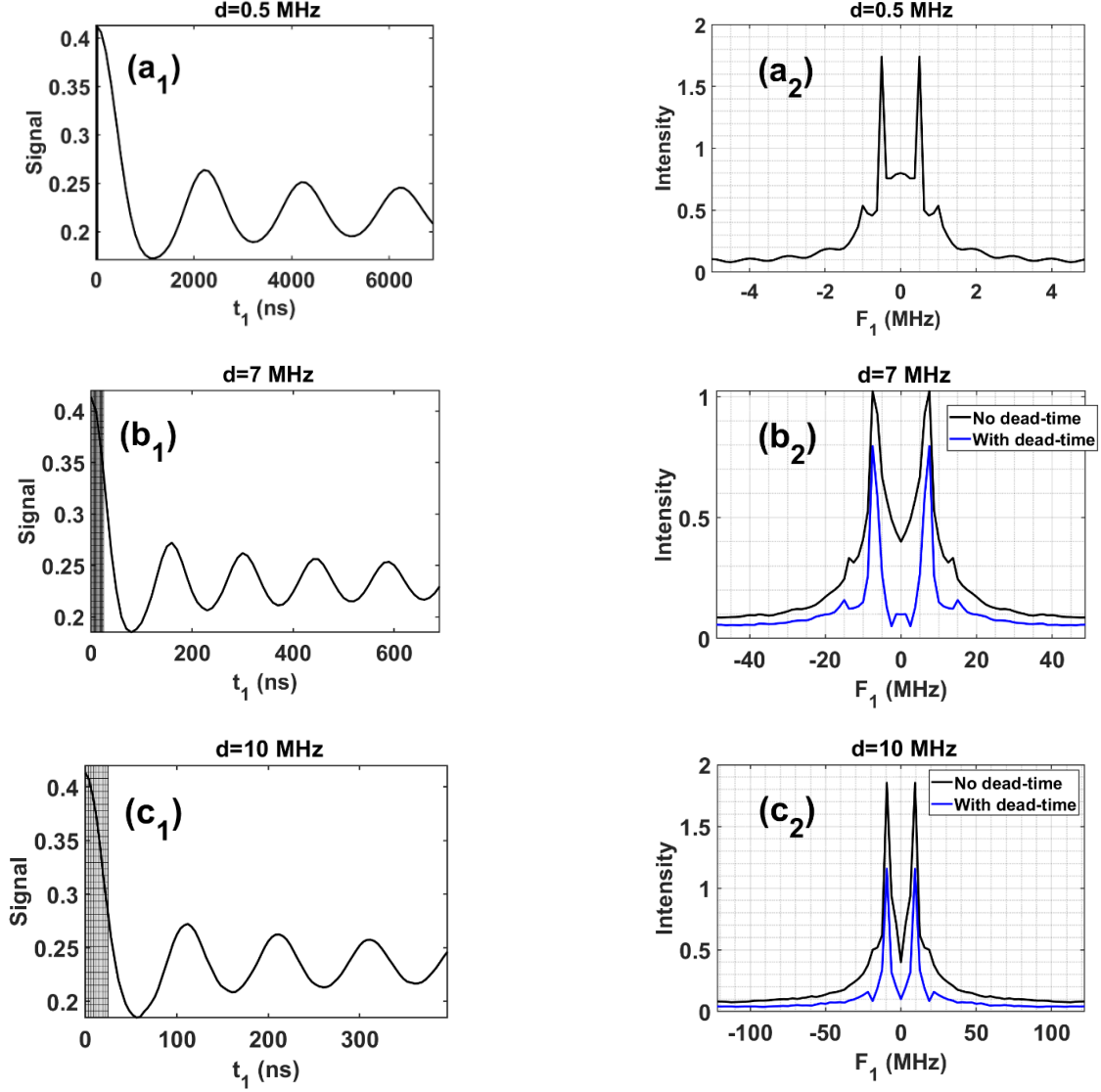
Figure 3.3. **COSY signal at Ku-band for $B_1 = 30G$.** Dependence of COSY signal on the dipolar constant for a polycrystalline sample. (left) The time domain COSY signals for $t_2 = t_1$ and (right) their Fourier transforms for four different values of the dipolar coupling constant: Figs $(3a_1)$ and $(3a_2)$: $d = 0.5$; Figs $(3b_1)$ and $(3b_2)$: $d = 7$ MHz; Figs $(3c_1)$ and $(3c_2)$: $d = 10$ MHz. The parameters used for the simulations are listed in Table 3.1. The relaxation effect is not considered in these simulations. The initial 25 ns interval of the time domain signals, included in the dead-time of the pulse, is shown as hatched; it cannot be recorded in the experiment. The corresponding Fourier transform with respect to both t_1 and $t_1 - t_d$ are plotted, shown in black and blue, respectively.
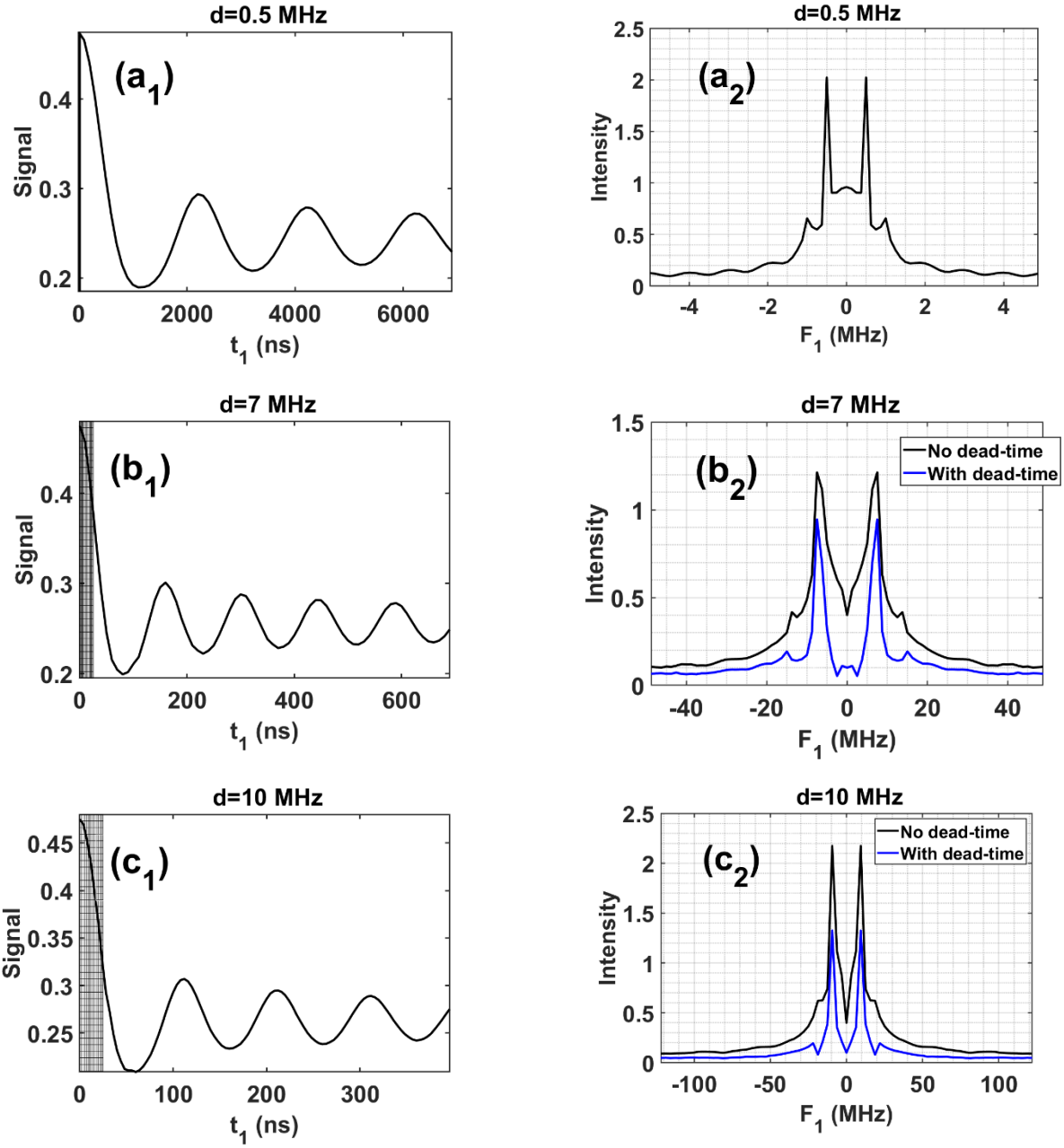
Figure 3.4. **COSY signal at Ku-band with a stronger $B_1 = 60G$.** The same details as in the caption of Figure 3.3, except here $B_1 = 60$ G. By comparing these results with those obtained in Figure 3.3 for $B_1 = 30$ G, it is seen that at Ku-band, increasing B_1 from 30 G to 60 G does not affect the shape of the simulated COSY signals and their Fourier transform significantly. However, the intensity of the signal is increased by about 15% for $B_1 = 60$ G.

3.2.4. Modulation depths of the calculated signals and Fourier transforms

3.2.4.1 Absence of dead-time; General considerations

The one-dimensional time-dependent COSY signal due to the dipolar modulation for the orientation $\eta = (\theta, \varphi)$ of the external magnetic field with respect to the dipolar axis connecting the two nitroxides, and the five independent Euler angles $\lambda_1 = (\alpha_1 = 0, \beta_1, \gamma_1)$, $\lambda_2 = (\alpha_2, \beta_2, \gamma_2)$, in the limit of infinite pulses is expressed as (Borbat and Freed 2002)

$$S'(t, \eta, \lambda_1, \lambda_2) = S'_0\big[1 - \delta_m(\eta, \lambda_1, \lambda_2)\big(1 - cos(\omega(\theta)t)\big)\big] \tag{3.16}$$

where S'_0 is the amplitude of the signal at time $t = 0$; $\delta_m(\eta, \lambda_1, \lambda_2)$ is the modulation depth at the orientation $(\eta, \lambda_1, \lambda_2)$ and

$$\omega(\theta) = (3cos^2(\theta) - 1)d \tag{3.17}$$

For a polycrystalline sample, the unnormalized signal averaged over the Euler angles, λ_1, λ_2, of the two nitroxides, and the angle θ, as given by Eq. (3.16), is then:

$$S'(t) = \sum_{\lambda_1, \lambda_2} \int_0^{\pi/2} S'_0\big[1 - \delta_m(\eta, \lambda_1, \lambda_2)\big(1 - cos(\omega(\theta)t)\big)\big] sin\theta \, d\theta \tag{3.18}$$

As derived in Appendix D, the resulting time-domain signal, for isotropic $\delta_m(\eta, \lambda_1, \lambda_2) = \Delta$, can be expressed as

$$S'(t) = S'_{eq} + S'_0 \Delta u(d, t) \tag{3.19}$$

where,

$$u(d, t) = \int_0^{\pi/2} cos\big((3cos^2(\theta) - 1)d \, t\big) sin\theta \, d\theta \tag{3.20}$$

and $S'_{eq} = S'_0 (1 - \Delta)$.

$S'(t)$ as given by Eq. (3.19) has its maximum value S'_0 at time $t = 0$, then it drops instantaneously and undergoes decaying oscillations around the equilibrium value S'_{eq} (Figure 3.3 and Figure 3.4) as time increases. A simplified analytical expression for $S'(t)$ and its Fourier transform for the case of isotropic $\delta_m(\eta, \lambda_1, \lambda_2)$, is given in Appendix D, which show that the resulting Pake doublets occur at $\pm d$.

As a percentage, the modulation depth for a polycrystalline sample, Δ is:

$$\Delta(\%) = \big(S'_0 - S'_{eq}\big)/S'_0 \times 100 \tag{3.21}$$

The depths of the dipolar modulation, $\Delta(\%)$, for the time domain signal of two-pulse COSY, as calculated here, are $\Delta \approx 30\%$ $\Delta \approx 40\%$ and $\Delta \approx 45\%$ for $B_1 = 10G$, $B_1 = 30G$ and $B_1 = 60G$, respectively, as shown in Figure 3.5 for $d = 0.5 \, MHz$ and 7.0 MHz. It is noted that, for $d = 0.5$ MHz, the dead-time does not affect the signal and therefore the modulation depth significantly. However, as d increases, the effect of the dead-time on the modulation depth becomes more significant, since a considerable initial time interval of the signal is lost. It is seen from the value of the modulation depth, calculated for $d = 7$ MHz whose values are about 1/3 of those calculated for $d = 0.5$ MHz. It was found that the modulation depth cannot be measured for $d > 7$ MHz.

The values of Δ calculated here for $d \leq 7$ MHz imply that the two-pulse COSY technique is feasible for distance measurement for B_1 values greater than a certain minimum which is found to be $B_1 = 30$ G.
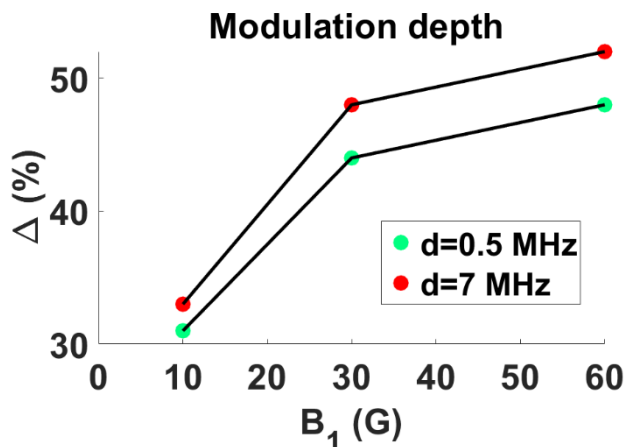
Figure 3.5. The modulation depth Δ(%) of the COSY signal at Ku-band, plotted as a function of the amplitude of the irradiation microwave field B_1 for $d = 0.5$ *MHz* and 7.0 *MHz*, with the dead-time considered. The red dots indicate the values for $d = 7.0$ MHz, whereas the green dots indicate the values for $d = 0.5$ MHz. All the other parameters used are the same as those listed in Table 3.1. The value of Δ(%) is calculated by a linear extrapolation of the signal during the period t_d to 0; this estimate is expected to give a modulation depth larger by ~2-4% than that calculated without extrapolation.

3.2.4.2 Effect of dead time after the second pulse: modulation depth and Fourier transform

Due to not considering the initial part of the signal during the dead-time, t_d, the modulation depth can only be measured at Ku- band for 0.5 MHz $\leq d \leq 7.0$ MHZ, as seen from Figure 3.3 and Figure 3.4. However, the Pake doublets as a function of $t_1 - t_d$ after the dead-time are still found undistorted and centered at $\pm d$, albeit slightly narrowed and reduced in intensities, as seen from Figure 3.3 and Figure 3.4. Thus, the Fourier transform with respect to $t_1 - t_d$, also provides a measure of the dipolar constant, which, in turn, enables one to calculate the distance between the two nitroxides over an extended range 0.5 MHz $\leq d \leq 10.0$ MHz.

3.2.5 Discussion of various simulations performed for COSY at Ku-band

The results of simulations are plotted in Figs. 3.3 – 3.7 and their analysis is presented below. It is noted that in the following discussion the term Fourier transform applies to both transforms, taken with respect to t_1 and $t_1 - t_d$, since they are situated at the same dipolar frequencies, $\pm d$.

Figure 3.3. It shows the dependence of the time-domain COSY signals, and their Fourier transforms at Ku-band on time $t_1 (= t_2)$ as functions of the strength of the dipolar interaction in the absence of relaxation for seven different values of the dipolar coupling constant: (a) $d = 0.5$ MHz; (b) $d = 7$ MHz; (c) $d = 10$ MHz, for the amplitude of the irradiation microwave field $B_1 = 30$ G. The same dead time of $t_d = 25$ ns, in accordance with (Borbat and Freed 2002), is considered here. The initial 25 ns interval of the time domain signals, included in the dead-time of the pulse, is shown as hatched; it cannot be recorded in the experiment. The corresponding Fourier transform with respect to both t_1 and $t_1 - t_d$ are plotted, shown in black and blue,

respectively. For all values of the dipolar coupling constant in the range $0.5\ MHz < d < 50$ MHz, the predominant Pake doublets occur at $\pm d$ for the two transforms with respect to t_1 and $t_1 - t_d$. It is found that the Pake doublets are not distorted due to the dead-time effect, except that their intensities and widths are reduced. Furthermore, the relative intensities of the side peaks with respect to the main peaks, situated at $\pm d$, are reduced when the dead-time effect is considered. For $d = 0.5$ MHz, the dead-time effect on both the time signal and its Fourier transform is insignificant, because the dead-time is much smaller than the periodic time corresponding to this small dipolar value. In addition, the modulation depth of about 30% is found from the simulated signal. On the other hand, the modulation depth for $d > 7.0$ MHz cannot be measured in the experiment because a significant initial part of the signal is lost in the dead-time after the second pulse.

Figure 3.4. It shows the time-dependent COSY signals, and their Fourier transforms at Ku-band for $B_1 = 60\ G$ for $d = 0.5, 7, 10$MHz. All other parameters used for simulation are the same as those used for the simulations in Fig. 3. By comparing these results with those obtained in Fig. 3 with $B_1 = 30$ G, it is seen that by increasing B_1 from 30 G to 60 G the shapes of the simulated COSY signals and their Fourier transforms are not affected significantly. However, the intensities of the signals are increased by about 15% for $B_1 = 60\ G$ as compared to those at $B_1 = 30\ G$.

Figure 3.5. It shows the modulation depth Δ of the COSY signal at Ku-band, as functions of the amplitude of the irradiation microwave field B_1 , for two values of the dipolar coupling constants: $d = 0.5$ MHz and $d = 7$ MHz. All the other parameters are the same as those listed in Table I. In Fig. 5, Δ is calculated by linear extrapolation of the signal beyond the dead-time to $t = 0$ It is seen from Fig. 5 that Δ increases with B_1, in a non-linear fashion with respect to B_1, for both $d = 7$ MHz and $d = 0.5$ MHz. Similar behavior is expected for other d values.

Figure 3.6 It shows the Fourier transforms of the COSY signals with and without relaxation for the relaxation time $T_2^S = 500\ ns$ for comparison, using the dipolar coupling constant $d = 7$ MHZ and the amplitude of the irradiation microwave field $B_1 = 60.0\ G$. It is seen that by including the relaxation, the Pake doublets become broadened. The shape of the broadened peaks can be used to estimate the relaxation time since their full width at half maximum is proportional to $\frac{1}{T_2^S}$.
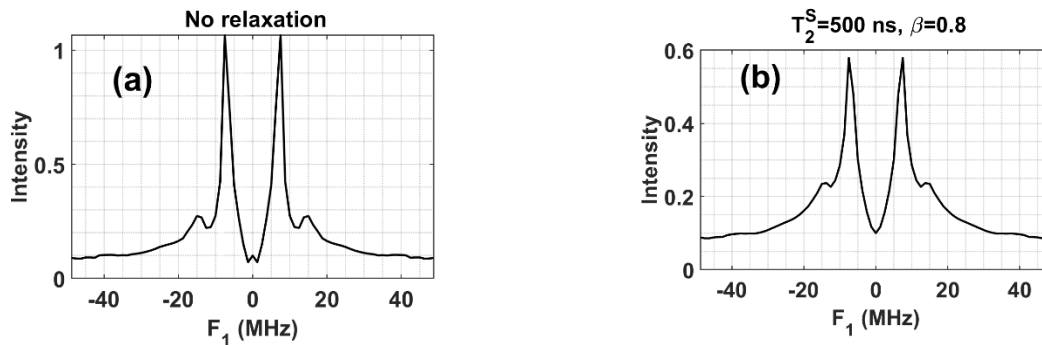
Figure 3.6.   Effect of relaxation on the COSY signal for a polycrystalline sample at Ku-band. The Fourier transform of the COSY signal as a function of F_1, the frequency corresponding to $t_1 - t_d$, to consider the dead-time effect for: (left) without taking relaxation into account and

28

(right) with relaxation considered for $T_2^S = 500\ ns$ and $\beta = 0.8$. The dipolar coupling constant $d = 7$ MHz and amplitude of the irradiation microwave field $B_1 = 60.0\ G$ are used for these simulations. The values of all the other parameters used for the simulations are listed in Table 3.1. The effect of relaxation is clearly seen to broaden the Pake-doublet peaks.
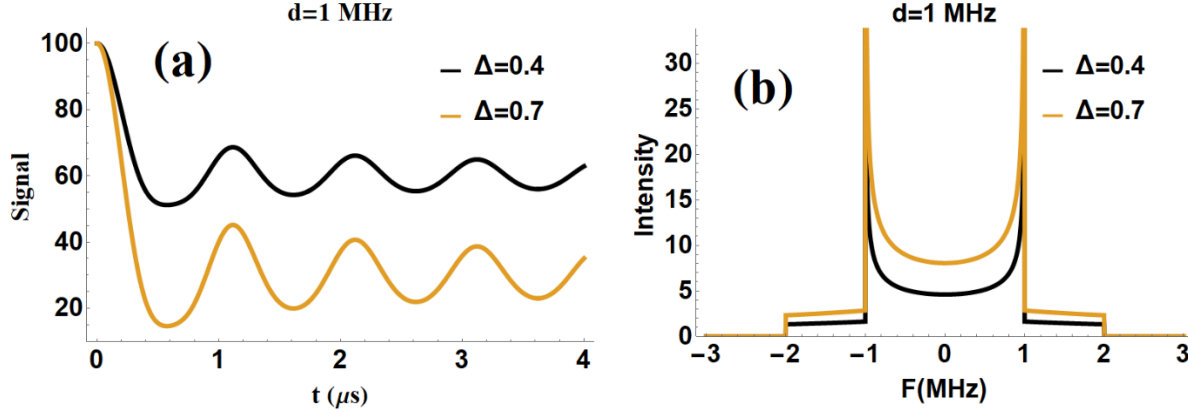
Figure 3.7.   (a) The time-domain signal $S'(t)$ and (b) its Fourier transform (Pake doublets) $S''(\omega)$, as given by Eqs. (D.1) and (D.5) in Appendix D, respectively, plotted for two values of the modulation depth $\Delta = 0.4$ and $\Delta = 0.7$. The dipolar coupling constant $d = 1\ MHz$ and $S_0' = 100$ are used in these plots.

Figure 3.7 It shows the time-domain signal of the dipolar modulation $S'(t)$ and its Fourier transform as given by Eqs. (D.1) and (D.5) in Appendix D, respectively, for two values of the dipolar modulation $\Delta = 0.4$ and $\Delta = 0.7$ for $d = 1\ MHz$. The value of $S_0' = 100$ is used in these plots. It is seen that as the value of Δ increases, the equilibrium position about which the signal oscillates, approaches zero. whereas the intensity of the Pake doublet increases.

3.3 Four-, five-, six-pulse DQC at Ku-band

In this section, the analytical techniques are developed to calculate pulsed EPR signals, utilized for distance measurements in biological systems, using nitroxide biradicals, for the cases of: (i) four- (ii) five- and (iii) six-pulse double quantum coherence (DQC). The analytical signals are then compared with the experimental data as well as the numerically calculated signals using the procedure described in Sec. 3.1 Numerical procedure

3.3.1 Pulse schemes

The four-pulse DQC pulse sequence is shown in Figure 3.8(a). In this sequence, the first pulse $(\pi/2)_x$ generates the single-quantum coherence pathway ($p = +1$), over which it evolves for a period t_1. The second $(\pi/2)_x$ pulse transfers this magnetization to $p = \pm 2$ as well as $p = 0$ coherence pathways and the density matrix evolves on it over the period t_2. Thereafter, the third refocussing pulse $(\pi)_x$ transfers the density matrix to the double quantum $p = \mp 2$ and $p = 0$ coherence pathways, over which the density matrix undergoes free evolution for the time interval t_3. The fourth $(\pi/2)_x$ pulse finally transfers the density matrix to the single quantum coherence pathway $p = -1$, on which the signal is detected after the time interval t_4. In the

29

experiment, t_1 is stepped and $t_2 = t_3 = t_{DQ}^{(4)}$ is kept fixed. The echo in this four-pulse DQC sequence occurs at the time $t_4 = t_1$.

The five-pulse DQC pulse sequence is shown in Figure 3.8 (b). Here, compared to four-pulse DQC sequence, an additional refocusing pulse $(\pi)_x$ is added after the last pulse. After the application of the first $(\pi/2)_x$ pulse, the system can evolve freely over time t_1 on coherence pathway $p = +1$ before the application of the second $(\pi/2)_x$ pulse, after which the coherence pathways $p = \pm 2$ are chosen. After the free evolution over time t_2, the third refocussing pulse $(\pi)_x$ transfers the density matrix to the double quantum $p = \mp 2$ over which the density matrix evolves for the time interval t_3. The fourth $(\pi/2)_x$ in this pulse sequence generates $p = +1$ coherence pathway over which the system undergoes a free evolution for time t_4. Finally, the fifth $(\pi/2)_x$ pulse converts the density matrix into the observable $p = -1$ coherence pathway. The time interval between the first and the last pulse is here kept constant, to be equal to t_{max}, and t_1 is varied. The echo is detected at the time t_{max} after the last pulse, independent of the varied time t_1. For this five-pulse sequence, the constant times $t_2 = t_3$, corresponding to the pathways $p = \pm 2$, will be denoted as the double quantum time $t_{DQ}^{(5)}$.

The pulse sequence and the coherence pathways involved in six-pulse DQC are shown in Figure 3.8 (c). It consists of three-pulse preparation sequence $(\pi/2)_x - t_1 - \pi_x - t_2 - (\pi/2)_x$, which generates double-quantum (DQ) coherence. It is then refocused after the time t_3 by the $\pi_x - t_4$ sequence. The fifth, $(\pi/2)_x$, pulse produces anti-phase coherences, which evolve into observable single quantum coherences. Finally, the sixth, π_x, pulse, applied after the time t_5, refocuses them to form an echo. Here $t_1(= t_2)$ is varied with fixed time $t_{max} = t_1 + t_5$, wherein, t_1 is stepped from zero to t_{max}. As well, $t_3 = t_4 = t_{DQ}^{(6)}$, which is the period for the double-quantum filter, over which the spins are on the double quantum, $p = \pm 2$, pathways, over a constant time in the experiment. $t_5 = t_{max} - t_1$ and $t_6 = t_5 + t_{echo}$. The echo in this six-pulse DQC sequence occurs at the time $t_{echo} = 0$, i.e., when $t_6 = t_5$. In the present calculations, the time variable $t_{dip} = t_{max} - 2t_1$ is used to calculate the final DQC signal as $S(t_{dip}, \eta, \lambda_1, \lambda_2)$.
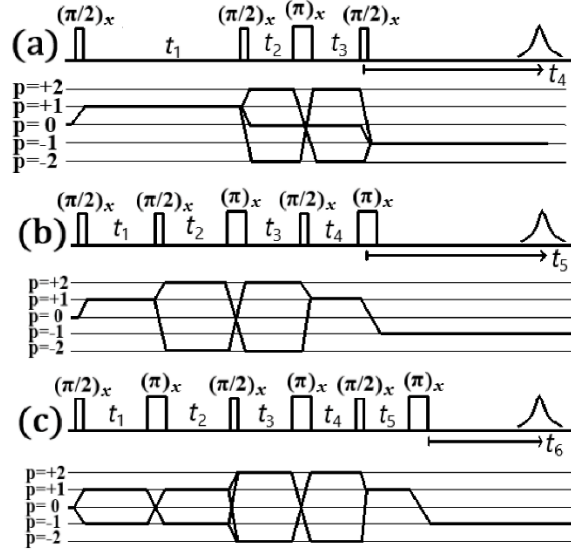
Figure 3.8. The pulse schemes and the relevant coherence pathways for (a) four-pulse DQC, (b) five-pulse DQC, and (c) six-pulse DQC. Perfect $(\pi/2)_x$ or $(\pi)_x$ pulses are used for all sequences, where the duration of the pulses, t_p, is determined by $t_p = \gamma_e B_1/\beta$, knowing B_1, where B_1 is the amplitude of the microwave field and $\beta = \pi/2$; π is the tip angle.

3.3.2 General procedure to derive analytical expressions for multi-pulse-EPR Signals

The procedure to calculate the analytical expression of multi-pulse EPR signal is similar to the numerically calculated signal described in Sec. 3.1 Numerical procedure There are, however, some differences between the two approaches which are outlined below.

In the analytical approach, the density matrix, as transformed by the application of a pulse of duration t_p, is given as (Saxena and Freed 1997):

$$\rho(t_0 + t_p) = e^{-i(H_0 + H_p)t_p}\rho(t_0) \, e^{i(H_0 + H_p)t_p} = P \, \rho(t_0) \, P^\dagger \qquad (3.22)$$

The matrix for the propagation operator $P = e^{-i(H_0 + H_p)t_p}$ in Eq. (3.22), has the general form in the electronic magnetic basis (Saxena and Freed 1997):

$$\{\{P\}\} = \begin{pmatrix} [[P_{11}]] & [[P_{12}]] \, e^{-i\phi} & [[P_{13}]]e^{-i\phi} & [[P_{14}]]e^{-2i\phi} \\ [[P_{21}]]e^{i\phi} & [[P_{22}]] & [[P_{23}]] & [[P_{24}]]e^{-i\phi} \\ [[P_{31}]]e^{i\phi} & [[P_{32}]] & [[P_{33}]] & [[P_{34}]]e^{-i\phi} \\ [[P_{41}]]e^{2i\phi} & [[P_{42}]]e^{i\phi} & [[P_{43}]]e^{i\phi} & [[P_{44}]] \end{pmatrix} \qquad (3.23)$$

31

In Eq. (3.23), $[[P_{ij}]]$ are 9×9 matrices in the hyperfine space, with ϕ being the pulse phase. The 9×9 matrix elements of $[[P_{ij}]]$ in the hyperfine space of the propagator operator in Eq. (2.8) are rather long expressions, but they can be easily can be calculated using Mathematica. On the other hand, all significant interpretations of relevance here can be made without including them. *The double square brackets around $[[P_{ij}]]$ will hereafter be dropped, with the understanding that they are 9x9 matrices in the hyperfine space.*

To consider the time evolution of the density matrix during free evolution, one needs to first calculate $e^{-iH_0 t}$ which is given by Eq. (E.11) in Appendix E. After the application of a pulse, free evolution of the density matrix ρ, over time t on a given coherence pathway, in the absence of the relaxation, is given by

For $p = 0$

$$
e^{-iH_0 t}\rho^{(0)}e^{iH_0 t} =
\begin{pmatrix}
\rho_{11} & 0 & 0 & 0 \\
0 & a_1 & a_2 & 0 \\
0 & a_3 & a_4 & 0 \\
0 & 0 & 0 & \rho_{44}
\end{pmatrix}
\tag{3.24}
$$

where,

$$
\begin{aligned}
a_1 &\equiv S_1^{(0)}(t)\rho_{33} + S_2^{(0)}(t)\rho_{23} + S_2^{(0)}(t) * \rho_{32} + S_3^{(0)}(t)\rho_{22} \\
a_2 &\equiv S_1^{(0)}(t)\rho_{32} + S_2^{(0)}(t)(\rho_{22} - \rho_{33}) + S_4^{(0)}(t)\rho_{23} \\
a_3 &\equiv S_1^{(0)}(t)\rho_{23} - S_2^{(0)}(t) * \rho_{33} + S_2^{(0)}(t) * \rho_{22} + S_4^{(0)}(t) * \rho_{32} \\
a_4 &\equiv S_1^{(0)}(t)\rho_{22} + S_2^{(0)}(t)\rho_{23} - S_2^{(0)}(t) * \rho_{32} + S_3^{(0)}(t)\rho_{33}
\end{aligned}
$$

For $p = +1$

$$
e^{-iH_0 t}\rho^{(+1)}e^{iH_0 t} =
\begin{pmatrix}
0 & S_1^{(+1)}(t)\rho_{12} + S_2^{(+1)}(t)\rho_{13} & S_2^{(+1)}(t)\rho_{12} + S_5^{(+1)}(t)\rho_{13} & 0 \\
0 & 0 & 0 & S_3^{(+1)}(t)\rho_{24} + S_4^{(+1)}(t)\rho_{34} \\
0 & 0 & 0 & S_4^{(+1)}(t)\rho_{24} + S_6^{(+1)}(t)\rho_{34} \\
0 & 0 & 0 & 0
\end{pmatrix}
\tag{3.25}
$$

For $p = +2$

$$
e^{-iH_0 t}\rho^{(+2)}e^{iH_0 t} =
\begin{pmatrix}
0 & 0 & 0 & S_1^{(+2)}(t)\rho_{14} \\
0 & 0 & 0 & 0 \\
0 & 0 & 0 & 0 \\
0 & 0 & 0 & 0
\end{pmatrix}
\tag{3.26}
$$

where $\rho^{(0)}$, $\rho^{(+1)}$ and $\rho^{(2)}$ are the density matrices before the free evolutions on pathways $p = 0, +1, +2$, respectively, after phase cycling. The $S^{(k)}{}_i(t)$; $k = 0,1,2$ terms for different coherence pathways, used in Eqs. (3.24)-(3.26), are listed in Table 3.2. The evolutions of the density matrix over the coherence pathways $p = -1$ and $p = -2$ are the conjugate transpose of those for $p = +1$ and $p = +2$, respectively, as given above. The resulting density matrix at the end of a coherence pathway will serve as the starting density matrix for the next pulse. The same procedure is repeated for all other pulses in turn to calculate the final density matrix.

$S_1^{(0)}(t)$	$-\dfrac{1}{4}\sin^2(2\Xi)(e^{it\omega_{23}} + e^{it\omega_{32}} - 2)$
$S_2^{(0)}(t)$	$(-\dfrac{1}{4}\sin(4\Xi) + \sin(\Xi)\cos^3(\Xi)e^{it\omega_{23}} - \sin^3(\Xi)\cos(\Xi)e^{it\omega_{32}})$
$S_3^{(0)}(t)$	$\dfrac{1}{4}(\cos(4\Xi) + \sin^2(2\Xi)(e^{it\omega_{23}} + e^{it\omega_{32}}) + 3)$
$S_4^{(0)}(t)$	$2\sin^2(\Xi)\cos^2(\Xi) + \sin^4(\Xi)e^{it\omega_{32}} + \cos^4(\Xi)e^{it\omega_{23}}$
$S_1^{(+1)}(t)$	$e^{-it\omega_{13}}\sin^2(\Xi) + e^{-it\omega_{12}}\cos^2(\Xi)$
$S_2^{(+1)}(t)$	$(e^{-it\omega_{13}} - e^{-it\omega_{12}})\sin(\Xi)\cos(\Xi)$
$S_3^{(+1)}(t)$	$e^{-it\omega_{34}}\sin^2(\Xi) + e^{-it\omega_{24}}\cos^2(\Xi)$
$S_4^{(+1)}(t)$	$(e^{-it\omega_{34}} - e^{-it\omega_{24}})\sin(\Xi)\cos(\Xi)$
$S_5^{(+1)}(t)$	$e^{-it\omega_{12}}\sin^2(\Xi) + e^{-it\omega_{13}}\cos^2(\Xi)$
$S_6^{(+1)}(t)$	$e^{-it\omega_{24}}\sin^2(\Xi) + e^{-it\omega_{34}}\cos^2(\Xi)$
$S_1^{(+2)}(t)$	$e^{-it_1\omega_{14}}$

Table 3.2 The free evolution terms for $p = 0$, $p = +1$ and $p = +2$ used in the analytical expressions. The superscripts on $S_i(t)$ indicates the coherence pathway. The free evolution terms corresponding to $p = -1$ and $p = -2$ are the complex conjugate of those for $p = +1$ and $p = +2$, respectively.

3.3.3 One dimensional signals: Analytical Expressions for four-, five- and six- pulse DQC signals

In this section, expressions for four-, five-, and six-pulse DQC signals at the top of the echo will be derived analytically using the procedure outlined in Sec. 3.3.2 General procedure to derive analytical expressions for multi-pulse-EPR Signalsabove for the case of nonselective pulses, i.e., strong pulses, such that $H_p \gg H_0$. The free evolution part and the pulse propagator can be simplified in this limit as follows.

It is seen from the Eqs. (3.24)-(3.26) and Table 3.2 that the time-dependent part of a signal due to the free evolution over coherence pathways, depends on $S_m(t), S_m(t)^*, m = 1, \ldots, 6$, which contain the terms $e^{-i\omega_{ij}t_1}$ and $e^{i\omega_{ij}t_2}$, respectively, where $\omega_{ij} = (E_i - E_j)/\hbar$; the E_i, and E_j are defined by Eq. (E.10) in Appendix E. Using the approximation for "sufficiently

broad spectral excitation" (Borbat and Freed 2002) i.e., $|C_1 - C_2| \gg d(3\cos^2\theta - 1)$, the pseudo-secular terms (the H_{23} and H_{32} terms in Eq. (B.5) in Appendix B) become negligible and the term $\left(\frac{d}{4}(3cos^2\theta - 1)\right)^2$ appearing in Eq. (E.10) can be ignored compared to the Zeeman and hyperfine interactions. In this broad spectral excitation approximation limit, the explicit expressions for ω_{ij} are then:

$$\hbar\omega_{12} = k\sqrt{A_2^2 + 4B_2^2 k} + C_2 + \frac{1}{2}d(3\cos^2\theta - 1)$$

$$\hbar\omega_{13} = k\sqrt{A_1^2 + 4B_1^2 k} + C_1 + \frac{1}{2}d(3\cos^2\theta - 1)$$

$$\hbar\omega_{24} = k\sqrt{A_1^2 + 4B_1^2 k} + C_1 - \frac{1}{2}d(3\cos^2\theta - 1) \tag{3.27}$$

$$\hbar\omega_{34} = k\sqrt{A_2^2 + 4B_2^2 k} + C_2 - \frac{1}{2}d(3\cos^2\theta - 1)$$

Since $H_{23} \approx 0$, the matrix elements Ξ_i defined by Eq. (E.8), which are used in $S_i(t_k)$; $i = 1, ...,6$; $k = 1,2$, given in Table 3.2, become negligible.

The analytical expression for the pulse propagator, i.e., $e^{-iH_p t_p}$, in the magnetic basis is, as calculated using *Mathematica*:

$e^{-iH_p t_p} =$

$$\begin{pmatrix} \cos^2(\frac{\beta}{2}) & -\frac{i}{2}e^{-i\phi}\sin(\beta) & -\frac{i}{2}e^{-i\phi}\sin(\beta) & \frac{1}{2}e^{-2i\phi}(\cos(\beta)-1) \\ -\frac{i}{2}e^{i\phi}\sin(\beta) & \cos^2(\frac{\beta}{2}) & \frac{1}{2}(\cos(\beta)-1) & -\frac{1}{2}ie^{-i\phi}\sin(\beta) \\ -\frac{i}{2}e^{i\phi}\sin(\beta) & \frac{1}{2}(\cos(\beta)-1) & \cos^2(\frac{\beta}{2}) & -\frac{1}{2}ie^{-i\phi}\sin(\beta) \\ \frac{1}{2}e^{2i\phi}(\cos(\beta)-1) & -\frac{1}{2}ie^{i\phi}\sin(\beta) & -\frac{1}{2}ie^{i\phi}\sin(\beta) & \cos^2(\frac{\beta}{2}) \end{pmatrix} \tag{3.28}$$

where $\beta = \omega t_p$ is the tip angle and ϕ is the phase of the pulse.

3.3.3.1 Four-pulse DQC Signal

There are three different coherence pathways which contribute to the four-pulse DQC signal (i) $p: 0 \to +1 \to 2 \to -2 \to -1$; (ii) $p: 0 \to +1 \to -2 \to +2 \to -1$; (iii) $p: 0 \to +1 \to 0 \to 0 \to -1$. The signal from the first and second coherence pathways are calculated to be the same, each being:

$$= \frac{i}{2}\cos^2\left(\frac{1}{2}\left(j\sqrt{A_1^2 + 4B_1^2 j} - k\sqrt{A_2^2 + 4B_2^2 k} + C_1 - C_2\right)t_1\right)\sin^2\left(\frac{at_1}{2}\right) \tag{3.29}$$

In Eq. (3.29), $a = d(3cos^2\theta - 1)$. As for the signal due to the coherence pathway (iii), it is calculated to be

$$= -\frac{i}{4}\left(-(\cos{(at_1)} - 1) \times \cos{\left(\left(j\sqrt{A_1^2 + 4B_1^2}j - k\sqrt{A_2^2 + 4B_2^2}k + C_1 - C_2\right)t_1\right)}\right. \tag{3.30}$$

$$\left. + 3\cos{(at_1)} + 1\right)$$

Finally, the total 4-pulse DQC signal is the sum of these three signals:

$$\text{Signal}_{DQC}^{(4)}(t_1) = -i\cos(at_1) \tag{3.31}$$

3.3.3.2 Five-pulse DQC Signal

The coherence pathways involved in the five-pulse DQC sequence are: (i) $p: 0 \to +1 \to +2 \to -2 \to 1 \to -1$ and (ii) $p: 0 \to +1 \to -2 \to +2 \to 1 \to -1$. Each coherence pathway contributes equally to the final five-pulse DQC signal. Finally, the total five-pulse DQC signal is:

$$\text{Signal}_{DQC}^{(5)}(t_1) = iV\sin\left[a(t_1 - \frac{1}{2}t_{\max})\right] \tag{3.32}$$

where $V = \sin\left(\frac{1}{2}at_{\max}\right)$.

3.3.3.3 Six-pulse DQC Signal

The four coherence pathways involved in six-pulse DQC as shown in Fig 2(c) are:
(i) $p: 0 \to +1 \to -1 \to +2 \to -2 \to 1 \to -1$; (ii) $p: 0 \to +1 \to -1 \to -2 \to +2 \to 1 \to -1$;
(iii) $p: 0 \to -1 \to +1 \to +2 \to -2 \to 1 \to -1$; (iv) $p: 0 \to -1 \to +1 \to -2 \to +2 \to 1 \to -1$.
The analytical expression for each of these coherence pathways is calculated to be the same. Finally, the overall signal is expressed as

$$\text{Signal}_{DQC}^{(6)}(t_1) = i\left[K - \cos\{a\left(t_1 - \frac{1}{2}t_{max}\right)\}\right], \tag{3.33}$$

where $K = \cos\left(\frac{1}{2}at_{max}\right)$.

It is seen from Eq. (3.33) that the six-pulse DQC signal has an additive constant term determined by K, so the signal is shifted by this amount. However, the time-dependent term in the signal is $cos\{a\left(t_1 - \frac{1}{2}t_{max}\right)\}$ that determines the Fourier transform of the signal, from which the distance between the two nitroxide dipoles of the biradical can be estimated.

An inspection of Eqs. (3.31)-(3.33) reveals that the Fourier transform of any - four-, five-, or six-pulse sequence as a function of t_1 will have peaks at $\pm a$, where $a = d(3\cos^2\theta - 1)$. Furthermore, there is no dependence of the signals, given by Eqs. (3.31)-(3.33), upon the Euler angles of the two nitroxides, so an average over the Euler angles is not needed to find Pake doublets.

It is noted that, the analytical expressions of Eqs. (3.31)-(3.33) which are found by applying the algorithm given in Sec. 2, are in agreement with the analytical expressions given in (Borbat and Freed 2002), derived using the product operator (PO) method (Slicther 2013).

3.3.4 Two-dimensional signal

The two-dimensional signals for four-, five- and six-pulse DQC are obtained by extending the calculations of the one-dimensional signals to include a second time variable It is carried out here by replacing the time after the last pulse, which are t_4, t_5 and t_6 in four-, five- and six-pulse DQC sequences, respectively, by

$$t_4 \rightarrow t_1 + t_{echo}^{(4)} \quad \text{for four} - \text{pulse DQC signal}$$

$$t_5 \rightarrow t_{max} + t_{echo}^{(5)} \quad \text{for five} - \text{pulse DQC signal} \qquad (3.34)$$

$$t_6 \rightarrow t_5 + t_{echo}^{(6)} \quad \text{for six} - \text{pulse DQC signal}$$

where $t_{echo}^{(4)}$, $t_{echo}^{(5)}$ and $t_{echo}^{(6)}$ are the second time variables which are stepped from the top of the echo in four-, five- and six- pulse DQC sequences, respectively. Using the algorithm given in Sec. 3.1, the two-dimensional signals for four-, five- and six-pulse DQC signals are found to be

$$\text{Signal}_{DQC}^{(4)}(t_1, t_{echo}) = \text{Signal}_{DQC}^{(4)}(t_1) \times G\left(t_{echo}^{(4)}\right)$$

$$\text{Signal}_{DQC}^{(5)}(t_1, t_{echo}) = \text{Signal}_{DQC}^{(5)}(t_1) \times G\left(t_{echo}^{(5)}\right) \qquad (3.35)$$

$$\text{Signal}_{DQC}^{(6)}(t_1, t_{echo}) = \text{Signal}_{DQC}^{(6)}(t_1) \times G\left(t_{echo}^{(6)}\right)$$

where,

$$G\left(t_{echo}^{(i)}\right) = \frac{1}{3} e^{\frac{1}{2} i a t_{echo}^{(i)}} [e^{-i t_{echo}^{(i)}\left(\sqrt{A_1^2 - 4B_1^2} - C_1\right)} + e^{i t_{echo}^{(i)}\left(\sqrt{A_1^2 + 4B_1^2} + C_1\right)}$$

$$+ e^{-i t_{echo}^{(i)}\left(\sqrt{A_2^2 - 4B_2^2} - C_2\right)} + e^{i t_{echo}^{(i)}\left(\sqrt{A_2^2 + 4B_2^2} + C_2\right)} + e^{i C_1 t_{echo}^{(i)}} + e^{i C_2 t_{echo}^{(i)}}] \qquad (3.36)$$

In Eq. (3.36), $i = 4,5,6$ for four-, five- and six-pulse DQC signal, respectively. The Fourier transform of the two-dimensional signal with respect to $t_{echo}^{(i)}$ gives the ESR signal in the frequency domain of the biradical, keeping the static field fixed at B_0. The coefficients A_i, B_i, C_i, $i = 1,2$ in Eq. (3.36) can be calculated using Eqs. (A.4)-(A.6) of Appendix A. However, it is more convenient to calculate it using a numerical algorithm, which is more exact at the same time.

3.3.5 Relaxation for chosen orientations $(\eta, \lambda_1, \lambda_2)$

According to Sec. 3.2.2 Relaxation in polycrystalline sample, the effect of the relaxation for a single-orientation of the external magnetic field with respect to the crystal axes after time t is described by multiplying the calculated signal by an exponential factor $exp(-t/T_2^S)$, $exp(-t/T_2^D)$ and $exp(-t/T_1)$ for coherence pathways $p = \pm 1$, $p = \pm 2$ and $p = 0$, respectively, with the time constants T_2^S, T_2^D, T_1 appropriate for that orientation. Then the cumulative effect of the relaxation on the multi-pulse signals, considering all coherence pathways is tantamount to a multiplication of four, five and six decaying exponential functions for four-pulse, five-pulse and six-pulse arrangements, respectively, with the relevant time constants multiplied by the

calculated signal for the single orientation of the magnetic field with respect to the crystal axes as calculated in the absence of any relaxation. For a given value of the orientations $\zeta = (\lambda_1, \lambda_2, \eta)$, the effect of the relaxation at the top of the echo can be expressed as (hereafter, the $Signal(t)$ is denoted as $S(t)$)

$$S_4{}^{DQC}(\{t_4\}, \zeta) = S_0^{(A)}(\{t_4\}, \zeta)exp\left(-2t_{DQ}^{(4)}/T_2^D(\zeta) - 2t_1/T_2^S(\zeta)\right)$$
$$+ S_0^{(B)}(\{t_4\}, \zeta)exp\left(-2t_2/T_1(\zeta) - 2t_1/T_2^S(\zeta)\right) \qquad (3.37)$$

$$S_5{}^{DQC}(\{t_5\}, \zeta) = S_0(\{t_5\}, \zeta)exp\left(-2t_{DQ}^{(5)}/T_2^D(\zeta) - 2t_{max}/T_2^S(\zeta)\right) \qquad (3.38)$$

$$S_6{}^{DQC}(\{t_6\}, \zeta) = S_0(\{t_6\}, \zeta)exp\left(-2t_{DQ}^{(6)}/T_2^D(\zeta) - 2t_{max}/T_2^S(\zeta)\right) \qquad (3.39)$$

where $S_0(\{t_i\}, \zeta)$; i = 4, 5, 6 are the signals calculated for the orientation ζ in the absence of any relaxation and $\{t_i\} = (t_1, t_2, ..., t_i)$. In Eq. (3.37), t_2 is the time of free evolution over the coherence pathway $p = 0$ after the second pulse and $S_0^{(A)}$ and $S_0^{(B)}$ are the four-pulse DQC signals calculated in the absence of the relaxation over the coherence pathway routes $(A) + 1 \rightarrow \pm 2 \rightarrow \pm 2 \rightarrow -1$ and $(B) + 1 \rightarrow 0 \rightarrow 0 \rightarrow -1$, respectively.

For a polycrystalline sample, the signal is averaged over different values of (θ, ϕ), the orientation of the dipolar axis in the laboratory frame, characterized by different relaxation times $T_1(\zeta)$, $T_2^S(\zeta)$, $T_2^D(\zeta)$ on the coherence pathways p = 0, 1, 2, respectively. In the stretched exponential approach one considers relaxation over a polycrystalline sample by multiplying the signal for any orientation $(\eta, \lambda_1, \lambda_2)$ by the same factor, called stretched exponential, $exp\left(-[t/T_{str}]^\beta\right)$, where t is the time for relaxation and T_{str} is the average relaxation time over all orientations, and β is the stretched-exponential exponent.

The effect of relaxation at the top of the echo, i.e., at $t_4 = t_1$ for four-pulse DQC, at $t_5 = t_{max}$ for five-pulse DQC and at $t_6 = t_5$ for six-pulse DQC, is then expressed as

$$S_4{}^{DQC}(\{t_4\})_{Avg} = \sum_\zeta S_4{}^{DQC}(\{t_4\}, \zeta)$$
$$S_5{}^{DQC}(\{t_5\})_{Avg} = \sum_\zeta S_5{}^{DQC}(\{t_5\}, \zeta) \qquad (3.40)$$
$$S_6{}^{DQC}(\{t_6\})_{Avg} = \sum_\zeta S_6{}^{DQC}(\{t_6\}, \zeta)$$

where the subscript Avg denotes the average over the orientations $\zeta = (\eta, \lambda_1, \lambda_2)$. Assuming the same dependence on ζ of the three relaxation times $T_1(\zeta), T_2^S(\zeta)$ and $T_2^D(\zeta)$, Eq. (3.40), can be expressed, in the stretched exponential approach, as follows:

$$S_4^{DQC}(\{t_4\})_{Avg}$$

$$= S^{(A)}(\{t_4\}) \, exp\left(-\left[2t_{DQ}^{(4)}/T_{2str}^D + 2t_1/T_{2str}^S\right]^\beta\right)$$

$$+ S^{(B)}(\{t_4\}) \, exp\left(-[2t_2/T_{1str} + 2t_1/T_{2str}^S]^\beta\right)$$

(3.41)

$$S_5^{DQC}(\{t_5\})_{Avg} = S(\{t_5\})exp\left(-\left[2t_{DQ}^{(5)}/T_{2str}^D + 2t_{max}/T_{2str}^S\right]^\beta\right) \qquad (3.42)$$

$$S_6^{DQC}(\{t_6\})_{Avg} = S(\{t_6\})exp\left(-\left[2t_{DQ}^{(6)}/T_{2str}^D + 2t_{max}/T_{2str}^S\right]^\beta\right) \qquad (3.43)$$

where $S(\{t_i\}), i = 4,5,6$ are the averages of the four-, five- and six-pulse DQC signals, respectively, over all the orientations ζ. The $T_{1str}, T_{2\,str}^S$ and $T_{2\,str}^D$ are the "stretched" relaxation times over zero ($p = 0$), single ($p = 1$ pathway) and double ($p = 2$ pathway) quantum states, respectively. The stretching parameter, β, which is related to the distribution function of the relaxation times, ranges between zero and one. It is noted that, in general, there are three different stretching parameters, $\beta^{(0)}, \beta^{(S)}$ and $\beta^{(D)}$, characterizing the orientational distribution of the zero, single and double quantum relaxation times, respectively, which are to be found by fitting the simulation to the experimental data. In this thesis, since the experimental values for $\beta^{(0)} \beta^{(S)}$ and $\beta^{(D)}$ are not available, they are all assumed to be the same, i.e., $\beta^{(0)} = \beta^{(S)} = \beta^{(D)} = \beta = 0.8$, being the average of the two values 0.78 and 0.85, derived in (Stein *et. al.* 2019 and Pfenninger *et.al.* 1995).

It is noted that the effect of relaxation on five- and six-pulse DQC signals can be considered by multiplying the signal calculated in the absence of relaxation by the exponential factors, given by Eqs. (3.42)and (3.43), respectively. On the other hand, for the four-pulse sequence, the DQC signal, is obtained by multiplying the signal calculated in the absence of relaxation over a pathway by the relevant exponential factor, given by Eq. (3.41).

3.3.6. Comparison of four-, five-, and six-pulse DQC sequences for distance measurement

In this section, four-, five- and six-pulse DQC signals are compared in terms of the effect of relaxation on the signal and the intensity of their Pake doublets.

Main peaks As seen from the analytical expressions for four-, five- and six-pulse DQC signals given in Sec. 3.3.3 above for 1D signals i.e., at the top of the echo, the signals depend only on the factor $d(3cos^2\theta - 1)$ and all the other interactions e.g., Zeeman and hyperfine are absent. In the Fourier transform domain, these signals exhibit peaks at $\pm d(3cos^2\theta - 1)$ for the orientation θ of the dipolar axis with respect to the magnetic field; thereby resulting in their Pake doublets at

$\pm d$. Therefore, all these three pulse arrangements can be used for distance measurement in biological systems.

In Figure 3.9, the Pake doublets for four-, five- and six-pulse DQC signals are calculated using the rigorous numerical simulation which confirm that the Pake doublets occur at $\pm d$, in agreement with the analytical expressions found in Sec. 3.3.3.

Effect of the relaxation. As described in Sec. 3.3.5, the effect of the relaxation is considered by multiplying the signals with appropriate exponential factors related to their coherence pathways. It is seen from Eqs. (3.42) and (3.43) that the exponential factors due to the relaxation for five- and six-pulse DQC signals do not contain any time variable, and they just depend on the constant times $t_{DQ}^{(5,6)}$ and t_{max}. Therefore, the relaxation does not affect the broadening of the Fourier transform peaks of five- and six-pulse DQC signals and it only reduces the intensity of the peaks. However, the exponential factor in four-pulse DQC signal does contain the time variable t_1; thereby the relaxation affects the broadening as well as the intensity of four-pulse DQC Fourier transform peaks.

Intensities For distance measurement, it is important to have an intense signal to improve S/N ratio. The analytical expressions given in Sec. 3.3.3, however, do not reveal the actual relative intensities of four-, five- and six-pulse DQC signals since nonselective pulses rather than finite pulses are used to obtain those expressions. Therefore, rigorous numerical simulations using finite pulses are carried out to compare the intensities of the Pake doublets of four-, five- and six-pulse DQC signals. From the y-axis of Pake plot shown in Figure 3.9, the intensity of the Pake doublets obtained for four-pulse DQC signal is the largest, three times and 10 times larger than those of five- and six-pulse DQC, respectively. The properties of four-, five- and six-pulse DQC sequences in terms of the splitting of the Pake doublet, intensity of their Fourier transform and the effect of the relaxation on them are summarized in Table 3.3.

Pulse sequence	Splitting of the Pake doublet	Intensity of the Fourier transform	Affected by Relaxation	Depth of the dipolar modulation
Four-pulse DQC	$\pm d$	1.20	Yes	100%
Five-pulse DQC	$\pm d$	0.13	No	100%
Six-pulse DQC	$\pm d$	0.34	No	100%

Table 3.3 Comparison between different pulse sequences in terms of the intensities of their Fourier transforms and the effect of the relaxation on them.

The modulation depth, $\Delta(\%)$, for the time domain signals of four-, five- and six-pulse DQC signals, as calculated here, are listed in Table 3.3. It is seen that for all the three pulse sequences considered here, the dipolar depth of the dipolar modulation for each is $\Delta \approx 100\%$. These high values for the four-, five- and six-pulse DQC signals are well above 30%, realized in DEER and RIDME (relaxation-induced dipolar modulation enhancement) experiments, to be considered worthy of experimental measurements.
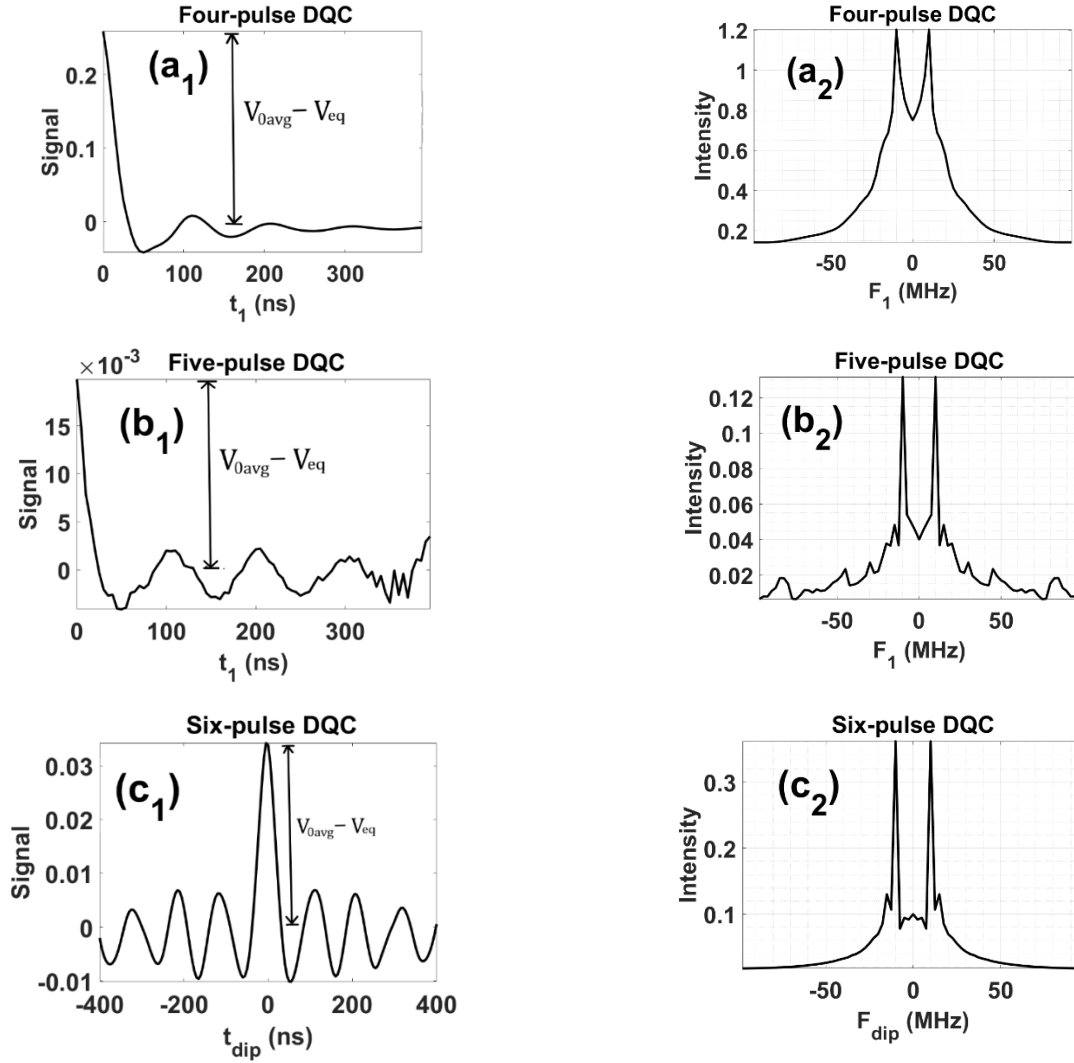
Figure 3.9. Comparison between the intensity of the Pake doublets obtained for (a) four-pulse; (b) five-pulse and (c) six-pulse DQC. The amplitude of the irradiation microwave field $B_1 = 60.0\ G$ and the dipolar coupling constant $d = 10$ MHz are used in the simulations. The intensity of the Pake doublet in four-pulse DQC is almost 4 times and 10 times larger than those of five- and six-pulse DQC Pake doublets, respectively. In order to make a valid comparison between the intensities, the relaxation effect is considered in all the simulations using $T_2^S = 500ns$ and $T_2^D = 300ns$. The depths of dipolar modulation of ~100% are found in all three cases. It is noted from Figs. $(a_2), (b_2), (c_2)$ that even though the Pake doublets of the four-pulse DQC sequence are broadened by relaxation, they are still sufficiently distinguishable from each other to be exploited for distance measurements. The advantage for the four-pulse DQC sequence is that the intensity of the Fourier transform is significantly larger than those of the five- and six-pulse DQC signals, although the latter have much sharper Pake doublets.

41

3.3.7. Details of simulations

In the numerical simulations for distance measurement carried out here, only one variable time is used, which is the time corresponding to the top of the echo for each pulse sequence. The result obtained from the analytical expressions for non-selective pulses are shown for comparison. Although these results show a reasonable agreement with the experimental data, a perfect agreement of analytical simulation with the experiment is not expected, since experimental data are obtained with selective pulses, whereas the analytical expressions are obtained for non-selective pulses. On the other hand, the numerical simulations are always expected to show an excellent agreement with the experimental data, as they have not been subjected to any approximation. Of course, experimental errors are always present in the data.
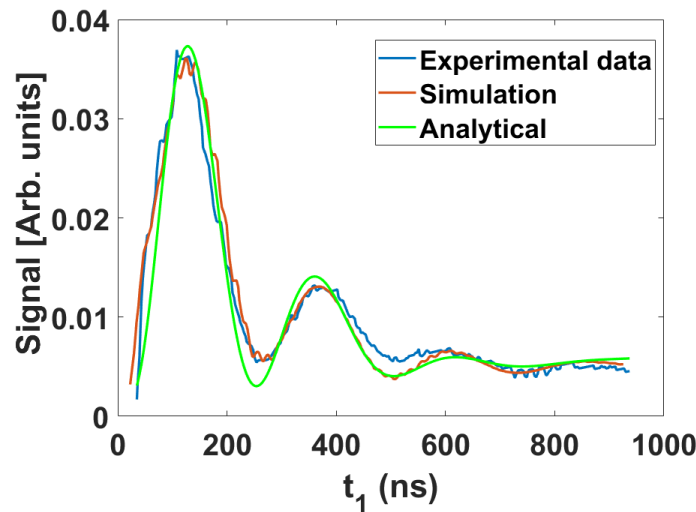
Figure 3.10. Experimental four-pulse DQC spectrum of the nitroxide biradical and the best fit numerical simulation. The value of θ representing the orientation of the external magnetic field with respect to the dipolar axis of the coupled nitroxide in the experiment is 0°. The duration of the π and $\pi/2$ pulses are 6.2 ns and 3.6 ns, respectively. The value of $t_{DQ}^{(4)} = 26.5$ ns is chosen to be the same as that used in the experiment, and the step size in t_1 is 8 ns. This simulation carried out, using the value of the dipolar interaction constant $d = 2.1$ MHz, shows a very good agreement with the experiment, within experimental error. The experimental data is reproduced from (Borbat and Freed 2002).

Four-pulse DQC signal The best fit to the experimental data of four-pulse DQC signal for the nitroxide biradical of the numerical simulation is shown in Figure 3.10. The value of θ representing the orientation of the external magnetic field with respect to the dipolar axis of the coupled nitroxide is chosen to be 0° in accordance with the experiment. The frequency of the microwave field used in the simulation is 17.39 GHz, in accordance with the experimental value (Borbat and Freed 2002); The duration of the $(\pi)_x$ and $(\pi/2)_x$ pulses are 6.2 ns and 3.6 ns, respectively. The value of $t_{DQ}^{(4)} = 26.5$ ns is chosen, and the step size in t_1 is 8 ns, the same as those used in the experiment. The relaxation time $T_2^S = 870$ ns and the stretching parameter $\beta = 0.8$ were found by fitting in the simulation. The value of the dipolar interaction constant used for the simulation was $d = 2.1$ MHz, as reported in (Borbat and Freed 2002). The simulated signal

shows an excellent agreement with the experiment. The effect of the relaxation is seen in Figure 3.10, as evidenced by the reduction of the heights of subsequent maxima, which would not happen had there not been any relaxation effect present.

Five-pulse DQC signal The best fit to the experimental data for five-pulse DQC signal of a nitroxide biradical of the numerical simulation is shown in Figure 3.11. The value of θ used for the five-pulse DQC experiment was 90° in the experiment; the same was used in the numerical simulation. All the other simulation parameters are the same as those used for the four-pulse DQC sequence. The simulated and the experimental signals are found to be in very good agreement with each other. It is noted that, since the relaxation affects equally the intensity of the five-pulse DQC signal at all time points in the plot, the two peaks shown in this figure remain with the same relative heights, as they would have been in the absence of relaxation, unlike the case of four-pulse DQC sequence.
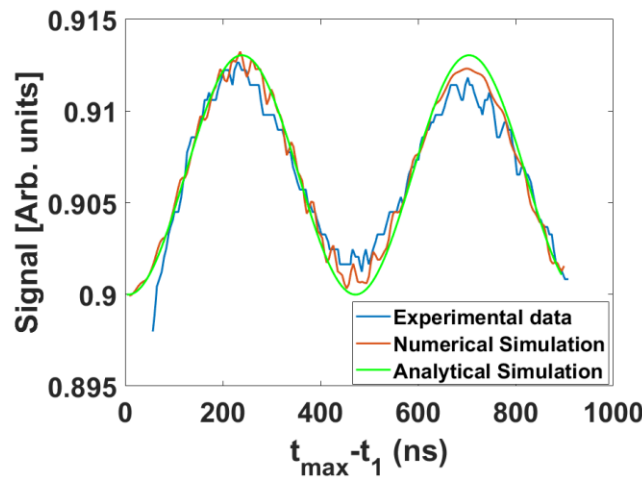
Figure 3.11. Experimental five-pulse DQC spectrum of the nitroxide biradical and the best fit numerical simulation. The value of θ for the five-pulse experiment was 90°. The value of the double quantum time was chosen to be $t_{DQ}^{(5)} = 26.5$. All the other parameters used in the simulation are the same as those mentioned in the caption of Figure 3.10. The five-pulse data is plotted as a function of $t_{max} - t_1$ with $t_{max} = 947\ ns$. The simulated signal calculated using the procedure given in Sec. 4 is found to be in good agreement with the experiment. The experimental spectrum is reproduced from (Borbat and Freed 2002).

Six-pulse DQC signal In the present calculations of six-pulse DQC, the time variables $t_{dip} = t_{max} - 2t_1$ and $t_{echo} = t_6 - t_5$ are used to calculate the final signal. In the present work, following (Saxena and Freed 1997), the inhomogeneous broadening is assumed to be Gaussian and real, whose effect is included by multiplying the final DQC signal $S(t_1, \ldots, t_6)$ for each orientation (θ, ϕ) by the same factor $e^{-2\pi^2 \Delta_G^2 (t_6 - t_1)^2}$, where Δ_G is the Gaussian inhomogeneous broadening parameter for the nitroxide biradical. Since $t_{echo} = t_6 - t_1$, the Gaussian inhomogeneous broadening factor becomes $e^{-2\pi^2 \Delta_G^2 t_{echo}^2}$. Thus, the Gaussian inhomogeneous broadening, which is a function of t_{echo} only, does modify the DQC signal along the echo-time axis together with the relaxation. In the case of 2D six-pulse DQC signal, the effect of the

relaxation for a single-orientation of the external magnetic field with respect to the crystal axes is described by multiplying the calculated signal by an exponential factor $exp\left(-(2t_{max} + t_{echo})/T_2^S - 2t_{DQ}/T_2^D\right)$, with the time constants T_2^S and T_2^D appropriate for that orientation. For a polycrystalline sample, the signal is averaged over different values of (θ, ϕ), each characterized by different relaxation times $T_2^S(\eta, \lambda_1, \lambda_2)$, $T_2^D(\eta, \lambda_1, \lambda_2)$, the effect of the relaxation can be expressed by a stretched exponential as

$$S\left(t_{dip}, t_{echo}\right)_{Avg} = S_{0\,Avg}\left(t_{dip}, t_{echo}\right) \exp\left(-[(2t_{max} + t_{echo})/T_{2\,str}^S]^{\beta^{(S)}}\right. \tag{3.44}$$

$$\left.-\left[2t_{DQ}/T_{2\,str}^D\right]^{\beta^{(D)}}\right)$$

where, $S_{0\,Avg}\left(t_{dip}, t_{echo}\right)$ is the average of $S_0\left(t_{dip}, t_{echo}, \eta, \lambda_1, \lambda_2\right)$ over all orientations $(\eta, \lambda_1, \lambda_2)$:

$$S_{0\,Avg}\left(t_{dip}, t_{echo}\right) = \sum_{\eta, \lambda_1, \lambda_2} S_0\left(t_{dip}, t_{echo}, \eta, \lambda_1, \lambda_2\right) \tag{3.45}$$

and $T_{2\,str}^S$ and $T_{2\,str}^D$ are the stretched relaxation times over single ($p = 1$ pathway) and double ($p = 2$ pathway) quantum states, respectively. In Eq. (3.44), $\beta^{(S)}$ and $\beta^{(D)}$ are the stretching parameters characterizing the single and double spin-spin relaxation times, respectively, which range between zero and one (Stein *et. al.* 2015). Here, three illustrative values of $\beta^{(S)}=\beta^{(D)} = \beta = 0.6, 0.8, 0.9$ are used. It is noted that $\beta^{(D)}$ affects only the intensity of the signal since it is associated with a constant time, t_{DQ}, as implied by Eq. (3.44).

As for the signal along both t_{echo} and t_{dip}, their amplitudes are reduced by the stretched exponential factor when calculating the powder average with relaxation, as given by Eq. (3.44). The shape of the signal along the dipolar axis still remains the same despite reduction in its amplitude because the relaxation factor in Eq. (3.44) does not depend on t_{dip}. On the other hand, the signal along the echo-axis does become broadened due to relaxation, as seen from Figs. 3.14, which shows plots of the signal versus the dipolar and echo times, respectively along with their Fourier transforms. Thus, the value of $T_{2\,str}^S$ can be estimated by fitting the data to Eq. (3.44). Furthermore, the value of $T_{2\,str}^D$ can be deduced, knowing $T_{2\,str}^S$, using the relationship $T_{2\,str}^D \approx T_{2\,str}^S/2$ as deduced experimentally by (Saxena and Freed 1996).

For six-pulse DQC, there are shown six figures, as follows.
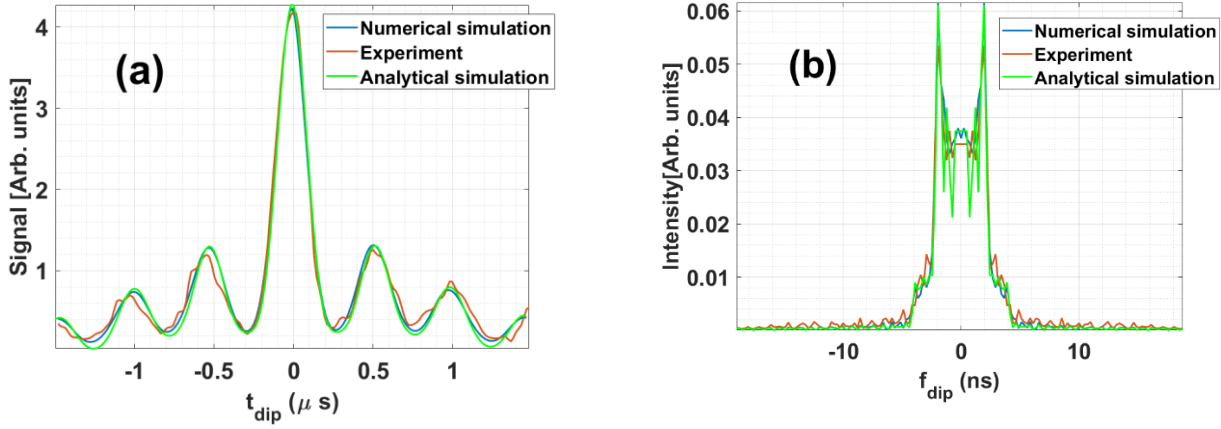
Figure 3.12. Experimental spectrum for a polycrystalline sample of the nitroxide biradical and the best fit numerical simulation of the six-pulse (a) DQC time domain signal and (b) its Fourier transform. The value of the double quantum time was chosen to be $t_{DQ}^{(6)} = 26.5$. All the other parameters used in the simulation are the same as those mentioned in the caption of Figure 3.10. The six-pulse signal is plotted as a function of $t_{dip} = t_{max} - 2t_1$ with $t_{max} = 1200\ ns$. A baseline correction has been applied to the experimental time-domain signal. The simulated signal its Fourier transform are in very good agreement with those of the experiment. The experimental spectra reproduced from (Borbat and Freed 2002).

    (i)   Figure 3.12 displays the experimental six-pulse DQC spectrum for a polycrystalline sample of the nitroxide biradical and the best fit numerical simulation for (a) one-dimensional time-domain signal and (b) its Fourier transform (Pake doublets). The value of the double quantum time was chosen to be $t_{DQ}^{(6)} = 26.5$, the same as that used in the experiment (Borbat and Freed 2002). All the other parameters used in the simulation are the same as those listed in Table 3.1. The simulated six-pulse time-domain signal is plotted as a function of $t_{dip} = t_{max} - 2t_1$ with $t_{max} = 1200\ ns$. The signal and its Fourier transform are in very good agreement with those of the experiment.

    (ii) The experimental six-pulse DQC ESR spectrum of the nitroxide biradical and the best fit numerical simulation is shown in Figure 3.13. The calculated ESR spectrum, in the frequency domain, is plotted by taking a constant slice along f_{echo} of 2D Fourier transform as a function of f_{dip} and f_{echo} at $f_{dip} = 2.1 MHz$. For the simulation, the value of $(\theta, \varphi) = (\pi/2, 0)$ with the combination of three sets of Euler angles, which are (i) $(\alpha_1, \beta_1, \gamma_1) = (\alpha_2, \beta_2, \gamma_2) = (0, \pi/2, 0)$; (ii) $(\alpha_1, \beta_1, \gamma_1) = (0, \pi/2, 0)$, $(\alpha_2, \beta_2, \gamma_2) = (0, 0, 0)$ and (iii) $(\alpha_1, \beta_1, \gamma_1) = (0, \pi/2, 0)$, $(\alpha_2, \beta_2, \gamma_2) = (\pi/3, \pi/4, \pi/3)$ was used. The value of the double quantum time was chosen to be $t_{DQ}^{(6)} = 26.5\ ns$. The simulated Fourier transform calculated using the numerical procedure is found to be in good agreement with the experiment.
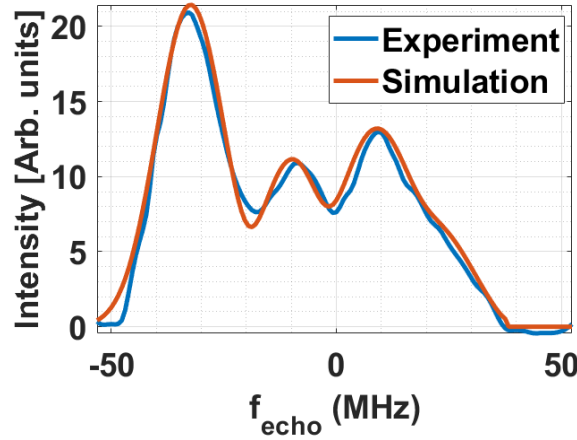
Figure 3.13. Experimental six-pulse DQC ESR spectrum of the nitroxide biradical and the best fit numerical simulation. The ESR frequency is a constant slice along f_{echo} of 2D magnitude Fourier transform vs. f_{dip} and f_{echo}, which are respective Fourier variables of t_{dip} and t_{echo}, at $f_{dip} = 2.1 MHz$. For the simulation, the value of $(\theta, \phi) = (\pi/2, 0)$ with the combination of three sets of Euler angles which are (i) $(\alpha_1, \beta_1, \gamma_1) = (\alpha_2, \beta_2, \gamma_2) = (0, \pi/2, 0)$; (ii) $(\alpha_1, \beta_1, \gamma_1) = (0, \pi/2, 0)$, $(\alpha_2, \beta_2, \gamma_2) = (0, 0, 0)$ and (iii) $(\alpha_1, \beta_1, \gamma_1) = (0, \pi/2, 0)$, $(\alpha_2, \beta_2, \gamma_2) = (\pi/3, \pi/4, \pi/3)$ was used. The value of the double quantum time was chosen to be $t_{DQ}^{(6)} = 26.5$.

(iii) Figure 3.14 illustrates the effect of $(T_{2\,str}^S, T_{2\,str}^D)$ on the magnitude, i.e. the absolute value of the complex signal, of the one-dimensional (1D) time and Fourier- transform signals along the echo time, t_{echo}, axis for three different cases: (a) no relaxation, (b) $(T_{2\,str}^S, T_{2\,str}^D) = (500, 300)$ ns, (c) $(T_{2\,str}^S, T_{2\,str}^D) = (50, 25)$ ns. The 1D signals along t_{echo} are obtained from the two-dimensional (2D) signal, $S(t_{dip}, t_{echo})$, by choosing constant slices along $t_{dip} = 0$. The effect of $T_{2\,str}^S$ on 1D signal along t_{echo} for large values of $T_{2\,str}^S$ and $T_{2\,str}^D$ is less significant here, owing to the rather short duration of the echo times considered, as compared to $T_{2\,str}^S$.

(iv) Figure 3.15 displays the 2D time-domain DQC signals as functions of (t_{dip}, t_{echo}) and their Fourier transforms for three different cases: (a) without relaxation, (b) $(T_{2\,str}^S, T_{2\,str}^D) = (500, 300)$ ns, the same values as those used in (Saxena and Freed 1997), and (c) $(T_{2\,str}^S, T_{2\,str}^D) = (100, 50)$ ns. The decaying effect of relaxation for various $T_{2\,str}^S$ and $T_{2\,str}^D$ $(= T_{2\,str}^S/2)$ times on the 2D time-domain signals and the consequent broadening of their Fourier transforms become more significant for smaller values of $T_{2\,str}^S$ as seen clearly from Figure 3.15 (f).

(v) In Figure 3.16, the top view plots of the Fourier transforms corresponding to Figure 3.15 are plotted in the central square. On the sides of it, the 2D Fourier transforms are integrated and normalized, i.e., dividing by the number of data points, along the f_{echo} and f_{dip} axes to obtain the 1D signals shown on the top and right-hand side of the central square, respectively. The right-hand side plots show the ESR spectrum. In these integrated 1D plots, the effect of the relaxation along f_{echo} can be seen as the broadening of the peak at around $f_{echo} = 50$ MHz

(vi) Figure 3.17 compares the effect of the relaxation on the intensity and broadening of the Fourier transform of the DQC signal on a semi-log scale for different values of the relaxation
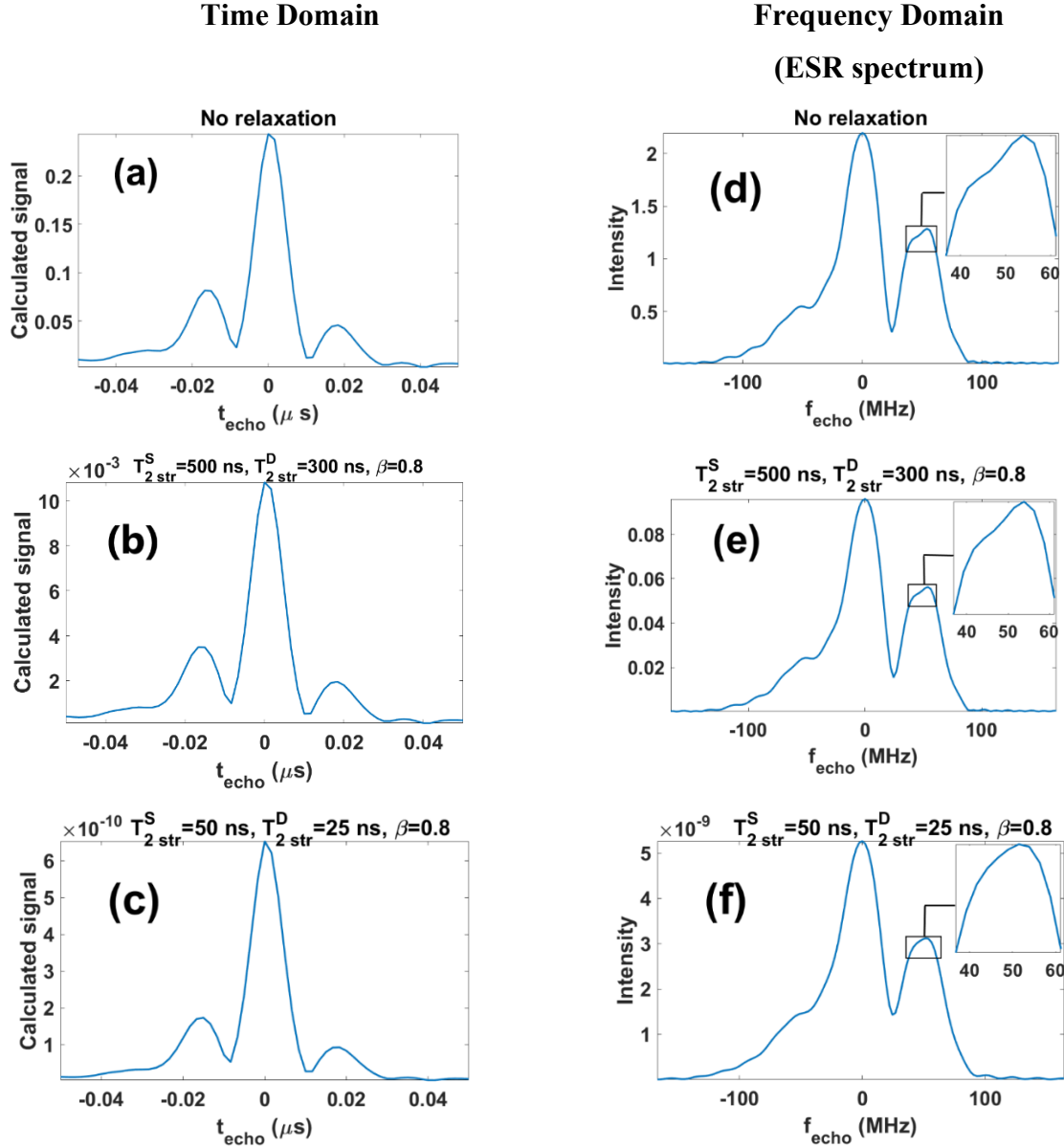
Figure 3.14. The absolute value of the time-domain DQC signals (left) and their corresponding Fourier transforms (right) for the coupled nitroxides radicals system along the t_{echo} axis, sliced about the middle of the dipolar axis in the 2D (t_{dip}, t_{echo}) plot, as calculated for the cases: (a) without relaxation; (b) with relaxation for $(T^S_{2\,str}, T^D_{2\,str}) = (500\text{ ns}, 300\text{ ns})$; (c) with relaxation for $(T^S_{2\,str}, T^D_{2\,str}) = (50\text{ ns}, 25\text{ ns})$. The chosen values of $T^D_{2\,str}$ are consistent with $T^D_{2\,str} \approx T^S_{2\,str}/2$ as found experimentally (Saxena and Freed 1996). It should be noted that the Gaussian broadening is in competition with the relaxation broadening due to $T^D_{2\,str}$, as discussed in Sec. 4. The insets in the right panel show the amplified part of the signal in the range 40-60 MHz to accentuate the effect of relaxation.

times. It is seen that along f_{dip}, relaxation does affect the intensity of the Fourier transform by several orders of magnitude. The shape of the Fourier transform, however, remains totally unaffected. On the other hand, along the f_{echo} axis, both the intensity of the Fourier transforms, and the widths of the peaks are significantly affected by relaxation.

Time Domain   **Frequency Domain**

No relaxation   No relaxation

(a)

$T_{2\,str}^{S}$=500 ns, $T_{2\,str}^{D}$=300 ns, β=0.8

(d)

$T_{2\,str}^{S}$=500 ns, $T_{2\,str}^{D}$=300 ns, β=0.8

(b)

$T_{2\,str}^{S}$=100 ns, $T_{2\,str}^{D}$=50 ns, β=0.8

(e)

$T_{2\,str}^{S}$=100 ns, $T_{2\,str}^{D}$=50 ns, β=0.8

(c)

(f)
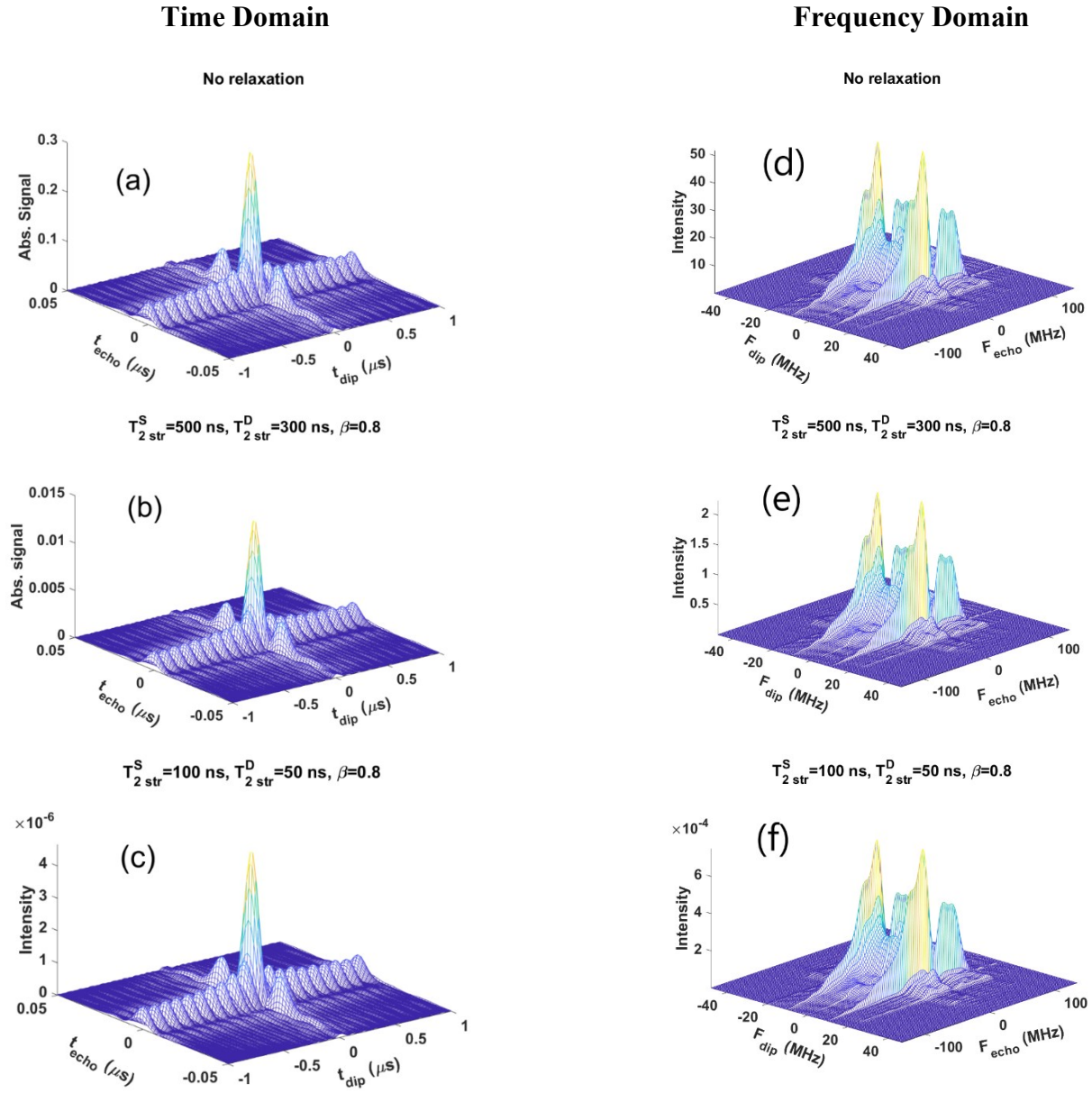
Figure 3.15.   Plots of the absolute values of the two-dimensional time domain DQC six-pulse signals for the coupled nitroxide system for three cases: (a) without relaxation and (b) and (c) with relaxation for two different values of $(T_{2\,str}^{S}, T_{2\,str}^{D})$ as noted on the top of each figure.

49

Fig. 6
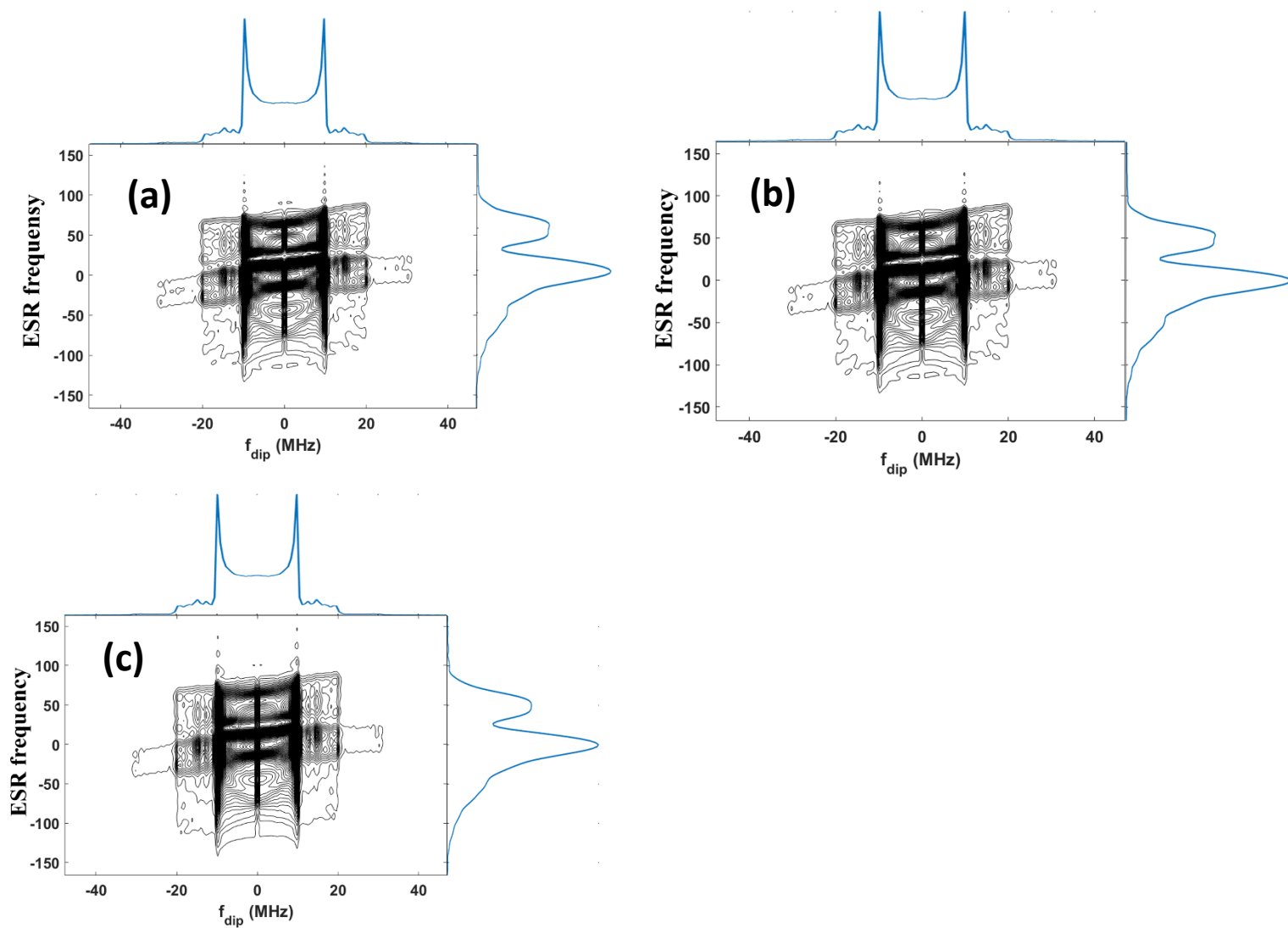
Figure 3.16. Contour plots of the 2D-Fourier transform of DQC six-pulse signals for three cases corresponding to Fig. 5. The corresponding 1D spectra, joined on the top and on the right-hand side of the contour plots, are obtained by integration along the f_{echo} and f_{dip} axes, respectively, and dividing by the number of data points to calculate averages.   The joined figures on the right-hand side represent the absorption CW ESR spectra.
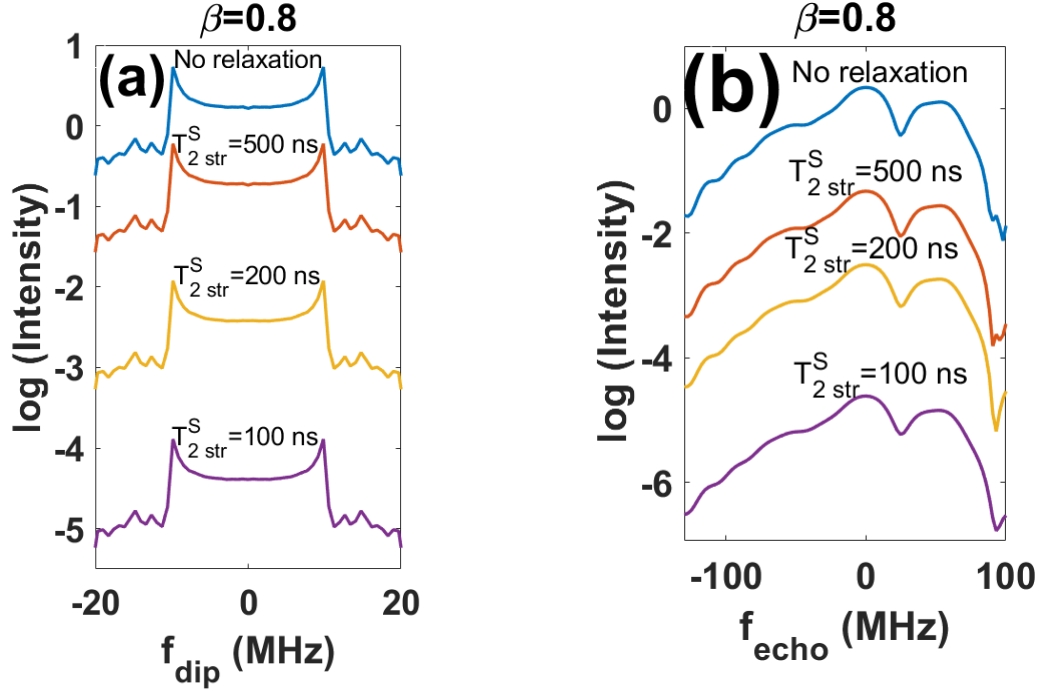
Figure 3.17. Semi-log plot intensity of the Fourier transforms versus (a) f_{dip} and (b) f_{echo} for different values of the relaxation times. The values of the parameter used for the simulation are given in Table I. The intensity of the Fourier transform of the signal is reduced by several orders of magnitudes due to the relaxation in both cases. The relaxation also broadens the peaks along f_{echo} axis.

3.4 Two-pulse DQ and five-pulse DQM at X-band (9.26 GHz) and Ku-band (17.3 GHz)

In this section, double-quantum (DQ) coherence transfers and signals in two-pulse DQ and five-pulse DQM (double quantum modulation) pulsed EPR sequences, utilized for orientation selectivity and distance measurements in biological systems using nitroxide biradicals, have been calculated here for both X-band (9.26 GHz) and Ku-band (17.3 GHz) pulsed EPR using a rigorous numerical algorithm. It is shown, in general, that both, a finite (selective) pulse, rather than an infinite (nonselective) pulse, and the dipolar interaction between the two nitroxide radicals, are needed to produce non-zero coherence transfers in $0\rightarrow2$ and $2\rightarrow-1$ transitions.

3.4.1 Pulse schemes

Two pulse DQ The pulse sequence for a DQ experiment is shown in Fig. Figure 3.18(a). It consists of two finite arbitrary pulses each with the duration t_p. After the application of the first pulse, the system can evolve freely with relaxation over time t_1 on coherence pathway $p = 2$ before the application of the second pulse, after which the coherence pathway $p = -1$ is chosen. The signal is measured after time t_2 after the second pulse. The echo in this two-pulse DQ sequence occurs at the time $t_2 = 2t_1$.

Five pulse DQM. It is shown in Figure 3.18 (b). In this sequence, the first pulse $(\pi/2)_x$ moves the density matrix on to the single-quantum coherence pathway ($p = +1$), over which it evolves for a period t_1. The second pulse $(\pi)_x$ transfers this magnetization to $p = 0$ coherence pathway and the density matrix evolves on it over the period t_2. Thereafter, the third pulse $(\pi/2)_x$ transfers the density matrix on to the double quantum ($p = \pm2$) coherence pathways, over which the density matrix undergoes free evolution for the time interval t_3. It is then subjected to the fourth, refocussing pulse $(\pi)_x$. After the time interval t_4 on the coherence pathways $p = \pm2$, the fifth pulse $(\pi/2)_x$ finally transfers the density matrix on to the single quantum coherence pathway $p = -1$, on which the signal is detected after the time interval t_5. In the experiment, $t_1 = t_2$, which are stepped. As well, $t_3 = t_4$ which will here be denoted for this pulse sequence as $t_{DQ}^{(DQM)}$; it is kept fixed. The echo in this five-pulse DQM sequence occurs at the time $t_5 = t_1$.
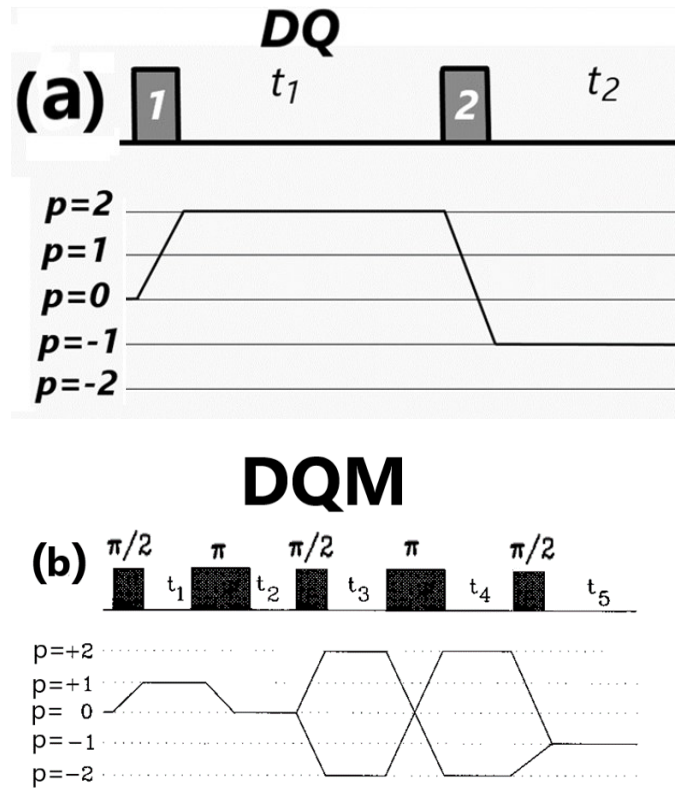
Figure 3.18. The pulse schemes and the relevant coherence pathways for (a) two-pulse DQ sequence; (b) five-pulse DQM sequence. The time intervals (t_i; $i = 1,2$ for DQ and $i = 1,2,3,4,5$ for DQM) between the pulses, as well as after the last pulse for the two sequences are indicated.

3.4.2 Analytical expressions of two-pulse DQ and five-pulse DQM one-dimensional signals

Analytical expressions of the signals are useful in deducing important features of the signal and its Fourier transform. In this section, the analytical expression for two-pulse DQ and five-pulse DQM one-dimensional signals i.e., at the top of the echo, are expressed, following the general algorithm to calculate the analytical expression of pulsed EPR signal given in Sec.3.3.2.

One-dimensional-two-pulse DQ signal Using the same approximations to calculate the analytical expressions of the pulsed EPR signals as in Sec. 3.3.2, the 1D signal for two-pulse DQ sequence i.e., at $t_1 = t_2/2$ is expressed as

$$\mathrm{DQ}^{\mathrm{Signal}}(t_2) = e^{i(3\phi_2 - 2\phi_1)} e^{-t_2/2T_2^D} e^{-t_1/T_2^S}$$
$$\times \mathrm{Tr}\left[\left(P_{11}^{(1)} P_{41}^{(1)\dagger} - P_{14}^{(1)} P_{44}^{(1)\dagger} \right) \left\{ \left(P_{24}^{2\,\dagger} + P_{34}^{2\,\dagger} \right) P_{41}^2 \, e^{-i\frac{3}{4}d\times(3\cos^2\theta - 1)t_2} \right.\right.$$
$$\left.\left. + P_{14}^{2\,\dagger}(P_{21}^2 + P_{31}^2) e^{+i\frac{3}{4}d\times(3\cos^2\theta - 1)t_2} \right\}\right] \tag{3.46}$$

where ϕ_1 and ϕ_2 are the phase of the first and second pulses, respectively, and the trace is taken over the 9×9 hyperfine space. The $P_{ij}^k, i = 1, \dots, 4; j = 1,4; k = 1,2$ terms in Eq. (3.46) are 9×9 matrices in the hyperfine space as defined in Sec. 3.3.2 General procedure to derive analytical expressions for multi-pulse-EPR Signals. An examination of Eq. (2.19) reveals that the signal depends on $\pm\frac{3d}{4} \times (3\cos^2\theta - 1)t_2$, whose Fourier transform, as a function of t_2, would yield peaks at the frequencies $\pm\frac{3d}{4} \times (3\cos^2\theta - 1)$ for the orientation of the dipolar axis with the external magnetic field at angle θ. It is now seen that when the average over θ, ϕ is calculated for any choice of the five independent Euler angles, the orientations with $\theta \sim \pi/2$ contribute predominantly to the polycrystalline averaging because of using the weighting factor of $\sin\theta$ in the powder average. This leads to the conclusion that the peaks of the signal, i.e., the Pake doublet, will occur at $\pm\frac{3d}{4}$ when averaged over the orientations of the two nitroxide dipoles.

One-dimensional Five-pulse DQM signal

The five-pulse DQM sequence, shown in Figure 3.18 (b), is tantamount to two coherence pathways, both of which lead to the formation of an echo at $t_5 = t_1$. These are:

(i) $p = 0 \to +1 \to 0 \to +2 \to -2 \to -1$ (3.47)

(ii) $p = 0 \to +1 \to 0 \to -2 \to +2 \to -1$

In the analytical calculations here, finite pulses are used to affect the transitions $1\to 0$ and $0 \to \pm2$, otherwise for the remaining pathways strong pulses are used, which do not require inclusion of H_0, so that $H_p \gg H_0$.

Following the procedure described in Sec. 3.3.2, the 1D five-pulse DQM signals for the two coherence pathways in Eq. (3.47) are calculated for $t_1 = t_5$, for the orientation of the dipolar

axis, oriented at an angle θ with respect to the external magnetic field (lab frame), indicated by the superscripts (i) and (ii), respectively, to be as follows:

$$Signal_{DQM}^{(i)}(t_5) = \frac{1}{4}e^{-i(\phi_1-\phi_2+2\phi_3-4\phi_4+\phi_5)}e^{-2t_{DQ}^{(DQM)}/T_2^D}e^{-2t_5/T_2^S}e^{-t_5/T_1}$$

$$\times Tr\left[\left(P_{11}^3 M_1 P_{14}^{2\,\dagger} P_{41}^{3\,\dagger} + P_{14}^3 M_2 P_{44}^{2\,\dagger} P_{44}^{3\,\dagger} + (P_{12}^3 M_3 + P_{13}^3 M_4)\left(P_{24}^{2\,\dagger} P_{42}^{3\,\dagger} + \right.\right.\right.$$

$$\left. P_{34}^{2\,\dagger} P_{43}^{3\,\dagger}\right)\right)e^{id(3cos^2\theta-1)t_5} - \left(P_{11}^3 P_{11}^2 M_1^\dagger P_{41}^{3\,\dagger} + P_{14}^3 P_{41}^2 M_2^\dagger P_{44}^{3\,\dagger} + (P_{12}^3 P_{21}^2 + \right.$$

$$\left. P_{13}^3 P_{31}^2)\left(M_3^\dagger P_{42}^{3\,\dagger} + M_4^\dagger P_{43}^{3\,\dagger}\right)\right)e^{-id(3cos^2\theta-1)t_5}\bigg] \tag{3.48}$$

$$Signal_{DQM}^{(ii)}(t_5) = -\frac{1}{4}e^{-i(\phi_1-\phi_2-2\phi_3+4\phi_4+3\phi_5)}e^{-2t_{DQ}^{(DQM)}/T_2^D}e^{-2t_5/T_2^S}e^{-t_5/T_1}$$

$$\times Tr\left[\left(P_{41}^3 M_1 P_{14}^{2\,\dagger} P_{11}^{3\,\dagger} + P_{44}^3 M_2 P_{44}^{2\,\dagger} P_{14}^{3\,\dagger} + (P_{42}^3 M_3 + P_{43}^3 M_4)\left(P_{34}^{2\,\dagger} P_{13}^{3\,\dagger} + \right.\right.\right.$$

$$\left. P_{24}^{2\,\dagger} P_{12}^{3\,\dagger}\right)\right)e^{id(3cos^2\theta-1)t_5} - \left(P_{41}^3 P_{11}^2 M_1^\dagger P_{11}^{3\,\dagger} + P_{44}^3 P_{41}^2 M_2^\dagger P_{14}^{3\,\dagger} + (P_{42}^3 P_{21}^2 + \right.$$

$$\left. P_{43}^3 P_{31}^2)\left(M_3^\dagger P_{12}^{3\,\dagger} + M_4^\dagger P_{13}^{3\,\dagger}\right)\right)e^{-id(3cos^2\theta-1)t_5}\bigg] \tag{3.49}$$

The $M_i, i = 1,2,3,4$ terms in Eqs. (3.48) and (3.49) are

$$M_1 = P_{12}^{(2)} + P_{13}^{(2)}$$

$$M_2 = P_{42}^{(2)} + P_{43}^{(2)} \tag{3.50}$$

$$M_3 = P_{22}^{(2)} + P_{23}^{(2)}$$

$$M_4 = P_{32}^{(2)} + P_{33}^{(2)}$$

The five-pulse DQM signal, is then:

$$Signal_{DQM}(t_1) = Signal_{DQM}^{(i)}(t_1) + Signal_{DQM}^{(ii)}(t_1) \tag{3.51}$$

It is seen from Eqs. (3.48) and (3.49) that the main dipolar peaks for a chosen orientation of the two nitroxide dipoles with respect to the dipolar axis, oriented at an angle θ with respect to the lab axis, occur at $\pm d \times (3cos^2\theta - 1)$ in the Fourier transform taken with respect to time variable t_5. This shows that the Pake doublet for the 1D five-pulse DQM signal, occurs at $\pm d$ in the Fourier transform of the signal.

3.4.3 Coherence transfer and orientational selectivity in two-pulse DQ and five-pulse DQM signals

3.4.3.1 Coherence transfer efficiency

It is important to have an estimate of the coherence transfer, $T_{m\to n}$, which is the probability of transition from the pathway m to the pathway n, since the intensity of the signal increases with increasing coherence transfer. It is calculated as follows.

The density matrix for the pathway n after phase cycling subsequent to the application of a pulse is proportional to the spin operator corresponding to the coherence pathway n, which is S_z for the coherence pathway $p = 0$ (needed for five-pulse DQM only), $S_{\pm}$ for the coherence pathways $p = \pm 1$ and $(S_{\pm}.S_{\pm})$ for the coherence pathways $p = \pm 2$ The coherence transfer, $T_{m\to n}$, for the pathway n is then obtained by taking the trace of the density matrix resulting by the action of the pulse with the adjoint of the projection operator matrix for the coherence pathway n, listed in Appendix B.

The coherence-transfer efficiency for the transitions 0→2 and 2→-1 occurring in a DQ and DQM experiments is zero for a nonselective pulse (Saxena and Freed 1997). With the application of a finite pulse, however, one can obtain non-zero coherence transfers $T_{0\to 2}$ and $T_{2\to -1}$. Using the rigorous numerical calculation, wherein one considers the full static spin Hamiltonian during the pulse, it is shown here that, indeed, $T_{0\to 2}$ and $T_{2\to -1}$ are non-zero for the system of coupled nitroxides as effected by a pulse of finite duration.

The results of numerical simulations for the coherence transfers $T_{0\to 2}$ and $T_{2\to -1}$ described above for a polycrystalline sample are plotted as functions of the amplitude of the irradiation microwave field B_1 and the duration of the pulse t_p in Figure 3.19, Figure 3.20 and Figure 3.21 for $d = 10, 20, 30$ MHz, respectively. It is seen by comparison that a maximum efficiency is found to occur for both $T_{0\to 2}$ and $T_{2\to -1}$, with an experimentally achievable B_1=60 G and $t_p = 65$ ns for all the three values of d considered here. The coherence transfers are found to be significantly affected by the dipolar interaction; specifically, the efficiency of the coherence transfer in the transition $T_{0\to 2}$ and $T_{2\to -1}$ values are about (0.03, 0.08, 0.11) and (0.03, 0.06, 0.10) for $d = 10, 20, 30$ MHz, respectively.

3.4.3.2 Orientational selectivity

There occurs orientational selectivity when the signal is determined predominantly by those biradicals, whose dipolar axes are oriented in a narrow range about the static magnetic field direction.

Exact numerical calculation. For these calculations, it is first noted that the forbidden transition $p = 0 \to 2$ in the two-pulse DQ and five-pulse DQM sequences becomes possible only in the presence of the dipolar interaction and a for a finite pulse as discussed later in this section. When this condition is satisfied, the coherence transfer $T_{0\to 2}$ is found to be much larger in a very narrow range about four specific values of θ, the angle between the dipolar axis and the external magnetic field. These specific four angles depend on the amplitude of the irradiation field, B_1, and the dipolar interaction, d, as the simulations presented here show for $T_{0\to 2}$ for three values of $d = 20, 30,$ and 40 MHz as displayed in Figure 3.22(a), Figure 3.22(b), Figure 3.22(c),
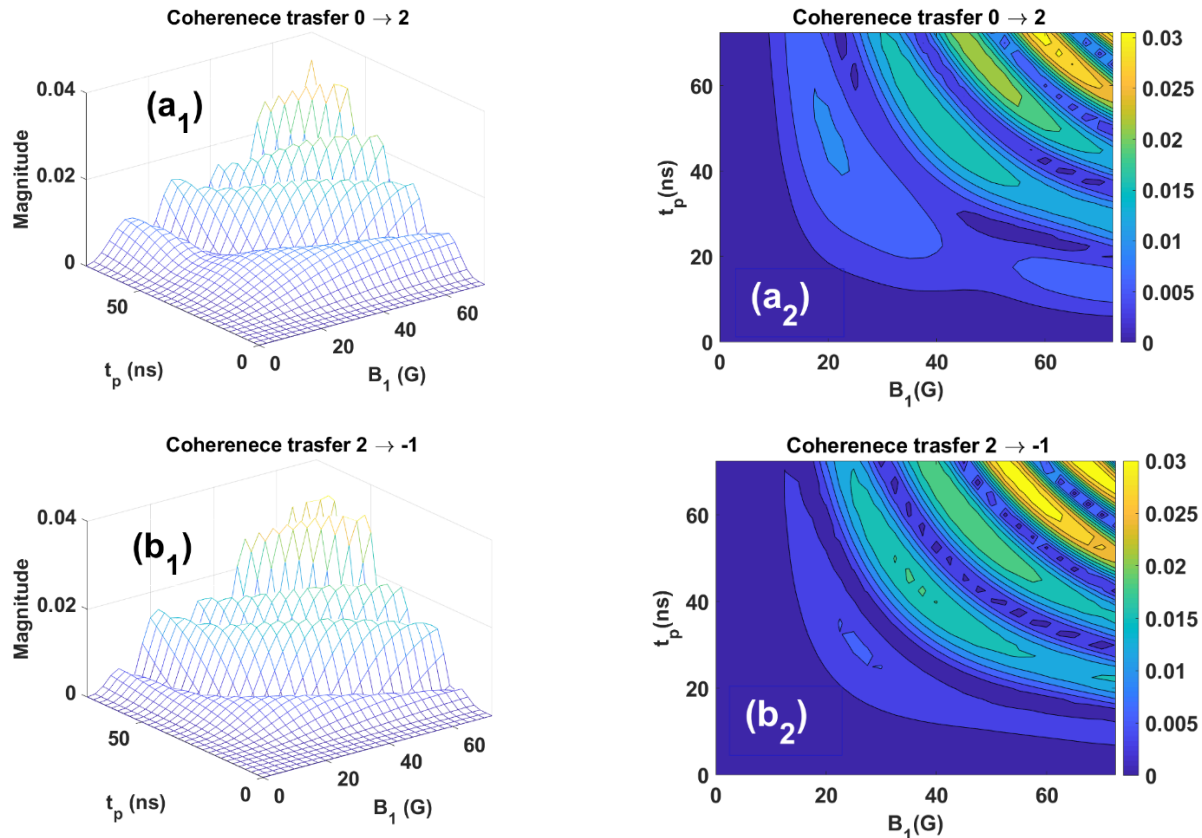
Figure 3.19 Two-pulse DQ coherence transfers for a polycrystalline sample, averaged over twenty Monte-Carlo orientations of the nitroxide dipoles of the biradical: (left) the absolute values and (right) their contour plots of the coherence transfers; (top) $T_{0 \to 2}$ and (bottom) $T_{2 \to -1}$, as functions of the intensity of the irradiation microwave magnetic pulse, B_1 and the duration of the pulses, t_p for the dipolar coupling constant $d = 10$ MHz. All the parameters used for simulations are the same as those listed in Table 3.1. It is seen from these simulations that the maximum coherence transfer is achieved for both $0 \to 2$ and $2 \to -1$ transitions with $B_1 = 60$ G and $t_p = 65$ ns, which are experimentally feasible values.
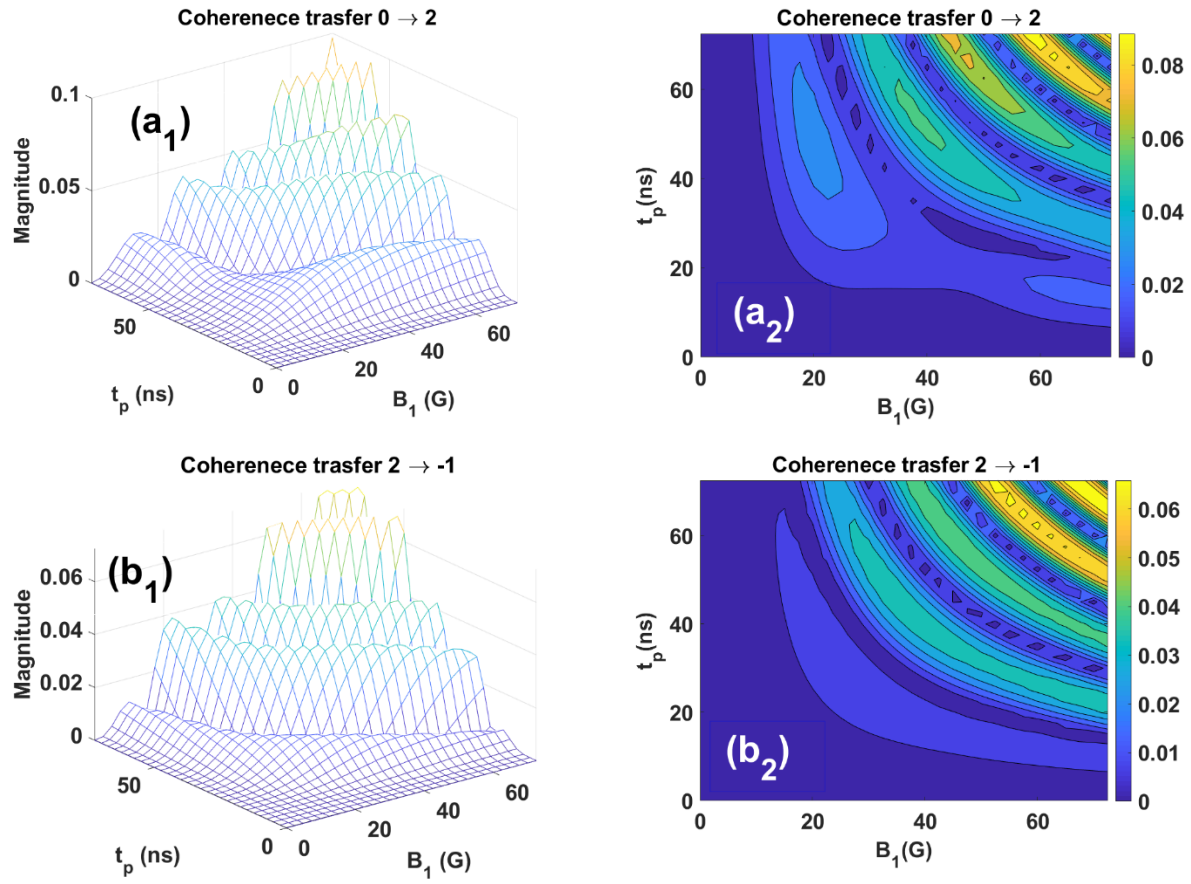
Figure 3.20 The same details as those for Figure 3.19, except that here the simulations are for the dipolar-coupling constant *d = 20 MHz*
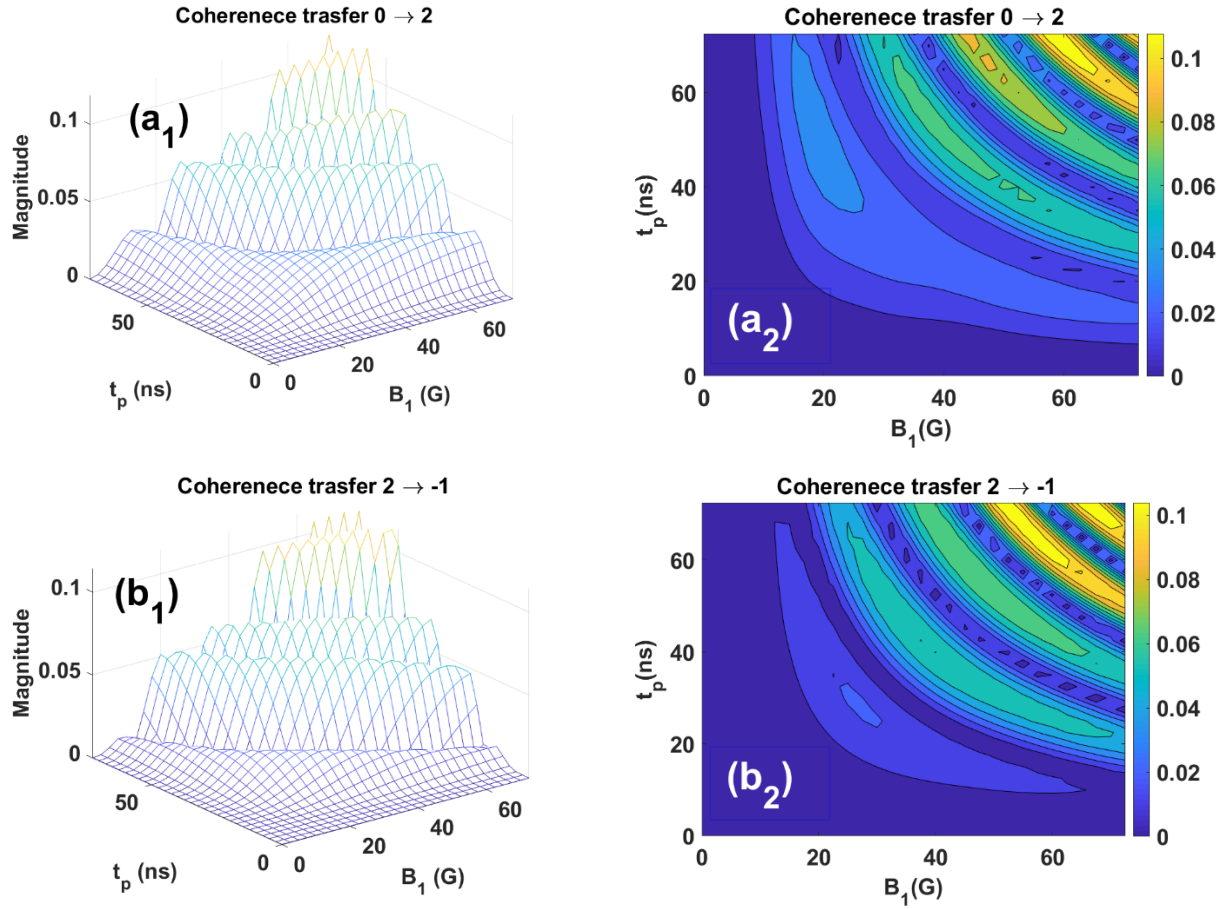
Figure 3.21 The same details as those for Figure 3.19, except that here the simulations are for the dipolar-coupling constant *d = 30 MHz*.

respectively, for varying values of B_1. It is found from these figures that for smaller B_1 there are, indeed, two such values of θ in the range $0° \leq \theta_0 \leq 90°$, and two more about its supplementary angle $125.26°$, for which the $T_{0\rightarrow2}$ value is much larger than those for other values of θ. These values are found to be situated symmetrically within $10°$ away from the magic angle $54.74°$ at which $(3cos^2\theta - 1) = 0$, and its supplementary angle $125.26°$, becoming closer to the magic angle as d increases, as seen from Figure 3.22, giving rise to orientational selectivity; implying that these spins will be preferentially pumped from the $p = 0$ to the $p = 2$ coherence state. This implies that there occurs ***orientational selectivity***. This orientational selectivity of the forbidden DQ signal occurs up to a maximum value of B_1 that depends on d. These maximum B_1 values are 1.5, 2.0, and 3.0 G for *d = 20, 30, and 40 MHz* for both, the two-pulse DQ and five-pulse DQM sequences.

In order to display orientational selectivity, the coherence transfer efficiency $T_{0\rightarrow2}$ is plotted as a function of θ, the angle between the dipolar axis and the external magnetic field, as calculated using the analytical expression (3.59), in Figure 3.22$(a_1), (b_1)), (c_1)$ for *d = 20, 30, 40 MHz*,

58

respectively, for several weak irradiation microwave fields $B_1 (\leq 5.0$ G), each for an appropriate time interval t_p, so that the tip angle $\beta = \pi/2$. In each case, a polycrystalline average is taken over 20 simulations, carried out with randomly generated set of the five independent orientation angles for the two nitroxide dipoles, using the Monte-Carlo technique. For comparison, the same simulations are carried out numerically without neglecting any terms in the spin Hamiltonian. The results are plotted in Figure 3.22 (a_2), (b_2), (c_2), alongside the ones obtained using the analytical expressions. The two sets are found to be in very good agreement with each other, justifying the validity of the analytical expressions (3.59) and (3.60)

Analytical treatment of orientational selectivity. It is useful to have analytical expressions for a quick calculation and evaluation of important features of coherence transfer, i.e., orientational selectivity. To this end, some approximations are made to simplify the calculation. One of the approximations made in the following treatment is to neglect the Zeeman and hyperfine terms with coefficients (C_1, C_2) and (A_1, B_1, A_2, B_2), respectively, in the spin Hamiltonian given by Eq. (2.1). However, one has to compensate for it by modifying the frequency ω_1 to an effective frequency, ω_{1eff}, as discussed below.

Effective frequency of rotation, ω_1 (ω_{1eff}). The presence of the pulse, i.e., the microwave field, B_1, tips the magnetization differently out of the precession about the z-axis, where it was before the application of the pulse. This implies that the magnetization is now tipped by an effective magnetic field $\boldsymbol{B_{eff}}$, which is the vector sum of $\boldsymbol{B_1}$ and $\boldsymbol{B_0}$, causing the magnetizations of the two electrons to tip around their respective $\boldsymbol{B_{eff}} = \boldsymbol{B_1} + \boldsymbol{B_0}$, at a faster effective rate (Raitsimring and Borbat 1996). This is considered for the two dipoles of the biradical by taking the average of the effective angular velocities for the two dipoles, since only one dipole is flipped by the pulse at a time:

$$\omega_{1eff} = \gamma_e B_{1eff} = \{(\omega_1{}^2 + C_1{}^2)^{1/2} + (\omega_1{}^2 + C_2{}^2)^{1/2}\}/2 \qquad (3.52)$$

where $\omega_1 = \gamma_e B_1$ and C_1, C_2, respectively, are the coefficients of S_{z_1} and S_{z_2} in the spin Hamiltonian, Eq. (2.2), given by Eq. (A.4) in Appendix A. From Eq. (5.1), it is seen that for a strong pulse, i.e., $\omega_1 \gg C_1, C_2$, one can approximate ω_{1eff} by ω_1, whereas for a weak pulse, the effect of Zeeman terms must be included. The Zeeman and hyperfine terms in the static Hamiltonian, given by Eq. (*3.2*), are responsible for a detuning from the carrier frequency as discussed above in this section. As a result, ω_1 will be substituted here by ω_{1eff}, which is given by Eq. (3.52), following the discussion given by (Raitsimiring and Borbat 1996). Then only the dipolar-interaction term H_{12} need to be taken into consideration for the calculation of coherence transfer, which makes it simpler to derive analytical expressions, as follows.

In the magnetic basis of the two electrons, the matrix for H_0 in the direct-product space (see Appendix B), is then given as

$$H_{12} = a/3 \left(2S_z^2 - S_x^2 - S_y^2\right) = \begin{pmatrix} a/3 & 0 & 0 & 0 \\ 0 & -a/3 & -a/3 & 0 \\ 0 & -a/3 & -a/3 & 0 \\ 0 & 0 & 0 & a/3 \end{pmatrix} \qquad (3.53)$$
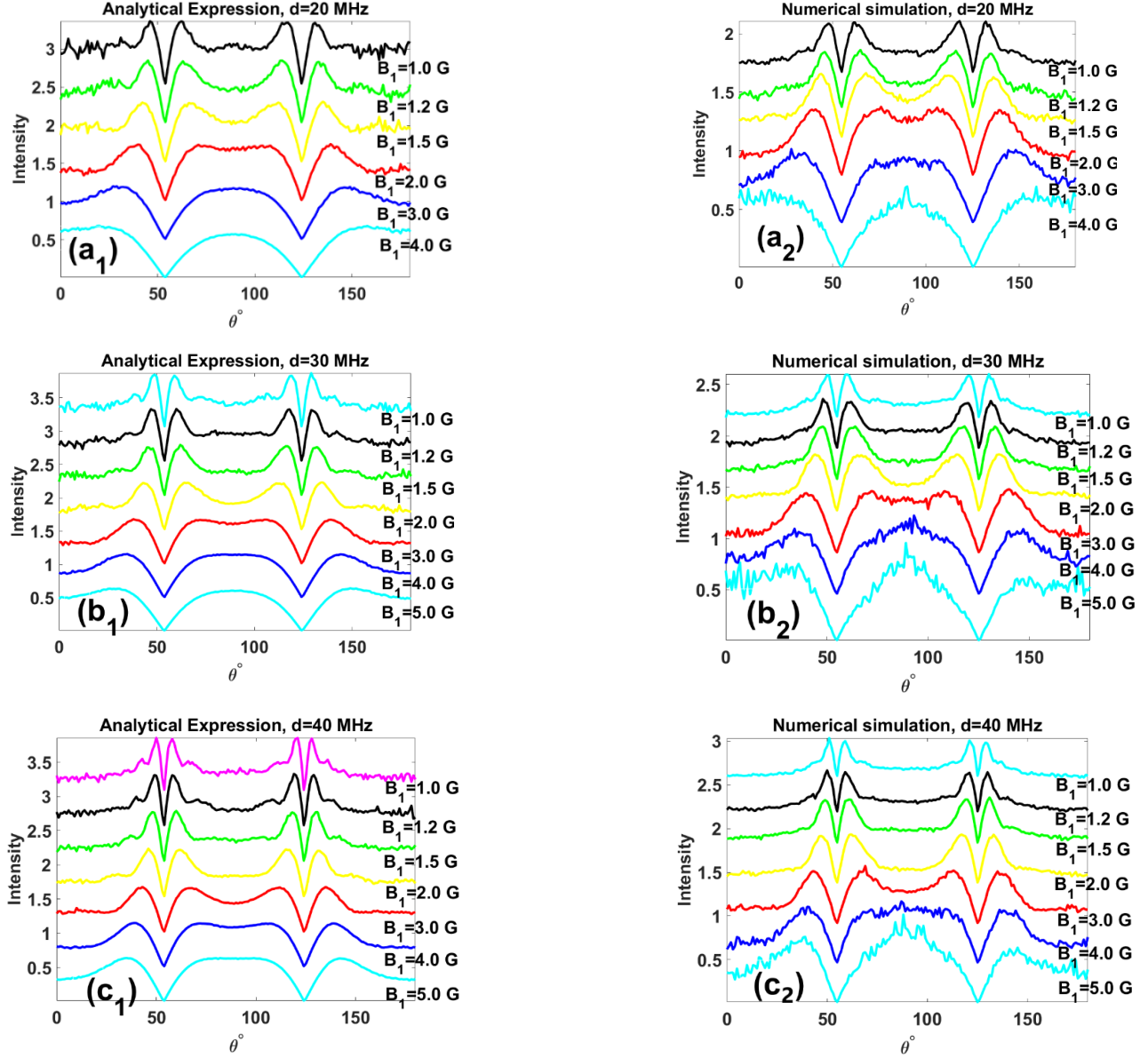
Figure 3.22 The coherence transfer $T_{0\rightarrow2}$ plotted as function of θ, as calculated: left (a_1, b_1, c_1) using the analytical expression, Eq.(3.59), and right (a_2, b_2, c_2) rigorously using numerical simulations for different values of the amplitude of the irradiation microwave pulse, B_1, indicated next to each plot for (a_1, a_2) $d = 20$ MHz, (b_1, b_2) $d = 30$ MHz and (c_1, c_2) $d = 40$ MHz. The duration of the pulse t_p in each case is chosen consistent with a nominal $\pi/2$ pulse and amplitude B_1. The two sets, calculated using analytical expressions and exact numerical algorithm, are found to be in very good agreement with each other. Regardless of the values of d and B_1, the coherence transfer is zero at the magic angle $\theta = 54.74°$ and at its supplementary angle $\theta = 125.26°$, i.e., the values which make $(3cos^2(\theta) - 1) = 0$. The orientational selectivity, determined by the sharpness of the peaks, occurs at lower values of B_1 for each d value. These values are less than 1.5, 2.0, and 3.0 G for *d = 20, 30, and 40 MHz*, respectively.

where $S_z = S_{z_1} \otimes \mathbb{1}_{S_2} + \mathbb{1}_{S_1} \otimes S_{z_2}$, $S_x = S_{x_1} \otimes \mathbb{1}_{S_2} + \mathbb{1}_{S_1} \otimes S_{x_2}$, $S_y = S_{y_1} \otimes \mathbb{1}_{S_2} + \mathbb{1}_{S_1} \otimes S_{y_2}$, and $a = \frac{3d}{4}(3cos^2\theta - 1)$. The matrix for H_p, using ω_{1eff}, is:

$$H_p = \begin{pmatrix} 0 & \frac{1}{2}\omega_{1eff}\, e^{-i\phi} & \frac{1}{2}\omega_{1eff}\, e^{-i\phi} & 0 \\ \frac{1}{2}\omega_{1eff}e^{i\phi} & 0 & 0 & \frac{1}{2}\omega_{1eff}e^{-i\phi} \\ \frac{1}{2}\omega_{1eff}\, e^{i\phi} & 0 & 0 & \frac{1}{2}\omega_{1eff}\, e^{-i\phi} \\ 0 & \frac{1}{2}\omega_{1eff}e^{i\phi} & \frac{1}{2}\omega_{1eff}\, e^{i\phi} & 0 \end{pmatrix} \quad (3.54)$$

For the calculation of the coherence transfer, the phase of the pulse, ϕ, is set equal to zero. The eigenvalues, E_p and the eigenvectors, U, of matrix $H_{12} + H_p$, using Eqs. (3.53) and (3.54) are given as

$$E_p = U^\dagger.(H_{12} + H_p).U = \begin{pmatrix} 0 & 0 & 0 & 0 \\ 0 & \dfrac{a}{3} & 0 & 0 \\ 0 & 0 & -\dfrac{1}{6}(a + 3\Omega) & 0 \\ 0 & 0 & 0 & \dfrac{1}{6}(3\Omega - a) \end{pmatrix} \quad (3.55)$$

where

$$U = \begin{pmatrix} 0 & -\dfrac{1}{\sqrt{2}} & \dfrac{\sqrt{2}\omega_{1eff}}{\sqrt{(a+\Omega)^2 + 4\omega_{1eff}^2}} & \dfrac{\sqrt{2}\omega_{1eff}}{\sqrt{(a-\Omega)^2 + 4\omega_{1eff}^2}} \\[3mm] -\dfrac{1}{\sqrt{2}} & 0 & -\dfrac{\Omega + a}{\sqrt{2}\sqrt{(a+\Omega)^2 + 4\omega_{1eff}^2}} & \dfrac{\Omega - a}{\sqrt{2}\sqrt{(a-\Omega)^2 + 4\omega_{1eff}^2}} \\[3mm] \dfrac{1}{\sqrt{2}} & 0 & -\dfrac{\Omega + a}{\sqrt{2}\sqrt{(a+\Omega)^2 + 4\omega_{1eff}^2}} & \dfrac{\Omega - a}{\sqrt{2}\sqrt{(a-\Omega)^2 + 4\omega_{1eff}^2}} \\[3mm] 0 & \dfrac{1}{\sqrt{2}} & \dfrac{\sqrt{2}\omega_{1eff}}{\sqrt{(a+\Omega)^2 + 4\omega_{1eff}^2}} & \dfrac{\sqrt{2}\omega_{1eff}}{\sqrt{(a-\Omega)^2 + 4\omega_{1eff}^2}} \end{pmatrix} \quad (3.56)$$

and

$$\Omega = \sqrt{a^2 + 4\omega_{1eff}^2} \quad (3.57)$$

Then the pulse propagator, including the dipolar Hamiltonian, is expressed as

$$e^{-i(H_{12} + H_p)t_p} = U.e^{-iE_p t_p}.U^\dagger \quad (3.58)$$

The coherence transfer for the transition 0 →2 is then:

$$T_{0 \to 2} = Abs\{Tr[(S_-.S_-)/2.\, e^{-i(H_{12}+H_p)t_p}.S_z.\, e^{i(H_{12}+H_p)t_p}]\}$$

$$= Abs\left(\frac{a\,\cos(\frac{at_p}{2})\,\sin(\frac{\Omega t_p}{2})}{\Omega} - \sin(\frac{at_p}{2})\cos(\frac{\Omega t_p}{2}) \right) \qquad (3.59)$$

In the middle part of Eq. (3.59), a division of 2 has been added after the first equality to extract the (1,4) element of the transformed density matrix. Likewise, for the transition $2 \to -1$, the magnitude of the coherence transfer is:

$$T_{2 \to -1} = Abs\{Tr[S_+.\, e^{-i(H_{12}+H_p)t_p}.(S_+.S_+)/2.\, e^{i(H_{12}+H_p)t_p}]\}$$

$$= Abs\left(\frac{2\omega_{1eff}\ \sin\left(\frac{1}{2}\Omega t_p\right)\left(a\sin\left(\frac{1}{2}\Omega t_p\right) - \Omega\sin\left(\frac{a\,t_p}{2}\right)\right)}{\Omega^2} \right) \qquad (3.60)$$

After the first equality in Eq. (3.60), a division of 2 has been added to render the (1,4) element of the density matrix corresponding to $p = +2$ state equal to unity. It is noted from Eqs. (3.59) and (3.60) that in the limit when the dipolar coupling, d, or the duration of the pulse, t_p approaches zero, both the coherence transfers $T_{0 \to 2}$ and $T_{2 \to -1}$ vanish. *This implies that one needs a finite pulse, together with the dipolar interaction, to produce a non-zero coherence transfer.*

3.4.4 Results of numerical simulations of two-pulse DQ and five-pulse DQM at X-band

The numerical simulations for calculations of two-pulse DQ and five pulse DQM for a coupled nitroxide biradical are performed following the procedure described in Sec. 3.1 Numerical procedure. The results are shown in Figures 3.23 – 3.25 displaying the dependence of the time-domain and Fourier transforms of DQ and DQM signals for the dipolar-coupling constants: $d = 0.5, 7, 10, 20, 30, 40, 50\ MHz$, simulated at the top of the echo i.e., at $t_2 = 2t_1$ and $t_5 = t_1$ for DQ and DQM pulse sequences, respectively. In Fig. 3.19, the amplitude of the radiation microwave field $B_1 = 10G$ and the duration of the finite pulses $t_p = 80$ ns and in Fig. 3.20, $B_1 = 60G$ and $t_p = 65$ ns, corresponding to the maximum coherence efficiency as discussed in Sec. 3.4.3, are used. The dead time of $t_d = 35$ ns, as that reported experimentally in (Borbat and Freed 2002), is assumed here. This means that the signal during the initial 35 ns, shown as hatched in Figs. 3.23-3.24, cannot be recorded in the experiment. To consider the effect on the Fourier transform of the signal that can be recorded, the Fourier transforms with respect to both actual time variables and reduced times are plotted in Figs. 3.23–3.25, shown in black and blue, respectively. It is seen that the Fourier transform taken with respect to the reduced times does not distort the Pake doublets, or its position. It reduces only the intensity and the width of the Fourier transform. For $d = 0.5$ MHz, the dead-time covers only a negligible part of the signal. The modulation depth, Δ, can then be calculated for this case. It is found to be almost 100%, as seen from Figs. 3.23-3.25. As for $d > 7$ MHz, Δ cannot be measured, because a significant part of the initial signal is lost in the dead-time. The Pake doublets in the Fourier transform of the DQ signals shown in Figs. 3.19 and 3.20, indeed, appear at $\pm\frac{3}{4}d$, whereas in the case of DQM signals, it appears at $\pm d$, as deduced theoretically in Sec. 3.4.2.
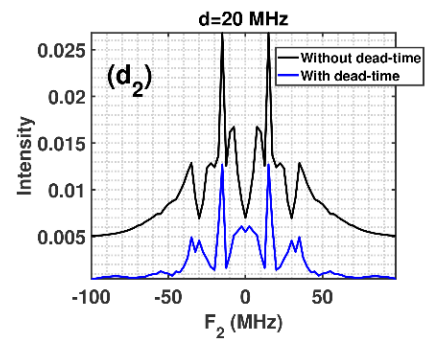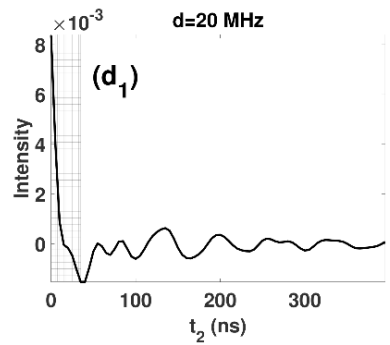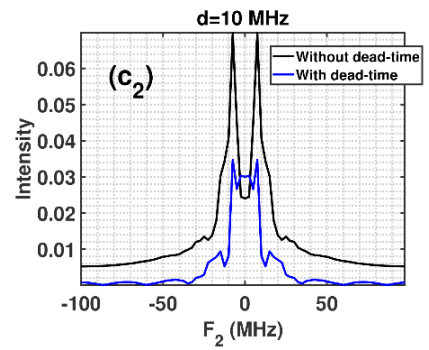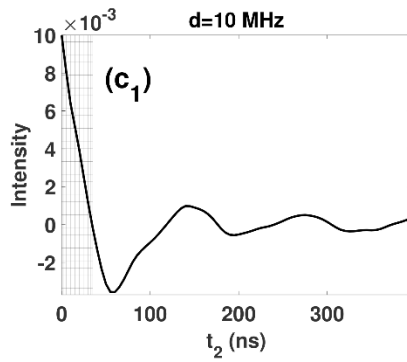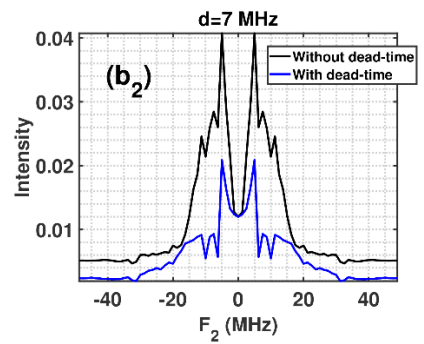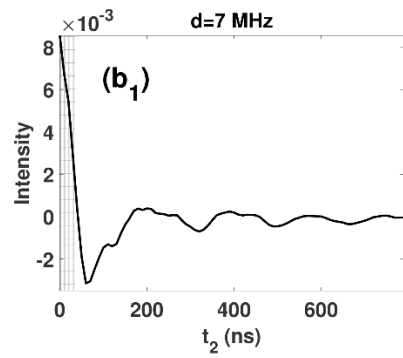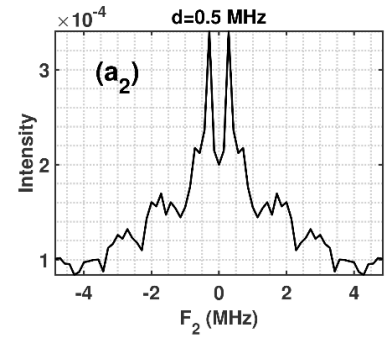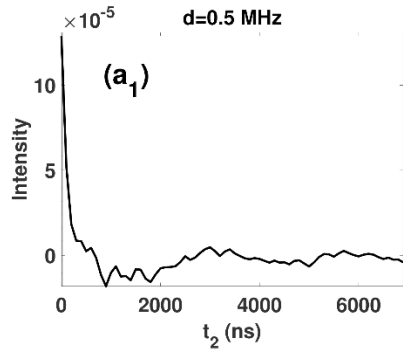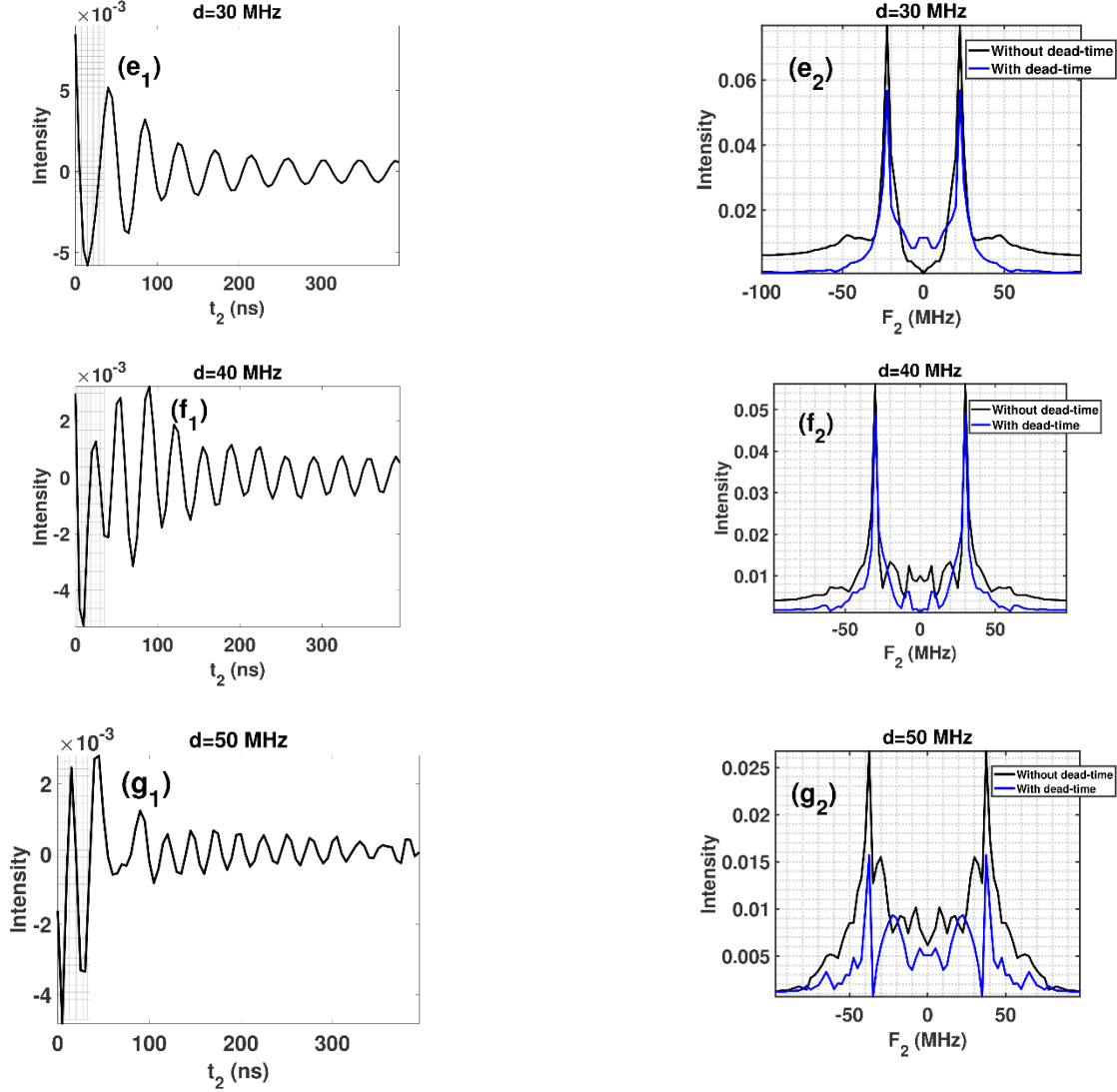
Figure 3.23 Dependence of the two-pulse DQ signal on the dipolar-coupling constant for a polycrystalline sample, averaged over twenty Monte-Carlo orientations of the nitroxide dipoles: left ($a_1, b_1, c_1, d_1, e_1, f_1, g_1$): time domain DQ signals for $t_2 = 2t_1$ and right ($a_2, b_2, c_2, d_2, e_2, f_2, g_2$): their Fourier transforms (Pake doublets) for three different values of the dipolar-coupling constant $d = 10, 20, 30$ MHz. In all simulations, the amplitude of the irradiation microwave pulse B_1 is $10G$ and the duration, t_p, for both pulses is 80 ns. All the other parameters used for the simulations are the same those listed in Table 3.1. The relaxation is not considered in these simulations. All Pake doublets appear at $\pm 3d/4$. The same dead time, t_d=35 ns, as that reported in (Borbat and Freed 2002), is used here. The time-domain signal in the initial 35 ns interval, shown as hatched is lost in the dead-time of the pulse. The corresponding Fourier transform with respect to both t_2 and $t_2 - t_d$ are plotted, shown in black and blue, respectively.
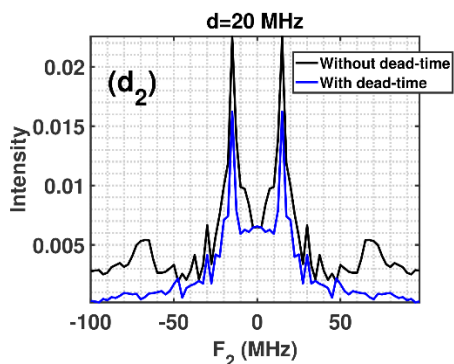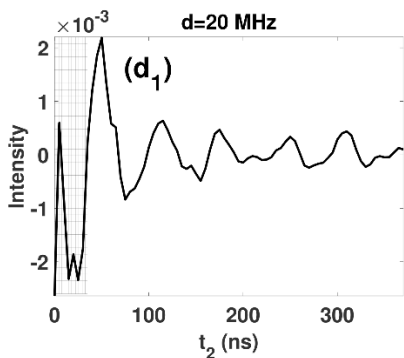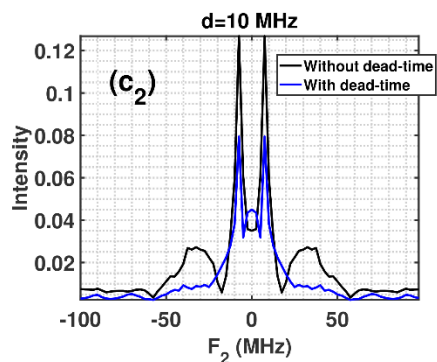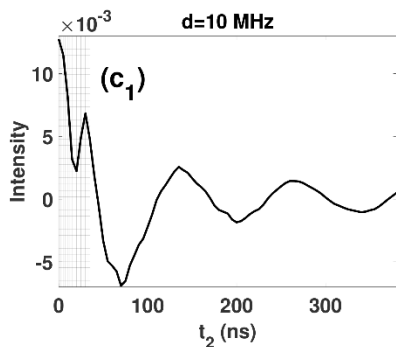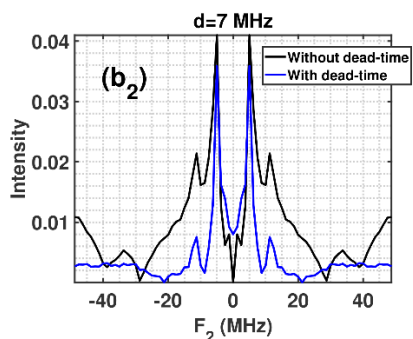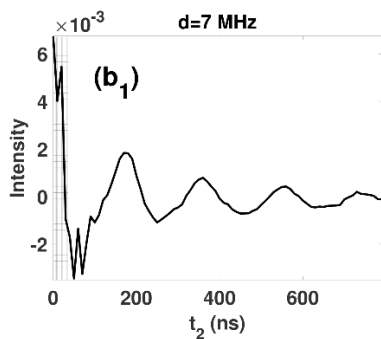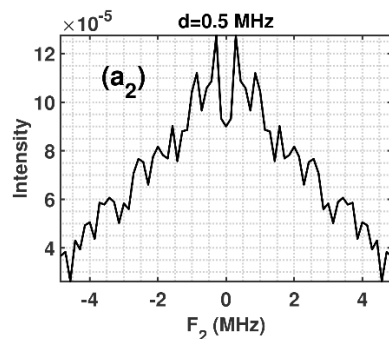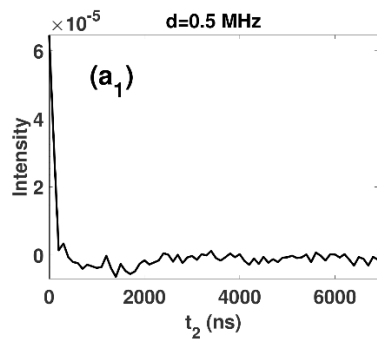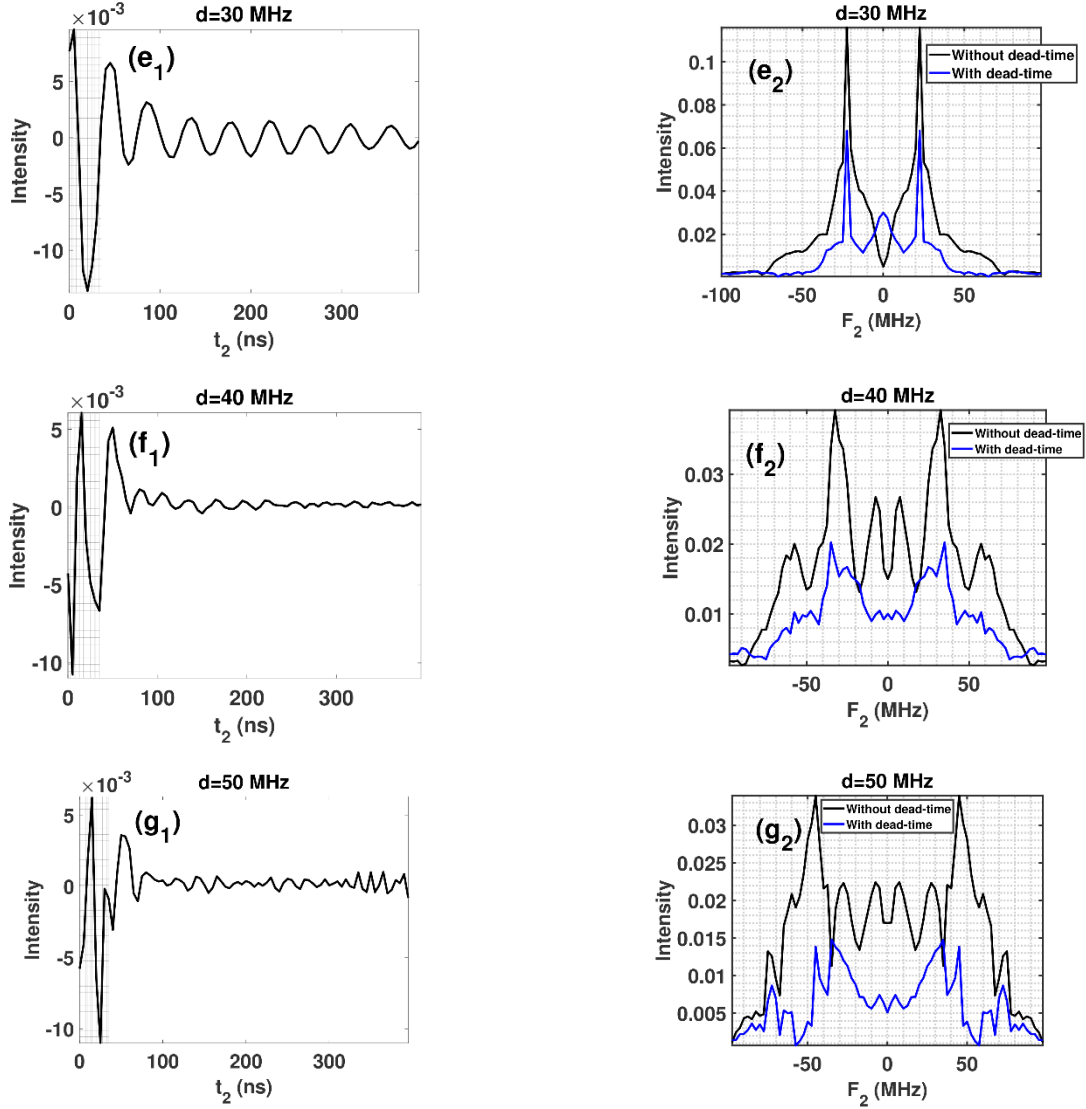
Figure 3.24. The same details as in the caption of Figure 3.23, except here $B_1 = 60G$ and $t_p = 65$ ns, corresponding to the maximum coherence efficiencies for both $T_{0\to2}$ and $T_{2\to-1}$ as discussed in Sec. 3.4.3.1 Coherence transfer efficiency.
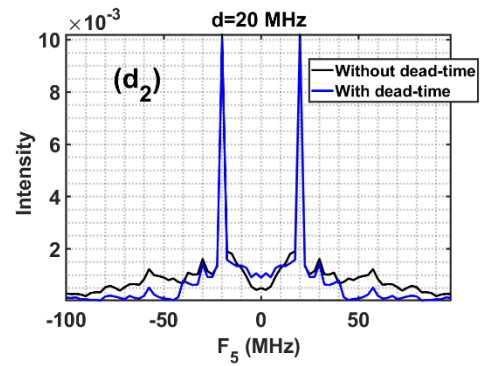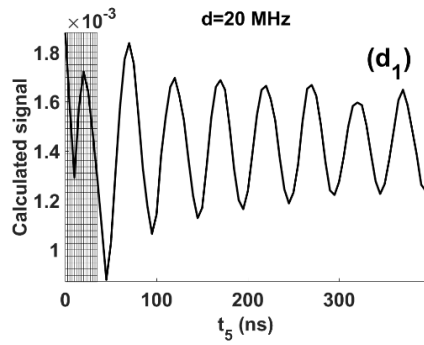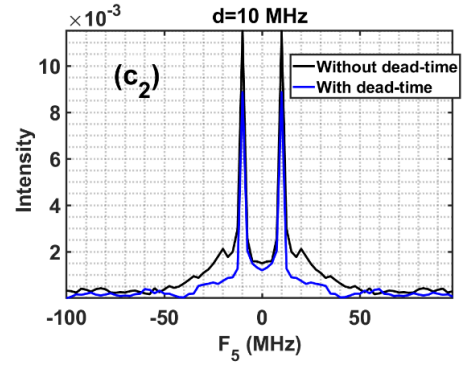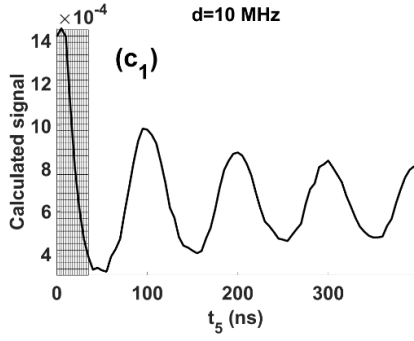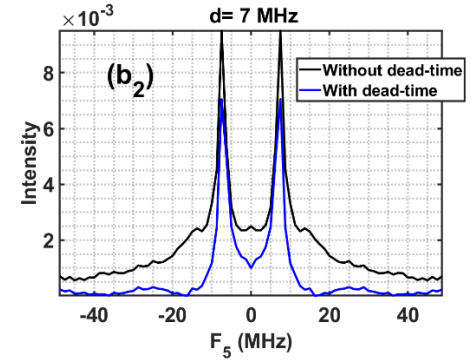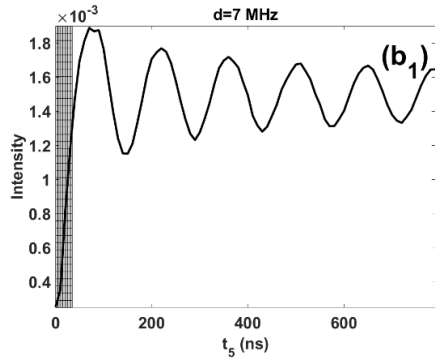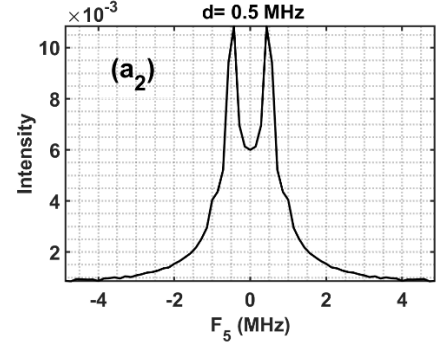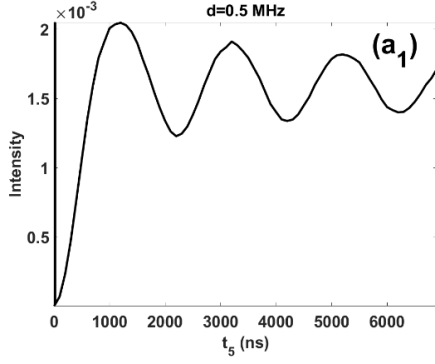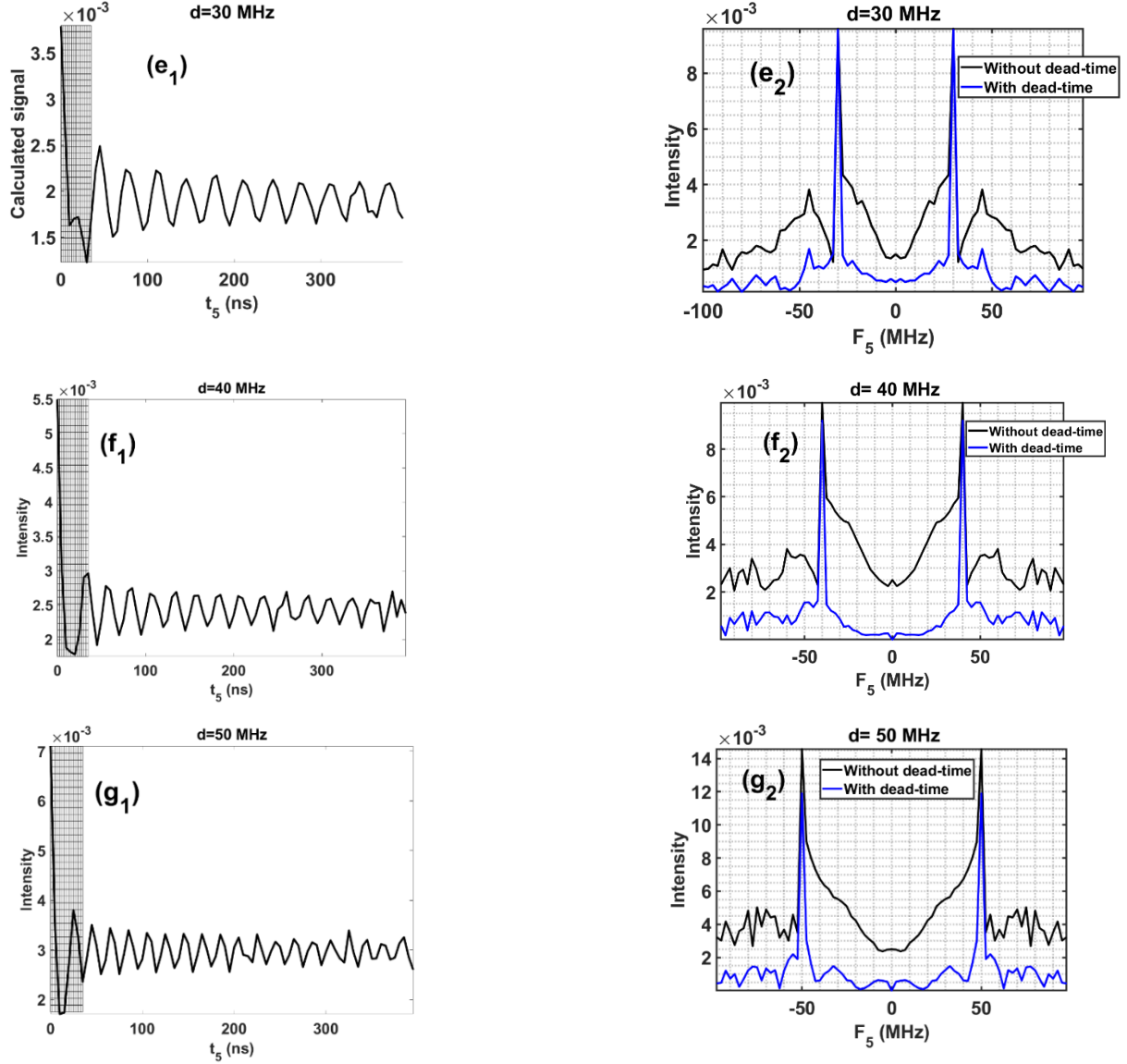
Figure 3.25. Dependence of the five-pulse DQM signal on dipolar coupling constant for a polycrystalline sample, averaged over twenty Monte-Carlo orientations of the nitroxide dipoles: left (a_1, b_1, c_1) time domain DQ signals for $t_5 = t_1$ and right (a_2, b_2, c_2) their Fourier transforms (Pake doublets) for three different values of the dipolar coupling constant $d = 10, 20. 30$ MHz. The amplitude of the irradiation microwave pulse $B_1 = 17.8G$ and the duration of the finite pulses $(t_p)_1 = (t_p)_3 = (t_p)_5 = 5ns$ ($\pi/2\ pulses$) and $(t_p)_2 = (t_p)_4 = 10ns$ ($\pi\ pulses$) ns are used for all simulations.. The relaxation is not considered in these simulations. The dead-time of $t_d = 35$ ns, as used experimentally in (Borbat and Freed 2002), at X-band is used. The initial 35 ns interval of the time domain signals, included in the dead-time of the pulse, is shown as hatched; it cannot be recorded in the experiment. The Fourier transform shown in blue is taken with respect to $t_1 - t_d$ whereas that in black is taken with respect to t_1. All Pake doublets appear at $\pm d$.

The top view plots of the two-dimensional Fourier transform of DQ signal for a coupled nitroxides biradical with the coupling constants: (a) $d = 20$ MHz and (b) $d = 30$ MHz, are shown in Fig. 3.26. The 2D Fourier transform is plotted as a function of the double quantum frequency, F_1 and F_{ESR}, the ESR frequency which are the Fourier variables corresponding to t_1 and t_2 in the DQ sequence, respectively. The corresponding 1D spectra, joined on the top and on the right-hand side of the contour plots, respectively, are obtained by integration along the ESR frequency and F_1 axes, and dividing by the number of data points to calculate averages. The joined figures on the right-hand side represent the absorption CW ESR spectra. The amplitude of the radiation microwave field $B_1 = 60G$ and the duration of the finite pulses $t_p = 65$ ns, corresponding to the maximum coherence efficiencies for both $T_{0\to2}$ and $T_{2\to-1}$ are used for all simulations. All other parameters used for the simulations are listed in Table *3.1*. Relaxation is not considered in these simulations.
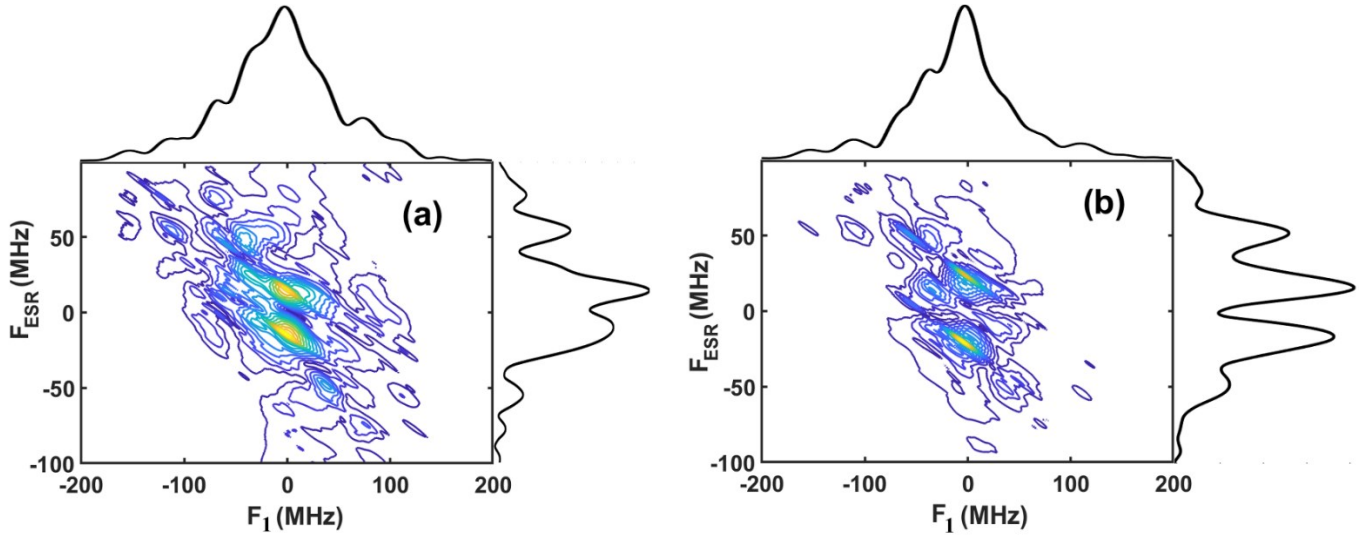
Figure 3.26 The two-dimensional top views of the Fourier transforms of the DQ signal as a function of the double quantum frequency, denoted as F_1, corresponding to the time t_1 in Figure 3.18(a), showing the pulse sequence, and the ESR frequency, F_{ESR}, corresponding to the time t_2 after the second pulse as shown in Figure 3.18 (a) for a coupled nitroxides biradical with the coupling constants: (a) $d = 20$ MHz and (b) $d = 30$ MHz. The corresponding 1D spectra, are joined on the top and on the right-hand sides of the top views, as obtained by the summation along the F_{ESR} and F_1 axes, respectively, and by dividing by the number of data points to calculate averages. The attached figures on the right-hand sides represent the absorption CW ESR spectra, wherein the static field is kept at the fixed value and the frequency is varied. The amplitude of the radiation microwave field $B_1 = 60G$ and the duration of the pulse $t_p = 65$ ns is used for both pulses, corresponding to the maximum coherence efficiencies for both $T_{0\to2}$ and $T_{2\to-1}$ are used for the simulations. All other parameters used for the simulations are the same as those listed in Table 3.1. The relaxation is not considered here.
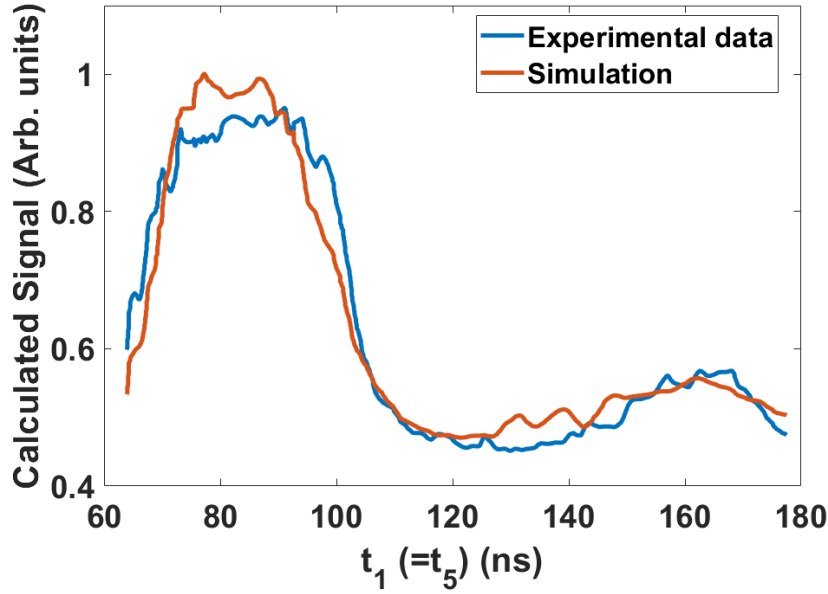
Figure 3.27 The simulation made using the numerical algorithm to fit the experimental five-pulse DQM signal of the nitroxide biradical (Saxena and Freed 1996). The experimental data shown is a profile of the three-dimensional experiment along the maximum slice at $t_5 = t_1$ reported in (Saxena and Freed 1996). The simulation parameters are: $B_1 = 17.8$ G, $d=12.3$ MHz, $T_2^S = 500ns$, $T_2^D = 300ns$. The duration of the pulses is: $(t_p)_1 = (t_p)_3 = (t_p)_5 = 5ns$ and $(t_p)_2 = (t_p)_4 = 10ns$. The other parameters are the same as those listed in Table 3.1.

Figure 3.27 shows the simulation of the five-pulse DQM signal of the nitroxide biradical to fit the experimental data obtained by (Saxena and Freed 1996). The simulations are carried out, using the same parameters as those listed in (Saxena and Freed 1996), employing the numerical algorithm as given in Sec. 3.1 Numerical procedure. The experimental data shown here is a profile of the maximum of the intensity that occurs for $t_5 = t_1$ of the intensity versus (t_5, t_1) data, reported in (Saxena and Freed 1996). The parameters used for the simulation are the same as that used in (Saxena and Freed 1996), which are specifically: $B_1 = 17.8$ G; $d=12.3$ MHz, $T_2^S = 500ns$, $T_2^D = 300ns$; $(t_p)_1 = (t_p)_3 = (t_p)_5 = 5ns$ and $(t_p)_2 = (t_p)_4 = 10ns$. The other parameters are the same as those listed in Table 3.1. The simulation shows a reasonably good agreement, within experimental errors, to the experiment (Saxena and Freed 1996).

3.4.5 Two-pulse DQ and five-pulse DQM at Ku-band

The two pulse DQ and five pulse DQM signals at Ku-band are plotted in Figure 3.28, along with their Fourier transforms. The same parameter as those used for the simulation of two-pulse DQ and five-pulse DQM signals in Figure 3.23 c_1 and Figure 3.25 c_1, respectively, are used for the simulation at Ku- band except that here $B_0 = 6200G$. The dead-time of 25~ns is used at Ku-band in accordance with the experiment (Borbat and Freed 2002). The initial 25 ns interval of the time domain signals covered by the dead time of the pulse, which cannot be

recorded in the experiment, is shown as hatched. The Fourier transforms shown in blue are taken with respect to the reduced times $t_2 - t_d$ and $t_5 - t_d$, where t_d is the dead time, whereas those in black are taken with respect to t_2 and t_5 for two-pulse DQ (Figure 3.28 a_2) and five-pulse DQM (Figure 3.28 b_2), respectively. The Pake doublets in two-pulse DQ and five-pulse DQM at Ku-band appear at $\pm 3d/4$ and $\pm d$, respectively, the same as that at X-band. It is noted that the intensities of the signals and their respective amplitudes of Fourier transforms are larger at Ku-band as compared to those at X-band.

The numerical simulation for the coherence transfer $T_{0\to 2}$ as function of θ, were also carried out at Ku-band (not included here) and there was found absence of orientational selectivity, i.e., the coherence transfer is not especially large for any range of θ values, unlike that at X-band (Figure 3.22).
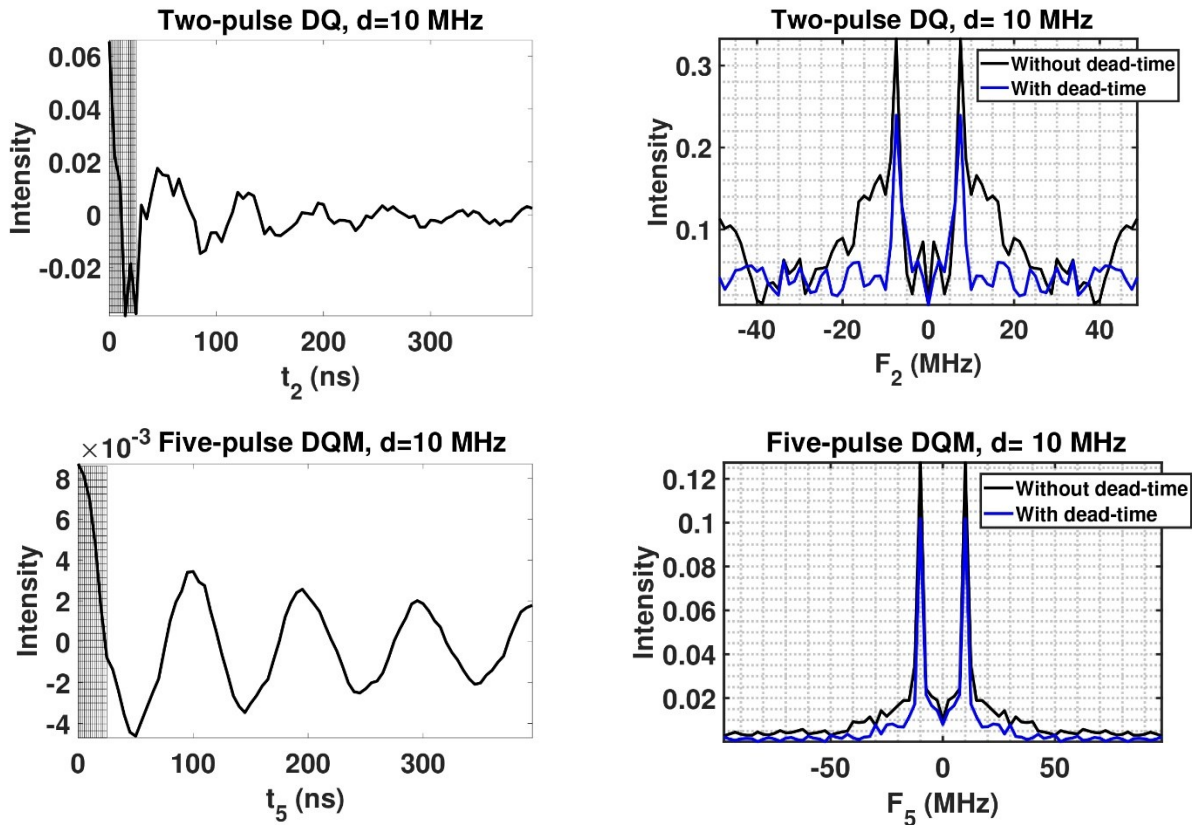
Figure 3.28 The two pulse DQ and five pulse DQM signals at Ku-band for a polycrystalline sample, averaged over twenty Monte-Carlo orientations of the nitroxide dipoles: left (a_1) time domain DQ signal for $t_2 = 2t_1$; (a_2) time domain DQM signal for $t_5 = t_1$ and right (a_2, b_2) their Fourier transforms (Pake doublets) for $d = 10$ MHz. For simulation of DQ signal, the amplitude of the irradiation microwave pulse was $B_1 = 60$G and the duration of the finite pulses t_p for both pulses was 65 ns, whereas for the simulation of five-pulse DQM signal $B_1 = 17.8$G and the duration of the finite pulses $(t_p)_1 = (t_p)_3 = (t_p)_5 = 5$ns ($\pi/2$ pulses) and $(t_p)_2 = (t_p)_4 = 10$ ns (π pulses) ns are used. All other parameters used for the simulations are the same as those listed in Table 3.1. The effect of relaxation is not considered in these simulations.
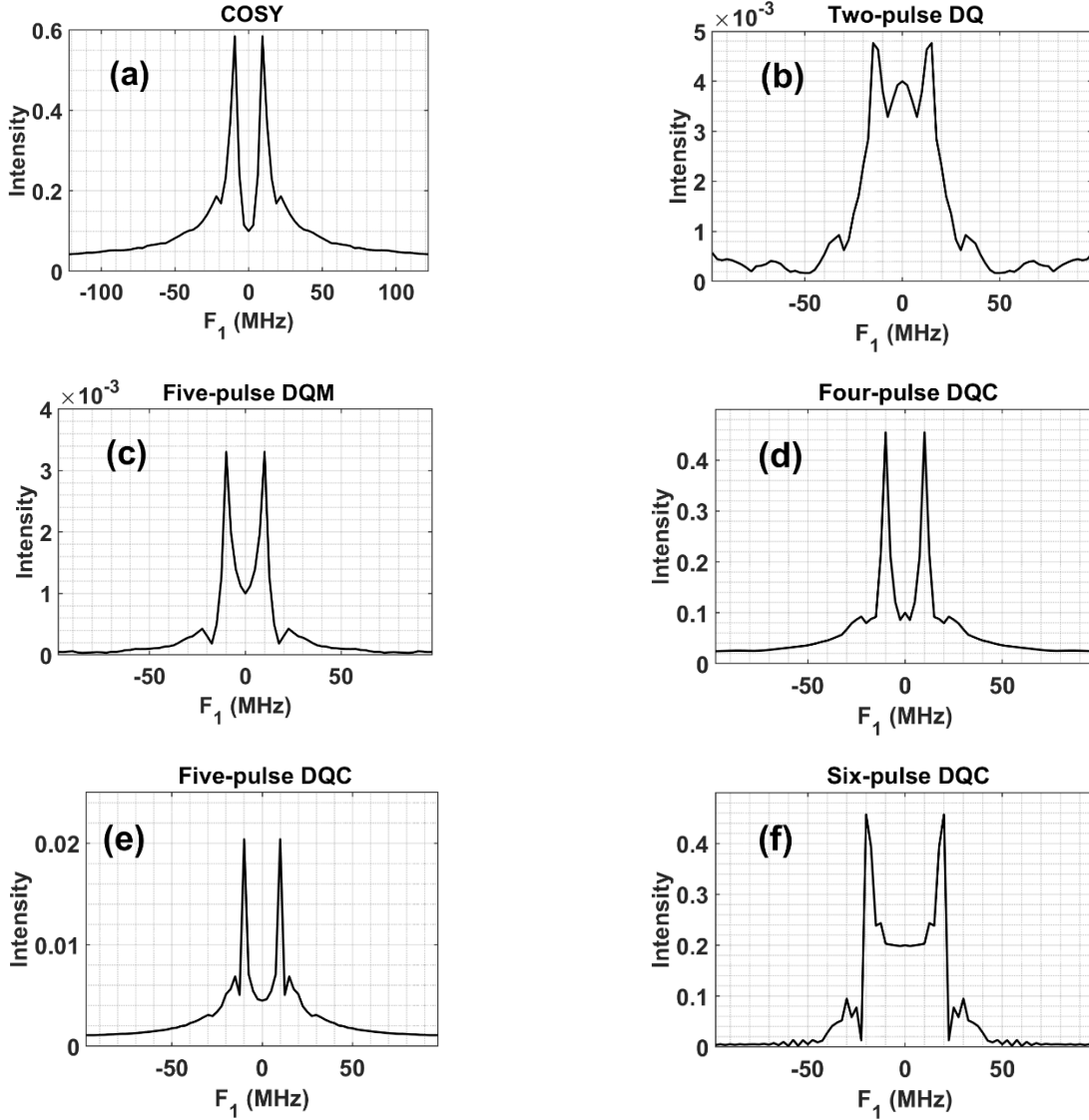
Figure 3.29 Comparison between the intensities of the Pake doublets at Ku-band obtained for (a) COSY; (b) two-pulse DQ; (c) five-pulse DQM; (d) four-pulse DQC; (e) five-pulse DQC and (f) six-pulse DQC at Ku-band. The Fourier transform of the various signals are taken with respect to $t_1 - t_d$ to consider the dead-time effect, except for five- and 6-pulse DQC sequences, where the dead-time effect is absent. The amplitude of the irradiation microwave field is $B_1 = 60.0\ G$ and the dipolar coupling constant $d = 10$ MHz are used in the simulations. All the other parameters used are the same as those listed in Table I. In order to make a valid comparison between the intensities, the relaxation effect is considered in all the simulations, using $T_2^S = 500\ ns$, $T_2^D = 300\ ns$ and $\beta = 0.8$.

3.5 Comparison of the various multi-pulse techniques used for distance measurements

A meaningful comparison of the various pulse sequences for distance measurements can be made by comparing their one-dimensional signals, calculated at the top of the echo after the second pulse, and their Fourier transforms, for a polycrystalline sample with Monte Carlo averaging, performed using the same parameters. Furthermore, the Fourier transforms here are taken with respect to $t_1 - t_d$, the time counted after the dead-time. The various pulse sequences considered here, are specifically, two-pulse DQ; five-pulse DQM, four-pulse DQC, five-pulse DQC, and six-pulse DQC. To make a realistic comparison of the various intensities, the relaxation effect must also be included, since different pulse sequences are affected by relaxation differently. In this context, it is noted that, although relaxation does not broaden the Fourier transforms of the five-pulse and six-pulse DQC signals (Sec. 3.3), their intensities are indeed reduced by relaxation. Figure 3.29 shows the Pake doublets for the various sequences at Ku-band It is seen that the Pake doublets occur at $\pm d$ for all sequences, except for the two-pulse DQ sequence, for which they occur at $\pm \frac{3d}{4}$. It is found that the six-pulse DQC sequence shows the cleanest Pake pattern, whereas the intensity of the Fourier transform of two-pulse COSY is the largest. The intensity of the Pake doublet for COSY is anywhere from one to three orders of magnitude larger than those for the other pulse sequences. Table 3.4 lists the intensities of the signals obtained with the various sequences for comparison. It is found that the intensity of the Pake doublet for the one-dimensional COSY signal at Ku-band is the largest, one-to-two orders of magnitude larger, than those obtained with the other multi-pulse sequences considered here. The COSY technique is also found to have the smallest side peaks as compared to the other pulse sequences, as seen from Figure 3.29 for Ku-band.

Pulse sequence	Position of Pake doublet	Intensity of the Fourier transform at Ku band	Broadened by Relaxation
Two-pulse COSY	$\pm d$	6×10^{-1}	Yes
Two-pulse DQ	$\pm 3d/4$	4.8×10^{-3}	Yes
Four-pulse DQC	$\pm d$	4.6	Yes
Five-pulse DQC	$\pm d$	2	No
Five-pulse DQM	$\pm d$	3.4×10^{-4}	Yes
Six-pulse DQC	$\pm d$	7.5	No

Table 3.4. Comparison of the intensities of the Pake doublets and the effect of relaxation on them for the various pulse sequences. The same parameters as those given in Table 3.1 are used in these simulations.

3.6 Conclusions

The salient features of this chapter are as follows

(i)   A complete algorithm for the numerical simulations for multi-pulse pulse sequences, as is given in this chapter.
(ii)   It is shown that the one-dimensional multi-pulse techniques can be used for distance measurements in biological systems using nitroxide biradicals.
(iii) It is demonstrated here that the Fourier transform of all the multi-pulse signals exhibit the Pake doublet at $\pm d$ except for two-pulse DQ where the Pake doublet occurs at $\pm \frac{3}{4} d$.
(iv)   It is shown here that a finite, rather than an infinite, pulse is needed, in conjunction with the dipolar interaction, to produce a non-zero coherence transfer in the transitions 0→2 and 2→-1 for both the two-pulse DQ and five-pulse DQM sequences.
(v)   The simulations show that the coherence transfer, $T_{0\rightarrow 2}$, as effected by a finite pulse in conjunction with the dipolar interaction, is found to increases as the amplitude of the irradiation field (B_1) decreases, being maximum for those coupled nitroxides, whose dipolar axes are oriented symmetrically within 10 degrees about the angle $\theta_0 \sim 54.74°$

(vi)   The amplitudes of the Pake doublets for the COSY signal are calculated here to be the most intense, one to two orders of magnitude larger, than those obtained with other multi-pulse sequences, namely, two-pulse DQ (Double Quantum), five-pulse DQM (Double Quantum Modulation), four-, five-, and six-pulse DQC (Double Quantum Coherence).

Chapter 4

4. Calculation of DEER spectrum and distance distribution, $P(r)$, by the use of doubly rotating frames

Double electron-electron resonance (DEER, also called PELDOR, Pulsed Electron Double Resonance) has been frequently exploited for distance measurements in biological systems using biradicals, consisting of pairs of paramagnetic nitroxide dipoles in interaction with each other, referred to as the "observer" and "pump" spins, characterized by different values of their g matrices in an ensemble of spins. This pulse EPR method normally involves the application of two or three "observer" pulses and one "pump" pulse, referred to as three- or four-pulse sequences, respectively. The observer and pump pulses act on spins, which resonate at slightly different magnetic fields. The advantage of four-pulse DEER over three-pulse DEER is that in the former, the pulses do not need to overlap or even come close to each other, thereby avoiding significant, dead-time effects. Also, the four-pulse DEER sequence permits using larger B_1's than those, which are feasible in three-pulse DEER sequence (Pannier *et. al.* 2011, Borbat and Freed 2007). This four-pulse sequence is rather simple in its technical implementation, thereby allowing commercial production.

Currently, the DEER signal is calculated by considering the spin Hamiltonian in a special coordinate system known as two-frequency rotating frame (TFRF), described by (Maryasov and Tsvetkov 2000), in which the observer and pump spins rotate with the frequencies ω_{obs} and ω_{pump}, respectively, around the external magnetic field (the laboratory z axis). The Zeeman interactions for the two-spin system in the frequency unit can written in this frame as $C_{1_{TFRF}} = C_{1_{lab}} - \omega_{obs}$ and $C_{2_{TFRF}} = C_{2_{lab}} - \omega_{pump}$, where $C_{k_{TFRF}}$ and $C_{k_{lab}}$; $k = 1,2$ are the Zeeman interactions in frequency unit in the TFRF and lab frames, respectively, which are not identically zero. The details of this technique, applied to analytical calculations of three-pulse DEER signal can be found in (Maryasov and Tsvetkov 2000). Recently, specialized comprehensive computer packages have been developed, using the same rotating frames as TFRF (Maryasov and Tsvetkov 2000), to calculate DEER signals, see, e.g., SPINACH (Hogben et. al 2011) and EasySpin (Stoll and Schweiger 2006) , which are rather complex, prohibiting understanding of the various steps of calculation, whose algorithm cannot be easily carried out on a common laptop within a reasonably short time using Matlab or Fortran.

The procedure to calculate DEER signal, proposed in this thesis, offers an advantage in that its algorithm can be easily carried out on a common laptop within a reasonably short time using Matlab or Fortran, thereby one can investigate various aspects of signals obtained by the DEER technique. To this end, DEER signal is calculated rigorously by exploiting the algorithm developed in Sec. 2, using doubly rotating frames (hereafter referred to as DRF), wherein one uses two rotating frames, which address the observer and pump spins, so that the respective Zeeman interactions are rendered identically zero, unlike those used in (Maryasov and Tsvetkov 2000). The DRF technique is applied to calculate the three- and four-pulse DEER signals of (i) two nitroxide dipoles of a biradical on a sample of bis-nitroxide nanowire, P1, in deuterated ortho-terphenyl solvent with 5% BnPy (d14-oTP/BnPy), characterized by the fully asymmetric g and hyperfine matrices, and the angular geometry of the biradical and (ii) two coupled Gd^{3+} ions with significant zero-field splitting. The DRF technique is then used to estimate the probabilities of the distance distribution, $P(r)$, between the two spins in the various biradicals separated by the distances, r. This is accomplished by using Tikhonov regularization, as implemented in the software *DeerAnalysis* (Jeschke *et al.* (2006))*,* using the kernel signals calculated using the DRF

technique for different r values. This procedure is successfully illustrated by applying it to the reported experimental DEER data

4.1 Three-pulse and four-pulse nitroxide biradical DEER signals using DRF technique

The configuration of two coupled nitroxides in a biradical is shown in Figure 3.1. The Liouville-von Neumann equation as given in Sec. 2 is used to describe the time evolution of the density matrix during the application of a pulse and during the free evolution. Specifically, the density matrix at time $t + t_0$, undergoing the free evolution after the application of a pulse at time t_0, is given by

$$\rho(t_0 + t) = e^{-iH_0 t} \rho(t_0) e^{iH_0 t} , \tag{4.1}$$

where H_0 is the static spin Hamiltonian of the coupled nitroxide system given in (3.1) and $\rho(t_0)$ is the density matrix just after the application of a pulse.

4.1.1 Calculation of the effect of observer and pump pulses using doubly rotating frames.

In the present calculation of DEER signal, there are used two rotating frames, one for all times, except for the duration of the pump pulse, for both the observer and pump spins and the other only during the application of the pump pulse for both the observer and pump spins. The latter is accomplished by changing the value of the external magnetic field during the action of the pump pulse by an amount equivalent to the difference in the frequency of the pump pulse from that of the observer pulse. Specifically, a difference of $70 \, MHz$, in a typical experiment (Georgieva et.al. 2012), is equivalent to a difference in the intensity of the external field by $70(MHz)/2.8(MHz/G) = 25.0$ G.

For a powder calculation, one uses a (θ, ϕ) grid over the unit sphere as described in Sec. 3, keeping the rotating frame fixed for the observer spins for *all* calculations, except for those during the application of the pump pulse, to be those chosen for a fixed orientation, say for $\theta = \phi = 0°$, for which the Euler angles $(\alpha_1 = 0°, \beta_1, \gamma_1)$ are appropriately chosen so that the resonant field for this spin is B_0, the applied external field. This means that the coefficient C_1 of the S_{z_1} term for the observer spin in the static spin Hamiltonian, Eq. (3.2), is rendered zero in its rotating frame, by subtracting the Zeeman energy, represented by the coefficient of the S_{z_1} term, by C_1. As for the other spins in the various biradicals with the various orientations (θ, ϕ) of their dipolar axes with respect to the external magnetic field over the unit sphere, their coefficients of the S_{z_2} terms in the static spin Hamiltonian, (3.2) are changed to $C_2 - C_1$ so that these spins, are in the rotating frame of the observer spin at $\theta = \phi = 0$, as chosen above. For calculations during the application of the pump pulse, one keeps the same values of the coefficients C_{1P} $(= C_{1P_0}$, i.e., for $\theta = \phi = 0)$ for all (θ, ϕ) values , as those calculated for $\theta = \phi = 0$ for the external magnetic field $B_0 + \Delta B$, where ΔB considers appropriately the equivalent shift in the external magnetic field from the observer to the pump frequency, as described above. As for the second nitroxide of the biradical, the coefficient of the S_{z_2} term, C_{2P} , as calculated for the external magnetic field $B_0 + \Delta B$, is changed for the various (θ, ϕ) values over the unit sphere, from C_{2P}

to $C_{2P} - C_{2P} = 0$, so that it is in its rotating frame, changing $C_{1P}(= C_{1P_0})$ to $C_{1P} - C_{2P}(= C_{1P_0} - C_{2P})$, so that the observer spin is also in the rotating frame of the second spin. For each (θ, ϕ) orientation, the Zeeman energy is now shifted, as represented by the C_{2P} value, so that the Zeeman coefficients of the S_{z_1} and S_{z_2} terms in Eq. (3.2) are now $C_{1P_0} - C_{2P}$ and $C_{2P} - C_{2P} = 0$, to be in the rotating frame of the second spin for both the observer and pump spins, for the various (θ, ϕ) values over the unit sphere

During the application of a pulse, the spin relaxation is here neglected as it has negligible effect, since the durations of the pulses are much smaller than the relaxation time. In that case, the evolution of the density matrix is described in Hilbert space, as follows:

$$\frac{d}{dt}\rho(t) = -i[(H_0 + H_p), \rho(t)] \tag{4.2}$$

where H_p; with $p = obs, pump$ are the observer and pulse Hamiltonians for the observer and pump pulses, respectively. They are expressed as:

$$H_{obs} = \frac{\omega_{1obs}}{2}\left(e^{-i\phi}S_{1+} + e^{i\phi}S_{1-}\right), \tag{4.3}$$

$$H_{pump} = \frac{\omega_{1pump}}{2}\left(e^{-i\phi}S_{2+} + e^{i\phi}S_{2-}\right) \tag{4.4}$$

where $B_{1p}(= \omega_{1p}/\gamma_e)$; with $p = obs, pump$ are the amplitudes of the observer and pump pulses, respectively; ϕ is the phase of the pulse and $S_{k\pm}$; $k = 1,2$ are the raising/lowering operators of the total electronic spin of the coupled nitroxide system in the 36×36 direct product Hilbert space. The solution of Eq. (4.2) after the application of a pulse with duration t_p is

$$\rho(t_0 + t_p) = e^{-i(H_0 + H_p)t_p}\rho(t_0)\, e^{i(H_0 + H_p)t_p}, \tag{4.5}$$

where H_p is defined by Eqs. for the observer and pump pulses, respectively.

The complex DEER signal, as calculated for the orientation, (θ, ϕ), of the static magnetic field relative to the dipolar axis that connects the magnetic dipoles of the two nitroxides, for the orientations of the two nitroxide radicals with respect to the respective molecular frames, characterized by six Euler angles, $\{\alpha_1, \beta_1, \gamma_1, \alpha_2, \beta_2, \gamma_2\}$, as shown in Fig. 1, is then,

$$S^{(DEER)}(t, \theta, \phi, \beta_1, \gamma_1, \alpha_2, \beta_2, \gamma_2) = Tr(S_{1+}\rho_f(t)), \tag{4.6}$$

It is noted that, only five of the six Euler angles are independent; one is arbitrary, which can be chosen to be $\alpha_1 = 0$. This is achieved by choosing the x axis to be along the line of nodes, N_1, of the first nitroxide (Fig. 1). Thus, in Eq. (4.6) the signal is shown to be a function of five independent Euler angles $(\beta_1, \gamma_1, \alpha_2, \beta_2, \gamma_2)$.

(a) Three-pulse DEER signal. For the calculation of three-pulse DEER signal, the final density matrix $\rho_f(t)$, where t is the time between the first observer pulse and pump pulse, as shown in Figure 4.1, is carried out by the following steps.
(i)　　Transform the initial density matrix by the first $\pi/2$ observer pulse using Eq. (4.5);

(ii)   Calculate the density matrix after free evolution of the density matrix obtained in step (i) over the duration t between the first observer pulse and the pump pulses using Eq. (4.1);

(iii)   Transform the density matrix obtained in step (ii) by the pump pulse, using Eq. (4.5);

(iv)   Calculate the density matrix after free evolution of the density matrix obtained in step (iii) over the duration $\tau - t$ between the pump pulse and second observer pulse using Eq. (4.1);

(v)   Transform the density matrix obtained in step (iv) by the π observer pulse using Eq. (4.5);

(vi)   The final density matrix $\rho_f(t)$ is obtained after free evolution of the density matrix obtained in step (v) over the time τ.

(b) Four-pulse DEER signal. The four-pulse DEER sequence is an improvement over the three-pulse DEER sequence. Here both the times τ_1 and τ_2, where τ_1 is the time between the first observer π-pulse and the top of the inverted echo formed by the first observer $\pi/2$ and π pulses, and τ_2 is the time between the top of this echo and the second observer π pulse, are kept fixed, as seen from Figure 4.1(b). Since the echo forms after a constant time from the last pulse, relaxation does not cause broadening of the Fourier transform of the signal.

For the four-pulse DEER, signal, the final density matrix $\rho_f(t)$, where t is the time between the inverted echo and the pump pulse, as shown in Figure 4.1(b), is obtained by following the same steps as those described above for the three-pulse sequence, along with extra steps which address the additional second observer pi pulse, considering the effect of successive applications of the observer and pump pulses to the initial density matrix, using Eq. (4.5), followed by the free evolutions over the various times, i.e., τ_1, t and τ_2, as shown in Figure 4.1 (b), using Eq. (4.1).

(c) Calculation of polycrystalline signal for biradicals containing coupled nitroxides using doubly rotating frames. A uniform distribution of the various dipolar axes, with the Euler angles of the magnetic axes of the various nitroxides distributed evenly in all orientations, is assumed in the present calculations. One considers, in the DEER experiment, those nitroxide spins of the biradicals which resonate at the applied magnetic field, B$_0$, referred to as the observer spins, with the other nitroxide spin of the biradical being at the fixed distance, r, from the first spin, having the same Euler angles $(\alpha_2, \beta_2, \gamma_2)$ for all the latter spins.

The EPR signal for a polycrystalline sample is, finally, calculated by integrating Eq. (4.6) over (θ, ϕ) over the unit sphere. The numerical calculations of the DEER signals in the present work were performed over the quadrant: $\theta = [0, \pi/2]$ and $\phi = [0, \pi]$, since the values over the three are the same as that for this quadrant following (Misra *et. al.* 2009). Finally, the signal over the entire unit sphere turns out to be as follows

$$S^{(DEER)}(t,\lambda_1,\lambda_2) = 4 \int_0^{\pi} d\phi \int_0^{\pi/2} S^{(DEER)}(t,\eta,\lambda_1,\lambda_2)\, d(cos\,\theta) \qquad (4.7)$$
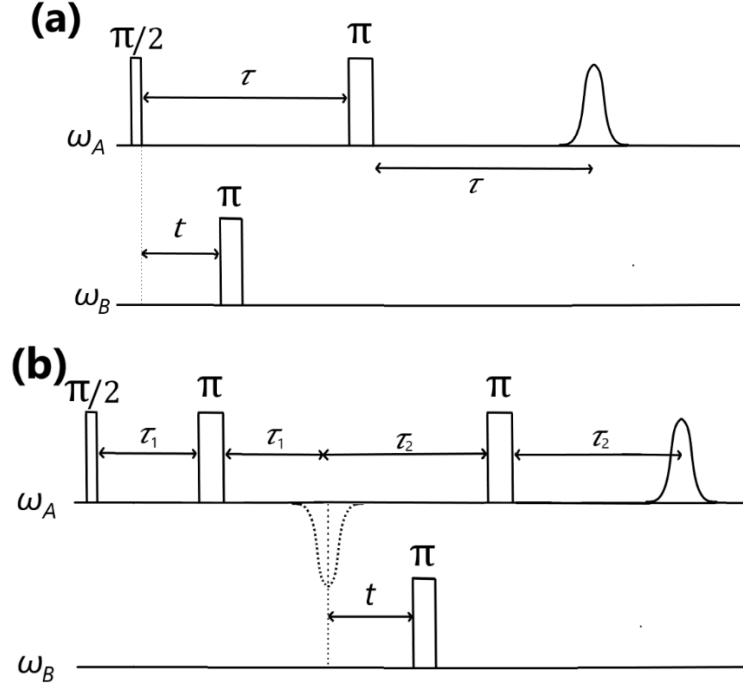
Figure 4.1 The pulse schemes for (a) three-pulse and (b) four-pulse DEER sequences. Here ω_A and ω_B are the observer and pump frequencies, respectively. The pulses at frequency ω_A induce echo signals. The time τ in (a) and the times τ_1, τ_2 (independent of each other) in (b), are kept fixed, whereas the time interval t in (a), and after the time interval t after the first inverted echo in (b) at which the pump pulse is applied, is stepped from 0 to τ and from 0 to τ_2 for three- and four-pulse DEER sequences, respectively.

In Eq. (4.7) the set of Euler angles, $(\alpha_1 = 0, \beta_1, \gamma_1); (\alpha_2, \beta_2, \gamma_2)$, and the orientation of the external magnetic field with respect to the dipolar axis (θ, ϕ) are denoted, respectively, as $\lambda_j; (j = 1,2)$ and η. In the present work, the distance between the two nitroxide fragments is considered to be fixed and the orientations of the Euler angles $(\beta_1, \gamma_1, \alpha_2, \beta_2, \gamma_2)$ for the polycrystalline sample are chosen to be completely random.

      (d) Calculation of Pake doublets. In order to calculate the Pake doublets, one needs to take the average over the Euler angles λ_1, λ_2, which represent the orientations of the dipoles of the two nitroxides. This is an enormous task as there are infinite many such possibilities. However, one can, instead, use Monte-Carlo averaging, wherein one varies λ_1, λ_2 randomly as follows:

$$S_{avg}^{(DEER)}(t) = \sum_{\text{random } (\lambda_1, \lambda_2)} S^{(DEER)}(t, \lambda_1, \lambda_2) \tag{4.8}$$

Twenty such averaging were found to be sufficient here, because another set of twenty-five Monte-Carlo averaging gave almost identical results. The parameters used in the simulations are listed in Table 4.1.

Parameters	Values for 3-pulse DEER	Values for 4-pulse DEER
Static magnetic field (B_0)	$3,323 G$	$6,180 G$
Microwave frequency ω_A	$9.34\ GHz$	$17.3 GHz$
Difference between the observer and pump frequencies $\lvert \omega_A - \omega_B \rvert$	$70\ MHz$	
Exchange constant (J)	$0\ MHz$	
g-matrix $\tilde{g} = \left(g_{xx}, g_{yy}, g_{zz} \right)$	$(2.0086, 2.0066, 2.0032)$	
Hyperfine matrix $\tilde{A} = \left(A_{xx}, A_{yy}, A_{zz} \right)$	$(6.0\ G, 6.0\ G, 35.0\ G)$	

Table 4.1 The values of the parameters used in the simulations of the DEER signals of the coupled nitroxide biradical.

4.1.2 Illustrative examples

The calculation of DEER signal by the DRF technique is illustrated here for three- and four-pulse DEER. In the former, the range of the dipolar coupling constants which can be measured in a typical three-pulse DEER experiment for $B_1 = 2 - 4\ G$ (Borbat and Freed 2002) is investigated as no reliable experimental data are available, whereas the latter is applied to analyze the four-pulse DEER experimental data reported by Georgieva *et al*. 2012.

4.1.2.1 Calculation of three-pulse DEER signal for coupled electrons in a biradical: limits of dipolar interaction that can be measured for a given B₁

There is no reliable experimental data available, giving the details of the specific relevant parameters used, to which the DRF technique can be applied. As a consequence, the illustrative examples to which the DRF technique is applied here, are carried out to find the limits of the dipolar interactions that can be measured with the commonly used amplitudes of the irradiation field $B_1 = 2.0, 3.0, 4.0\ G$ (Borbat and Freed 2002) by three-pulse DEER for a coupled nitroxide system. This goal is accomplished by finding the limits for which the predominant peaks in the Fourier transforms of the signals are $\pm d$. The simulations are carried out following the procedure outlined in Sec 4.1.1 Calculation of the effect of observer and pump pulses using doubly rotating frames. for a number of dipolar coupling constant, d, values assuming the same amplitudes of the

irradiation microwave fields for the observer and pump pulses, i.e., $B_{1obs} = B_{1pump} = B_1$. The resulting signals and their Fourier transforms are shown in Figure 4.2-Figure 4.4 for $B_1 = 2.0, 3.0, 4.0\ G$, for the ratios of $r = \frac{d(MHz)}{B_1(G)} = 0.5, 1.0, 2.0, 4.0\ MHz/G$. The Fourier transforms are taken with respect to the reduced time $t - t_d$, where t_d is the dead-time after the observer π pulse, assumed to be 35 ns (Borbat and Freed 2002), during which the signal cannot be recorded. It is found by taking the Fourier transforms with respect to t that the Pake doublets still occur at the same frequencies, albeit with somewhat increased amplitudes. The positions of the main peaks, along with all the significant side peaks, with their relative magnitudes, for the various B_1 and r values are listed in Table 4.2. The features of the various simulations are as follows.

	$B_1 = 2.0\ G$	$B_1 = 3.0$	$B_1 = 4.0$
$r = 0.5\ MHZ/G$	Main peaks: $\pm d$ Side peaks: $\pm 2d$ (15%)	Main peaks: $\pm d$ Side peaks: $\pm 2d$ (25%)	Main peaks: $\pm d$ Side peaks: $\pm 2d$ (40%)
$r = 1.0\ MHZ/G$	Main peaks: $\pm d$ Side peaks: $\pm 2d$ (15%)	Main peaks: $\pm d$	Main peaks $\pm d$ Side peaks: $\pm 2d$ (30%)
$r = 2.0\ MHZ/G$	Main peaks: $\pm d/2$ Side peaks: $\pm d$ (45%), $\pm 2d$(25%)	Main peaks: $\pm d/2$ Side peaks: $\pm d$ (80%)	Main peaks: $\pm d$
$r = 4.0\ MHZ/G$	Main peaks: $\pm d/2$ Side peaks: $\pm d$ (20%)	Main peaks: $\pm d/2$ Side peaks: $\pm 2d/$ 3 (85%), $\pm d$ (70%), $\pm 4d/$ 3 (40%)	Main peaks: $\pm d/2$ Side peaks: $\pm d$(25%), $\pm 3d/$ 2(20%), $\pm 2d$ (15%)

Table 4.2 List of the side peaks present along with the main peaks in the Fourier transform of the three-pulse DEER signal for chosen values of dipolar coupling constant $d(MHz)$ and $r = d(MHz)/B_1(G)$. The side peaks are listed in a descending order when there is more than one significant side peak. The relative intensity of each side peak with respect to the corresponding main peak is indicated by the percentage in the bracket.

$B_1 = 2.0G$. For $d = 1.0, 2.0\ MHz$ (Figure 4.2 (a_2, b_2)), the main peaks in the Fourier transform of the DEER signal occur at $\pm d$, with smaller side peaks at $\pm 2d$ (~15%). For $d = 4.0$ and 8.0 MHz, (Figure 4.2 (c_2, d_2)), the main peaks now occur at $\pm d/2$, with the side peaks at $\pm d$ (~45% for 4.0 MHz and ~20% for 8 MHz). Only for $d = 4.0\ MHz$, there occur second largest side peaks at $\pm 2d$ (~25% of the main peak).

$B_1 = 3.0G$. For $d = 1.5, 3.0\ MHz$, the main peaks occur at $\pm d$. Side peaks at $\pm 2d$ (~25%) are seen only for $d = 1.5\ MHz$ (Figure 4.3 a_2). For $d = 6.0, 12.0\ MHz$ the predominant peaks occur at $\pm d/2$, with side peaks at $\pm d$ (~80%, ~70%, respectively) . For $d = 12.0$ MHz (Figure 4.3 (d_2)), two other side peaks occur at $\pm 2d/3$ (~85%) , $\pm 4d/3$ (~40%).

$\boldsymbol{B_1 = 4.0 G}$. For $d = 2.0, 4.0, 8.0\ MHz$, the predominant peaks occur at $\pm d$, with the side peaks occurring at $\pm 2d$, $\sim 40\%$, $\sim 30\%$, for $d = 2.0, 4.0\ MHz$, respectively; there being no side peaks for $d = 8.0\ MHz$. For $d = 16.0\ MHz$, the $\pm d/2$ peaks become predominant with the side peaks at $\pm d\ (\sim 25\%), \pm 3d/2(\sim 20\%), \pm 2d(\sim 15\%)$.
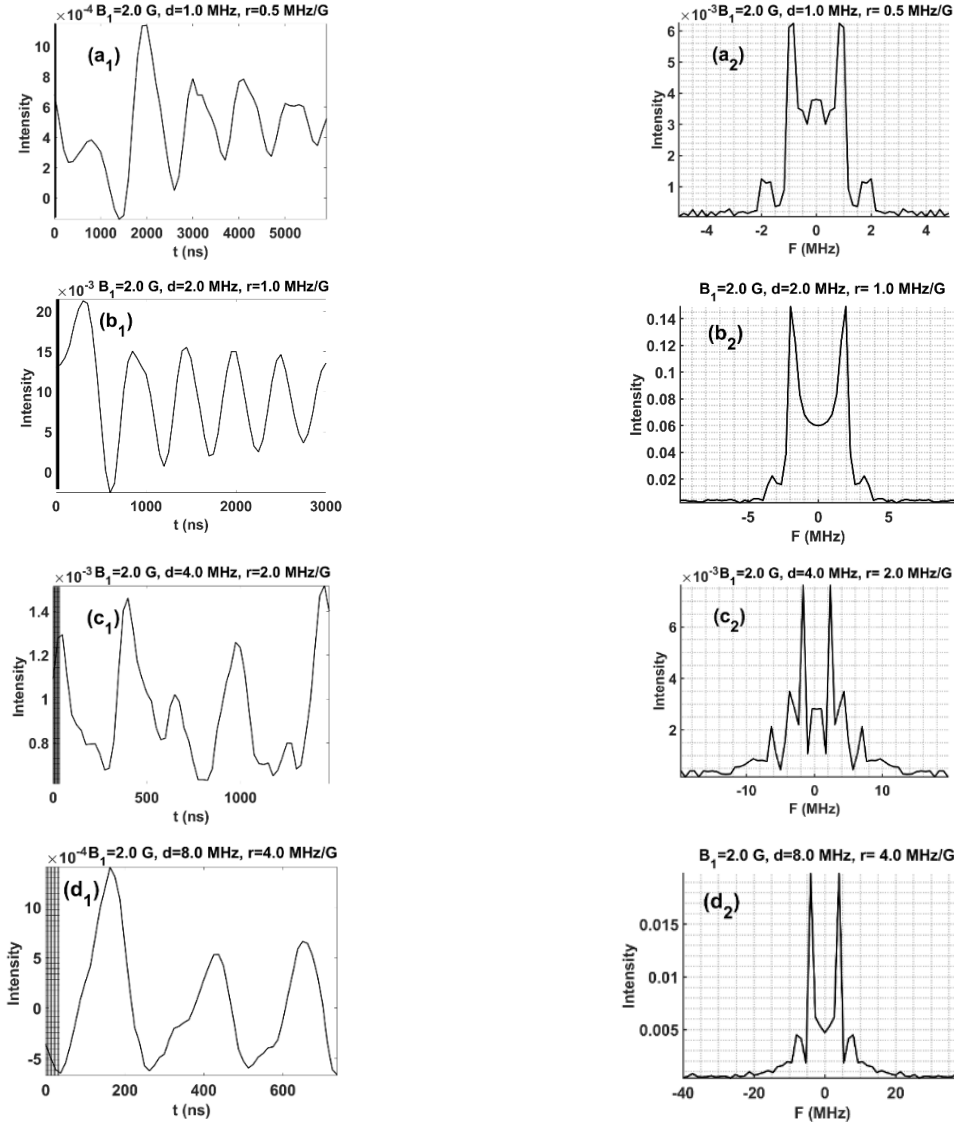
Figure 4.2   Dependence of three-pulse DEER signal on the dipolar coupling constant, d, for a fixed value of the amplitude of the irradiation microwave field, assumed to be the same for the observer and pump pulses $(B_{1obs} = B_{1pump} = 2.0\ G)$ for a polycrystalline sample. The time domain signals (a_1, b_1, c_1, d_1) and their Fourier transforms (a_2, b_2, c_2, d_2) are shown for the ratios $r(= \frac{d(MHz)}{B_1(G)}) = 0.5, 1.0, 2.0, 4.0\ MHz/G$. The time-domain signal in the initial $t_d = 35$ ns interval, shown as the hatched area on the left, is lost in the dead-time of the pulse. The Fourier transforms are taken with respect to the reduced time $t - t_d$.
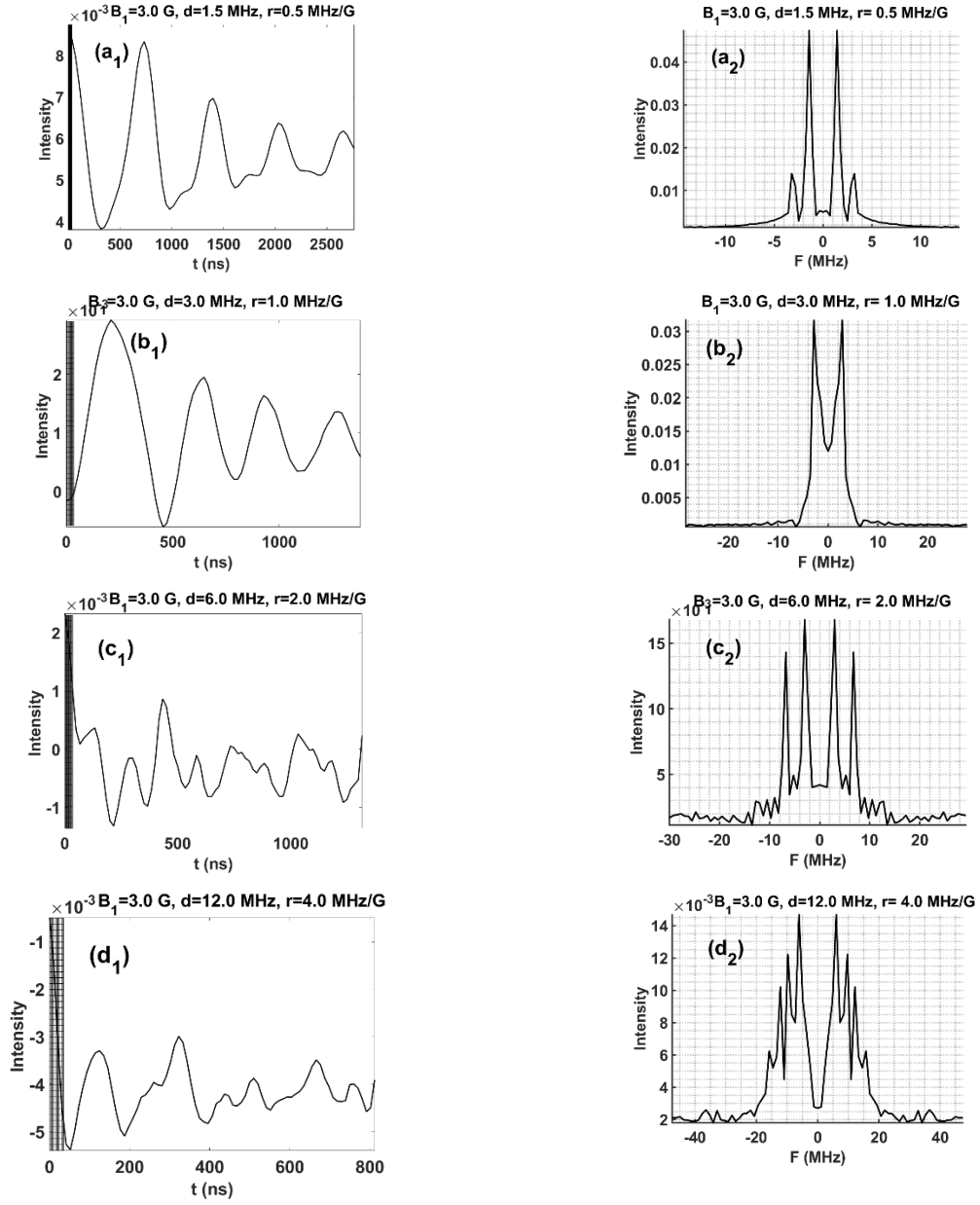
Figure 4.3   The same details as in the caption of Figure 4.2, except here $B_{1obs} = B_{1pump} = 3.0\ G$.
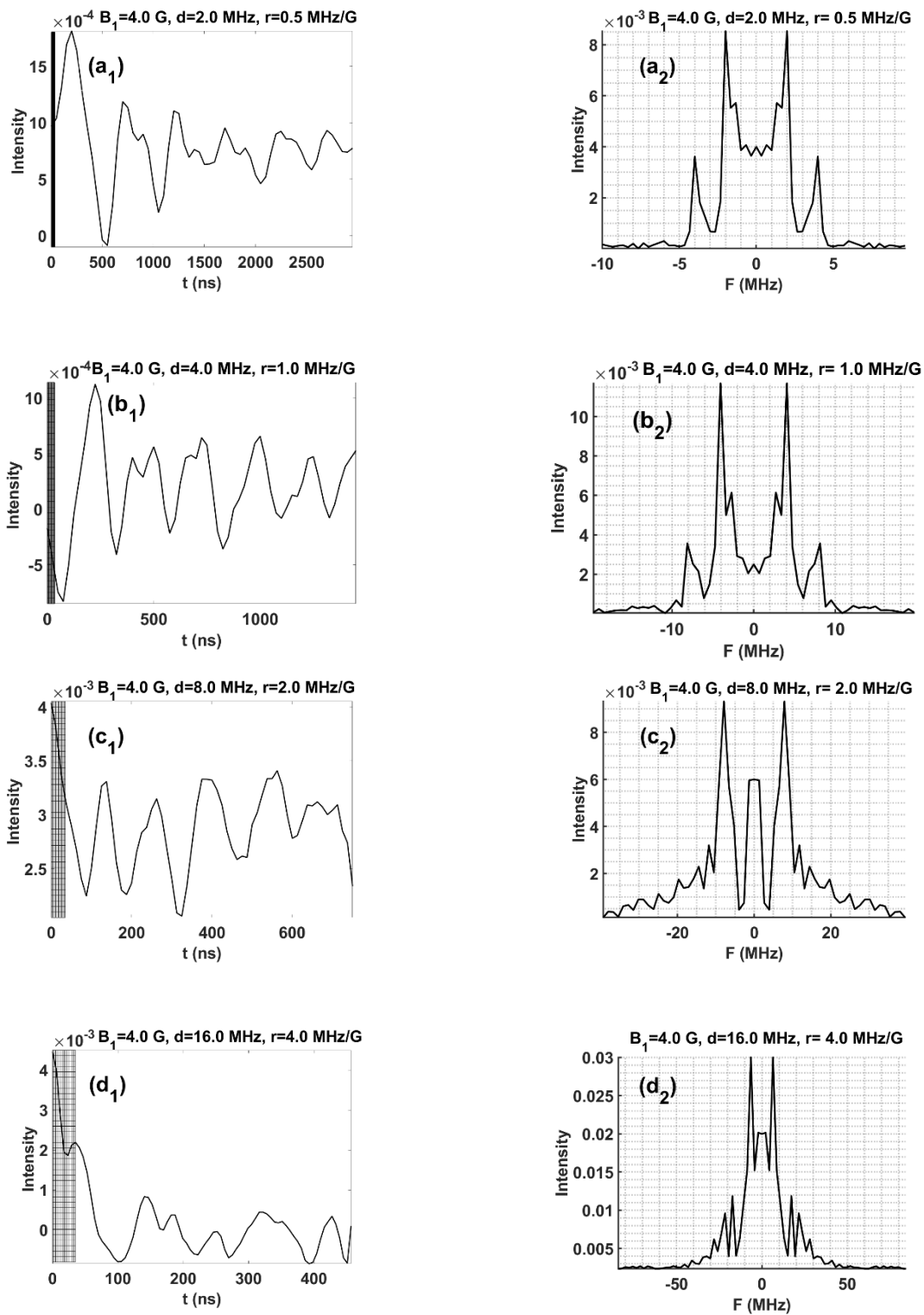
Figure 4.4. The same details as in the caption of Figure 4.2, except here $B_{1obs} = B_{1pump} = 4.0\ G$

The intensities of the $\pm d/2$ peaks, which are the only peaks that can become more intense than the $\pm d$ peaks in some cases, relative to the corresponding $\pm d$ peaks for $B_1 = 2.0$, 3.0, 4.0 G as functions of the value of d, for $r = 0.25, 0.5, 0.75, 1.0, 1.25, 1.5, 1.75, 2.0, 4.0$, are plotted in Figure 4.5. From this figure, one can conclude that the dipolar values that can be unequivocally determined by 3-pulse DEER are those for which the $\pm d$ peaks are predominant. These values are: $d < 3.4\ MHz, < 4.5\ MHz$, and $< 8.0\ MHz$ for $B_1 = 2.0\ G$, $3.0\ G$, and $4.0\ G$, respectively, which correspond to the distances $r > 24.8$ Å, >22.6 Å, 18.7 Å, respectively. The limit for $B_1 = 4.0\ G$, i.e., $r > 18.7$ Å, as found here theoretically, is consistent with that reported in (Borbat and Freed), i.e., $r > 20.0$ Å.
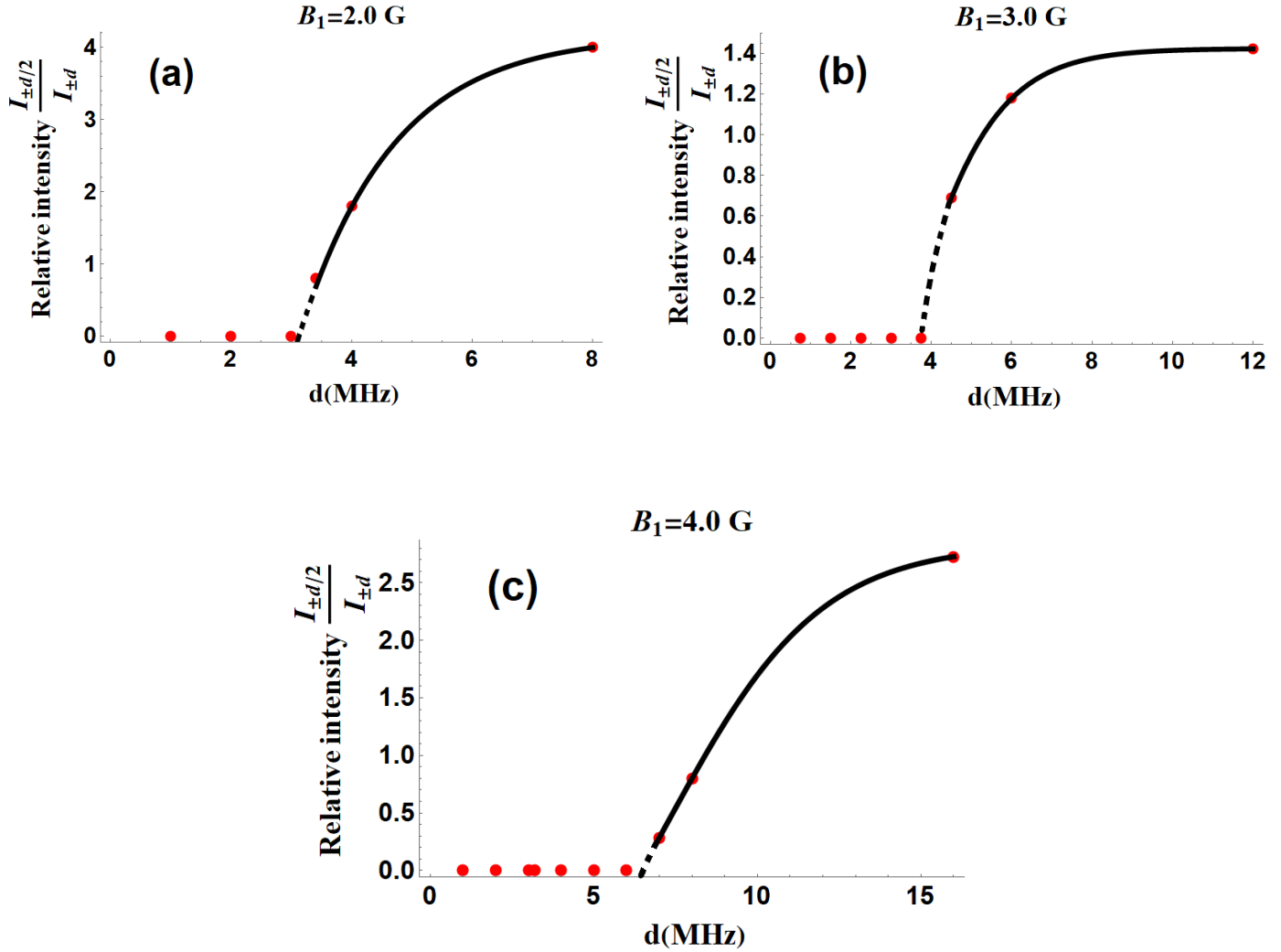
Figure 4.5. The relative intensity of the peak at $\pm d/2$ with respect to the peak at $\pm d$ in the Fourier transform of the three-pulse DEER signal as a function of $d(MHz)$ calculated for three values of the amplitude of the irradiation microwave field (a) $B_1 = 2.0G$, (b) $B_1 = 3.0G$ and (c) $B_1 = 4.0G$, assumed to be the same for the observer and pump pulses. The value of d up to which the Pake doublets at $\pm d$ increases as the amplitude B_1 increases, being $d = 3.4\ MHz$, $4.5\ MHz$ and $8.0\ MHz$ for $B_1 = 2.0\ G$, $3.0\ G$, and $4.0\ G$, respectively.

4.1.2.2 Calculation of the four-pulse DEER signal reported in (Georgieva *et. al.* 2012)

As the second illustrative example, the doubly rotating frame technique is applied to reproduce the experimental four-pulse DEER signal of doubly spin-labeled T4 lysozyme mutants reported in (Georgieva *et. al.* 2012). This, in turn, also tests further the validity of the DRF technique. The pulse scheme for the four-pulse DEER experiment is shown in Figure 4.1(b). The procedure to reproduce the experimental signal is as follows:

(i)   The four-pulse DEER signal is calculated for different dipolar coupling constant values separately, corresponding to each green point specified on the probability, $P(r)$, of distance distribution curve shown in Figure 4.6(a). The simulations are carried out following the procedure of the DRF technique, described in Sec 4.1.1 Calculation of the effect of observer and pump pulses using doubly rotating frames..

(ii)   From the calculated time-domain signals for the points on the distance distribution of Figure 4.6 (a), specified by a green point, the cubic spline package in *Matlab* is exploited to produce the time-domain signal for the other points, not specified by the green points, to make calculated signal smoother. The signals are calculated here for the total number of 64 points.

(iii)   The various time-domain signals, so calculated are multiplied by their respective probabilities of distance distribution, $P(r)$, as given by Figure 4.6(a), and added with each other to simulate the overall signal.

(iv)   The effect of local spin concentration is considered by multiplying the overall signal as calculated in step (iv) by $exp(-k\,t)$, as described in Sec. 4.1.3 below, and least-squares fitting it with the experimental signal to find the best-fit value of k.

For the simulations, a standard 4-pulse DEER sequence was used with $\pi/2, \pi, \pi$ pulse widths of 16 ns, 32 ns and 32 ns, respectively, and a 32 ns π pump pulse was used, the same as those used in the experiment. The frequency separation between observer and pump pulses was 70 MHz. The simulated four-pulse DEER signal shows an excellent agreement with the experimental signal as shown in Figure 4.6 (b) which indicates that the doubly rotating frame technique is very useful and accurate in describing the experimental data.

4.1.3 Inter-molecular interaction

In the interpretation of experimental DEER data spin relaxation is not normally considered. However, there is the mechanism of inter-molecular interaction that has an effect similar to spin relaxation as described below.

Due to the interaction of spins with neighboring molecules, an exponentially decaying function with time, proportional to the local spin-concentration, contributes to the DEER signal (Georgieva *et. al.* 2012). In DEER, the inter-molecular interactions are characterized by the following equation (Georgieva *et. al.* 2012):

$$V_{inter}(t) = \mathrm{e}^{-k\mathrm{t}} \qquad\qquad (4.9)$$

where k^{-1} is decay rate per microsecond, expressed as

$$k^{-1} = 1.0027 \frac{10^{-3}}{p.C} \qquad (4.10)$$

where p is the probability of flipping B spins by the pumping pulse, and C is the molar concentration. The value of p was found to be equal to 0.23, in general (Georgieva *et. al.* 2012). Therefore, the local spin-concentration, C, can be calculated from the measured decay rate of the DEER signal.
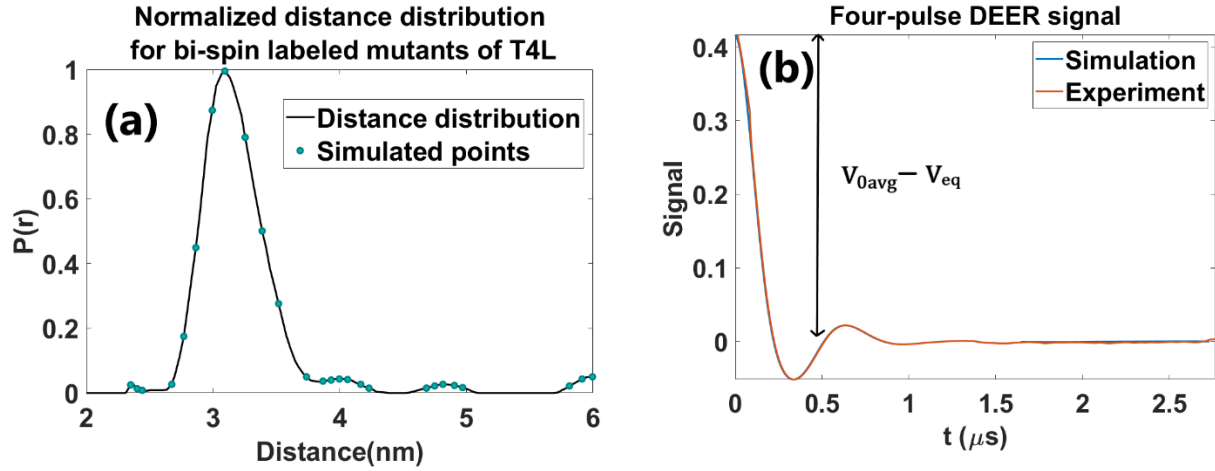
Figure 4.6 (a) The probability of distribution of distances $P(r)$ as reported in (Georgieva *et. al.* 2012) and (b) the calculated resulting signal, by overlapping time-dependent DEER signals, calculated for the various r values using doubly rotating frame, in accordance with the probability distribution given in (a). An excellent agreement is found between the simulated (blue) and experimentally measured (brown) signals. A modulation depth $\Delta(\%)$ of about 100% is found from the simulation of the four-pulse DEER signal.

4.2 Four-pulse DEER signal for two coupled Gd³⁺ ions using DRF technique

The DRF technique proposed in Sec. 4.1 for nitroxide radicals characterized by the spin $S = 1/2$, is here extended to Gd^{3+} ions in a sample of Gd-DOTA (Dalaloyan *et. al.* 2015), possessing a larger spin $S = 7/2$ and exhibiting zero-field splitting (ZFS). To this end, coupled Gd^{3+} ions in dipolar interaction with each other in a Gd^{3+} complex, have been exploited in biological systems, as shown in Figure 4.7. The dipolar interaction is manifested in the Fourier transform of DEER signal, wherein the spacing between the Pake doublets is inversely proportional to the cube of the distance between the two ions. Such an effort has been made at Q- and W-bands (Dalaloyan *et. al.* 2015, Raitsimring *et.al.* 2007, Potapov *et. al.* 2010, Yagi *et. al.* 2011, Edwards *et. al.* 2014, Manukovsky *et. al.* 2015). The advantage of using Gd^{3+} complexes as spin labels is that (i) it provides higher sensitivity in distance measurement in comparison to that obtained with nitroxide radicals, because of the absence of orientational selectivity, which

prevents a large fraction of the spins from contributing to the signal, allowing for the use of pulses with larger amplitude (Dalaloyan *et. al*. 2015), and (ii) the absence of hyperfine interaction, which complicates the signal.

4.2.1 Theoretical Details

The numerical calculations are carried out in the direct-product space of the two Gd^{3+}ions.

4.2.1.1 Static spin Hamiltonian

The static spin Hamiltonian for the coupled Gd^{3+} ions in the laboratory frame, with the z-axis being coincident with the external magnetic field direction, can be expressed in the rigid limit as (Dalaloyan *et. al*. 2015)

$$H_0 = H_{01} + H_{02} + H_{12};$$

where

$$H_{0k} = \frac{g\beta_e B_0}{h} S_{zk} + D_k \left[S_{zk}^2 - \frac{1}{3} S_k(S_k + 1) \right] + E_k \left[S_{xk}^2 - S_{yk}^2 \right]; k = 1,2, \qquad (4.11)$$

$$H_{12} = \frac{\omega_{dd}}{2\pi} (3cos^2\theta - 1) \left(S_{z_1} S_{z_2} - \frac{1}{4} (S_{+_1} S_{-_2} + S_{-_1} S_{+_2}) \right).$$

In Eq. (4.11), the first term represents the Zeeman term, the second and third terms represent the ZFS terms. The subscript k refers to the two Gd^{3+} spins. The observer and pump spins are assumed to remain at the fixed distance, r, from each other and are denoted by the subscripts $k = 1$ and 2, respectively. The nuclear Zeeman and nuclear quadrupole interactions are neglected. g is the isotropic g values for the Gd^{3+} ion, $\beta_e$is Bohr magneton, h is the Planck's constant and D_k, E_k are the zero-field interaction constants for the two Gd^{3+} ions. The last term on the right-hand side of Eq. (4.11) denotes the dipolar interaction between the two Gd^{3+} ions, which includes the pseudo-secular term, in the last bracket. Here ω_{dd}, called the dipolar-interaction constant. is related to r, the distance between the Gd^{3+} ions of the Gd^{3+}complex, as $\omega_{dd}[MHz] = \frac{52.04}{r[nm]^3}$. More details of the ZFS term and its transformation from the principal-axes frames of the two ZFS-tensors to the laboratory frame are given in Appendix F.

4.2.1.2 Initial density matrix

In thermal equilibrium, the initial density matrix for Boltzmann distribution is:

$$\rho_0 \propto \exp{(-H_0/K_B T)} \qquad (4.12)$$

where H_0 is the static spin Hamiltonian given by Eq. (4.11), K_B is the Boltzmann constant and T is the temperature. This density matrix evolves during the application of a pulse, as well as during the free evolution, i.e., in the absence of any pulse. This is discussed below.

4.2.2 Rotating-frames technique to calculate DEER signal for two coupled Gd^{3+} ions for a polycrystalline sample

In this model, first the Zeeman terms included in the first term in Eq. (4.11) are subtracted off, which are equal for the observer and pump spins, because of the isotropic value of g = 1.9925 for the Gd^{3+} ion. The observer spins are chosen to be those at resonance at the transition $M_s = -3/2$ and $M_s = -1/2$ of the Gd^{3+} ion 1, whereas the pump spins are chosen to be those at resonance at the transition $M_s = -1/2$ and $M_s = 1/2$ of the Gd^{3+} ion 2. Accordingly, there are used two rotating frames to calculate the DEER signal, one of these is always used at the observer-spin frequency, which is achieved by subtracting the reference of energy by the energy difference of the levels $M_s = -3/2$ and $M_s = -1/2$ of the Gd^{3+} ion 1, except for the duration of the pump pulse, during which the rotating frame is at the pump-spin frequency, which is achieved by subtracting the reference of energy by the energy difference of the levels $M_s = -1/2$ and $M_s = 1/2$ of the Gd^{3+} ion 2. In order to calculate the signal for a polycrystalline sample, one uses a (θ, ϕ) grid over the unit sphere, keeping the rotating frame fixed for the observer spins for *all* orientations, except for those during the application of the pump pulse. It can be chosen for a fixed orientation, i.e., for $\theta = \phi = 0°$, of the dipolar axis with respect to the external magnetic field, for any choice of the Euler angles $(\alpha_1 = 0°, \beta_1, \gamma_1)$ for the orientation of the dipoles of the observer spins. This is completely valid for the Gd^{3+} ion, because its g-matrix is isotropic, rendering the Zeeman term to be the same for all the orientations of the Euler angles in a polycrystalline sample. The two spins are close to, but not precisely in their rotating frames, because of the energy difference between the respective transitions participating in resonance, required to bring in exact coincidence with the observer, or pump, spins. This is accomplished by changing the reference of energy by subtracting all energies by the difference in the energy levels $[E_1(M_{s_1} = -3/2) - E_1(M_{s_1} = -1/2)]$ of the observer spins at the magnetic field B_0, participating in resonance at the transition $-3/2 \leftrightarrow -1/2$, for the orientation $\theta = \phi = 0°$. (Here $M_{s_{1i}}, i = \frac{7}{2}, \frac{5}{2}, \dots \dots, -\frac{5}{2}, -\frac{7}{2}$ are the magnetic quantum numbers of observer spin 1.) Then the pump spins, at orientations (θ, ϕ) of their dipolar axes with respect to the external magnetic field, distributed over the unit sphere, are slightly off their rotating frames as they correspond to the transition $M_{s_2} = -1/2 \leftrightarrow M_{s_2} = 1/2$ for the various (θ, ϕ) values over the unit sphere. In order to bring to the rotating frame of the pump spins for the various (θ, ϕ) values over the unit sphere during the application of the pump pulse, the reference of energy is changed by subtracting all energies by $[E_1(M_{s_2} = -1/2) - E_1(M_{s_2} = 1/2)]$, which varies for different (θ, ϕ) values, since the *ZFS* term is dependent on (θ, ϕ) values. (Here $M_{s_{2i}}, i = \frac{7}{2}, \frac{5}{2}, \dots \dots, -\frac{5}{2}, -\frac{7}{2}$ are the magnetic quantum numbers of observer spin 1.) In this manner, the pump spins are brought precisely to their rotating frames for different (θ, ϕ) values during the pump pulse, whereas the observer spins remain slightly off their rotating frames.

It is noted that the rotating-frames technique presented here is an approximation in the presence of zero-field splitting term and it is true only for weak ZFS. The calculations in this work are performed for Gd-DOTA-based spin labels, which have a rather small D value ($D = 561$ MHz); the value of E was chosen to be about one-thirteenth of it: $E = 44$ MHz to conform to the weak ZFS regime. These values are much smaller compared to the Zeeman energies of 35 *GHz* (Q-band) or 95 *GHz* (W-band).
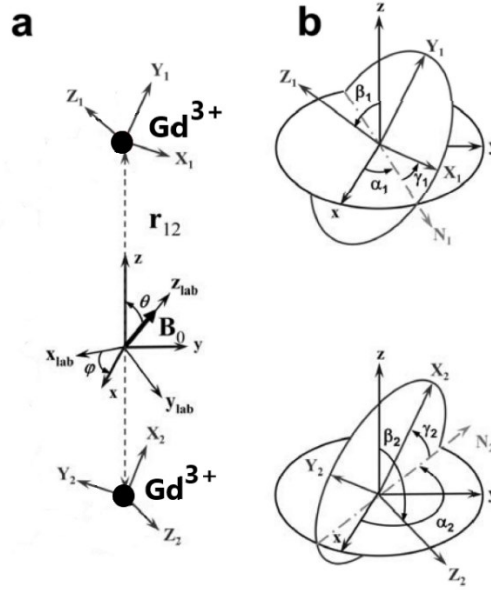
Figure 4.7 (a) Figure showing the configuration of the two coupled Gd^{3+} ions, as shown in the dipolar (molecular) frame of reference, wherein the z-axis is chosen parallel to the vector r_{12}, connecting the dipoles of the two Gd^{3+} ions. The z_{lab} − axis in the laboratory frame is oriented along the external magnetic field B_0. The Euler angles, shown in (a), which define the dipolar frame, are given by $\eta = (0, \theta, \phi)$ with respect to the laboratory frame. (b) The orientations of the principal axes of the zero-field splitting tensors for the Gd^{3+} ions 1 and 2, denoted by $X_k, Y_k, Z_k; k = 1,2$. are defined by the set of Euler angles $\lambda_k = (\alpha_k, \beta_k, \gamma_k), (k = 1, 2)$ with respect to the dipolar (molecular) frame of reference (x, y, z). The lines of nodes for the two Gd^{3+} ions frames are N_1 and N_2. as shown in (b). The x axis of the first Gd^{3+} ion magnetic frame is chosen to be along its line of nodes, N_1, for the numerical calculations in the present work, so that $\alpha_1 = 0$, since only five of the six Euler angles are independent (Sec. 3.3). (This figure is reproduced from (Misra *et.al* 2009) by permission.)

4.2.3 Calculation of Gd^{3+} DEER signal by using DRF technique

The details of calculation of Gd^{3+} DEER signal by using DRF technique are the same as those for the coupled nitroxides in a biradical given in Sec 4.1.1 except for the choice of the pulse Hamiltonian, which is as follows

$$H_{obs} = \frac{\omega_{1obs}}{2} \left(e^{-i\phi}(S_{1+})_{(5,6)} + e^{i\phi}(S_{1-})_{(6,5)} \right), \tag{4.13}$$
$$H_{pump} = \frac{\omega_{1pump}}{2} \left(e^{-i\phi}(S_{2+})_{(4,5)} + e^{i\phi}(S_{2-})_{(5,4)} \right). \tag{4.14}$$

In Eqs. (4.13) and (4.14) ω_{1p}; with $p =$ obs, pump are the amplitudes of the observer and pump pulses, respectively, in frequency units $(= \gamma_e B_{1p})$; $B_{1p} =$ amplitudes of the pulses in Gauss (Table 4.3) and γ_e is the gyromagnetic ratio of the electron; ϕ is the phase of the pulse and $S_{k\pm}$; $k = 1,2$ are the raising/lowering operators of the kth electronic spin of the coupled Gd^{3+} ions system in the 64×64 direct product Hilbert space. The indices in Eqs. (4.13) and (4.14)

indicate that the pulse Hamiltonians are adjusted to the specific transitions, $-3/2 \leftrightarrow -1/2$ and $-1/2 \leftrightarrow 1/2$, which define the observer and pump pulses, respectively.

Overall, taking into account the transition probabilities, $P_{S,M} = S(S+1) - M(M+1)$ for the transition $S, M \leftrightarrow S, M+1$ (Kaminker, Ph. D. Thesis), one can express the effective rotation tip angle of the Gd^{3+} spin by the pump or observer pulse of amplitude, B_{1p}, and of duration t_p, as

$$\beta_p = \gamma_e \sqrt{P_{S,M}} \, B_{1p} t_p = \gamma_e \sqrt{S(S+1) - M(M+1)} B_{1p} t_p \tag{4.15}$$

where, $p = obs, pump$, β_p is the flip angle, which is either $\pi/2$ or π in the four-pulse DEER sequence, shown in Fig. 2 The transitions $M \leftrightarrow M+1$, are $M = 1/2$ for the observer pulse, and $M = -1/2$ for the pump pulse.

4.2.4 Illustrative examples

The calculated four-pulse DEER signals by the DRF technique for three values of the dipolar interaction constant, corresponding to the typical values of the range of ω_{dd} values, as evaluated in the W-band four-pulse data of Gd-DOTA sample (Cohen *et. al.* 2016) : $\omega_{dd} = 0.63$ MHz ($r = 4.36$ nm), $\omega_{dd} = 0.49 \, MHz$ ($r = 4.73$ nm), and $\omega_{dd} = 0.39$ MHz ($r = 5.10$ nm), are shown in Figure 4.8 (a_1), (b_1) and (c_1), respectively, along with their Fourier transforms in Figure 4.8 (a_2), (b_2), and (c_2), showing the respective Pake doublets. The various parameters required for the simulations are listed in Table 4.3.
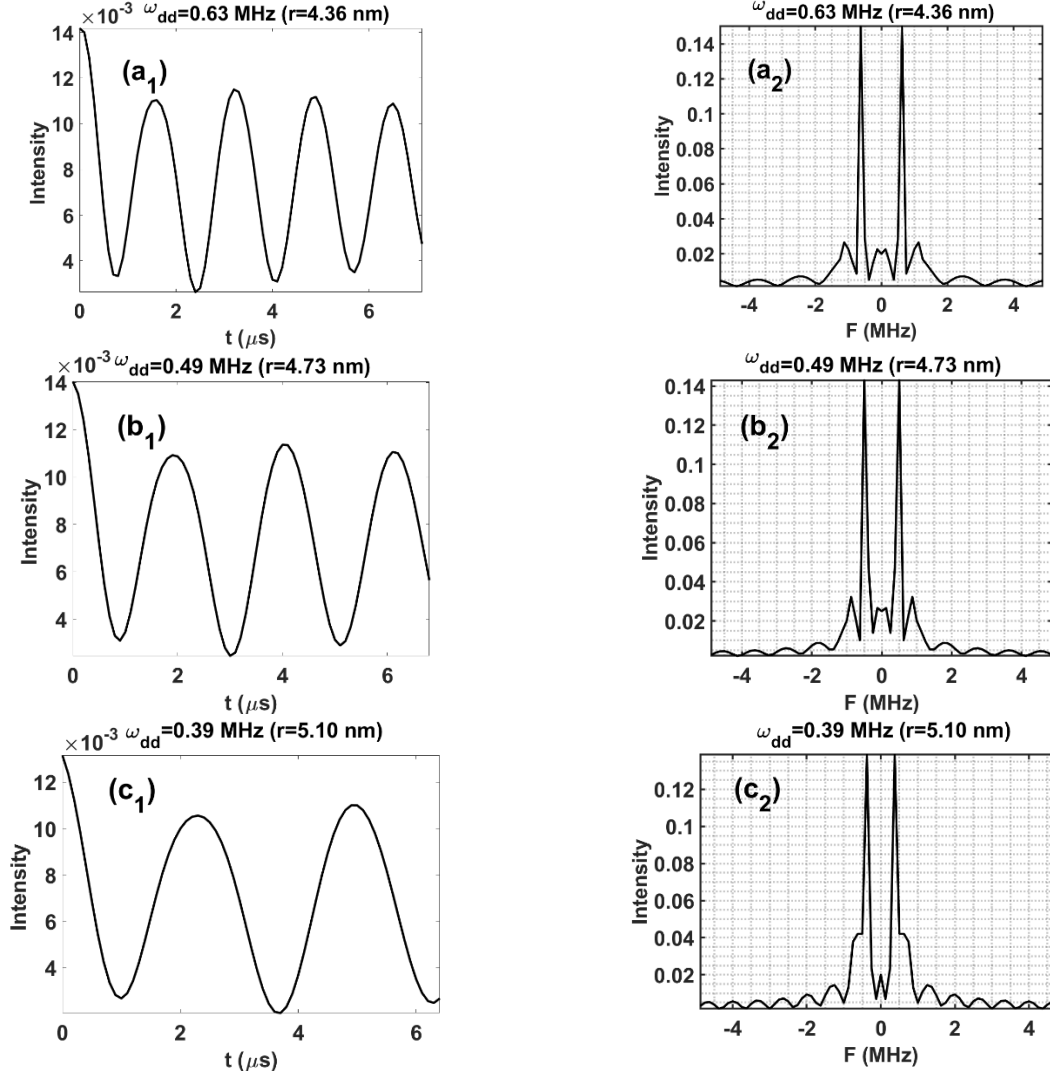
Figure 4.8 Simulation of four-pulse DEER signals using the RF technique for three values of the dipolar coupling constant: $\omega_{dd} = 0.63 \, MHz \, (r = 4.36 \, nm)$, $\omega_{dd} = 0.49 \, MHz \, (r = 4.73 \, nm)$ and $\omega_{dd} = 0.39 \, MHz \, (r = 5.10 \, nm)$, representing the two end and one middle values of the range of d values considered here for the calculation of basis DEER signals for a polycrystalline sample. The time-domain signals and their Fourier transforms are shown in (a_1, b_1, c_1) and (a_2, b_2, c_2), respectively. The parameters used for the simulations are listed in Table 4.3.

Parameters	Values of the parameters
Static magnetic field (B_0)	34,050 G
Microwave frequency	94.9 GHz
Difference between the observer and pump frequencies $\|\omega_A - \omega_B\|$	difference between the frequencies for the transitions $-1/2 \leftrightarrow +1/2$ (pump) and $-1/2 \leftrightarrow -3/2$ (observer)
Exchange constant (J)	0 MHz
g-values $= \left(g_{xx}, g_{yy}, g_{zz}\right)$	(1.9925, 1.9925, 1.9925)
ZFS components for each Gd^{3+} ion B_m^2 ($m = 2, 1, 0, -1, -2$)	(44 MHz, 0, 187 MHz, 0, 44 MHz) ($D = 3B_0^2 = 561$ MHz; $E = B_2^2 = 44$ MHz)
Constant time between the two observer π pulses (τ_1)	350 ns
Constant time between the last observer pulse and the top of the echo (τ_2)	6.5 µs
Durations of the pulses (the intensities of the irradiation fields, B_1, are in brackets after each duration)	$t_{pump,\pi}(B_1 = 2.98G) = 15$ ns $t_{obs,\pi}(B_1 = 1.54G) = 30$ ns $t_{obs,\pi/2}(B_1 = 1.54G) = 15$ ns

Table 4.3 The values of the parameters used in the simulations of four-pulse W-band DEER signals of two coupled Gd^{3+} ions in DOTA.

4.3 Estimation of distance-distribution probabilities from DEER data of two coupled nitroxide and two coupled Gd^{3+} spin labels using doubly rotating frames

From DEER data, one can obtain the probability of distance distribution, $P(r)$, where r is the distance between the two nitroxide in a biradical or the distance between the two Gd^{3+} spins in Gd^{3+} complex, distributed within a biological system, by a penalized least-squares fitting (Edwards and Stoll 2018), since this is an ill-posed problem, most often by Tikhonov regularization (Chiang *et.al* 2005).

There are available comprehensive computer packages, e.g., *DeerAnalysis* (Jeschke *et. al.* 2006), which are frequently used to determine $P(r)$ between the biradicals in biological systems. These packages exploit Tikhonov regularization method, among others, using the basis kernel basis signals, which are calculated in the limit of hard (infinite) pulses, whereas in real experiments the pulses are of finite amplitude, on the order of a few Gauss. (These kernel basis

signals will hereafter be referred as analytical kernel signals.) Furthermore, the hyperfine interaction and the zero-field splitting, which can be significant for systems, are ignored.

The DRF technique to calculate the time-domain DEER basis kernel signals rigorously, as described in Secs. 4.1 and 4.2 for nitroxide radicals and gadolinium complexes, respectively. The objective of this section is to illustrate this method by application to the DEER data, reported by (Lovett *et. al.* 2012) on a sample of bis-nitroxide nanowire, P1, in deuterated ortho-terphenyl solvent with 5% BnPy (d14-oTP/BnPy) in semi-rigid state and a sample of Gd^{3+} ions in a sample of Gd ruler 1_5, is a combination of (i) a chelate to hold the Gd, (ii) a suitable linker and

(iii) an anchor to the biological macromolecule, in D_2O/glycerol-d_8 for Q (Doll *et. al.* 2015)- and W (Dalaloyan *et. al.* 2015)-bands, by first calculating rigorously the relevant basis kernel signals using DRF technique, to be used in the *DeerAnalysis* software, with Tikhonov regularization, to extract the distance-distribution probabilities, $P(r)$. Tikhonov Regularization (also called *penalized* least-squares fitting) is needed here, since the experimental signal cannot be directly least-squares fitted to $P(r)$, using a set of basis kernel functions, as this is an ill posed problem.

4.3.1 The general procedure of Tikhonov regularization.

To estimate the probabilities of distance distribution, $P(r_n)$, from the experimental DEER signal, $S(t)$, by fitting it to the calculated signal, $S_{cal} = \sum_n S(t, r_n)P(r_n)$, where the basis signals, $S(r_n, t)$, are weighted by $P(r_n)$, is an ill-posed problem in an ordinary least-squares fitting procedure. There are used three different methods in *DeerAnalysis* to find the solution of this ill-posed problem: (i) Approximate Pake transformation (APT); (ii) Tikhonov regularization; and (iii) *DEERNet*. The Tikhonov regularization method (TR) is the most used method for extracting distance distributions from experimental DEER data. It will here be used for the calculation of the probabilities. In particular, TR is a form of penalized least-squares fitting, wherein one minimizes (Edwards and Stoll 2018)

$$P_{\alpha,L} = argmin_{P \geq 0}\left(\left||S - KP\right||^2 + \alpha^2\left||LP\right||^2\right), \qquad (4.16)$$

where $K = K(r, t)$ are the basis kernel signals In eq. (4.16), P is the probability, and S is the experimental data. The least-squares term, i.e., the first term in Eq. (4.16) captures the misfit between the model-calculated signal KP and the experimental data S. The second term in Eq. (4.16) compensates for the unwanted properties of the solution P. It will thus depend on the particular form for the regularization operator L and the particular value for the regularization parameter α. The fit is then carried out, subject to the constraint that all the elements of P are non-negative (P ≥ 0). The subscripts in $P_{\alpha,L}$ indicate that the solution is dependent upon the choices of α and L (Edwards and Stoll 2018).

4.3.2 Use of *DeerAnalysis* software with analytical kernel signals

Here one uses analytical basis kernel signals as calculated in *DeerAnalysis* software. The analytical kernel signals built in the *DeerAnalysis* package are expressed as

Parameters	Values of the parameters
Static magnetic field (B_0)	$3,480G$
Microwave frequency ω_A (observer spins)	$9.346\ GHz$
Microwave frequency ω_B (pump spins)	$9.411\ GHz$
Difference between the observer and pump frequencies $\lvert \omega_A - \omega_B \rvert$	$65\ MHz$
Exchange constant (J)	$0\ MHz$
g-matrix $\tilde{g} = \left(g_{xx}, g_{yy}, g_{zz}\right)$	$(2.0086, 2.0066, 2.0032)$
Hyperfine matrix $\tilde{A} = \left(A_{xx}, A_{yy}, A_{zz}\right)$	$(6.0\ G, 6.0\ G, 35.0\ G)$
The constant time between the two observer pulses (τ)	$4.5\ \mu s$
The duration of the observer pulses ($t_{p_1} = t_{p_3}$)	$32\ ns$
The duration of the pulses (t_{p_2})	$12\ ns$

Table 4.4 The values of the parameters used in the simulations of the DEER signals of the coupled nitroxide biradical, for the data of (Lovett et al. 2012).

$$K(t,r) = \int_0^{\pi/2} \cos[(3cos^2\theta - 1)\omega_{dd}t]\, d(cos\,\theta) \qquad (4.17)$$

In Eq. (4.17), r is related to ω_{dd} as $\omega_{dd}[MHz] = \frac{52.04}{r[nm]^3}$.

For a given DEER signal, the software *DeerAnalysis* is used with Tikhonov Regularization, to obtain both the probability distribution $P(r)$, as well as the calculated time-dependent signal, $S_{cal}(t)$, using analytical kernel signals.

4.3.3 Use of *DeerAnalysis* software with DRF-calculated basis kernel signals

The distance-distribution probabilities, $P(r_n)$, are evaluated using the DRF-calculated kernel signals, $S(t, r_n)$, derived as follows.

Calculation of basis kernel DEER signals, $S(t, r_n)$, by the DRF technique for dipolar interaction-coupled nitroxide in a biradical.

The values and definitions of the constants used in the numerical simulations are listed in Table 4.4. In order to correspond to the experimental signal, the three-pulse time-domain DRF-calculated DEER signals were simulated, for the set of r values (or the corresponding d values as calculated using the the formula $d[MHz] = \frac{52.04}{r[nm]^3}$) for the various n values, r_n, corresponding to the green dots in Figure 4.9(a), showing the probability distribution as determined by *DeerAnalysis* using analytical kernel functions. These dots were chosen such that there are three points to each segment of the $P(r)$ curve that can be approximated by a straight line, one point each at the ends and one point in the middle. This resulted in a total of 39 points for which the time-domain signals were calculated using the DRF technique, from which 512 signals, $S(t, r_n)$, were calculated for equally spaced intervals of r, using the cubic spline package in *Matlab*, to be used as DRF-calculated basis signals in the *DeerAnalysis* software.

To use the DRF-calculated signal, the kernel functions $K(t, r)$ and the range of r values in *DeerAnalysis* were appropriately replaced by the normalized DRF-calculated basis signals, $S(t, r_n)$, over the corresponding range of r. The probabilities of distance distributions, corresponding to the experimental signal, so calculated by *DeerAnalysis* are shown in Figure 4.9 (b). The regularization parameter of 14.3 was found for this probability distribution as determined by *DeerAnalysis*, using the L-curve method, close to that found when the analytical kernel functions.

The steps used for the calculation of the probability distribution, $P(r)$, from the experimental signal using *DeerAnalysis*, modified for rotating-frames (DRF)-calculated kernel signals are as follows:

1. Determine the range of the distance, r, over which the probability distribution is non-zero, as calculated by the application of *DeerAnalysis* software.

2. Simulate the DEER signals using the DRF technique for a good number of evenly distributed points, r_n, over this range.

3. Use the *Spline* function in Matlab to derive 512 time-domain signals by the cubic-spline technique, each calculated as a function of time in 512 even steps over the range of time from 0 to τ_2 from the m DRF-calculated signals in the previous step.

4. Normalize the time-domain signals, as simulated by the DRF technique, for the various r_n values, by dividing each by its maximum value.

5. Stack these signals in a 512×512 matrix, $K(r, t)$, where r, t denote the rows and columns, respectively.

6. In the *DeerAnalysis* Matlab file, "make_bas_Tikh.m", make the following replacements: (i) *rmin* and *rmax* by the minimum and maximum of range of distance r, respectively, determined in step 1; (ii) dt by $\tau_2/512$; (iii) the already present analytically calculated kernel signals, $K(r, t)$, by the DRF-calculated kernel signals, $K(r, t)$, as described in step 5

7. In the Matlab file "get_Tikhonov_new.m" in *DeerAnalysis* folder, replace the conditional statement "if length(tdip) > 2048", which allows one to use already calculated and stored analytically calculated kernel signals, $K(r,t)$, by the statement "if length(tdip) > n_{RF}, where the integer n_{RF} < 512" , i.e., n_{RF} = 200 in the present case, for one to use the DRF-calculated kernel signals of size (512, 512) as in step 5.

8. Delete "pake_base_tikh_512.mat" file from the *DeerAnalysis* folder, so that the already stored analytically calculated kernel signals, $K(r,t)$ are removed, allowing the use of the DRF-calculated kernel signals, $K(r,t)$, Then open the "DeerAnalysis.m" file, run it, and wait until the *DeerAnalysis* workspace loads up (about 5 minutes).

9. When the workspace opens, click on the button "load", then from the "Data sets" box load the experimental data file (with the ending .DTA).

10. In the "Distance Analysis" box, select "Tikhonov" and "L curve" to obtain plots of L-shaped curve and the probability distribution as a function of distance.

The two calculated signals as obtained (i) by using the analytical kernel functions built in *DeerAnalysis* and (ii) the DRF-calculated signals are shown by solid blue and solid red lines, respectively, in Figure 4.9(c), which also includes the experimental signal as shown by the solid black line.

The probability distributions of distances obtained by using *DeerAnalysis* with Tikhonov regularization using the analytical kernel functions and the DRF-calculated basis signals are shown in Figure 4.9 (b) with blue and red solid lines, respectively. It is seen from this figure that for r > 3.3 nm the two probability distributions are almost the same. On the other hand, for smaller r values, r < 3.3 nm, the two distributions are distinctly different from each other, especially at $r \approx 2.3$ nm where there is found a peak in the probability distribution calculated with the DRF-calculated basis signals, unlike that calculated with the analytical kernel functions. This is a significant difference, indicating that the DRF-calculated accurate basis signals, considering finite pulses, provide better values of probabilities, especially for smaller distances, r < 3.3 nm, in this case.

Comparing the χ^2 values calculated for the two calculated signals with respect to the experimental data, as shown in Figure 4.9, one finds that using the DRF-calculated basis signals a better fit is obtained than that obtained by using the analytical kernel functions built in *DeerAnalysis*. This is clearly seen in Figure 4.9 (c), showing the signals as calculated by the DRF and analytical kernel functions.
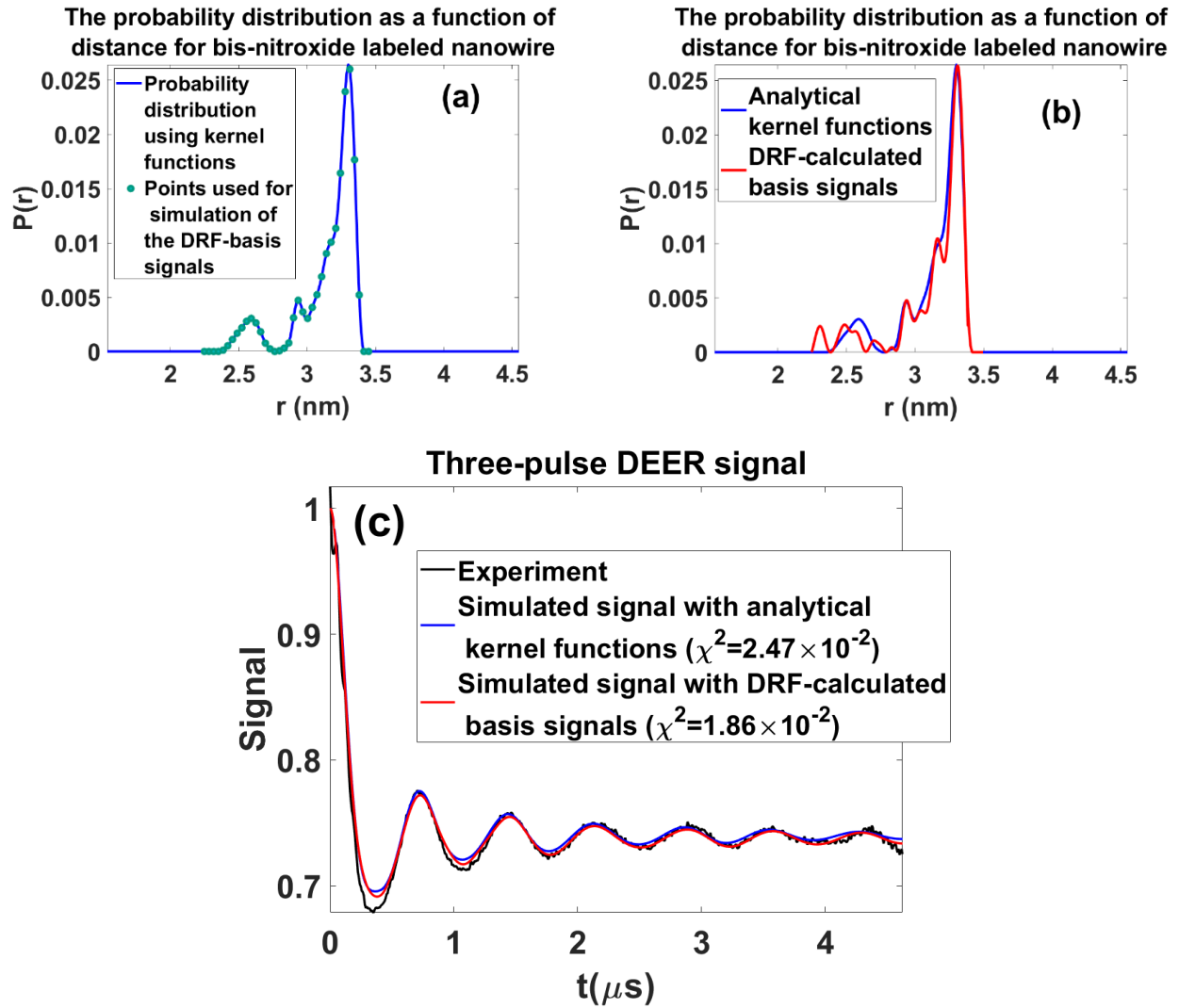
Figure 4.9 (a) The probability distribution as a function of distance as obtained from the experimental data, reported in (Lovett et. al. 2012) for bis-nitroxide labeled nanowire, calculated by *DeerAnalysis* with Tikhonov-regularization using analytical kernel functions, shown in blue, and the distances chosen for the calculation DRF signals indicated by green dots; (b) The probability of distance distribution calculated using the DRF-calculated signals described in Sec. 4.1, shown in red and that calculated using the analytical kernel functions, shown in blue {the same as that shown in (a)}; there are found significant differences in the two for distances $r <$ 3.3 nm; (c) The calculated time-domain signal, as obtained by using the DRF-calculated signals, shown by the red solid line, and the signal calculated by the *DeerAnalysis* software using the analytical kernels, shown by the blue solid line. An improvement is found in the overall signal calculated by using DRF-calculated signals as compared to that calculated using the analytical kernel functions. The zero of t is set just after the deadtime that occurs subsequent to the third pulse in the experiment. The experimental time trace, shown in (c) by black line, is the original data, obtained from Dr. J. E. Lovett, one of the authors of Ref. (Lovett et. al. 2012).

Calculation of basis kernel DEER signals, $S(t, r_n)$, by the DRF technique for dipolar interaction-coupled Gd^{3+} ions. The four-pulse time-domain DEER signals were simulated using the DRF technique, as described in Sec. 4.2 above, for the set of r values, over the range calculated for the experimental signal by *DeerAnalysis* using analytical kernel signals. such that they are equally spaced in r, the distance between the two Gd^{3+} ions in Gd ruler 1_5 in D_2O/glycerol-d_8 (7/3 volume ratio). This resulted in a total of 19 r values, for which the time-domain signals were calculated using the DRF technique. From these 19 DRF-calculates kernel signals, 512 signals, for equally spaced intervals of r, were obtained by using the cubic-spline package in *Matlab*, to serve as the basis kernel signals for the Gd^{3+} pairs, as required in *DeerAnalysis*. The steps used to modify *DeerAnalysis*, using the DRF-calculated DEER signals for the calculation of the probability distribution are the same as those listed for the coupled nitroxide system above.

Now the probability distribution, $P(r)$, are obtained using *DeerAnalysis* with Tikhonov Regularization using the basis DRF-calculated kernel signals as described above. Thereafter, the time-domain DEER signal, $S_{cal}(t)$, is calculated by overlapping the various $S(t, r_n)$, the RF-calculated kernel signals for the distances, r_n, weighted by the $P(r_n)$ values, as estimated above, as follows:

$$S_{cal}(t) = \sum_n S(t, r_n)P(r_n) \tag{4.18}$$

It is noted that *DeerAnalysis* software was not used to calculate the signal, $S_{cal}(t)$, unlike that done when using the analytical kernel functions which is built in the software, since it would have required a lot of effort to modify the software to accomplish this.

The values and definitions of the constants used in the numerical simulations are listed in Table 4.5. Using these, the basis kernel signals were calculated for both Q- and W-bands using the DRF technique, described in Sec. 4.2. This included the ZFS and finite pulses. The simulations for the polycrystalline sample were carried out over a grid of the unit sphere with 90×90 points of $\{\cos\theta, \phi\}$ for 10 different sets of five Euler angles $\{(0, \beta_1, \gamma_1), (\alpha_2, \beta_2, \gamma_2)\}$, chosen by Monte-Carlo averaging. This is tantamount to $90 \times 90 \times 10 = 8.1 \times 10^4$ simulations for each kernel signal. The basis kernel signals were then used in the software *DeerAnalysis* in place of the analytical kernel signals built therein, which are calculated for infinite pulse, valid for spin ½, implying that the ZFS has not been considered. For comparison, Figure 4.10, shows the kernel functions as calculated here using the DRF technique and including the ZFS, and the kernel function calculated using the analytical expression for infinite pulse, for the extreme ends and in the middle of the range of $P(r)$. It is seen from Fig 4.10 that there is a significant difference between the DRF-calculated signal and that by the use of analytical kernel.

The probability distributions as calculated by the use of DeerAnalysis software, equipped with the kernel signals, calculated here taking into account the ZFS and finite pulses at Q- and W-bands are plotted in Figs. 4.11(a) and 4.12(a), respectively, which also show the probability distributions, as obtained by using the basis kernel signals, using infinite pulses and neglecting

Parameters	Values of the parameters at W-band	Values of the parameters at Q-band
Static magnetic field (B_0)	$34{,}050 G$	$11{,}918 G$
Microwave frequency	$94.90\ GHz$	34.30 GHz
Difference between the observer and pump frequencies $|\omega_A - \omega_B|$ in the experiment	90 MHz	Chirp pump pulse with varying frequency used in the experiment
Difference between the observer and pump frequencies $|\omega_A - \omega_B|$ in the simulation	Difference between the energy levels in frequency units for the transitions $-1/2 \leftrightarrow +1/2$ (pump) and $-1/2 \leftrightarrow -3/2$ (observer)	Difference between the energy levels in frequency units for the transitions $-1/2 \leftrightarrow +1/2$ (pump) and $-1/2 \leftrightarrow -3/2$ (observer)
g-values $= \left(g_{xx}, g_{yy}, g_{zz}\right)$	(1.9925, 1.9925, 1.9925)	(1.9925, 1.9925, 1.9925)
ZFS components for each Gd^{3+} ion B_m^2 $(m = 2, 1, 0, -1, -2)$	$(95.8\ MHz, 0, 383.3\ MHz, 0, 95.896\ MHz)$ $(D = 3B_0^2 = 1150$ MHz; $E = B_2^2 = 95.8$ MHz$)$	$(95.8\ MHz, 0, 383.3\ MHz, 0, 95.896\ MHz)$ $(D = 3B_0^2 = 1150$ MHz; $E = B_2^2 = 95.8$ MHz$)$
Constant time between the two observer π pulses (τ_1)	350 ns	2.0 μs
Constant time between the last observer pulse and the top of the echo (τ_2)	7.4 μs ($dt = 74\ ns$, 100 points in time-domain signal)	14.1 μs ($dt = 100\ ns$, 140 points in time-domain signal)
Duration of the pulses	$t_{obs,\pi/2} = t_{pump} = 15$ ns $t_{obs,\pi} = 30$ ns	$t_{obs,\pi/2} = t_{obs,\pi} = 12$ ns $t_{pump} = 192$ ns
Intensities of the four pulses used for simulation of DRF-calculated basis signals, shown in Figs. 3- 5.	(1.54 G, 1.54G, 2.97G, 1.54G)	(1.92 G, 3.84 G, 0.23 G, 3.84 G)

Table 4.5 The values of the parameters used in the simulations of the four-pulse W-band DEER signals of the coupled Gd^{3+}ions.

the ZFS of the Gd^{3+} ions, as used in *DeerAnalysis*, valid for spin $S = 1/2$. The following results were found.

Q-band. It is seen that both distributions are maximum at the respective centers, falling off gradually to zero for decreasing and increasing r from this center, similar to a Gaussian distribution, with the maximum $P(r)$ at $r = 4.76$ nm. Upon comparing the two, it is seen that the centers of the two are almost coincident, but the DRF-calculated probability distribution is slightly narrower than that calculated using the analytical functions. The χ^2 values are 1.5×10^{-3} and 1.3×10^{-3} for the analytical and DRF-calculated kernel signals, respectively.

W-band. It is seen that both distributions are maximum at the respective centers, falling off gradually to zero for decreasing and increasing r from this center, similar to a Gaussian

distribution. Upon comparing the two, it is seen that the centers of the two are almost coincident, but the DRF-calculated probability distribution is slightly narrower than that calculated using the analytical functions. In addition, there exists a smaller peak at about $r = 4.2$ nm in the DRF-calculated probability distribution which is absent in the analytical calculated one. The χ^2 values are 3.6×10^{-3} and 3.2×10^{-3} for the fits using analytical and DRF-calculated kernel signals, respectively. It shows that a better fitting is obtained with the use of DRF-calculated signal kernels.

From these comparisons it appears that for an accurate analysis, taking into account the ZFS, one needs to simulate the DRF-calculated kernel signals. It is noted that the parameters of fitting, e.g., regularization parameter, obtained by the application of *DeerAnalysis* software using the DRF-calculated kernel signals are similar to those obtained with the use of analytical kernel signals, which can be considered to be realistic. Therefore, the fitting with the DRF-calculated kernel signals obtained here must also be considered realistic, rather than being an artifact of fitting.

4.4 Conclusions

The salient features of this chapter are as follows:

(i)   The time-dependent signals using DRF technique appear to have the expected shape of typical DEER signals and their Fourier transforms, indeed, show the Pake doublets with peaks at the dipolar frequencies $\pm \omega_{dd}$.

(ii)   Calculation of distance distributions from DEER data with the use of the DRF-calculated basis signals, considering finite pulses, using the *DeerAnalysis* software with Tikhonov regularization provides a more accurate estimation of the probabilities of distance distribution, $P(r)$.
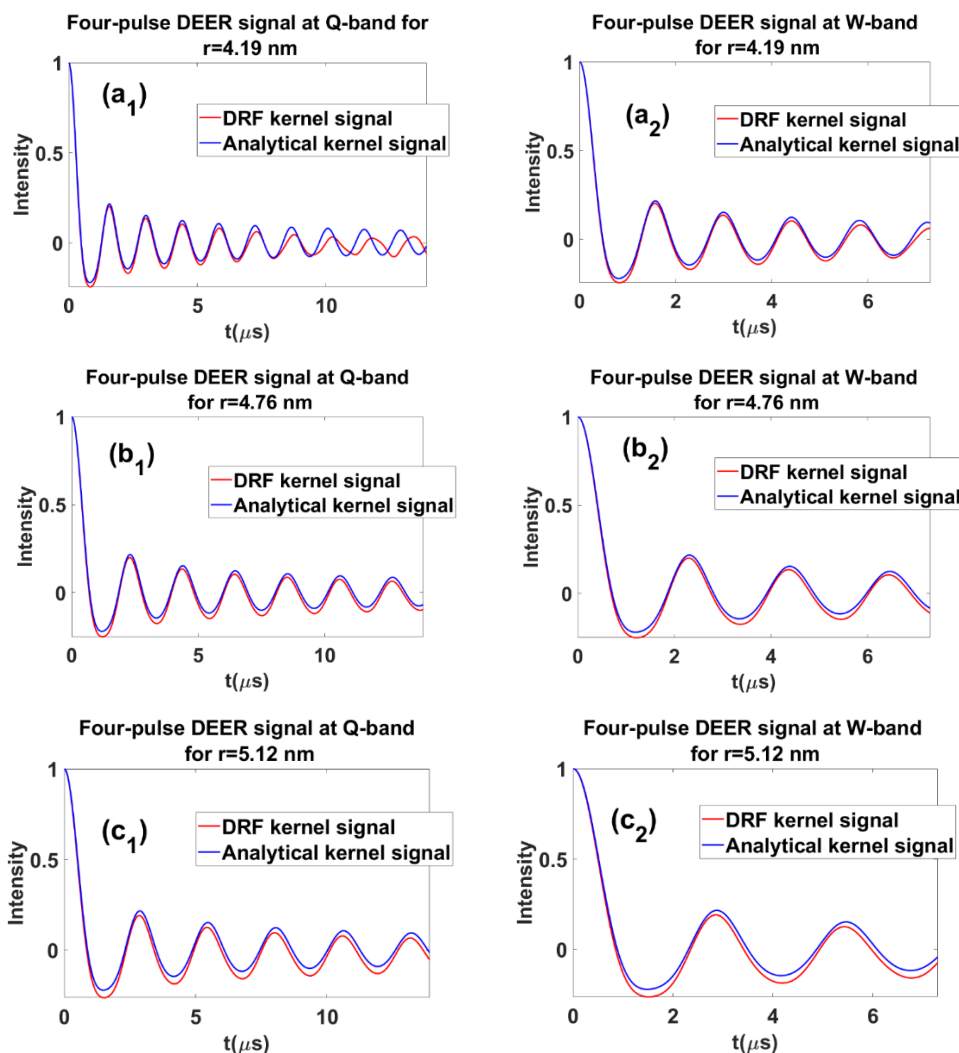
Figure 4.10 The kernel signals calculated using the DRF technique including the ZFS at (a_1) $r = 4.19$ nm; (b_1) $r = 4.76$ nm and (c_1) $r = 5.12$ nm and those calculated with the kernel functions, calculated using the analytical expression for infinite pulse without including the ZFS at (a_2) $r = 4.19$ nm; (b_2) $r = 4.76$ nm and (c_2) $r = 5.12$ nm corresponding to the maximum of the probability of distance distribution as determined from Figs 4.11(a) and 4.12(a), at Q- and W-bands, respectively. The DRF and the analytical kernel signals are shown by red and blue solid lines, respectively. There is seen a significant difference between the two sets of kernel signals.
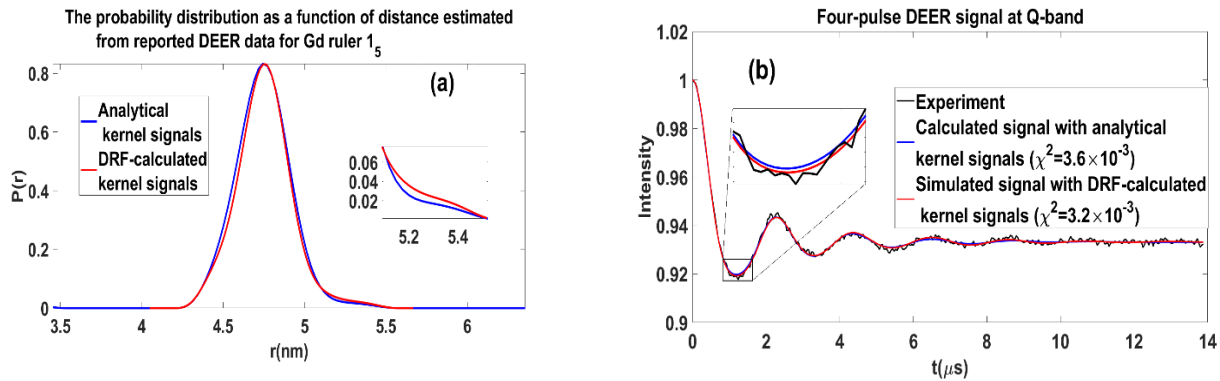
Figure 4.11 The probability distributions as functions of distance, obtained from the experimental data, for Gd ruler 1_5 in D_2O/glycerol-d_8 at Q-band, calculated by *DeerAnalysis* with Tikhonov-regularization using the DRF-calculated basis signals, with finite pulses including the ZFS, shown in red and those obtained using analytical kernel functions with infinite pulses and no ZFS, shown in blue; (b) The time-domain signals, as calculated by *DeerAnalysis* software using the DRF-calculated signals, shown by red solid line, and the time-domain signal, as calculated by *DeerAnalysis* software, obtained by using the analytical kernels, shown by the blue solid line. The inset in (b) amplifies the region around t = 1μs for a better comparison.
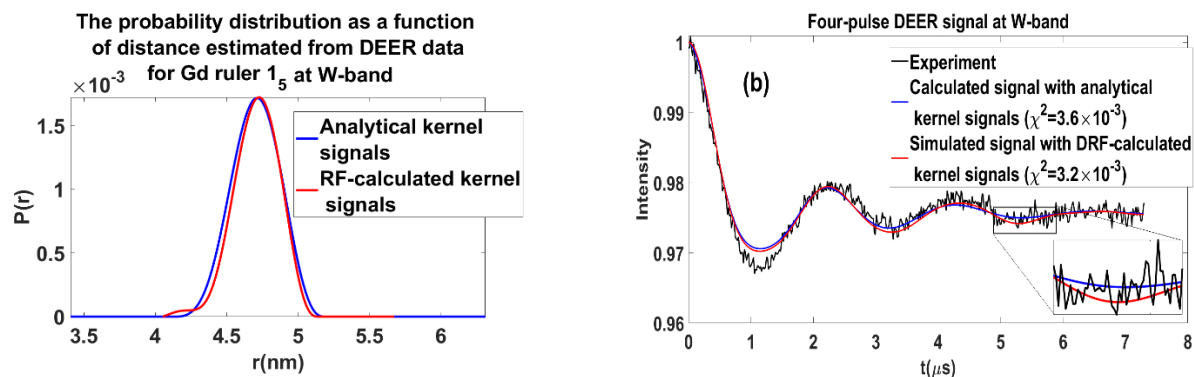
Figure 4.12 The probability distributions as functions of distance, obtained from the experimental data, for Gd ruler 1_5 in D_2O/glycerol-d_8 (7/3 volume ratio) at W-band, calculated by *DeerAnalysis* with Tikhonov-regularization using analytical kernel functions with infinite pulses, shown in blue, and that obtained using the DRF-calculated basis signals, with finite pulses, shown in red; (b) The time-domain signals, as calculated by *DeerAnalysis* software using the analytical kernels, shown by red solid line, and the time-domain signal, as calculated by *DeerAnalysis* software, obtained by using the DRF-calculated signals, shown by the blue solid line. The inset in (b) amplifies the region around t = 5.5μs for a better comparison.

Chapter 5

5. Relaxation in pulsed EPR: thermal variation of spin-Hamiltonian parameters of an electron-nuclear spin-coupled system in a γ-irradiated malonic acid single crystal

In this chapter, the numerical algorithm presented in Sec. 2.1 is exploited to calculate pulsed EPR spin echo correlation spectroscopy (SECSY) and echo-electron-electron double-resonance (echo-ELDOR) signals rigorously in Liouville space taking into account a phenomenological relaxation matrix in single crystal and polycrystalline materials for a spin-coupled electron-nuclear system with the electron spin S= ½ and nuclear spin I= ½. Two models of fluctuation, namely cylindrical and conical models of fluctuations of the spin Hamiltonian parameters are then introduced to calculate the elements of the relaxation matrix quantitively.

The examples considered for illustration here are the same as those considered in by Lee *et. al.* 1993 for the single-crystal case. The sample used is an irradiated malonic-acid crystal (McConnell *et. al.* 1960), wherein an unpaired electron spin $S = 1/2$, is in interaction with a single nucleus, $I = 1/2$, by hyperfine interaction, with the principal axes of the hyperfine tensor $\tilde{A}$ and those of the $\tilde{g}$ matrix assumed to be coincident. The orientations of the crystalline axes X, Y, Z are shown in Figure 5.1. The advantage of choosing the malonic acid radical is that it is a simple S= 1/2, I= 1/2 spin system, which is easy to analyze, and the detailed structural information is available by X-ray crystallography and from previous ESR studies (McConnell *et. al.* 1960).

The CW spectrum shows several HF lines due to different kinds of radicals produced, soon after irradiation, but in aged samples, only two lines are seen (Lee *et. al.* 1993). The strong doublet is due to the HF coupling of the π electron of the α carbon with the α proton of the C-H fragment of the $\circ CH\,(COOH)_2$ radical of malonic acid. The principal axis system of the HF tensor is defined in Ref. 30, and the procedure to identify the axes described therein were used in this study. Figure 5.1 shows the principal axes (x,y,z) of the HF tensor in relation to the structure of the malonic acid radical $\circ CH\,(COOH)_2$.

5.1 Calculation of single crystal and polycrystalline SECSY and echo-ELDOR signal

5.1.1 Spin Hamiltonian for an electron-nuclear spin-coupled system in an irradiated malonic acid crystal

For the specific case of a single nucleus ($I = 1/2$) interacting with an unpaired electron ($S = 1/2$) by the hyperfine interaction, where the HF-interaction matrix has the principal axes coincident with those of the $\tilde{g}$ matrix, the total Hamiltonian can be expressed as the sum of a static Hamiltonian and a pulse Hamiltonian (Lee *et. al.* 1993)

$$\hat{H} = \hat{H}_0 + \hat{H}_1 \tag{5.1}$$

In high-field approximation, non-secular terms are negligible and static Hamiltonian can be written as:

$$\widehat{\mathcal{H}}_0 = \frac{\widehat{H}_0}{\hbar} = CS_z - \omega_n I_z + AS_z I_z + \frac{1}{2} BS_z I_+ + \frac{1}{2} B^* S_z I_- \qquad (5.2)$$

where ω_n is the nuclear Larmor frequency. The coefficients of the spin Hamiltonian in Eq. (5.2) in angular frequency units (Energy unit/$\hbar$, where $\hbar$ is Planck's constant divided by 2π) are expressed as follows (Lee *et. al.* 1993):
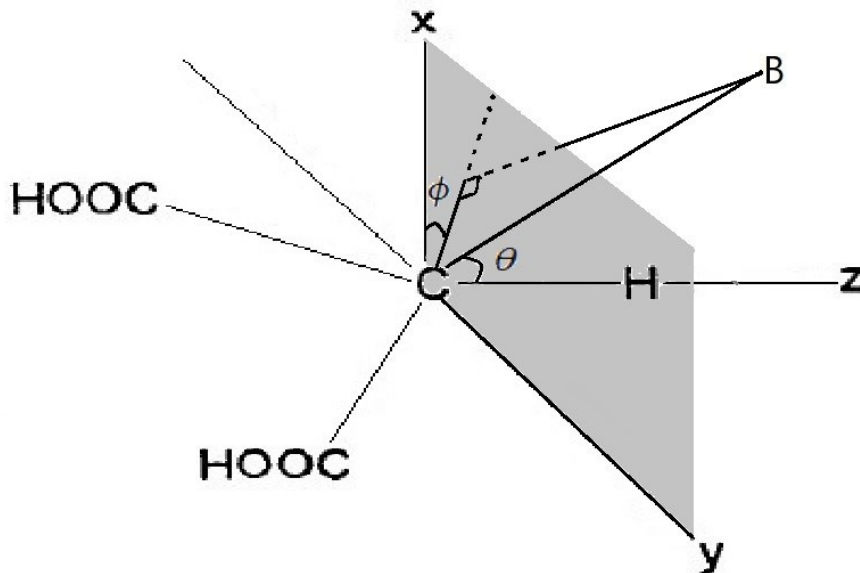
Figure 5.1 Relation of principal axes (x,y,z) of the $\widetilde{g}$ and $\widetilde{A}$ (hyperfine) matrices, assumed coincident to the structure of the malonic acid radical CH(COOH)$_2$ to the. Here, the z axis is along the C-H bond direction and the x- axis is perpendicular to the plane of the three carbon atoms). The direction of the external static field B$_0$ is defined by the angles θ and ϕ, where θ is the angle between B$_0$ and the z axis, and ϕ is the angle between the x axis and the projection of B$_0$ on the xy plane.

$$C = \frac{\beta_e B_0}{h}\left[\bar{g} + F\frac{1}{2}(3\cos^2\beta - 1) + F^{(2)}\sin^2\beta\cos(2\gamma)\right] \qquad (5.3)$$

$$A = -2\pi\left[\bar{a} + D\frac{1}{2}(3\cos^2\beta - 1) + D^{(2)}\sin^2\beta\cos(2\gamma)\right] \qquad (5.4)$$

$$B = -4\pi \left\{ D \frac{3}{4} \sin\beta \cos\beta - D^{(2)} \frac{1}{2} \sin\beta \left[\cos\beta \cos(2\gamma) - i\, sin(2\gamma) \right] \right\} (5.5)$$

and

$$\bar{g} = \frac{1}{3}(g_{xx} + g_{yy} + g_{zz}); \quad \bar{a} = \frac{1}{3}(A_{xx} + A_{yy} + A_{zz});$$

$$F = \frac{2}{3}\left(g_{zz} - \frac{1}{2}(g_{xx} + g_{yy})\right); D = \frac{2}{3}\left(A_{zz} - \frac{1}{2}(A_{xx} + A_{yy})\right); \qquad (5.6)$$

$$F^{(2)} = \frac{1}{2}(g_{xx} - g_{yy}); \quad D^{(2)} = \frac{1}{2}(A_{xx} - A_{yy});$$

In Eq. (5.3) and (5.4), $\bar{g}$ is the isotropic part of the $\tilde{g}$-matrix; $\bar{a}$ is the isotropic part of the A-tensor. (It is noted that in (Lee *et. al.* 1993), there were misprints, which have been corrected in the above equations. In particular, instead of having the factors of 2π in Eq. (5.4) and (5.5), there was the factor $\frac{\gamma_e}{\hbar}$ in both places in (Lee *et. al.* 1993).). The orientations $\Omega(\alpha, \beta, \gamma)$ are the Euler angles which describe the orientations of the principal axes of the $\tilde{g}$-matrix with respect to the static magnetic field (Figure 5.1). The principal axes of the hyperfine matrix $\tilde{A}$ are assumed to be coincident with those of the matrix $\tilde{g}$. Since all the calculations are carried out in the rotating frame, for which the effective field $B = B_{eff} = \mathbf{0}$, the value of C in Eq. (5.3) becomes equal to zero as it is proportional to B.

The pulse Hamiltonian used in the calculation of γ-irradiated malonic acid system is expressed as (Lee *et. al.* 1993):

$$\hat{H}_1 = B_1\gamma_e\left(S_x cos\phi + S_y sin\phi\right)I_n = \frac{\omega}{2}\left(e^{-i\phi}S_+ + e^{i\phi}S_-\right)\mathbf{1}_n \qquad (5.7)$$

In Eq. (5.7), B_1 is the amplitude of the microwave field, γ_e is the electron gyromagnetic factor, ω is the angular frequency of the microwave field, and $\mathbf{1}_n$ is 2×2 unit matrix in nucleus space.

5.1.2 Phenomenological relaxation matrix elements

The Liouville-von Neumann equation in the Liouville space is used to describe the time evolution of the density matrix. The numerical calculations here are performed following the

description given in Sec. 2.1. Using LVN equation, the time domain evolution of the matrix elements of the density matrix, including the relaxation matrix in the Liouville space, can be expressed as (Lee *et. al.* 1993):

$$\frac{d}{dt}\rho_{\alpha\alpha'}(t) = -i\omega_{\alpha\alpha'}\rho_{\alpha\alpha'} - \sum_{\beta\beta'}\widehat{\widehat{R}}_{\alpha\alpha'\beta\beta'}(\rho_{\beta\beta'} - \rho_{0\beta\beta'})\tag{5.8}$$

with

$$\omega_{\alpha\beta} = E_\alpha - E_\beta\tag{5.9}$$

where E_α, E_β are the eigenvalues of the static Hamiltonian, $\widehat{H}_0$, for the electron-nuclear coupled system (S = ½, I = ½) as given by Eq. (5.2).

In Eq. (5.8), $\widehat{\widehat{R}}_{\alpha\alpha'\beta\beta'}$ are the relaxation matrix elements, where α, α', β, β' designate the eigenstates of the Hamiltonian $\widehat{H}_0$. The following specific values for the matrix elements, as given by (Lee *et. al.* 1993) are used here:

$$\widehat{\widehat{R}}_{\alpha\beta,\alpha\beta} = \widehat{\widehat{R}}_{\beta\alpha,\beta\alpha} = -\left(\frac{1}{T_2}\right)_{\alpha\beta} \; ; \; \widehat{\widehat{R}}_{\alpha\alpha,\beta\beta} = W_{\alpha\beta}; \; \widehat{\widehat{R}}_{\alpha\alpha,\alpha\alpha} = -\sum_{\gamma\neq\alpha} W_{\alpha\gamma}\tag{5.10}$$

Otherwise

$$\widehat{\widehat{R}}_{\alpha\beta,\zeta\eta} = 0\tag{5.11}$$

The relaxation pathways among the various eigenstates of the coupled electron-nuclear spin system in the lattice, as defined in the H_0 basis (Lee *et. al.* 1993), are shown in Figure 5.2 below, where a and b indicate the nuclear sublevels coupled to the electronic magnetic quantum number $M_S = 1/2$, and c and d indicate the nuclear sublevels coupled to the electronic magnetic quantum number of $M_S = -1/2$.
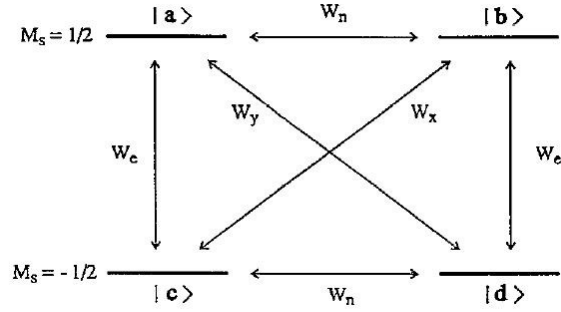
Figure 5.2 The energy levels of an electron-nuclear spin-coupled system

It is assumed, with reference to the above diagram, that (Lee *et. al.* 1993)

$$W_{ab} = W_{ba} = W_{cd} = W_{dc} = W_n$$

$$W_{ac} = W_{ca} = W_{bd} = W_{db} = W_e$$

$$W_{ad} = W_{da} = W_y$$

$$W_{bc} = W_{cb} = W_x \tag{5.12}$$

and

$$(T_2)_{ac} = (T_2)_{bd} = (T_2)_{ad} = (T_2)_{bc} = T_{2e}$$

$$(T_2)_{ab} = (T_2)_{cd} = T_{2n} \tag{5.13}$$

All matrix elements $\widehat{\widehat{R}}_{\alpha\beta,\zeta\eta} = 0$, except for the non-zero elements of the relaxation matrix corresponding to the above diagram. Specifically, the non-zero elements of the relaxation matrix are (Lee *et. al.* 1993)

$$\widehat{\widehat{R}}_{ab,ab} = \widehat{\widehat{R}}_{ba,ba} = \widehat{\widehat{R}}_{cd,cd} = \widehat{\widehat{R}}_{dc,dc} = -\frac{1}{T_{2n}}$$

$$\widehat{\widehat{R}}_{ac,ac} = \widehat{\widehat{R}}_{ca,ca} = \widehat{\widehat{R}}_{ad,ad} = \widehat{\widehat{R}}_{da,da} = \widehat{\widehat{R}}_{bc,bc} = \widehat{\widehat{R}}_{cb,cb} = \widehat{\widehat{R}}_{bd,bd} = \widehat{\widehat{R}}_{db,db}$$
$$= -\frac{1}{T_{2e}}$$

$$\widehat{\widehat{R}}_{aa,aa} = \widehat{\widehat{R}}_{dd,dd} = -W_e - W_n - W_y; \; \widehat{\widehat{R}}_{bb,bb} = \widehat{\widehat{R}}_{cc,cc} = -W_e - W_n - W_x$$

$$\widehat{\widehat{R}}_{aa,bb} = \widehat{\widehat{R}}_{bb,aa} = \widehat{\widehat{R}}_{cc,dd} = \widehat{\widehat{R}}_{dd,cc} = W_n + \frac{\omega_{HE}}{4}$$

$$\widehat{\widehat{R}}_{aa,cc} = \widehat{\widehat{R}}_{bb,dd} = \widehat{\widehat{R}}_{cc,aa} = \widehat{\widehat{R}}_{dd,bb} = W_e + \frac{\omega_{HE}}{4}$$

$$\widehat{\widehat{R}}_{bb,cc} = \widehat{\widehat{R}}_{cc,bb} = W_x - \frac{\omega_{HE}}{4}; \; \widehat{\widehat{R}}_{aa,cc} = \widehat{\widehat{R}}_{dd,aa} = W_y - \frac{\omega_{HE}}{4};$$

$$(5.14)$$

Here $\omega_{HE} = 0$ as used by (Lee *et. al.* 1993). It is noted that the values of the relexation matrix elements, including W_e, W_n, W_x, W_y are chosen phenomenologically here.

5.1.3 Pulse sequences and coherence pathways

The pulse sequences and the relevant coherence pathways are shown in Figure 5.3and Figure 5.4, respectively, for SECSY and echo-ELDOR experiments.
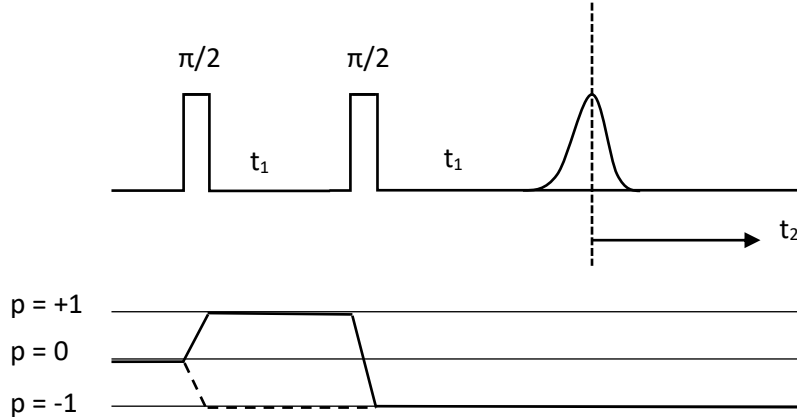
Figure 5.3 (Top) Pulse sequence for obtaining SECSY signal. The t_1 time between the two pulses and t_2 time from the echo are stepped. (Bottom) The coherence pathway S_{c-} used for calculating SECSY signal for an unpaired electron (S = ½) interacting with a single nucleus (I = ½) is shown by the solid line.
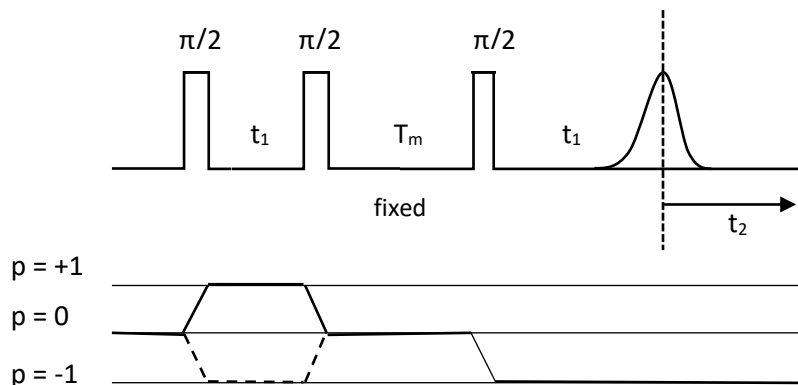
Figure 5.4 (Top) Pulse sequence for obtaining echo- ELDOR signal. The t_1 time between the first two pulses and t_2 time from the echo are stepped. Here T_m is the mixing time. (Bottom) The coherence pathways used for calculating 2D- ELDOR signal for an unpaired electron (S = ½) interacting with a single nucleus (I = ½) is shown by the solid line.

Selection of coherent pathways by appropriate selection of the corresponding elements of the density matrix. For single electron-nuclear coupled system with electron spin S=1/2, nuclear spin I=1/2, the dimension of the coupled spin Hamiltonian is $(2S_1 + 1) \times (2I_1 + 1) = 4$, so that the density matrix in the electron-nuclear spin-coupled direct product space the total density matrix $\rho = \rho_e \otimes \rho_n$, where ρ_e and ρ_n are, respectively, the density matrices in the electronic and nuclear subspaces, In the following, the coherence order p represents the transverse magnetization corresponding to the spins rotating in a plane perpendicular to the external field. The matrix elements for the various coherence orders are defined as follows, which will be consistent with the experimental technique to acquire a particular coherent pathway.

(i) For the pathway with the coherence order $p = 1$, all matrix elements of the density matrix, ρ_e , are put equal to zero, except for those corresponding to $\rho_e(1,2)$.

(ii) For the pathway with the coherence order $p = 0$ all matrix elements of the density matrix, ρ_e , are put equal to zero, except for those corresponding to $\rho_e(1,1)$ and $\rho_e(2,2)$.

(iii) For the pathway with coherence order $p = -1$, all matrix elements of the density matrix, ρ_e , are put equal to zero, except for those corresponding to $\rho_e(2,1)$.

5.1.4 Gaussian inhomogeneous broadening effect

In accordance with that used in (Lee *et. al.* 1993), the Gaussian inhomogeneous broadening effect in the frequency-domain along ω_2 (= $2\pi\nu$), corresponding to the step time t_2 (Figure 5.3 and Figure 5.4), is taken into account by the following time-domain dependence:

$$f_b(t_2) = f(t_2)\frac{1}{\sqrt{2\pi}\Delta}\int_{-\infty}^{\infty} exp\left(-\frac{\nu^2}{2\Delta^2}\right)e^{-i2\pi\nu t_2}d\nu = f(t_2)e^{-2(\pi\Delta t_2)^2} \qquad (5.15)$$

where $f_b(t_2)$ is the Gaussian-broadened signal along t_2 and Δ is the Gausssian inhomogeneous broadening parameter expressed in frequency units.

 5.1.5 Illustrative Examples

The examples considered for illustration here are the same as those considered in (Lee *et. al.* 1993) for the single-crystal case. In addition, they are generalized to cover polycrystalline case. The sample used is an irradiated malonic-acid crystal (McConnell *et. al.* 1960), wherein an unpaired electron spin $S = 1/2$, is in interaction with a single nucleus, $I = 1/2$, by hyperfine interaction, with the principal axes of the hyperfine tensor $\tilde{A}$ and those of the $\tilde{g}$ matrix assumed to be coincident. The orientations of the crystalline axes X, Y, Z are shown in Figure 5.1, whose caption describes the angles (θ, ϕ), which can be related to the Euler angles: $\eta = (\alpha, \beta, \gamma)$.

The values of the various parameters used are as follows: each $\pi/2$ pulse is of duration *5ns*; the nuclear Zeeman frequency $\omega_n = 14.5MHz$; the principal values of the $\tilde{g}$ and $\tilde{A}$ - matrices are: $\tilde{g} = (g_{xx}, g_{yy}, g_{zz}) = (2.0026, 2.0035, 2.0033)$; $\tilde{A} = (A_{xx}, A_{yy}, A_{zz}) = (-61.0MHz, -91.0MHz, -29.0MHz)$; the Gaussian inhomogeneous broadening $\Delta= 4MHz$ for SECSY signal and $\Delta= 5MHz$ for ELDOR signal.

The input values used for the parameters describing the relaxation matrix in the simulation of the time-domain signals are as follows (the same as those used in Lee *et. al.* 1993): electron spin–spin relaxation time, $T_{2e} = 0.900\mu s$; nuclear spin–spin relaxation time, $T_{2n} = 22\mu s$; the inverse electron spin–spin relaxation time, $W_e = 0.0167\mu s^{-1}$; the inverse nuclear spin–spin relaxation time, $W_n = 0.00714\mu s^{-1}$; the inverse electron nuclear spin–spin relaxation time, $W_x = 0.00617\mu s^{-1}$; the inverse electron-nuclear spin–spin relaxation time $W_x = W_y$; the inverse Heisenberg exchange relaxation time, $\omega_{HE} = 0.0\mu s^{-1}$.

The *single-crystal* SECSY and echo-ELDOR time-domain signals were calculated here for illustration for the orientation $(\theta, \phi) = (30°, 0°)$ in the zx-quadrant, so that $(\alpha, \beta, \gamma) = (0, -\theta, 0)$ (Lee *et. al.* 1993) as shown in Figure 5.5 and Figure 5.6, respectively. The *powder* simulations are included in Figure 5.7 and Figure 5.8, respectively for SECSY and echo-ELDOR signals without Gaussian broadening, and in Figure 5.9 and Figure 5.10, respectively, with Gaussian broadening.

	Simulation - Time-domain signal (this work)	Simulation – Fourier transform (this work)
Without Gaussian inhomogeneous broadening		
With Gaussian inhomogeneous broadening		

Experimental Spectrum With Gaussian Broadening
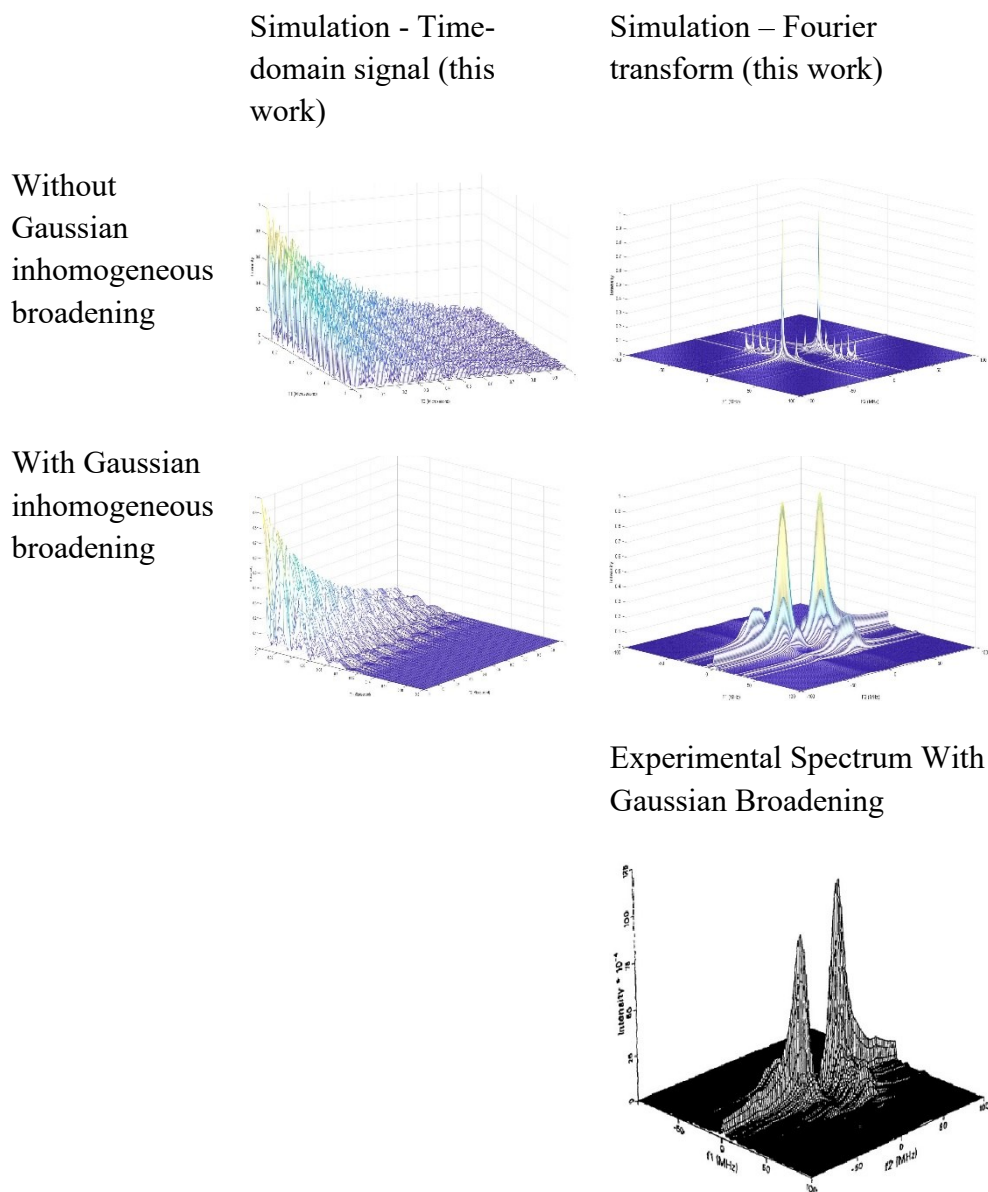
Figure 5.5 Simulated single-crystal SECSY time-domain signal with relaxation taken into account at $(\theta, \phi)= (30°, 0°)$ orientation of the external magnetic field with respect to the crystal axes in the zx-quadrant (Lee *et. al.* 1993), shown in the left column. The corresponding FT figures are shown in the column to the right. A Gaussian inhomogeneous broadening width $\Delta=4$ MHz in accordance with (Lee *et. al.* 1993) has been added along the t_2 axis in calculating the Fourier transform as shown in the second row for the time domain and FT signals. The corresponding SECSY experimental spectrum as extracted from (Lee *et. al.* 1993) is shown in the bottom row for comparison.

Simulation Time-domain
signal (this work)

Simulation – Fourier transform
(this work)

Without Gaussian
inhomogeneous
broadening

With Gaussian
inhomogeneous
broadening

Experimental Spectrum With
Gaussian Broadening
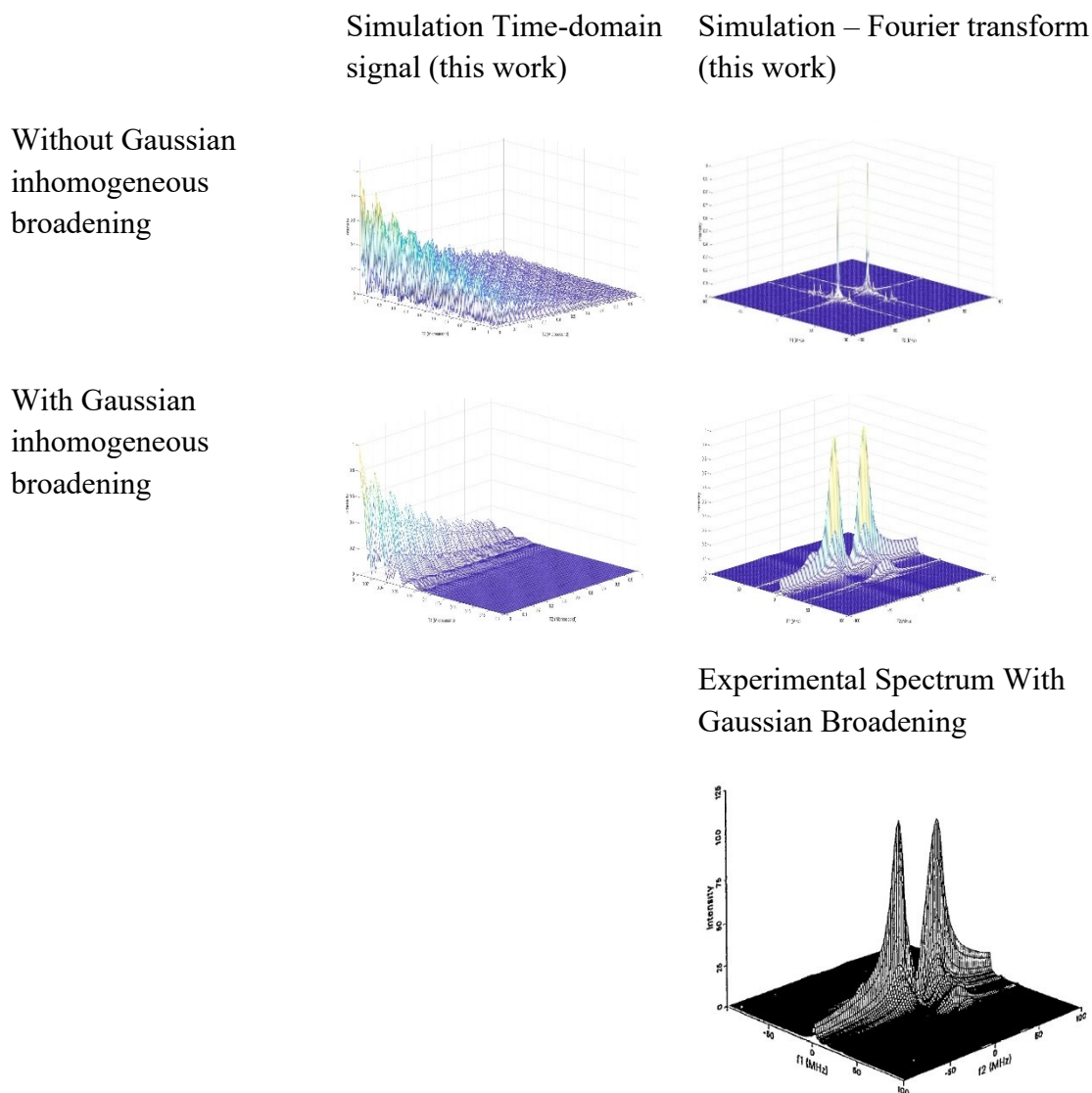
Figure 5.6 Simulated single-crystal echo-ELDOR time-domain signal with relaxation taken into account at $(\theta, \phi) = (30°, 0°)$ orientation of the external magnetic field with respect to the crystal axes in the zx-quadrant, with the mixing times $T_m = 40$ μs, shown in the left column. The corresponding FT figures are shown in the column to the right. A Gaussian inhomogeneous broadening width $\Delta = 5$ MHz has been added along the t_2 axis in calculating the Fourier transform as shown in the bottom row for the time domain and FT signals. The corresponding echo-ELDOR experimental spectrum as extracted from (Lee *et. al.* 1993) is shown in the bottom row for comparison.

114
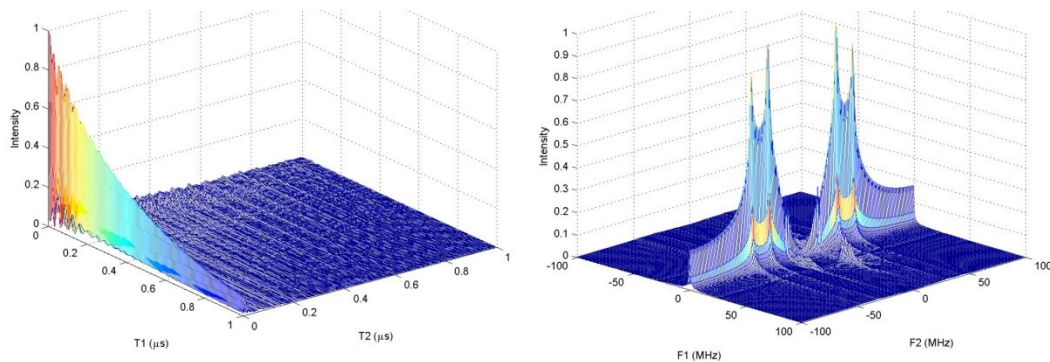
Figure 5.7 SECSY polycrystalline spectrum, for the (θ, ϕ) grid: n_{Theta} = 180, n_{Phi} = 180, without Gaussian inhomogeneous broadening. The simulated time-domain signal is shown at the left and the corresponding FT is shown on the right.
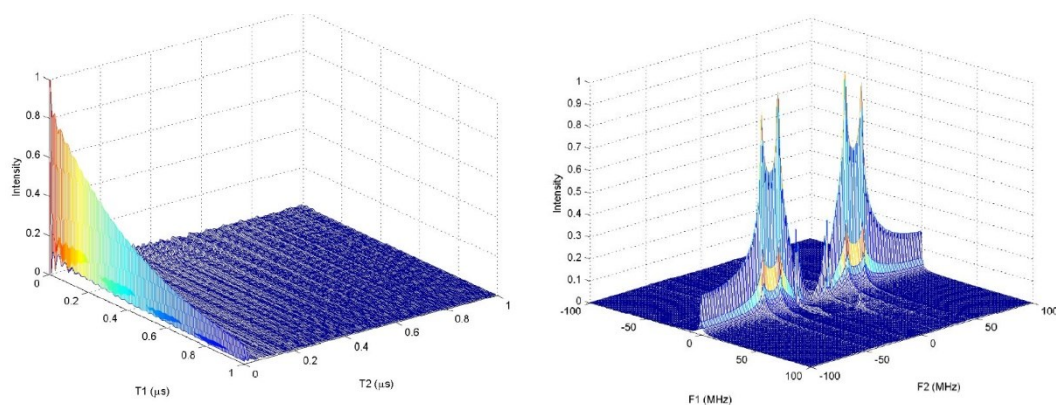
Figure 5.8 Echo-ELDOR polycrystalline spectrum, for the (θ, ϕ) grid: n_{Theta} = 180, n_{Phi} = 180, without Gaussian inhomogeneous broadening. The simulated time-domain signal is shown at the left and the corresponding FT is shown on the right. The mixing time, T_m, is 40 µs.
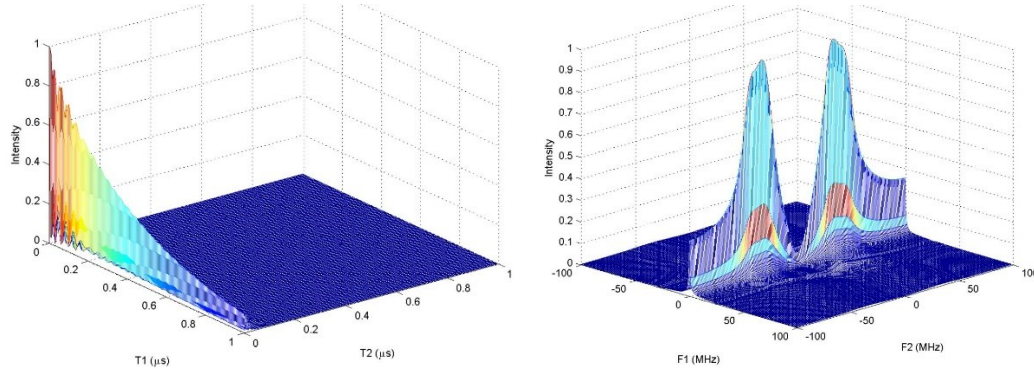
Figure 5.9 SECSY polycrystalline spectrum, for the (θ, ϕ)grid: $n_{Theta} = 180$, $n_{Phi} = 180$, with Gaussian inhomogeneous broadening of Δ=4 MHz added. The simulated time-domain signal is shown at the left and the corresponding FT is shown on the right.
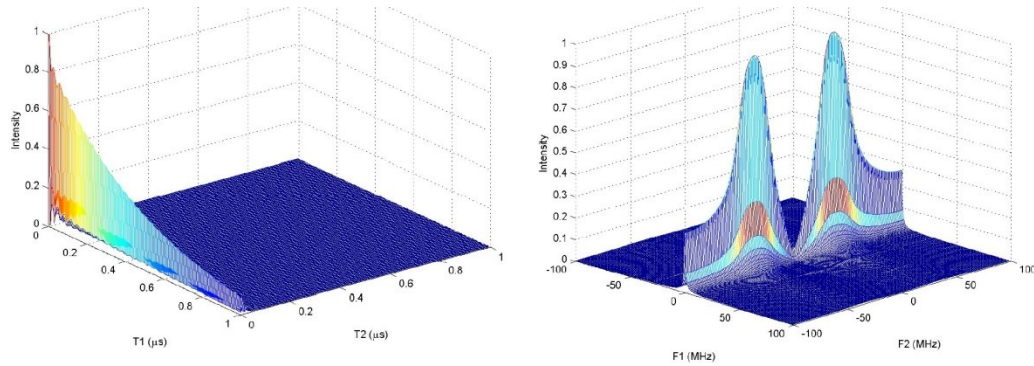
Figure 5.10 Echo-ELDOR polycrystalline spectrum, for the (θ, ϕ)grid: $n_{Theta} = 180$, $n_{Phi} = 180$, with Gaussian inhomogeneous broadening of Δ=5 MHz added. The simulated time-domain signal is shown at the left and the corresponding FT is shown on the right. The mixing time, T_m, is 40 μs.

It is noted that in the simulations carried out here, the static spin Hamiltonian and the relaxation matrix are ignored during the pulses. However, for a more rigorous simulation, one should include them during the pulses. To investigate the effects of including the static spin Hamiltonian, H_0 (Eq. (5.1)) and the relaxation matrix during the pulses, the 1D Fourier transform of the SECSY and echo-ELDOR signals are plotted in Figure 5.11 Comparison of SECSY 1D spectrum in the Fourier domain along f_2 for the slice along f_1=0 for four different cases: i) Without H_0 and relaxation ii) Without H_0 but with relaxation included iii) With H_0 without relaxation iv) With H_0 and with relaxation during the pulses. and Figure 5.12, respectively, for the four various cases: i) Without H_0 and without relaxation during the pulses; ii) Without H_0 but

116

with relaxation during the pulses; iii) with H_0 but without relaxation during the pulses and iv) With both H_0 and relaxation during the pulses.
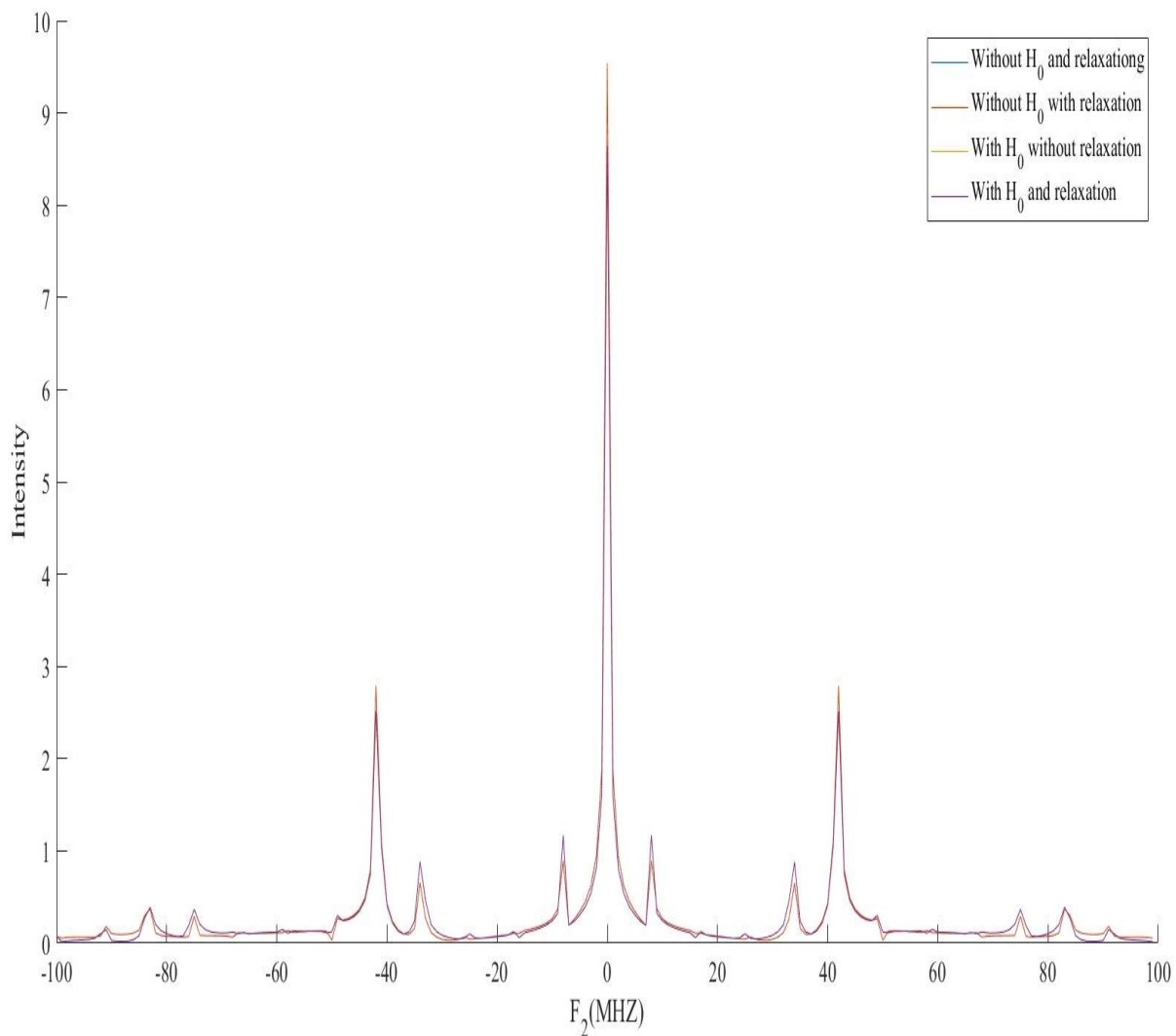
Figure 5.11 Comparison of SECSY 1D spectrum in the Fourier domain along f_2 for the slice along f_1=0 for four different cases: i) Without H_0 and relaxation ii) Without H_0 but with relaxation included iii) With H_0 without relaxation iv) With H_0 and with relaxation during the pulses.
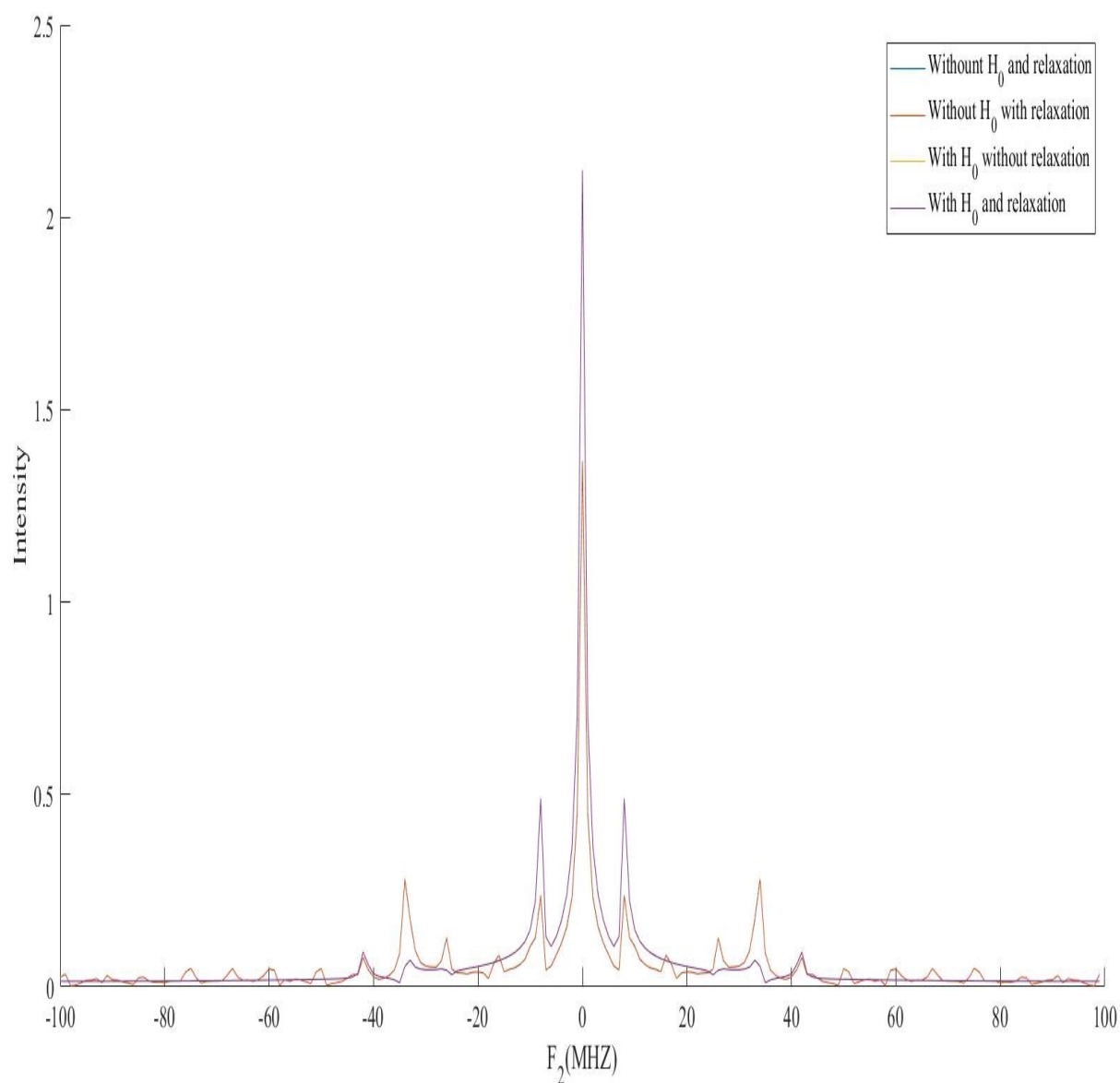
Figure 5.12 Comparison of echo-ELDOR 1D spectrum in the Fourier domain along f_2 for the slice along $f_1=0$ for four different cases: i) Without H_0 and relaxation ii) Without H_0 but with relaxation included iii) With H_0 without relaxation iv) With H_0 and with relaxation during the pulses.

It is seen from Figure 5.11 Comparison of SECSY 1D spectrum in the Fourier domain along f_2 for the slice along $f_1=0$ for four different cases: i) Without H_0 and relaxation ii) Without H_0 but with relaxation included iii) With H_0 without relaxation iv) With H_0 and with relaxation during the pulses. and Figure 5.12 that inclusion of the static Hamiltonian during the pulses does indeed change the spectra significantly, which enhances as the number of pulses in an experiment increase (SECSY-2 versus echo-ELDOR-3). On the other hand, taking into account the relaxation during the pulses does not have any significant effect on the spectra, since the spin-lattice and spin-spin relaxation times (T_1 and T_2) are several orders of magnitude longer than the duration of the pulses.

5.2 Quantitative calculation of relaxation matrix elements in a γ-irradiated malonic acid single crystal

In previous section, the original theory of two-dimensional (2D)-EPR with nuclear modulation introduced by (Gamliel and Freed 1990) was extended to treat the problem in Liouville space, and the combined effect of nuclear modulation and spin relaxation was taken into account to calculate SECSY and echo-ELDOR signals. However, the elements of the relaxation matrix used in the previous section were defined in a phenomenological manner. It is the purpose of this section to advance the theory further to treat relaxation due to molecular fluctuation as caused by thermal motion more rigorously for the coupled electron-nuclear system with electron spin S= ½ and nuclear spin I = ½ using i) the linear approximation model of fluctuation of spin- Hamiltonian parameters δ(SHP) proposed by (Frezzato *et al*. 2004), wherein the higher-order terms in fluctuation are neglected and ii) conical model governed by a restoring harmonic-oscillator potential wherein on average, the fluctuations of the tip of the director axis of the malonic acid then take place in a cone about the symmetry axis. The amplitude of the fluctuation of the SHP is here related to the fluctuation of the local director of the malonic-acid molecule, described by its orientation, assuming the average orientation of the director to be along the molecular axis, leading to the calculation of the relaxation matrix. Accordingly, the relaxation-matrix elements used in Sec. 5.1 for a coupled electron-nuclear system are here replaced by those calculated taking into account the fluctuation of SHP to treat the effect of relaxation on a pulsed-EPR signal.

5.2.1 Spin Hamiltonian due to thermal fluctuation

The time-dependent matrix elements for the four-level $S = 1/2$; $I = 1/2$ spin system of the Hamiltonian, $\widehat{H}_1(t)$, causing relaxation, can be written in general form, in the eigenvalue basis, as follows (Lee *et. al.* 1993):

$$\widehat{H}_1(t)_{\gamma\delta} = \sum_p F^p(t)A^p{}_{\gamma\delta}; \ \gamma, \delta = a, b, c, d; p = 1,10 \tag{5.16}$$

where *a, b, c, d* refer to the four energy levels of the spin Hamiltonian given in Eq. (5.2), defined by their energy as

$$E_a = \frac{C}{2} + \frac{1}{2}\omega_\alpha; \quad E_b = \frac{C}{2} - \frac{1}{2}\omega_\alpha; \quad E_c = -\frac{C}{2} - \frac{1}{2}\omega_\beta; \quad E_d = -\frac{C}{2} + \frac{1}{2}\omega_\beta \quad (5.17)$$

where ω_α, ω_β are defined as follows:

$$\omega_\alpha = \left[\left(\omega_n - \frac{A}{2}\right)^2 + \left(\frac{B}{2}\right)^2\right]^{1/2}; \quad \omega_\beta = \left[\left(\omega_n + \frac{A}{2}\right)^2 + \left(\frac{B}{2}\right)^2\right]^{1/2} \quad (5.18)$$

and the eigenvectors are (Lee *et. al.* 1993):

$$|a\rangle = [c_1 \quad -c_2 \quad 0 \quad 0]^T; \quad |b\rangle = [c_2 \quad c_1 \quad 0 \quad 0]^T$$
$$|c\rangle = [0 \quad 0 \quad c_3 \quad -c_4]^T; \quad |d\rangle = [0 \quad 0 \quad c_4 \quad c_3]^T \quad (5.19)$$

In Eq. (5.19) the superscript T denotes the transpose, and the coefficient $c_i, i = 1, \cdots, 4$ are:

$$c_1 = \frac{1}{\sqrt{2}}\left[1 \pm \frac{(A/2) - \omega_n}{\omega_\alpha}\right]^{1/2}; \quad c_2 = -\frac{1}{\sqrt{2}}\left[1 \mp \frac{(A/2) - \omega_n}{\omega_\alpha}\right]^{1/2};$$

$$c_3 = \frac{1}{\sqrt{2}}\left[1 + \frac{(A/2) + \omega_n}{\omega_\beta}\right]^{1/2}; \quad c_4 = -\frac{1}{\sqrt{2}}\left[1 - \frac{(A/2) + \omega_n}{\omega_\beta}\right]^{1/2} \quad (5.20)$$

Here ω_n is the nuclear Larmor frequency and A, B are the coefficients of the $S_z I_z$ and $S_z I_\pm$ spin operators given in Eq. (5.2) . It is noted that ω_α, ω_β and c_i depend on the molecular orientation, because of the dependence of A and B on the Euler angles.

In Eq. (5.16), A^p are the spin operators in the laboratory frame that appear in the spin Hamiltonian, which are orientation dependent and are listed in Table 5.1, and $F^p(t)$ are functions of spatial variables, which are, in fact, the time-dependent fluctuating parts of the spin-Hamiltonian, $\delta(SHP)$, as listed below for the various $F^p(t)$ terms in the spin Hamiltonian (5.2):

$$F^1(t) = \frac{\beta_e B_0}{\hbar} \delta g;$$

$$F^2(t) = \delta F \frac{1}{2}(3\cos^2\beta - 1) + \delta F^{(2)} \sin^2\beta \cos(2\gamma)$$

$$F^3(t) = \delta F \frac{3}{8}\sin(2\beta) - \delta F^{(2)} \frac{1}{4}\sin(2\beta)\cos(2\gamma)$$

$$F^4(t) = -\frac{\gamma_e}{\hbar} \delta a;$$

$$F^6(t) = \delta D \frac{1}{2}(3\cos^2\beta - 1) + \delta D^{(2)}\sin^2\beta\cos(2\gamma)$$

$$F^8(t) = \delta D \frac{3}{8}\sin(2\beta) - \delta D^{(2)}\frac{1}{4}\sin(2\beta)\cos(2\gamma)$$

$$F^{10}(t) = \delta D \frac{3}{8}\sin^2 - \delta D^{(2)}\frac{1}{4}(1 + \cos^2\beta)\cos(2\gamma) \tag{5.21}$$

$$F^5(t) = F^7(t) = F^9(t) = 0;$$

It is noted that in the above expressions the interaction constants (δg, δa, δF, δD, $\delta F^{(2)}$, $\delta D^{(2)}$) are time dependent, representing the deviations from the respective average values e.g. $\delta g = g(t) - \bar{g}$.

The diagonal elements of the T_2-type relaxation in Liouville space are expressed as (Lee *et. al* 1993):

$$(T_2^{-1})_{\alpha\beta} = -R_{\alpha\beta\alpha\beta}$$

$$= \int_0^\infty d\tau\, \overline{\omega_{\alpha\beta}(t)\omega_{\alpha\beta}(t+\tau)} + \frac{1}{2}\left(\sum_{\gamma\neq\alpha} W_{\alpha\gamma} + \sum_{\gamma\neq\beta} W_{\beta\gamma}\right) \tag{5.22}$$

where the time-dependent values of $\omega_{\alpha\beta}(t) = H_1(t)_{\alpha\alpha} - H_1(t)_{\beta\beta}$, which are stochastic, and thus only their time-correlation values are estimated, as shown below.

The integral and the transition probabilities $W_{\alpha\gamma}$ in Eq. (5.22) are (Lee *et. al.* 1993):

$$\int_0^\infty d\tau\, \overline{\omega_{\alpha\beta}(t)\omega_{\alpha\beta}(t+\tau)}$$

$$= \sum_{q,r}(A_{\alpha\alpha}^q - A_{\beta\beta}^q)(A_{\alpha\alpha}^r - A_{\beta\beta}^r) \times \int_{-\infty}^\infty d\tau\, \overline{F^q(t)F^{r*}(t+\tau)} \tag{5.23}$$

$$W_{\alpha\gamma} = R_{\alpha\alpha,\gamma\gamma} = \sum_{q,r} A_{\alpha\gamma}^q A_{\gamma\alpha}^r \times \int_{-\infty}^\infty d\tau\, \overline{F^q(t)F^{r*}(t+\tau)}\, e^{-i\,\omega_{\alpha\gamma}\tau} \tag{5.24}$$

Calculation of the non-zero elements of the relaxation matrix, $R_{\alpha\beta\alpha\beta}$, in Eq. (2.3) due to the fluctuating perturbation can be carried out by considering the auto-correlation function, $\overline{F^q(t)F^{r*}(t+\tau)}$, between the fluctuating parts of the spin Hamiltonian at times $t = 0$ and $t = \tau$. According to Eq (5.21)., all required autocorrelation functions can be expressed in terms of the $\delta(SHP)$s: δg, δA, δD. $\delta D^{(2)}$, δF. $\delta F^{(2)}$, which are here calculated using i) cylindrical model of fluctuation and ii) the conical model of fluctuation. The procedure to calculate $\delta(SHP)$ exploiting the two models is described in Secs. 5.2.2 and 5.2.3 below.

A^q	$|A_{ac}|^2$	$|A_{bd}|^2$	$|A_{ad}|^2$	$|A_{bc}|^2$	$|A_{ab}|^2$	$|A_{cd}|^2$	$|A_{aa}|^2$, $|A_{bb}|^2$	$|A_{cc}|^2$, $|A_{dd}|^2$
S_z							$\frac{1}{4}$	$\frac{1}{4}$
S_z							$\frac{1}{4}$	$\frac{1}{4}$
$S_+ + S_-$	m_1^2	m_1^2	m_1^2	m_1^2				
$S_z I_z$					$\frac{1}{4}[Re(c_1^* c_2)]^2$	$\frac{1}{4}[Re(c_3^* c_4)]^2$	$\frac{1}{16}(|c_1|^2 - |c_2|^2)^2$	$\frac{1}{16}(|c_3|^2 - |c_4|^2)^2$
$\frac{1}{2}(S_+I_- + S_-I_+)$	$\frac{1}{4}|c_2^* c_3|^2$	$\frac{1}{4}|c_1^* c_4|^2$	$\frac{1}{4}|c_2^* c_4|^2$	$\frac{1}{4}|c_1^* c_3|^2$				
$S_z I_z$					$\frac{1}{4}[Re(c_1^* c_2)]^2$	$\frac{1}{4}[Re(c_3^* c_4)]^2$	$\frac{1}{16}(|c_1|^2 - |c_2|^2)^2$	$\frac{1}{16}(|c_3|^2 - |c_4|^2)^2$
$-\frac{1}{4}(S_+I_- + S_-I_+)$	$\frac{1}{16}|c_2^* c_3|^2$	$\frac{1}{16}|c_1^* c_4|^2$	$\frac{1}{16}|c_2^* c_4|^2$	$\frac{1}{16}|c_1^* c_3|^2$				
$S_z I_+ + S_z I_-$					$\frac{1}{4}(|c_1|^2 - |c_2|^2)^2$	$\frac{1}{4}(|c_3|^2 - |c_4|^2)^2$	$[Re(c_1^* c_2)]^2$	$[Re(c_3^* c_4)]^2$
$S_+I_z + S_-I_z$	$\frac{1}{4}|c_1^* c_3 - c_2^* c_4|^2$	$\frac{1}{4}|c_1^* c_3 - c_2^* c_4|^2$	$\frac{1}{4}|c_1^* c_4 + c_2^* c_3|^2$	$\frac{1}{4}|c_1^* c_4 + c_2^* c_3|^2$				
$S_+I_+ + S_-I_-$	$|c_1^* c_4|^2$	$|c_2^* c_3|^2$	$|c_1^* c_3|^2$	$|c_2^* c_4|^2$				

Table 5.1 Illustration of the various spin operators in the laboratory frame. The m_1 and m_2 terms are defined as $m_1 = c_1 c_3 + c_2 c_4$, $m_2 = c_1 c_4 - c_2 c_3$.

5.2.2 Cylindrical model of fluctuation for calculation of $\delta(SHP)$

The average director frame ADF = (x; y; z), of a γ-irradiated malonic-acid molecule, is shown in Figure 5.13, with the x axis being chosen along the average orientation of the director. The unit vector along the instantaneous orientation of the director will be denoted by the unit vector **n**, with the property that the averages of fluctuation of the director in the transverse, y and z directions, is zero: $\bar{n}_\perp = 0$. Now, the normalized **n** can be expressed as (see Figure 5.13)

$$\boldsymbol{n} = \sqrt{1 - 2\,\overline{n^2}_\perp}\ \boldsymbol{i} + n_\perp \boldsymbol{j} + n_\perp \boldsymbol{k} \qquad (5.25)$$

where $n_\perp$ is the time-dependent fluctuating components of the director in the y and z directions and **i; j; k** are the unit vectors along the x; y; z axes, respectively. Choosing the ADF, with the y axis being coincident with the Y axis of the laboratory frame (LF), as shown in Figure 5.14, the transformation from the LF frame to the ADF frame can be specified by the Euler angles $\Omega(\alpha, \beta, \gamma) = (0, -\theta, 0)$ in agreement with the echo-ELDOR experiment in Lee $et.\ al.$ 1993), where θ is the angle between the static magnetic field B_0 (assumed to be along the Z axis of the LF and the z-axis of ADF; the average director axis, $\bar{n}$ is assumed to be along the x-axis of ADF, coincident with the principal-axes of g and A matrices.

122
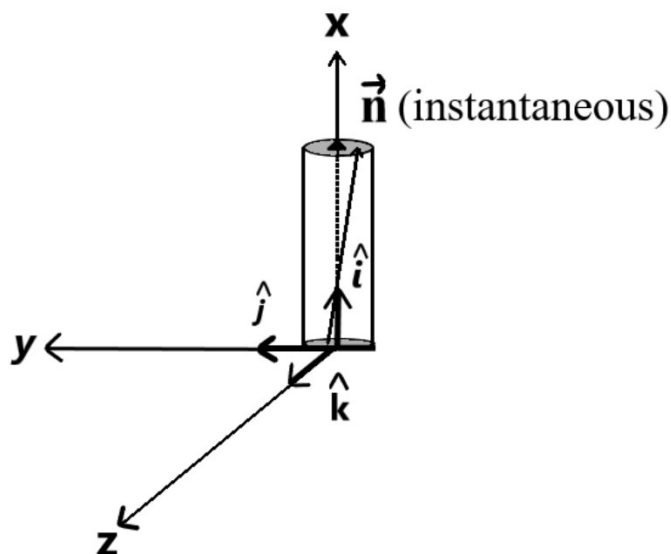
Figure 5.13 The fluctuation of the director of the molecule. The directors fluctuate in such a way that the end points remain on the upper and bottom circular ends to the cylinder. The vector along A refers to the average director along the symmetric axis (x).
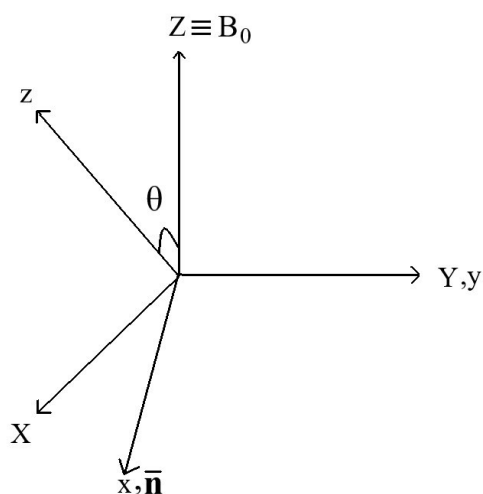
Figure 5.14 Relative orientations of the laboratory frame (**X,Y,Z**) and the average director frame (**x,y,z**). The Euler angles $(0,\theta,0)$ relate the two frames. Here B_0 denotes the external magnetic field and $\bar{n}$ denotes the average orientation of the director axis.

At time scales longer than the correlation time, the spin Hamiltonian, averaged over the molecular orientations, can be used in the relevant LVN equation. Such an average spin Hamiltonian is constructed by inserting the fluctuating g - and A- matrices which can be expressed in ADF, in general form, ($\sigma = g$ or A) as

$$\sigma = \sigma_\perp \mathbb{1} + (\sigma_\parallel - \sigma_\perp + \Delta\sigma_\perp \, \epsilon) \, \boldsymbol{m} \otimes \boldsymbol{m} + \Delta\sigma_\perp \, \epsilon \tag{5.26}$$

where $\sigma_\parallel = \sigma_{xx}$ and $\sigma_\perp = \frac{1}{2}(\sigma_{yy} + \sigma_{zz})$, denoting the partially averaged fluctuating components parallel and perpendicular of those matrices, respectively, to the local director (x-axis); $\Delta\sigma_\perp$ is the rhombic parameter denoted as $\Delta\sigma_\perp = 1/2(\sigma_{yy} - \sigma_{zz})$, $\otimes$ stands for the outer product, $\mathbb{1}$ is the diagonal 3×3 unit matrix, and ϵ is the matrix that defines the anisotropy in the x-y plane, as defined below

$$\epsilon = \begin{pmatrix} 0 & 0 & 0 \\ 0 & 1 & 0 \\ 0 & 0 & -1 \end{pmatrix} \tag{5.27}$$

In Eq. (5.26),

$$\boldsymbol{m} = \sqrt{1 - 2\,\overline{m^2}_\perp} \; \boldsymbol{i} + m_\perp \boldsymbol{j} + m_\perp \boldsymbol{k} \tag{5.28}$$

where $m_\perp = f\, n_\perp$, translates the spatial fluctuation into the fluctuation of g- and A- matrices, assuming the same proportionality factor, f, for both.

In writing Eq. (5.26), it is assumed that the fluctuations in the g- and A-matrices are due to their anisotropy (Kuprov *et. al.* 2007 and Dubinskii *et. al.* 1994). In accordance with the experimental values (McConnell *et. al.* 1960), $g_{yy} \approx g_{zz}$, so $\Delta g_\perp$ becomes negligible, so that Eq. (5.26) with axial g-matrix is expressed as

$$g = \begin{pmatrix} g_\perp + (g_\parallel - g_\perp)(1 - 2m_\perp^2) & (g_\parallel - g_\perp)\sqrt{1 - 2m_\perp^2} & (g_\parallel - g_\perp)\sqrt{1 - 2m_\perp^2} \\ (g_\parallel - g_\perp)\sqrt{1 - 2m_\perp^2} & g_\perp + (g_\parallel - g_\perp)(m_\perp^2) & (g_\parallel - g_\perp)(m_\perp^2) \\ (g_\parallel - g_\perp)\sqrt{1 - 2m_\perp^2} & (g_\parallel - g_\perp)(m_\perp^2) & g_\perp + (g_\parallel - g_\perp)(m_\perp^2) \end{pmatrix} \tag{5.29}$$

As for the A-matrix without axial symmetry (McConnell *et. al.* 1960), one has

$$A = \begin{pmatrix} A_{xx} - 2m_\perp^2 & A'm_\perp\sqrt{1 - 2m_\perp^2} & A'm_\perp\sqrt{1 - 2m_\perp^2} \\ A'm_\perp\sqrt{1 - 2m_\perp^2} & A_{yy} + (A_{xx} - A_{yy})m_\perp^2 & A'm_\perp^2 \\ A'm_\perp\sqrt{1 - 2m_\perp^2} & A'm_\perp^2 & A_{zz} + (A_{xx} - A_{zz})m_\perp^2 \end{pmatrix} \tag{5.30}$$

Where $A' = A_{xx} - 1/2(A_{yy} - A_{zz})$. It is noted that, in the absence of any fluctuation, $m_\perp$ is equal to zero and Eqs. (5.29) and (5.30) become diagonal, g- and A- matrices. Since the amplitude of the fluctuation is considered to be small, one can now invoke the first-order perturbation theory to calculate the effect of the fluctuations of the director on the eigenvalues of

124

Eqs. (5.29) and (5.30), which are the corrections to the diagonal elements due to fluctuation, and ignore the off-diagonal terms. Accordingly, the fluctuation-perturbation corrections due to thermal motion to the diagonal elements of the g- and A- matrices are:

$$\delta g_{xx} = -2m_\perp^2(g_\parallel - g_\perp);$$
$$\delta g_{yy} = m_\perp^2(g_\parallel - g_\perp) = \delta g_{zz};$$
$$\delta A_{xx} = -2m_\perp^2 A';$$ $\qquad$ (5.31)
$$\delta A_{yy} = m_\perp^2(A_{xx} - A_{yy});$$
$$\delta A_{zz} = m_\perp^2(A_{xx} - A_{zz}).$$

The $\delta(SHP)$ are then calculated to be, in terms of fluctuating diagonal elements of g- and A-matrices, expressed above in Eq. (5.31)

$$\delta g = \frac{1}{3}(\delta g_{xx} + \delta g_{yy} + \delta g_{zz});$$

$$\delta a = \frac{1}{3}(\delta A_{xx} + \delta A_{yy} + \delta A_{zz});$$

$$\delta F = \frac{2}{3}\left(\delta g_{zz} - \frac{1}{2}(\delta g_{xx} + \delta g_{yy})\right);$$

$$\delta D = \frac{2}{3}\left(\delta A_{zz} - \frac{1}{2}(\delta A_{xx} + \delta A_{yy})\right);$$ $\qquad$ (5.32)

$$\delta A_{xx} = -2m_\perp^2 A';$$

$$\delta F^{(2)} = \frac{1}{2}(\delta g_{xx} - \delta g_{yy});$$

$$\delta D^{(2)} = \frac{1}{2}(\delta A_{xx} - \delta A_{yy});$$

Substituting the above expressions in Eq. (5.21) and then substituting it Eq. (5.16), the auto-correlation functions $\overline{F^q(t)F^{r*}(t+\tau)}$ can be caiculated. They are needed to obtain the relaxation matrix elements given by Eq. (5.22). Since all $\delta(SHP)$s in Eq. (5.32) are linear in $\delta\sigma$, which are proportional to $m_\perp^2(t)$, according to Eq. (5.31), the correlation functions $\overline{F^q(t)F^{r*}(t+\tau)}$ can be expressed as

$$\overline{F^q(0)F^{r*}(\tau)} = f^q f^{r*}\langle \overline{m_\perp^2(0)m_\perp^2(\tau)} \rangle = f^q f^{r*}h^2 e^{-|\tau|/\tau_c} \quad (5.33)$$

Here f^i represents the amplitude of fluctuating $F^i(t)$ and h represents the limiting factor for fluctuations in the transverse plane.

5.2.2.1 Estimation of the correlation time $\boldsymbol{\tau_c}$

In order to estimate the amplitude of the fluctuation and the correlation time, one first needs to calculate the relaxation matrix elements. The relaxation matrix elements, given by Eqs. (5.22)-(5.24), can be calculated as functions of the correlation time, τ_c, and the amplitude of the fluctuation (h^2). The six values of the relaxation times, T_2, for the various electron and nuclear spin transitions are related to the relaxation matrix elements, as (Lee $et.\ al.$ 1993)

$$
\begin{aligned}
(T_2)_{ac} &= \frac{1}{R_{13,13}}; \ (T_2)_{bd} = \frac{1}{R_{24,24}}; \\
(T_2)_{ad} &= \frac{1}{R_{14,14}}; \ (T_2)_{bc} = \frac{1}{R_{23,23}}; \\
(T_2)_{ab} &= \frac{1}{R_{12,12}}; \ (T_2)_{cd} = \frac{1}{R_{34,34}};
\end{aligned}
\qquad (5.34)
$$

where the energy levels a, b, c, d are defined by Eq. (5.19). Therefore, one can calculate $(T_{2e})_{\alpha\beta}(\tau_c, h^2) = (T_{2e})_{exp}$ and $(T_{2n})_{\alpha\beta}(\tau_c, h^2) = (T_{2n})_{exp}$; $\alpha, \beta = a, b, c, d$ from the calculated values of the elements of the relaxation matrix. Note that in (Lee $et.\ al.$ 1993), only two experimental values $(T_{2e})_{exp}$ and $(T_{2n})_{exp}$ were estimated, so it is assumed here that $(T_2)_{ac} = (T_2)_{bd} = (T_2)_{ad} = (T_2)_{bc} = T_{2e}$ and $(T_2)_{cd} = (T_2)_{ab} = T_{2n}$.

In Figure 5.15, all values of $(T_2)_{\alpha\beta}; \alpha \neq \beta$ corresponding to the four different electron spin transitions $((T_2)_{ac} = (T_2)_{bd} = (T_2)_{ad} = (T_2)_{bc})$ and two different nuclear spin transitions $(T_2)_{cd} = (T_2)_{ab}$ are plotted as functions of (τ_c, h^2), using the experimental values, reported in (Lee $et.\ al$ 1993): T_{2e}= 900 ns and $T_{2n} = 22\ \mu$s. One then obtains six lines as shown in Figure 5.15, in the (τ_c, h^2) plane. The average values of $(\tau_c = 8.9 \times 10^{-8}\ s, h^2 = 1.18 \times 10^{-2})$, i.e. those situated at the center of this area are now chosen to calculate the relaxation-matrix elements as defined in Eqs. (5.22)-(5.24). This matrix is then used in the simulation of the time-domain echo-ELDOR (Figure 5.4) signal and its Fourier transform (FT), as shown in Figure 5.16a, together with the simulated FT using the phenomenological relaxation matrix Figure 5.16b, the experimental FT as reported in (Lee $et.\ al.$ 1993) Figure 5.16c and simulated FT in the absence of the relaxation matrix Fig. 4d. Comparing the FT of this signal with the experimental signal reported in (Lee $et.\ al.$ 1993), a very good agreement is found; as well, it is also in good agreement with that simulated phenomenologically. The simulation without relaxation (Figure 5.16d) is distinctly different from that with relaxation (Figure 5.16a), indicating that relaxation is an important effect to consider.

Figure 5.15 Contour plots of $(T_2)_{ac}$; $(T_2)_{bd}$; $(T_2)_{ad}$; $(T_2)_{bc}$ for the experimental value $(T_{2e})_{exp}$ = 900 ns and those for $(T_2)_{cd}$, $(T_2)_{ab}$, for the experimental value $(T_{2n})_{exp}$ = 22 μs as a function of the correlation time τ_c and h^2 .The red point inside the overlapping region represents the average values $\tau_c = 8.9 \times 10^{-8}$ s and $h^2 = 1{:}18 \times 10^{-2}$.
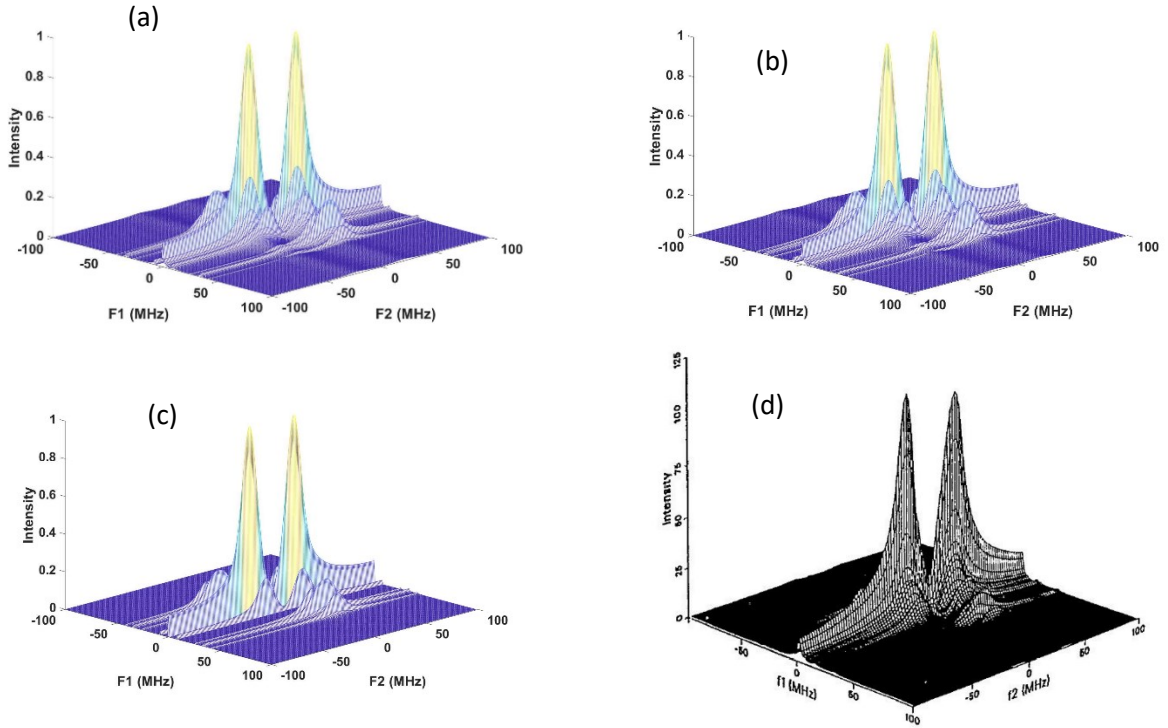
Figure 5.16 (a) Fourier transform of the simulated echo-ELDOR spectrum with the relaxation matrix calculated in this work (b) with phenomenological relaxation matrix introduced in (Lee *et. al.* 1993) (c) experimental Fourier transforms of the echo-ELDOR signal (d) simulated without any relaxation at the orientations $(\alpha, \beta, \gamma) = (0°, 30° , 0°)$, with the mixing times $T_m = 40 \mu$s. The experimental Figure (c) is reproduced with the permission of the authors of (Lee *et. al.* 1993).

5.2.3 Conical model of fluctuation for calculation of $\delta(SHP)$

In this model, in the absence of any thermal fluctuations, the molecules in the crystal are oriented along the x axis, their symmetry axis, as shown in Figure 5.17. One can then assume that that the spatial fluctuation of the malonic acid molecules in the crystal exhibit axial symmetry about their x-axes. Due to thermal fluctuations, the molecules in malonic-acid crystal vibrate about their symmetry axes. In the presence of a restoring potential, as assumed in this work, and described in detail in (Polnaszek *et. al.* 1973), the molecules tend to return to their equilibrium positions, to become oriented along their symmetry axis. The thermal fluctuations, which change the instantaneous orientations of the molecules on the one hand, and the presence of a restoring potential, on the other hand, lead to motions of the directors of malonic acid molecules within a cone about their symmetry axes as shown in Figure 5.17.
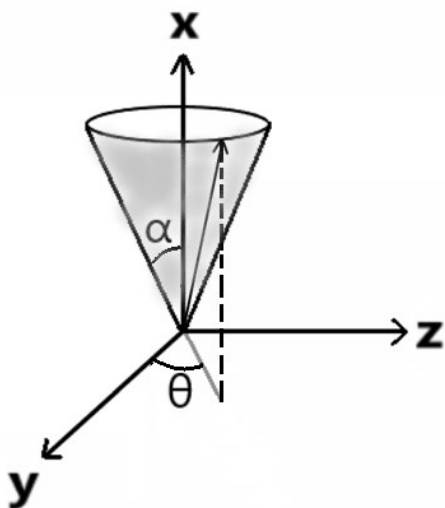
Figure 5.17 Figure to show the fluctuations of the ensemble-average director of the molecules. The tip of the director indicated by the arrow fluctuates within the circular periphery of the cone. Here x-axis represents the symmetry axis of malonic molecule.

In the previous section, exploiting cylindrical fluctuations of the director, the restoring potential was assumed to operate only in the plane perpendicular to the symmetry axis, i.e., the y-z plane. The resulting model possessed cylindrical symmetry, wherein the tip of the director moved in the y-z plane. In the conical fluctuation model, on the other hand, the restoring potential is assumed to restore the director along x-axis, the axis of symmetry, subsequent to its fluctuation by an angle α (Figure 5.17) from the x axis, so that random fluctuations by an angle α will cause the director to execute the surface of a cone with the semi conical angleα. It is noted that the conical model of fluctuation is more sophisticated than the cylindrical model in that it is based on a realistic potential well, amenable to quantum mechanical treatment, as described later in this chapter.

To calculate the effect of thermal vibrations, the problem can be treated in a statistical manner as an ensemble of a large number of malonic-acid molecules. Of these, consider a molecule representing the average of all the molecules in the ensemble undergoing the low-amplitude orientational motion about its equilibrium position due to thermal fluctuations. The resulting changes in SHP due to the fluctuations, δ (SHP), caused by thermal motion, causes the relaxation. This is taken into account as follows.

In the magnetic frame, the average of $\tilde{g}$ and $\tilde{A}$ matrices, assumed to have the same principal axes, is

$$
\tilde{\sigma} = \begin{pmatrix} \sigma_{xx} & 0 & 0 \\ 0 & \sigma_{yy} & 0 \\ 0 & 0 & \sigma_{zz} \end{pmatrix}
\tag{5.35}
$$

where $\tilde{\sigma}$ stands for $\tilde{g}$, or $\tilde{A}$. Due to thermal motion of the molecule, its director executes infinitesimal random fluctuations about the symmetry axis of the molecule, assumed to be along the x axis. These fluctuations can be seen to be equivalent to infinitesimal rotations of the director of malonic acid molecule by angles α, about axes randomly distributed in the y-z plane. Now the matrix for rotation by angle α about an axis in the y-z plane, oriented at an angle θ from the y-axis, is

$$
L = \begin{pmatrix} \cos\alpha & -\sin\alpha\sin\theta & \cos\theta\sin\alpha \\ \sin\alpha\sin\theta & \cos^2\theta + \cos\alpha\sin^2\theta & (1-\cos\alpha)\cos\theta\sin\theta \\ -\cos\theta\sin\alpha & (1-\cos\alpha)\cos\theta\sin\theta & \sin^2\theta + \cos\alpha\cos^2\theta \end{pmatrix}
\tag{5.36}
$$

Using *Mathematica,* the diagonal elements of the transformed $\tilde{\sigma}$ matrix, for either $\tilde{g}$, or $\tilde{A}$ matrices: $\tilde{\sigma}' = L.\tilde{\sigma}.L^{-1}$ are calculated to be

$$
\sigma'_{xx} = \sigma_{xx}\text{Cos}^2\alpha + \text{Sin}^2\alpha\left(\sigma_{zz}\text{Cos}^2\theta + \sigma_{yy}\text{Sin}^2\theta\right)
$$

$$
\sigma'_{yy} = \sigma_{yy}(\text{Cos}^2\theta + \text{Cos}\,\alpha\;\text{Sin}^2\theta)^2 + \sigma_{zz}(1 - \text{Cos}\,\alpha)^2\text{Cos}^2\theta\text{Sin}^2\theta
$$
$$
+\sigma_{xx}\text{Sin}^2\alpha\text{Sin}^2\theta
$$

$$
\sigma'_{zz} = \sigma_{zz}(\text{Cos}\,\alpha\;\text{Cos}^2\theta + \text{Sin}^2\theta)^2 + \sigma_{xx}\text{Cos}^2\theta\;\text{Sin}^2\alpha
$$
$$
+\sigma_{yy}(1 - \text{Cos}\,\alpha)^2\text{Cos}^2\theta\;\text{Sin}^2\theta
$$

The random fluctuations of the director are now taken into account by considering all possible values of θ in the yz plane. Although a crystal contains molecules with random orientations of their directors due to random thermal fluctuations with respect to the symmetry axis, the director in Figure 5.17 represents the ensemble average of motion of all molecules in the crystal, confined to a cone, with the tails of all the directors made coincident. To calculate the average of all possible orientations of the director, one needs to integrate Eq. (5.37) over θ from 0 to 2π, and then dividing it by 2π. The average diagonal elements of the resulting $(\sigma')_{avg}$ are:

$$(\sigma'_{avg})_{xx} = \sigma_{xx}\text{Cos}^2\alpha + \frac{1}{2}(\sigma_{yy} + \sigma_{zz})\text{Sin}^2\alpha$$

$$(\sigma'_{avg})_{yy} = \frac{1}{16}\sigma_{yy}(9 + 4\,\text{Cos}\,\alpha + 3\,\text{Cos}(2\alpha)) + \frac{1}{4}\sigma_{xx}(1 - \text{Cos}(2\alpha))$$

$$+ \frac{1}{16}\sigma_{zz}(3 - 4\,\text{Cos}\,\alpha + \text{Cos}(2\alpha))$$

$$(\sigma'_{avg})_{zz} = \frac{1}{16}\sigma_{zz}(9 + 4\,\text{Cos}\,\alpha + 3\,\text{Cos}(2\alpha)) + \frac{1}{4}\sigma_{xx}(1 - \text{Cos}(2\alpha))$$

(5.38)

$$+ \frac{1}{16}\sigma_{yy}(3 - 4\,\text{Cos}\,\alpha + \text{Cos}(2\alpha))$$

Since α is infinitesimal, the above expressions can be expanded in a series in α. Keeping only the lowest order terms in α, one obtains

$$(\sigma'_{avg\,xx}) = \sigma_{xx} + \frac{1}{2}(-2\sigma_{xx} + \sigma_{yy} + \sigma_{zz})\alpha^2;$$

$$(\sigma'_{avg})_{yy} = \sigma_{yy} + \frac{1}{2}(\sigma_{xx} - \sigma_{yy})\alpha^2$$ (5.39)

$$(\sigma'_{avg})_{zz} = \sigma_{zz} + \frac{1}{2}(\sigma_{xx} - \sigma_{zz})\alpha^2$$

The changes in the diagonal elements of $\tilde{\sigma}$, i.e. those of $\tilde{g}$ and $\tilde{A}$ matrices, due to thermal motion of the director, $\delta\tilde{\sigma} = \tilde{\sigma}' - \tilde{\sigma}$, are thus:

$$\delta\sigma_{xx} = \frac{1}{2}\left(-2\sigma_{xx} + \sigma_{yy} + \sigma_{zz}\right)\alpha^2 \ ; \ \delta\sigma_{yy} = \frac{1}{2}\left(\sigma_{xx} - \sigma_{yy}\right)\alpha^2; \ \delta\sigma_{zz} = \frac{1}{2}\left(\sigma_{xx} - \sigma_{zz}\right)\alpha^2$$

$$(5.40)$$

The above expressions are consistent with the results obtained in (Dzuba *et. al.* 2006). $\delta(SHP)$ are then calculated to be, in terms of the fluctuating diagonal elements of the $\tilde{g}$ and $\tilde{A}$ matrices, as follows:

$$\delta g = \frac{1}{3}\left(\delta g_{xx} + \delta g_{yy} + \delta g_{zz}\right); \ \delta a = \frac{1}{3}\left(\delta A_{xx} + \delta A_{yy} + \delta A_{zz}\right);$$

$$\delta F = \frac{2}{3}\left(\delta g_{zz} - \frac{1}{2}\left(\delta g_{xx} + \delta g_{yy}\right)\right); \ \ \delta D = \frac{2}{3}\left(\delta A_{zz} - \frac{1}{2}\left(\delta A_{xx} + \delta A_{yy}\right)\right);$$

$$(5.41)$$

$$\delta F^{(2)} = \frac{1}{2}\left(\delta g_{xx} - \delta g_{yy}\right); \ \ \delta D^{(2)} = \frac{1}{2}\left(\delta A_{xx} - \delta A_{yy}\right).$$

Substituting the above expressions in Eq. (5.21) and then substituting it Eq. (5.16), the auto-correlation functions $\overline{F^q(t)F^{r*}(t+\tau)}$ can be caiculated. They are needed to obtain the relaxation matrix elements given by Eq. (5.22). Since all $\delta(SHP)$s in Eq. (5.40) are linear in $\delta\sigma$, which are proportional to $\alpha^2(t)$, according to Eq. (5.38), the correlation functions $\overline{F^q(t)F^{r*}(t+\tau)}$ can be expressed in terms of α^2 as

$$\overline{F^q(0)F^{r*}(\tau)} = f^q f^{r*}\langle \overline{\alpha^2(0)\alpha^2(\tau)} \rangle = f^q f^{r*} h \, e^{-|\tau|/\tau_c} \qquad (5.42)$$

Here f^i represents the amplitude of fluctuating $F^i(t)$ and $h(= \overline{\alpha^4})$ is the parameter that represents the average fluctuation of the director in the transverse (y-z) plane. The procedure of how to calculate h is described as follows.

5.2.3.1 Calculation of the average of the fluctuation angle in a strong restoring potential

As the malonic acid molecule fluctuates around its symmetry axis, it is brought back to its equilibrium position by the restoring potential acting on it. This can be treated by a quantum mechanical equation for the spherical top as described in (Polnaszek *et. al.* 1973). Assuming that the malonic acid molecule in the crystal experiences a strong harmonic-oscillator restoring potential, for which the wave function is (Polnaszek *et. al.* 1973)

$$\psi_{K,M}{}^n(\vartheta, \alpha, \xi) = \exp(iK\vartheta)y_n(\alpha)\exp(iM\xi), \qquad (5.43)$$

where (ϑ, α, ξ) are the Euler angles that relate the orientation of the director to the magnetic frame, with α assumed to be a small deviation from the equilibrium position of the molecule. as shown in Figure 5.17, and K, M, n are the quantum numbers that characterize the harmonic-oscillator wave functions in a restoring potential (Polnaszek *et. al.* 1973). Here the function $y_n(\alpha)$ is:

$$y_n(\alpha) = N_n \exp\left(-|\lambda|\frac{\alpha^2}{2}\right) H_n(|\lambda|^{1/2}\alpha) \tag{5.44}$$

In the above, $\lambda = -\frac{\chi}{k_B T}$, is the dimensionless parameter of the restoring potential, with χ being the strength of the restoring potential, k_B is Boltzmann's constant; H_n in Eq. (5.44) are Hermite polynomials and N_n are the normalization coefficients:

$$N_n = \left(\frac{\sqrt{\lambda}}{\sqrt{\pi}\ 2^n\ n!}\right)^{1/2} \tag{5.45}$$

The average fluctuation of the director axis, $h = \overline{\alpha^4}$, appearing in Eq. (5.42), needed to calculate the relaxation matrix elements, can be calculated, using the wave function of the spherical top in the strong restoring potential, as follows

$$\overline{\alpha^4} = \int \psi_{K,M}{}^n(\vartheta,\alpha,\xi)^*\alpha^4\ \psi_{K,M}{}^n(\vartheta,\alpha,\xi)\ d\vartheta\ d\alpha\ d\xi = \int\limits_{-\infty}^{\infty} y_n{}^*\alpha^4 y_n\ d\alpha \tag{5.46}$$

Note that the choice of the limits of the integral above from $-\infty$ to $+\infty$ instead of $(-\frac{\pi}{2},\frac{\pi}{2})$ is justified in the case when $\lambda \gg 1$. With $h = \overline{\alpha^4}$ calculated above and using Eqs. (5.40)-(5.42), one can calculate the elements of the relaxation matrix expressed in Eq. (5.22).

5.2.3.2 Estimation of the correlation time (τ_c) and the strength of the restoring potential λ

Similar to the procedure given in Sec. 5.2.2.1 for cylindrical model of fluctuation, the elements of the relaxation matrix, $R_{\alpha\beta\alpha\beta}(\tau_c,\lambda)$, can be calculated in the eigenvalue basis, denoted by a, b, c, d (also denoted equivalently hereafter as 1,2,3,4) as functions of the correlation time, τ_c, and the strength of the restoring potential λ . T_2-type relaxation elements for the various electron and nuclear spin transitions are related to the relaxation matrix elements as:

(a)

(b)

(c)
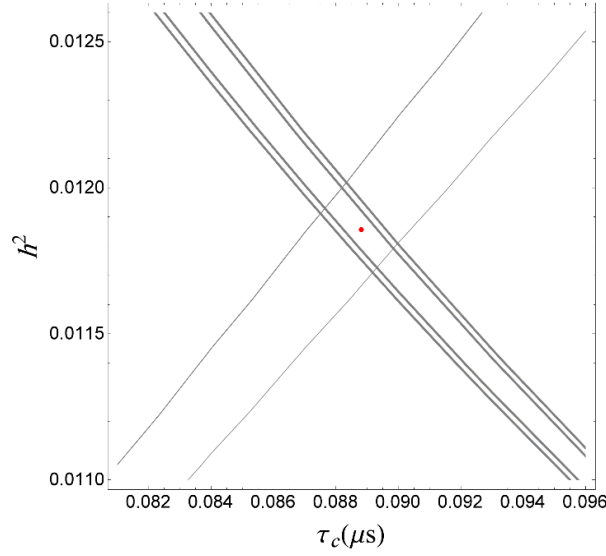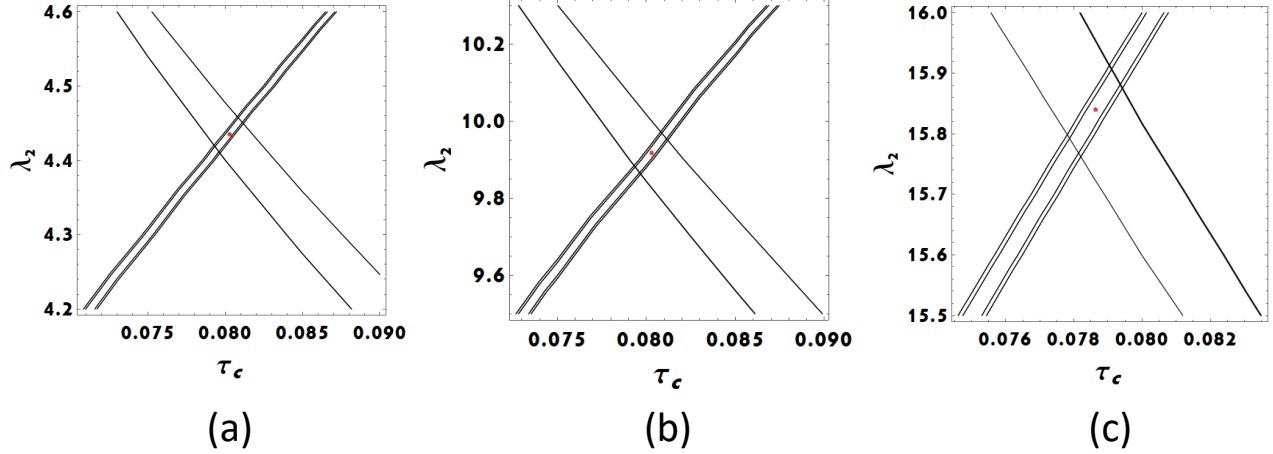
Figure 5.18 Contour plots of $(T_2)_{ac}$, $(T_2)_{bd}$, $(T_2)_{ad}$, $(T_2)_{bc}$ for the experimental value T_{2e}=900 ns and those for $(T_2)_{ab}$, $(T_2)_{cd}$ for the experimental value T_{2n}=22 μs as a function of the correlation time τ_c and λ for the ground state (a), first excited state (b) and second excited state (c) of the harmonic oscillator. The red circle in the overlapping region represents the average of (τ_c, λ) values used for simulation of the echo-ELDOR signal representing the best average which are found to be (a) $(8.1 \times 10^{-8}$ s, 4.43) (b) $((8.0 \times 10^{-8}$ s, 9.93)) and (c) $((7.9 \times 10^{-8}$ s, 15.85)).

$$(T_2)_{ac} = \frac{1}{R_{1313}}, \quad (T_2)_{bd} = \frac{1}{R_{2424}}, \quad (T_2)_{ad} = \frac{1}{R_{1414}}, \quad (T_2)_{bc} = \frac{1}{R_{2323}}, \quad (T_2)_{ab} = \frac{1}{R_{1212}}, \quad (T_2)_{cd} = \frac{1}{R_{3434}}.$$

Having the experimental values of electron spin-relaxation times $(T_{2e})_{exp}$ and nuclear spin-relaxation times $(T_{2n})_{exp}$ available from (Lee $et.\ al.$ 1993), one can now solve for (τ_c, λ) by assuming the four calculated $T_{2e\,\alpha\beta}(\tau_c, \lambda) = (T_{2e})_{exp}$, and the two calculated $T_{2n\,\alpha\beta}(\tau_c, \lambda) = (T_{2n})_{exp}$; for $\alpha, \beta = a, b, c, d$ by assuming $(T_2)_{ac} = (T_2)_{bd} = (T_2)_{ad} = (T_2)_{bc} = T_{2e}$ and $(T_2)_{cd} = (T_2)_{ab} = T_{2n}$ In fact, these relaxation times are slightly different from each other as shown in Figure 5.18. If an experiment is performed in which only one transition between the four levels is involved, e.g., a→c, then one can measure the electronic relaxation time $(T_{2e})_{ac}$ for that specific transition. However, when the experiment is not sensitive to individual transitions, one can replace our relaxation times for the various transitions by a single, average, relaxation time).

In Figure 5.18, all values of $(T_2)_{\alpha\beta}; \alpha \neq \beta$ corresponding to the four different electron spin transitions $((T_2)_{ac}, (T_2)_{bd}, (T_2)_{ad}, (T_2)_{bc})$ and two different nuclear spin transitions $((T_2)_{cd}, (T_2)_{ab})$ are plotted for the first three lowest energy states (n = 0, 1, 2) of the malonic acid molecule as functions of τ_c, λ, using the experimental values, reported in (Lee $et.\ al.$ 1993): $T_{2e} = 900 ns$ and $T_{2n} = 22 \mu s$. For each energy state, n, of the harmonic oscillator one then obtains six lines as shown in Figure 5.18 in the (τ_c, λ) plane . The average values of (τ_c, λ), i.e., those lying at the center of this area are then chosen to calculate the elements of the relaxation-matrix. The values of (τ_c, λ) that correspond best to the experimental values of T_{2e} and T_{2n} are found to be ($\tau_c = 8.1 \times 10^{-8}$ s and λ=4.43), ($\tau_c = 8.0 \times 10^{-8}$ s and λ=9.93) and ($\tau_c = 7.9 \times 10^{-8}$ s and λ=15.85) for the molecule in the ground state (n = 0), first excited state (n = 1) and second excited state (n = 2), respectively. (For comparison, it is noted that the value of the parameter λ, in NO crystal was $|\lambda| = 7.5$ (Polnaszek $et.\ al.$ 1973)). It is further noted that at the temperature (T) the experiment was performed (T~77 K), the molecule is predominantly in the ground state,
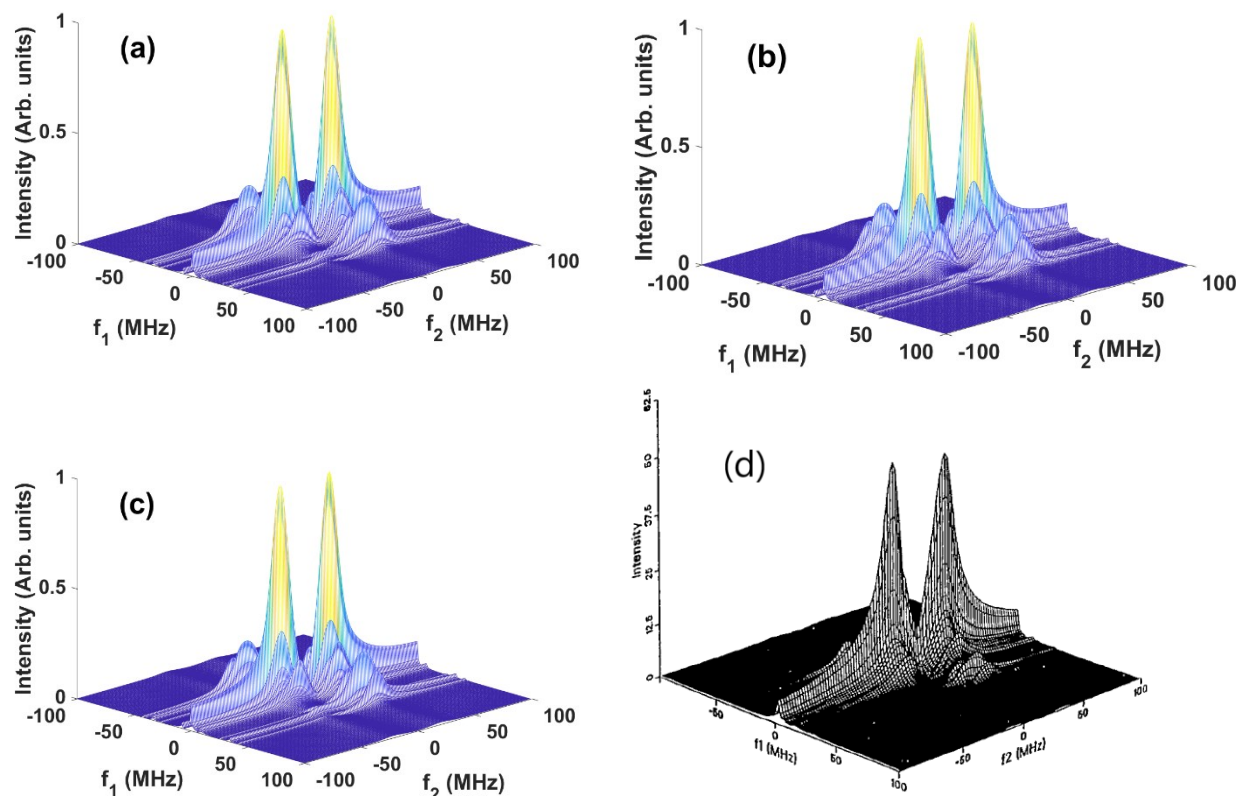
Figure 5.19 Fourier transform of the simulated echo-ELDOR spectrum for (a) second excited state (n=2), (b) first excited state (n=1), (c) ground state (n=0), and (d) the experimental Fourier transforms of the echo-ELDOR signal. The simulations are done for the orientation of the external magnetic field $(\alpha, \beta, \gamma) = (0, -30^o, 0)$, with the mixing times T_m = 40 μs. The same best fit values of the correlation time τ_c and λ, as determined in Figure 5.18 are used in these simulations. An inhomogeneous Gaussian broadening along the f_2 axis with the width Δ= 5 MHz is used in the simulations. All simulated figures, drawn using the best fit values, show excellent agreements with the experiment (Fig. (d), but (c), the one for n=0 (ground state), represents the most populated state at room temperature. The experimental Figure (d) is reproduced with the permission of the authors of (Lee *et. al.* 1993).

since the vibrational energy level differences due to the restoring potential are presumably much higher than $k_B T$, where k_B is Boltzmann's constant and T is 77 K. The relaxation matrix, consistent with the ground state, is then used to simulate the time-domain echo-ELDOR signal and its Fourier transform (FT), as shown in Figure 5.19. Comparing the calculated and experimental FTs, as reported in (Lee *et. al.* 1993), an excellent agreement is found.

5.3 Conclusions

The salient features of this chapter dealing with the calculation of the signal and the matrix elements of the relaxation matrix due to fluctuation of spin-Hamiltonian parameters caused by thermal motion in a γ-irradiated malonic acid crystal of an electron-nuclear spin-coupled system ($S = 1/2; I = 1/2$) are as follows.

(i) The numerical procedure of Chapter 2 is successfully applied to the system of γ-irradiated malonic acid crystal of an electron-nuclear spin-coupled system ($S = 1/2; I = 1/2$). The theory is further extended by including the static Hamiltonian during the pulses.

(i) Two models are presented of how to calculate the relaxation matrix due to changes in the spin-Hamiltonian parameters characterizing an electron-nuclear spin coupled system of a malonic-acid molecule due to thermal fluctuations of the director axis of the molecule in the transverse plane.

(ii) The correlation time (τ_c) have been estimated, using the experimental values of the electronic and nuclear spin relaxation times T_{2e} and T_{2n}, respectively.

(iii) With the elements of the relaxation matrix calculated using the presented models, the Fourier transform of the simulated echo-ELDOR signal using LVN equation turns out to be in excellent agreement with the experimental echo-ELDOR signal.

Chapter 6

6 Relaxation during free evolution and effects of many-body interactions in a γ-irradiated malonic-acid single-crystal SECSY signal of an electron-nuclear spin coupled system

This chapter addresses two important relaxation mechanisms that affect the SECSY signal of an electron-nuclear spin coupled system γ-irradiated malonic-acid single-crystal: (i) relaxation during free evolution and (ii) the many body effects, i.e., the instantaneous and spectral diffusions. This consideration is in addition to the relaxations of the same system discussed in Chapter 5, where these effects were not taken into considered. The effort is to bring the calculated signal by considering the various mechanisms that affect the signal. in agreement with that published by (Lee, Patyal, and Freed 1993) (Hereafter referred to as LPF).

6.1 Relaxation during free evolution

There is seen a disagreement between the Fourier transform (FT) of the two-dimensional SECSY signal shown in Figure 5.5 in chapter 5 and the Fourier transform of the experimental data reported by LPF in that, the heights of the main peaks in the calculated signal are about the same, whereas the main peaks in the experimental spectrum have different heights. This disagreement can be resolved by considering different relaxation times for the various matrix element of the density matrix along the pathway $p = -1$ during free evolution As discussed in chapter 5, all the matrix elements of the density matrix, ρ_e, were put equal to zero, except for those corresponding to $\rho_e(2,1)$ for the pathway with coherence order $p = -1$, after the application of the first pulse. This treatment does not consider relaxation during free evolution. In this case, the projection operator for $p = +1$ pathway (electronic matrix element for ($\frac{1}{2}$, -$\frac{1}{2}$) for the electron-nuclear coupled system with electron spin S=1/2, nuclear spin I=1/2, with the dimension of $(2S_1 + 1) \times (2I_1 + 1) = 4$ in the direct-product matrix in Hilbert space is expressed as

$$\begin{pmatrix} 0 & 0 & 1 & 1 \\ 0 & 0 & 1 & 1 \\ 0 & 0 & 0 & 0 \\ 0 & 0 & 0 & 0 \end{pmatrix} \tag{6.1}$$

whereas, for the pathway $p = -1$, chosen after the second pulse, the projection operator is

$$\begin{pmatrix} 0 & 0 & 0 & 0 \\ 0 & 0 & 0 & 0 \\ 1 & 1 & 0 & 0 \\ 1 & 1 & 0 & 0 \end{pmatrix} \tag{6.2}$$

The use of the projection operators given by Eq. (6.1) over the time t_1 for the pathway $p = 1$ and (6.2) over the pathway $p = -1$ after the second pulse for the time t_1 at which the echo occurs, and over the time t_1 at which the signal is recorded produces the two-dimensional Fourier transform (FT), shown in Figure 5.5. Here, the relaxations during the free evolutions over the pathways $p = 1$, followed by the pathway $p = -1$ are neglected. (Figure 5.3) One can now follow the procedure described in chapter 5 for the calculation of two-dimensional SECSY signal, but by introducing a modified projection operator, duly taking into account the relaxations during the free evolution, which leads to the correct difference in the heights of the main peaks in the experimental FT of the two-dimensional SECSY signal. In this approach, the matrix element (3,1) of the projection operators in Eqs. (6.1) and (6.2) are multiplied by an additional exponential factor $\exp(-(2t_1 + t_2)/T_2')$, where t_1 and t_2 are the times between the two pulses and the time after the echo in a SECSY experiment, respectively, and T_2' is a phenomenological parameter that determines the relaxation time along the (3,1) matrix element of the density matrix, assuming the same relaxation rate during the pathways $p = +1$ and $p = -1$. The resulting two-dimensional Fourier transform for the SECSY pulse sequence is shown in Figure 6.1a, which shows a much better agreement with the experiment than that calculated without relaxation taken into account as described here. The same parameters as those used for the simulations of Figure 5.5 are used here. As for the phenomenological parameter T_2', it was found that the best agreement with the experimental data is achieved for $T_2' = 600$ ns.

2D Fourier Transform calculated by using modified projection operator

(a)

2D Fourier of Figure 5.5

(b)

Experimental 2D FT

(c)
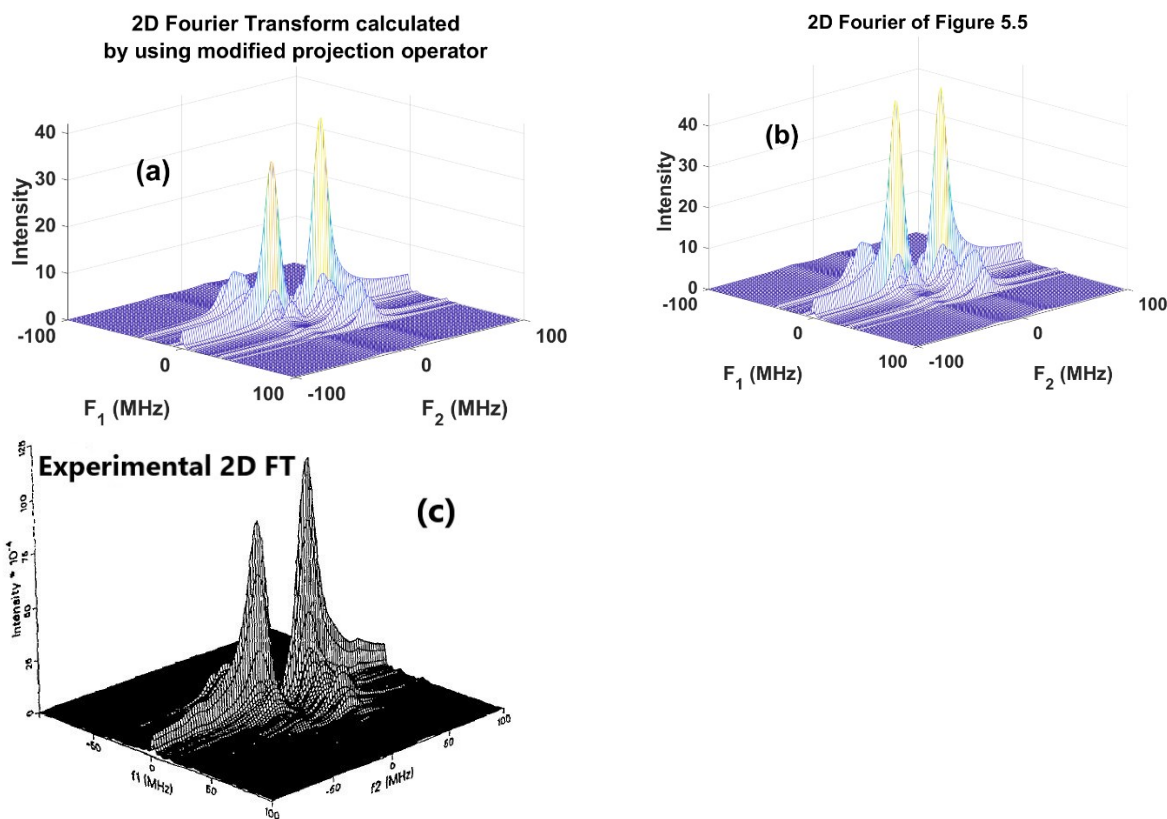
Figure 6.1 Comparison of two-dimensional Fourier transforms obtained from γ-irradiated malonic-acid single-crystal SECSY signals. (a) using the modified projection operator (b) same as Figure 5.5 and (c) Experimental Fourier transform. The same parameter as those used for Figure 5.5 is used for the simulation of (b). The value of the phenomenological relaxation time for matrix element (3.1) is chosen to be $T_2' = 600\ ns$.

6.2 Many-body effects on the malonic-acid-radicals single-crystal SECSY signal of the electron-nuclear spin coupled system

In the previous chapter, the simulation of the spin-coupled electron-nuclear system in a γ–irradiated single crystal of malonic acid, was improved by including the static spin Hamiltonian during the pulses and using a relaxation matrix, calculated by using the conical model of fluctuation. The simulation of the SECSY signal was further improved by using a modified projection operator as discussed in Sec. 6.1. However, the effect of electronic interactions with the surrounding molecules, i.e., the many-body effects, which cause relaxation of the signal by these effects, was not considered.

The electronic spin-spin dipolar interaction causes the electron spin-echo signal to decay in solids by two mechanisms: (i) spectral diffusion and (ii) instantaneous diffusion. In particular, the interacting electron on the lattice with the observer electron can affect the signal by its random spin flip, causing what is known as **spectral diffusion**, which contributes to the relaxation matrix elements in the relevant Liouville von Neumann (LVN) equation. On the other hand, there is another effect, known as **instantaneous diffusion**, which is greater the closer is to resonance is the interacting electron, which depends mainly on the orientation of the interacting electron's dipole magnetic moment. Previously, Salikhov *et al.* (1981) derived analytical expressions in the secular approximation of the dipolar interaction, but no numerical calculations were provided by them.

It is the purpose of this section to consider quantitatively the effect of instantaneous and spectral diffusions on the SECSY signal in a γ-irradiated malonic acid single crystal by numerically solving the relevant LVN equation in Liouville space. This is achieved here by first calculating separately the instantaneous and spectral diffusions for two coupled electrons, neglecting hyperfine interactions, in a SECSY pulse sequence and then multiplying the resulting signals by the SECSY signal calculated for a malonic acid radical in single crystal using finite pulses, a relaxation matrix calculated by conical model of fluctuation along with the use of modified projection operators as described in Sec. 6.1. As for the relaxation matrix elements due to random spin flip of an electron on the lattice, causing spectral diffusion, the analytical results derived by Salikhov *et al.* (1981) will be exploited. In addition, the spin Hamiltonian of the coupled system of the observer and interacting electrons will be exploited to consider the effect of instantaneous diffusion.

6.2.1 Spin Hamiltonian of two-coupled electron system (instantaneous diffusion)

The spin Hamiltonian describing two electrons coupled by the dipolar interaction is expressed as

$$H_{0e} = C_1 S_{z_1} + C_2 S_{z_2} + \omega_{dd}(3cos^2\delta - 1)\left(S_{z_1}S_{z_2} - \frac{1}{4}(S_{+_1}S_{-_2} + S_{-_1}S_{+_2})\right) \tag{6.3}$$

where the expressions for the coefficients $C_k, k = 1,2$ are given in Appendix A, ω_{dd} is the dipolar coupling constant which is related to the distance between the two electron spins as $\omega_{dd}[MHz] = \frac{52.04}{r[nm]^3}$ and δ is the angle between the line connecting the two spins and the external magnetic field. To study the effect of the instantaneous diffusion as discussed later in this chapter, it is more convenient to write the spin Hamiltonian given in Eq. (6.3) in the rotating frame of the first spin (hereafter reffered to as observer spin) where the first electron is exactly on resonance. In this rotating frame, the C_1 term in the spin Hamiltonian of Eq. (6.3) is substracted off i.e., $C_1 \rightarrow 0$. As for the second spin, the Zeeman interaction becomes $C_2 \rightarrow C_2 - C_1$.

The Hamiltonian of a pulse with amplitude, B_1, of radiation microwave magnetic field is given as

$$H_p = \frac{\omega_1}{2}\left(e^{-i\phi}S_+ + e^{i\phi}S_-\right) \tag{6.4}$$

where $\omega_1 = B_1\gamma_e$, ϕ is the phase of the pulse and $S_\pm$ are the raising/lowering operators of the total electronic spin of the coupled electron system in the 4×4 Hilbert-space, defined as

$$S_\pm = S_{\pm S_1} \otimes \mathbb{1}_{S_2} + \mathbb{1}_{S_1} \otimes S_{\pm S_2} \tag{6.5}$$

where $S_{\pm S_k}; k = 1,2$ are expressed in terms of the Pauli matrices σ_x and σ_y as $S_{\pm S_k} = \frac{1}{2}(\sigma_{x_k} \pm i\sigma_{y_k})$; $\mathbb{1}_{S_k}; k = 1,2$, are 2×2 identity matrices and $\otimes$ stands for the direct product.

In the numerical calculations performed here, the magnetic basis with the basis vectors $|M_{S_1}, M_{S_2}\rangle$ is used to calculate the matrix elements. Here M_{S_1}, M_{S_2} are the two electronic magnetic quantum numbers.

The initial density matrix, ρ_0, required to calculate the signal for a SECSY sequence, is governed by the Boltzmann distribution for the two electrons in thermal equilibrium, each with spin $\frac{1}{2}$. The initial density matrix in the high-temperature approximation is:

$$\rho_0 = \frac{\exp{(-\hat{H}_0/k_BT)}}{Tr[\exp{(-\hat{H}_0/k_BT)}]} \propto (\mathbb{1} - \frac{\hbar\omega_0}{k_BT} S_z + \cdots), \tag{6.6}$$

where H_0 is given by Eq. (6.3); k_B is Boltzmann constant; T is the temperature; S_z is the z-component of the total electronic spin $\mathbf{S} = \mathbf{S_1} + \mathbf{S_2}$; and $\hbar\omega_0$ is the Zeeman splitting of the total electron spin. As discussed in Chapter 3, during the evolution of the initial density matrix, ρ_0, to the final density matrix, ρ_f the term $\mathbb{1}$ in Eq. (6.6) remains invariant. But it does not contribute to

the signal $\{= Tr(S_+ \rho_f)\}$, since $Tr(S_+ \mathbb{1}) = 0$. For the calculation of the (unnormalized) signal, one can then replace ρ_0, as follows:

$$\rho_0 \rightarrow S_Z = S_{z_1} + S_{z_2} = (\frac{\sigma_{z_1}}{2}) \otimes \mathbb{1}_{S_2} + \mathbb{1}_{S_1} \otimes (\frac{\sigma_{z_2}}{2}) \tag{6.7}$$

where σ_{z_i} ; $i = 1,2$ are the Pauli spin matrices for the two electron spins.

To calculate the two-pulse SECSY EPR signal for the system of two electrons, each characterized by an electron spin $S = 1/2$, considering spin relaxation, Liouville von-Neumann (LVN) equation is exploited, which governs the time evolution of the density matrix during free evolution, i.e., in the absence of a pulse is expressed as

$$\frac{d}{dt}\chi(t) = -i[H_0, \chi(t)] + \widehat{\widehat{R}} \chi(t) \tag{6.8}$$

where $\chi = \rho - \rho_0$ is the reduced density matrix with $\rho_0 \propto S_{z_1} + S_{z_2}$ being the initial density matrix, and H_0 is given by Eq. (6.3). In Eq. (6.8), $\widehat{\widehat{R}}$ is the relaxation superoperator in Liouville space, whose matrix form is deduced from Salikhov *et. al.* 1981 as follows

One can write the equations for the diagonal elements of the density matrix in accordance with Salikhov *et. al.* (1981), as follows:

$$\dot{\rho}_{11} = -(W_1 + W_2)\rho_{11} + W_1\rho_{33} + W_2\rho_{22};$$

$$\dot{\rho}_{22} = -(W_1 + W_2)\rho_{22} + W_1\rho_{44} + W_2\rho_{11}$$

$$\dot{\rho}_{33} = -(W_1 + W_2)\rho_{33} + W_1\rho_{11} + W_2\rho_{44} \tag{6.9}$$

$$\dot{\rho}_{44} = -(W_1 + W_2)\rho_{44} + W_1\rho_{22} + W_2\rho_{33}$$

where W_1 and W_2 are the two phenomenological parameters expressing the relevant relaxation operators and the indices 1,2,3,4 refer to the matrix elements of the density matrix defined as

$$|1> = |++>, \quad |2> = |+->, |3> = |-+>, |4> = |-->, \tag{6.10}$$

where $|+>, |->$ are the eigenstates of the spin operator S_z corresponding to the eigenvalues $M_s = +1/2$ and $M_s = -1/2$, respectively.

As seen from Eq. (6.9), the relaxation matrix connects the matrix elements of the density matrix corresponding to the allowed transitions i.e., those for which $\Delta M_s = \Delta M_{s_1} + \Delta M_{s_2} = \pm 1$. The off-diagonal elements are governed by the following equations

$$\dot{\rho}_{12} = -i\left(C_2 + \frac{A}{2}\right)\rho_{12} - (W_1 + W_2)\rho_{12} + W_1\rho_{34} + W_2\rho_{21};$$

$$\dot{\rho}_{34} = -i\left(C_2 - \frac{A}{2}\right)\rho_{34} - (W_1 + W_2)\rho_{34} + W_1\rho_{12} + W_2\rho_{43};$$

$$\dot{\rho}_{13} = -i\left(C_1 + \frac{A}{2}\right)\rho_{13} - (W_1 + W_2)\rho_{13} + W_1\rho_{31} + W_2\rho_{24};$$

$$\dot{\rho}_{24} = -i\left(C_1 - \frac{A}{2}\right)\rho_{24} - (W_1 + W_2)\rho_{24} + W_1\rho_{42} + W_2\rho_{13};$$

$$\dot{\rho}_{14} = -i\frac{(C_1 + C_2)}{2}\rho_{14} - (W_1 + W_2)\rho_{14} + W_1\rho_{32} + W_2\rho_{23};$$

$$\dot{\rho}_{23} = -i\frac{(C_1 - C_2)}{2}\rho_{23} - (W_1 + W_2)\rho_{23} + W_1\rho_{41} + W_2\rho_{14};$$

(6.11)

where C_1 and C_2 are the coefficient of the spin operators S_{z_1} and S_{z_2} in the spin Hamiltonian of the two coupled electron, respectively, and $A = \omega_{dd}(1 - 3\cos^2 \delta)$ is the secular part of the dipolar interaction between the two electrons. The relaxation matrix deduced from Eqs. (6.9) and (6.1), expressed in Hilbert space, is found to have the following form in the Liouville space

$$R = \begin{pmatrix}
-W & 0 & 0 & 0 & 0 & W_2 & 0 & 0 & 0 & 0 & W_1 & 0 & 0 & 0 & 0 & 0 \\
0 & -W & 0 & 0 & W_2 & 0 & 0 & 0 & 0 & 0 & 0 & W_1 & 0 & 0 & 0 & 0 \\
0 & 0 & -W & 0 & 0 & 0 & 0 & W_2 & W_1 & 0 & 0 & 0 & 0 & 0 & 0 & 0 \\
0 & 0 & 0 & -W & 0 & 0 & W_2 & 0 & 0 & W_1 & 0 & 0 & 0 & 0 & 0 & 0 \\
0 & W_2 & 0 & 0 & -W & 0 & 0 & 0 & 0 & 0 & 0 & 0 & 0 & 0 & W_1 & 0 \\
W_2 & 0 & 0 & 0 & 0 & -W & 0 & 0 & 0 & 0 & 0 & 0 & 0 & 0 & 0 & W_1 \\
0 & 0 & 0 & W_2 & 0 & 0 & -W & 0 & 0 & 0 & 0 & 0 & W_1 & 0 & 0 & 0 \\
0 & 0 & W_2 & 0 & 0 & 0 & 0 & -W & 0 & 0 & 0 & 0 & 0 & W_1 & 0 & 0 \\
0 & 0 & W_1 & 0 & 0 & 0 & 0 & 0 & -W & 0 & 0 & 0 & 0 & W_2 & 0 & 0 \\
0 & 0 & 0 & W_1 & 0 & 0 & 0 & 0 & 0 & -W & 0 & 0 & W_2 & 0 & 0 & 0 \\
W_1 & 0 & 0 & 0 & 0 & 0 & 0 & 0 & 0 & 0 & -W & 0 & 0 & 0 & 0 & W_2 \\
0 & W_1 & 0 & 0 & 0 & 0 & 0 & 0 & 0 & 0 & 0 & -W & 0 & 0 & W_2 & 0 \\
0 & 0 & 0 & 0 & 0 & 0 & W_1 & 0 & 0 & W_2 & 0 & 0 & -W & 0 & 0 & 0 \\
0 & 0 & 0 & 0 & 0 & 0 & 0 & W_1 & W_2 & 0 & 0 & 0 & 0 & -W & 0 & 0 \\
0 & 0 & 0 & 0 & W_1 & 0 & 0 & 0 & 0 & 0 & 0 & W_2 & 0 & 0 & -W & 0 \\
0 & 0 & 0 & 0 & 0 & W_1 & 0 & 0 & 0 & 0 & W_2 & 0 & 0 & 0 & 0 & -W
\end{pmatrix}$$

(6.12)

where $W = W_1 + W_2$.

The solution of Eq. (6.8) after time t in Liouville space is given as

$$\hat{\chi}(t) = e^{-(t-t_0)\hat{\hat{L}}}\hat{\chi}(t_0) \tag{6.13}$$

where $\hat{\chi}$ is the column vector of dimension $16^2 \times 1$ i.e., $\hat{\chi} = Col(\chi)$ and the Liouville superoperator, $\hat{\hat{L}}$, in the Hamiltonian basis is defined as

$$\hat{\hat{L}} = i\hat{\hat{H}} + \hat{\hat{R}} = (I_n \otimes H_0 - H_0 \otimes I_n) + \hat{\hat{R}} \tag{6.14}$$

In Eq. (6.13), I_n is unit matrix of dimension 4×4.

The spin relaxation will here be neglected during the application of a pulse as it has negligible effect since the duration of the pulses are much smaller than the relaxation time. Then, the evolution of the density matrix due to the pulse is described in Hilbert space, as follows:

$$\frac{d}{dt}\rho(t) = -i[(H_0 + H_p), \rho(t)], \tag{6.15}$$

where H_0 and H_p are expressed by Eqs. (6.3) and (6.4), respectively.

The density matrix is transformed by the application of a pulse of duration t_p. The solution of Eq. (6.1), neglecting relaxation during the pulse, is given as:

$$\rho(t_0 + t_p) = e^{-i(H_0+H_p)t_p}\rho(t_0) e^{i(H_0+H_p)t_p} \tag{6.16}$$

After the application of a pulse, the density matrix is projected onto the coherence pathways of interest, which are: $p = 1, -1$ as shown in Figure 5.3, showing the SECSY pulse sequence along with the relevant coherence pathway. This is achieved, in the numerical simulation, by taking the *Hadamard* product, $\rho^{(k)} = P_k \circ \rho$, of the projection operator matrix, P_k; $k = 1, 2$. For the coherence pathways $p = 1$, the projection operator given in Appendix B is used whereas for $p = -1$, the modified projection operator as discussed in Sec. 6.1 is exploited.

The complex signal of the observer electron, for the orientation, (δ, ϕ), of the static magnetic field with respect to the dipolar axis that connects the magnetic dipoles of the two electron spins, and
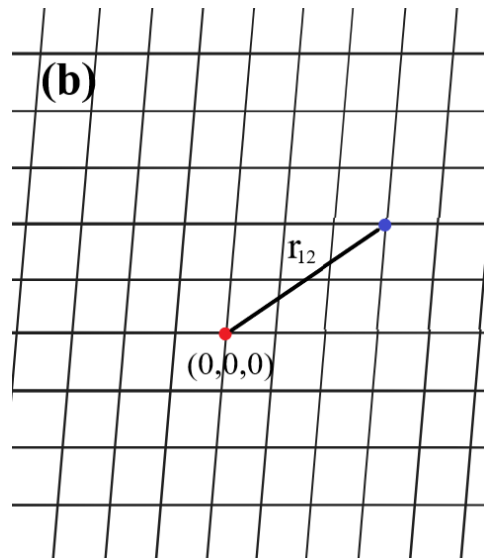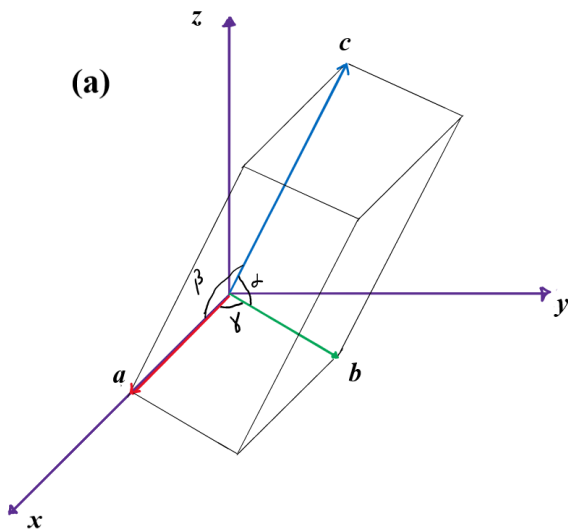
Figure 6.2 (a) The unit cell of malonic acid crystal. The unit cell parameters are (McConnell *et. al.* (1959)) ($a = 5.33$ Å, $b = 5.14$ Å, $c = 11.25$Å) and ($\alpha = 102°, \beta = 135°, \gamma = 85°$). (b) The top view of the triclinic lattice. The red dot represents observer spin which is located at $(l, m, n) = (0,0,0)$ whereas the interacting spins (blue dot) can be at any lattice point. The vector r_{12} connects the two spins.

the orientation of the electron spins with respect to the molecular frame, characterized by six Euler angles, $(\alpha_1, \beta_1, \gamma_1, \alpha_2, \beta_2, \gamma_2)$, is then,

$$S(t_1, t_2, \delta, \phi, \alpha_1, \beta_1, \gamma_1, \alpha_2, \beta_2, \gamma_2) = Tr(S_{1+}\rho_f), \qquad (6.17)$$

Where $S_{1+.}$ is the raising operator for the observer electron, denoted by the index 1

6.2.2 The Physical Picture

The many-body effects including the instantanoues and spectral diffusions on the SECSY signal of the γ-irradiated malonic acid single-crystal are considered here by taking into account the dipolar interaction between the electron of the molecule under study (observer spin) and the electrons of all the neighboring electrons (hereafter reffered to as interacting electrons), which undergo random spin flips and are chosen in a statistical manner by Monte-Carlo simulations in a triclinic lattice (McConnell *et. al.* (1959)) (Figure 6.2a). The top veiw of the triclinic lattice charactrizing the malonic acid crystal is shown in Figure 6.2b. Here, the dipolar interaction is considered between the observer electron, shown by a red point, and the interacting electron which is in the dipoalr interaction with the observer electron spin. The observer electron 1 is considered to be at the lattice site (0,0,0) whereas the interacting electrons is located anywhere in the lattice except at (0,0,0). The distance between the the observer electron and an interacting electron located at lattice site (l, m, n) moelcules, in a triclinic lattice is calcualetd as

$$r_{12} = \sqrt{l^2 a^2 + m^2 b^2 + n^2 c^2 + 2l\,m\,a\,b\,cos\gamma + 2l\,n\,a\,c\,cos\beta + 2m\,n\,b\,c\,cos\alpha} \qquad (6.18)$$

where a, b, c are the lattice constants of the unit cell of malonic acid lattice, (α, β, γ) are the triclinic angles, as shown in Figure. 6.2b and (l, m, n) are the integer numbers charactrizing the position of the interacting spin in a triclinic lattice with respect to the observer spin as $\vec{r}_2 = l\,\vec{a} + m\,\vec{b} + n\,\vec{c}$. The dipolar coupling constant, d, is calculated, based on the distance of the two electrons, r_{12}, as $\omega_{dd}[MHz] = \frac{52.04}{r_{12}[nm]^3}$. The angle δ which is the polar angle of the orientation of the static magnetic field with respect to the dipolar axis that connects the magnetic dipoles of the two electrons is calculated as

δ

$$= cos^{-1} \left(\frac{nc \sqrt{1 - cos^2\beta - \left(\frac{cos\alpha - cos\beta cos\gamma}{sin\gamma}\right)^2}}{\sqrt{l^2a^2 + m^2b^2 + n^2c^2 + 2l\,m\,a\,b\,cos\gamma + 2l\,n\,a\,c\,cos\beta + 2m\,n\,b\,c\,cos\alpha}} \right) \quad (6.19)$$

Knowing the dipolar coupling constant, ω_{dd}, and the angle δ, one can then obtain $\omega_{dd}(3cos^2\delta - 1)$ appearing in Eq. (6.3) which is needed to calculate the SECSY signal of two coupled electrons as described in Sec. 6.2.1.

The many-body effects of spectral and instantanous diffusions on the SECSY signal of the malonic acid single crystal are considered seperately here by performing separate Monte Carlo simulations.

To consider *spectral diffusion*, one generates three sets of random numbers: (i) the Euler angles charactrizing the Zeeman energy of the second spin, C_2 $(\alpha_2, \beta_2, \gamma_2)$; (ii) a set of three integer numbers, (l, m, n), charactirzing the position of the interacting spin, which are used to determine the dipolar coupling constant, ω_{dd} and the angle angle δ; and (iii) a random number charactrizing the random flip rate of the second spin, W_2, which is chosen according to a Gaussian distribution with an average value of W_{2avg} and a width of σW_2. The spectral diffusion is a two-dimensional SECSY signal, $F_1(t_1, t_2)$, which is calculated following the procedure given in Sec. 6.2.1 with the three sets of random numbers generated as described here.

As for the instantanous diffusion, it manifests itself when an interacting spin is near or on resonance. The interacting spins which are exactly on resonance will have $C_2 = 0$. To consider those electron spins which are near resonance, but not exactly at resonance, say between p and 1, where p is a number less than 1 but close to 1, to be used as a parameter to indicate the fraction of spins close to resonance by 100×p%. One then multiplies the resulting signal $F_2(t_1, t_2)$, as if the interacting spin was at resonance by $\{r + p(1 - r)\}$ for instantanous diffusion due to spins near respnance by $100 \times$ p%, where p is a parameter between 0 and 1and r is a random number between 0 and 1. (The 2D-SECSY signal, $F_2(t_1, t_2)$ is calculated following the procedure given in Sec. 6.2.1.) By doing so, the contribution of the spins which are near resonance to the final signal will indeed be smaller than those which are exactly on resonance. Thus, for instantanoues diffusion, one needs to generate two sets of random numbers: (i) three integer numbers, (l, m, n), charactirzing the position of the interacting spin and (ii) a random numebr r which determines how close a spin is to exact resonance.

Size of the lattice In the calculations of the SECSY signal, one needs to determine the size of the lattice. In this work, a lattice with 100× 100 × 100 lattice points along vectors a, b, c (Figure 6.2a.) is considered. A maximum distance of 10.2 nm between the obseving sping centered at (0,0,0) and the other interacting electron spins is considered. This maximum distance

corresponds to the dipolar coupling constant $\omega_{dd} = 0.05\ MHz$ which is significantly small to cause instantanous or spectral diffusions.

The effects of instantanous and spectral diffusions on the SECSY signal of γ-irradiated malonic acid single crystal, are shown in Figure 6.3. Figure 6.3 a is the LPF signal similar to that shown in Fig. 6.1 a ,except for the parameter $\omega_n = 14.5\ MHz$ in Figure 6.1, which is here chosen to be $\omega_n = 14.2\ MHz$, found to give a better agreement with the experimental data. In Figure 6.3b, the effect of spectral diffusion on Fourier transform of LPF signal is calculated by multiplying the LPF two dimensional signal, $S(t_1, t_2)$, by $F_1(t_1, t_2)$ and then taking the Fourier transform. The same procedure as that used to produce Figure 6.3c is applied to consider the eefect of instantanoues diffusion on the LPF signal by calculating $F_2(t_1, t_2)\ S(t_1, t_2)$. The effect of instantanous and spectral diffusions can be seen in Fig 6.3d simultaneously which is the Fourier transform of $F_1(t_1, t_2)F_2(t_1, t_2)S(t_1, t_2)$. The random spin flip rates W_1, W_{2avg} used for spectral diffusion are $W_1 = 5 \times 10^5 s^{-1}$, $W_{2avg} = 5 \times 10^5\ s^{-1}$, which are the typical values for random spin flips used by Salikhov *et. al*. (1981), and the width of the Gaussian distribution of random flip rates $\sigma W_2 = 1 \times 10^5 s^{-1}$, whereas for the simulation of the instantaneous diffusion, the parameter $p = 0.5$ is chosen.

The effects of instantanous and spectral diffusions on the SECSY signal of γ-irradiated malonic acid single crystal, so calculated, are shown in Figs 6.3.a – d. Figure 6.3 a is the LPF signal similar to that shown in Figiure 6.1 a except for the parameter ω_n which was $\omega_n = 14.5\ MHz$ in Figure 6.1 and is here chosen to be $\omega_n = 14.2\ MHz$ which gives a better agreement with the experimental data. In Figure 6.3b, the effect of spectral diffusion on Fourier transform of the LPF signal is calculated by multiplying the LPF two dimensional signal, $S(t_1, t_2)$, by $F_1(t_1, t_2)$ and then taking the Fourier transform. The same procedure as that used to produce Figure 6.3c is used by calculating $F_2(t_1, t_2)\ S(t_1, t_2)$ to consider the eefect of the instantanoues diffusion on the LPF signal. The effect of instantanous and spectral diffusions together is shown in Fig 6.3d,which is the Fourier transform of $F_1(t_1, t_2)F_2(t_1, t_2)S(t_1, t_2)$.

As seen from Figure 6.3, after a detailed inspection, the Fourier transform of the LPF signal with instantaneous diffusion with the parameters used here is found to be in the best agreement with the experiment, shown in Fig. 6.3 (e), indicating that the instantaneous diffusion is the dominant relaxation mechanism in the SECSY signal of the electron-nuclear spin-coupled system in γ-irradiated malonic acid single crystal. It is noted that in the simulations shown in Figure 6.3, only one set of parameters is considered. The effect of varying the various parameters on spectral and instantaneous diffusions is under investigation.
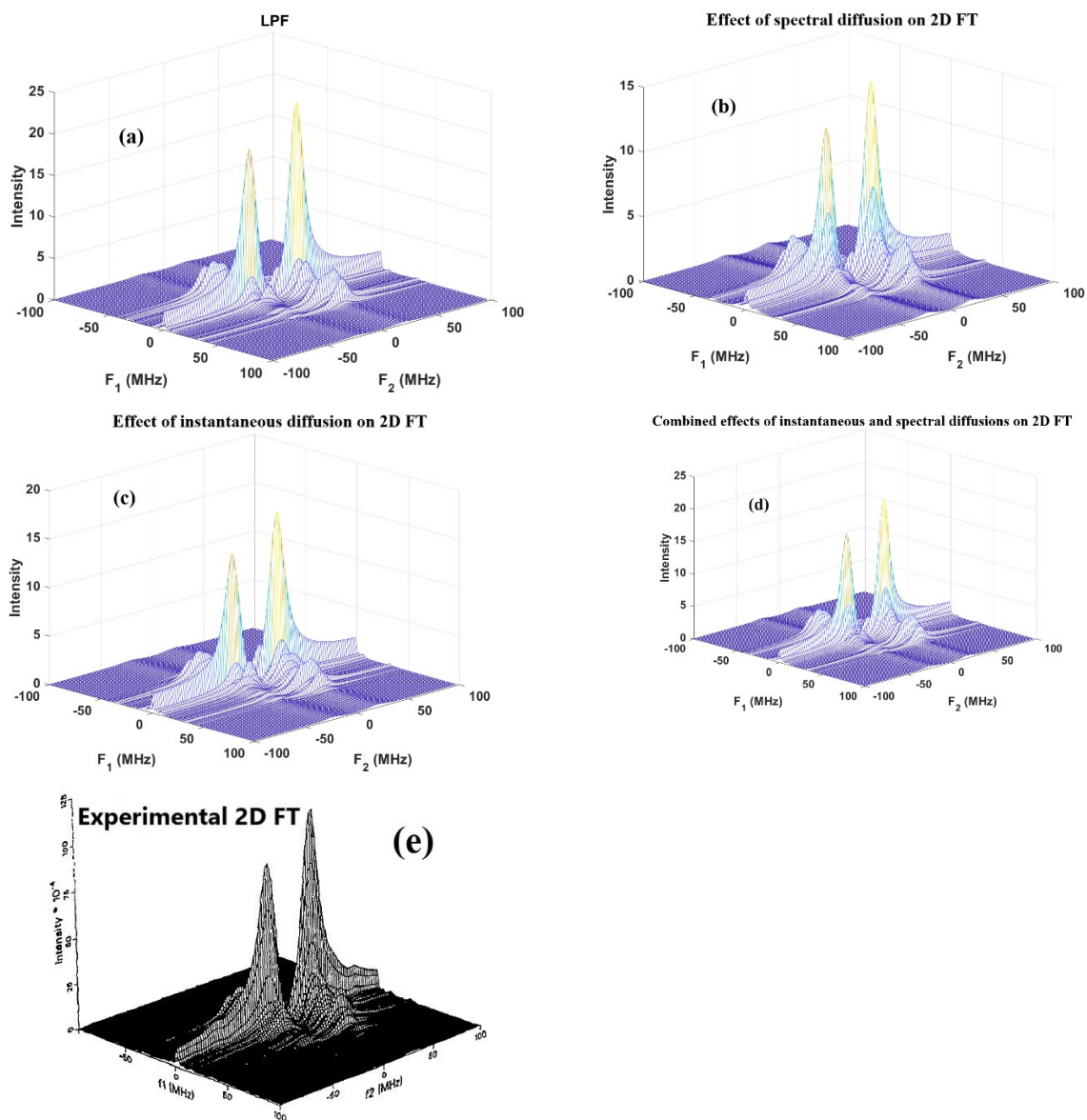
Figure 6.3 Two dimensional Fourier transforms obtained from γ-irradiated malonic acid single crystal SECSY signal. (a) Without spectral and/or instantaneous diffusion (b) with spectral diffusion (c) with instantaneous diffusion (d) with both instantaneous and spectral diffusions and (e) the experimental Fourier transform. The parameter used for instantaneous and spectral diffusions are $W_1 = 5 \times 10^5 s^{-1}$, $W_{2avg} = 5 \times 10^5 \ s^{-1}$, $\sigma W_2 = 1 \times 10^5 s^{-1}$, $p = 0.5$. The parameters used to simulate LPF signal are the same as those used for Figure 6.1 except for the nuclear Zeeman term, ω_n, which is chosen to be $\omega_n = 14.2$ MHz as found to give a better agreement with the experimental data.

146

It is noted that in the simulations shown in Figure 6.3, only one set of parameters are considered. The effect of the various parameters on spectral and instantaneous diffusions is under investigation.

6.3 Concluding remarks

The saliant features of this chapter are as follows

(i) Different matrix elements of density matrix may experience different relaxation times whose effect is seen from the different heights of the main peaks in the 2D Fourier transform of the SECSY signal of the electron-nuclear spin-coupled system in a γ-irradiated malonic acid single crystal.

(ii) The effects of instantaneous diffusion and spectral diffusion are calculated rigorously by the numerical simulation, considering the various relaxation mechanisms. described in this chapter.

(iii) The calculated 2D Fourier transform of the SECSY signal of the electron-nuclear spin-coupled system in a γ-irradiated malonic acid single crystal shows a better agreement with the experimental data by considering the effects of the instantaneous diffusion as compared to that calculated with spectral diffusion.

Chapter 7

7. Concluding remarks

In this thesis, numerical techniques to calculate pulsed EPR signals are exploited. Using numerical simulations, the multi-pulse signals including COSY, two-pulse DQ, 5-pulse DQM, 4-, 5-, 6-pulse DQC for the system of two coupled nitroxides in a biradical are calculated and the applicability of each pulse sequence for distance measurement is studied. It is shown, both analytically and numerically, that the one-dimensional multi-pulse techniques can be used for distance measurements in biological systems using nitroxide biradicals. This is because the Fourier transform of the various multi-pulse signals exhibit the Pake doublet at $\pm d$ except for two-pulse DQ where the Pake doublet occurs at $\pm\frac{3}{4}d$. The Fourier transform of COSY signal was found to have the maximum intensity whereas that for 6-pulse DQC is the cleanest. The Fourier transform of all the pulse sequences are broadened by including the relaxation effects except for 5- and 6-pulse DQC where the shape of the Fourier transform is not affected by considering the relaxation effects. Furthermore, the orientational selectivity occurring in two-pulse DQ and five-pulse DQM pulse sequences was investigated. It was found that the maximum coherence transfer occurs for those spins whose dipolar axis is oriented within $\pm 10°$ from the magic angle i.e., $\theta = 54.7°$ and its complementary angle.

This numerical approach was then extended to the doubly rotating frames (DRF) technique where one calculates the DEER signal rigorously by using two rotating frames. The doubly rotating frame was successfully applied to calculate the DEER signal which found to be in a very good agreement with reported experimental DEER data for both coupled nitroxides and coupled Gd^{3+} ions, the latter with a significant zero-field splitting. The signals calculated by the DRF technique were then used as kernel signals in *DeerAnalysis* software to estimate the distance distribution between the nitroxide biradicals on a sample of bis-nitroxide nanowire, P1, in deuterated ortho-terphenyl solvent with 5% BnPy (d14-oTP/BnPy) as well as between the Gd^{3+} ions in sample Gd ruler 1_5 in D_2O/glycerol-d_8 (7/3 volume ratio). An improvement in the distance distribution, $P(r)$, calculated by DRF calculated signal compared to that calculated by using analytical kernel signals was found. Therefore, for more accurate estimation of distance distribution probabilities, one should use DRF-calculated basis signal which considers the ZFS and finiteness of the pulses.

Two models to consider fluctuations of spin-Hamiltonian parameters, namely cylindrical and conical models, were exploited to calculate the effect of thermal fluctuations of malonic acid molecule. In the cylindrical model, the tip of the director of the malonic acid molecule is assumed to move in a plane whereas in conical model, the director can move on a cone. Using the cylindrical model, the amplitude of these fluctuations was estimated. In the conical model, a restoring potential was introduced, and the strength of the potential was estimated using the model presented. Both the models give an estimation of correlation times, τ_c. The conical and cylindrical models were then used to rigorously calculate the matrix elements of the relaxation

matrix in the Liouville space. Using the calculated relaxation matrix, the echo-ELDOR signal was simulated, which showed an excellent agreement with the published experimental data.

To further improve the theory of 2D Fourier transform EPR, the projection operator used in calculation of SECSY signal in γ-irradiated malonic acid crystal was modified to consider the different relaxation rates experienced by different matrix element of the density matrix. The Fourier transform obtained from two-dimensional SECSY signal using the modified projection operator was shown to give a better agreement with the experimental data.

Many body effects, including the instantaneous and spectral diffusions, were studied by a rigorous numerical approach in Liouville space for the system consisting of an electron-nuclear spin-coupled system in a γ-irradiated malonic acid single crystal.

Chapter 8

8. Future perspectives

The numerical algorithm to calculate the single-frequency multi-pulse sequences EPR signals presented here can be applied for more accurate analysis of pulsed EPR spectrum. In particular, a source code in Matlab to calculate COSY, two-pulse DQ, 5-pulse DQM, 4-, 5-, 6-pulse DQC EPR signals using the presented numerical algorithms has been developed which can be further exploited for other purposes. Furthermore, the doubly rotating frame technique for a rigorous calculation of DEER signal can be used to construct the basis kernel signals, to be used in other software, such as *DeerAnalysis* and *EasySpin* for more accurate estimation of distance distribution probabilities, $P(r)$, values more accurtely from DEER data in biological systems, doped with radicals with $S \geq 1$, exhibiting ZFS, using finite pulses, e.g., Gd^{3+}, Ni^{2+}, Mn^{2+}. In addition, the model developed to carry out this quantitative numerical study of the many-body effects on pulsed EPR signal including the instantaneous and spectral diffusions presented in this thesis can be extended to other systems in the solid state.

References

Abragam, Anatole. 1961. *The principles of nuclear magnetism.* Oxford university press.

Bodenhausen, Geoffrey, Herbert Kogler, and R. R. Ernst. 1984. "Selection of coherence-transfer pathways in NMR pulse experiments." *Journal of Magnetic Resonance (1969)* (Elsevier) 58: 370–388.

Borbat, Peter P., and Jack H. Freed. 2007. *Measuring distances by pulsed dipolar ESR spectroscopy: spin-labeled histidine kinases.* Vol. 423, in *Methods in enzymology*, 52–116. Elsevier.

Borbat, Petr P., and Jack H. Freed. 1999. "Multiple-quantum ESR and distance measurements." *Chemical Physics Letters* (Elsevier) 313: 145–154.

Borbat, Petr, Jack Freed, and others. 2002. "Double-quantum ESR and distance measurements." In *Distance measurements in biological systems by EPR*, 383–459. Springer.

Chiang, Yun-Wei, Peter P. Borbat, and Jack H. Freed. 2005. "The determination of pair distance distributions by pulsed ESR using Tikhonov regularization." *Journal of Magnetic Resonance* (Elsevier) 172: 279–295.

Cohen, Marie Ramirez, Veronica Frydman, Petr Milko, Mark A. Iron, Elwy H. Abdelkader, Michael D. Lee, James D. Swarbrick, et al. 2016. "Overcoming artificial broadening in Gd 3+–Gd 3+ distance distributions arising from dipolar pseudo-secular terms in DEER experiments." *Physical Chemistry Chemical Physics* (Royal Society of Chemistry) 18: 12847–12859.

Dalaloyan, Arina, Mian Qi, Sharon Ruthstein, Shimon Vega, Adelheid Godt, Akiva Feintuch, and Daniella Goldfarb. 2015. "Gd (III)–Gd (III) EPR distance measurements–the range of accessible distances and the impact of zero field splitting." *Physical Chemistry Chemical Physics* (Royal Society of Chemistry) 17: 18464–18476.

Doll, Andrin, Mian Qi, Nino Wili, Stephan Pribitzer, Adelheid Godt, and Gunnar Jeschke. 2015. "Gd (III)–Gd (III) distance measurements with chirp pump pulses." *Journal of Magnetic Resonance* (Elsevier) 259: 153–162.

Dubinskii, Alexander A., Günter G. Maresch, and Hans-Wolfgang Spiess. 1994. "Two-dimensional electron paramagnetic resonance spectroscopy of nitroxides: Elucidation of restricted molecular motions in glassy solids." *The Journal of chemical physics* (American Institute of Physics) 100: 2437–2448.

Dzuba, S. A., E. S. Salnikov, and L. V. Kulik. 2006. "CW EPR, echo-detected EPR, and field-step ELDOR study of molecular motions of nitroxides ino-terphenyl glass: Dynamical transition, dynamical heterogeneity and β-relaxation." *Applied Magnetic Resonance* (Springer) 30: 637–650.

Edwards, Devin T., Thomas Huber, Sunyia Hussain, Katherine M. Stone, Maia Kinnebrew, Ilia Kaminker, Erez Matalon, Mark S. Sherwin, Daniella Goldfarb, and Songi Han. 2014.

"Determining the oligomeric structure of proteorhodopsin by Gd3+-based pulsed dipolar spectroscopy of multiple distances." *Structure* (Elsevier) 22: 1677–1686.

Edwards, Thomas H., and Stefan Stoll. 2018. "Optimal Tikhonov regularization for DEER spectroscopy." *Journal of Magnetic Resonance* (Elsevier) 288: 58–68.

El Mkami, Hassane, and David G. Norman. 2015. *EPR distance measurements in deuterated proteins.* Vol. 564, in *Methods in enzymology*, 125–152. Elsevier.

El Mkami, Hassane, Richard Ward, Andrew Bowman, Tom Owen-Hughes, and David G. Norman. 2014. "The spatial effect of protein deuteration on nitroxide spin-label relaxation: Implications for EPR distance measurement." *Journal of Magnetic Resonance* (Elsevier) 248: 36–41.

Franck, John M., Siddarth Chandrasekaran, Boris Dzikovski, Curt R. Dunnam, and Jack H. Freed. 2015. "Focus: Two-dimensional electron-electron double resonance and molecular motions: The challenge of higher frequencies." *The Journal of Chemical Physics* (AIP Publishing LLC) 142: 212302.

Freed, J. H. 1976. "Spin labeling: theory and applications." *by LJ Berliner, Academic Press, New York, NY* 67–69.

Frezzato, Diego, Gerd Kothe, and Giorgio J. Moro. 2004. "Director fluctuations and ESR spectra: A slow-motional treatment." *The Journal of Physical Chemistry B* (ACS Publications) 108: 9505–9515.

Gamliel, Dan, and Haim Levanon. 1995. *Stochastic processes in magnetic resonance.* World Scientific.

Gamliel, Dan, and Jack H. Freed. 1990. "Theory of two-dimensional ESR with nuclear modulation." *Journal of Magnetic Resonance (1969)* (Elsevier) 89: 60–93.

Gemperle, C., G. Aebli, A. Schweiger, and R. R. Ernst. 1990. "Phase cycling in pulse EPR." *Journal of Magnetic Resonance (1969)* (Elsevier) 88: 241–256.

Georgieva, Elka R., Aritro S. Roy, Vladimir M. Grigoryants, Petr P. Borbat, Keith A. Earle, Charles P. Scholes, and Jack H. Freed. 2012. "Effect of freezing conditions on distances and their distributions derived from Double Electron Electron Resonance (DEER): A study of doubly-spin-labeled T4 lysozyme." *Journal of Magnetic Resonance* (Elsevier) 216: 69–77.

Håkansson, Pär, ThaoNguyen Nguyen, Prasanth B. Nair, Ruth Edge, and Eugen Stulz. 2013. "Cu (II)–porphyrin molecular dynamics as seen in a novel EPR/Stochastic Liouville equation study." *Physical Chemistry Chemical Physics* (Royal Society of Chemistry) 15: 10930–10941.

Hogben, Hannah J., Matthew Krzystyniak, Gareth T. P. Charnock, Peter J. Hore, and Ilya Kuprov. 2011. "Spinach–a software library for simulation of spin dynamics in large spin systems." *Journal of Magnetic Resonance* (Elsevier) 208: 179–194.

Jeener, Jean. 1982. *Superoperators in magnetic resonance.* Vol. 10, in *Advances in Magnetic and Optical Resonance*, 1–51. Elsevier.

Jeschke, G. 2007. *ESR Spectroscopy in Membrane Biophysics.* Boston, MA: Springer US.

Jeschke, Gunnar. 2007. "Instrumentation and experimental setup." In *ESR spectroscopy in membrane biophysics*, 17–47. Springer.

Jeschke, Gunnar, Victor Chechik, Petre Ionita, Adelheid Godt, Herbert Zimmermann, J. Banham, C. R. Timmel, D. Hilger, and H. Jung. 2006. "DeerAnalysis2006—a comprehensive software package for analyzing pulsed ELDOR data." *Applied magnetic resonance* (Springer) 30: 473–498.

Kaminker. 2012. "Ph. D. Thesis, Weizmann Institute of Science, Rehovot, Israel."

Kuprov, Ilya, Nicola Wagner-Rundell, and P. J. Hore. 2007. "Bloch-Redfield-Wangsness theory engine implementation using symbolic processing software." *Journal of Magnetic Resonance* (Elsevier) 184: 196–206.

Lee, Sanghyuk, Baldev R. Patyal, and Jack H. Freed. 1993. "A two-dimensional Fourier transform electron-spin resonance (ESR) study of nuclear modulation and spin relaxation in irradiated malonic acid." *The Journal of chemical physics* (American Institute of Physics) 98: 3665–3689.

Lovett, J. E., Brendon W. Lovett, and J. Harmer. 2012. "DEER-Stitch: Combining three-and four-pulse DEER measurements for high sensitivity, deadtime free data." *Journal of Magnetic Resonance* (Elsevier) 223: 98–106.

Magnus, Jan R., and Heinz Neudecker. 2019. *Matrix differential calculus with applications in statistics and econometrics.* John Wiley & Sons.

Manukovsky, Nurit, Veronica Frydman, and Daniella Goldfarb. 2015. "Gd3+ spin labels report the conformation and solvent accessibility of solution and vesicle-bound Melittin." *The Journal of Physical Chemistry B* (ACS Publications) 119: 13732–13741.

Maryasov, A. G., and Yu D. Tsvetkov. 2000. "Formation of the pulsed electron-electron double resonance signal in the case of a finite amplitude of microwave fields." *Applied Magnetic Resonance* (Springer) 18: 583–605.

McConnell, H. M., C. Heller, T. Cole, and R. W. Fessenden. 1960. "Radiation damage in organic crystals. I. CH (COOH) 2 in malonic acid1." *Journal of the American Chemical Society* (ACS Publications) 82: 766–775.

Misra, Sushil K. 2011. *Multifrequency electron paramagnetic resonance: theory and applications.* John Wiley & Sons.

Misra, Sushil K., and Hamid Reza Salahi. 2021. "Relaxation in pulsed EPR: thermal fluctuation of spin-hamiltonian parameters of an electron-nuclear spin-coupled system in a malonic

acid single crystal in a strong harmonic-oscillator restoring potential." *Applied Magnetic Resonance* (Springer) 52: 247–261.

Misra, Sushil K., and Jack H. Freed. 2011. "Distance measurements: continuous-wave (CW)-and pulsed dipolar EPR." *Multifrequency Electron Paramagnetic Resonance. Theory and Applications, 1st ed.; WILEY-VCH Verlag GmbH & Co. KGaA: Weinheim, Germany* 545–588.

Misra, Sushil K., and Lin Li. 2018. "A Rigorous Procedure for Calculation of Pulsed EPR Signals with Relaxation." *J Apl Theol* 2: 5–16.

Misra, Sushil K., Peter P. Borbat, and Jack H. Freed. 2009. "Calculation of double-quantum-coherence two-dimensional spectra: distance measurements and orientational correlations." *Applied magnetic resonance* (Springer) 36: 237–258.

Pannier, Matthias, Stephan Veit, Adelheid Godt, Gunnar Jeschke, and Hans Wolfgang Spiess. 2011. "Dead-time free measurement of dipole–dipole interactions between electron spins." *Journal of magnetic resonance* (Elsevier) 213: 316–325.

Perrin, Charles L. 2018. "Polynomial coefficients. Application to spin–spin splitting by N equivalent nuclei of spin I> 1/2." *Magnetic Resonance in Chemistry* (Wiley Online Library) 56: 799–802.

Pfenninger, Susanne, W. E. Antholine, M. E. Barr, James S. Hyde, P. M. Kroneck, and W. G. Zumft. 1995. "Electron spin-lattice relaxation of the [Cu (1.5)... Cu (1.5)] dinuclear copper center in nitrous oxide reductase." *Biophysical journal* (Elsevier) 69: 2761–2769.

Polnaszek, C. F., G. V. Bruno, and Jack H. Freed. 1973. "ESR line shapes in the slow-motional region: Anisotropic liquids." *The Journal of Chemical Physics* (American Institute of Physics) 58: 3185–3199.

Potapov, Alexey, Hiromasa Yagi, Thomas Huber, Slobodan Jergic, Nicholas E. Dixon, Gottfried Otting, and Daniella Goldfarb. 2010. "Nanometer-scale distance measurements in proteins using Gd3+ spin labeling." *Journal of the American Chemical Society* (ACS Publications) 132: 9040–9048.

Raitsimring, Arnold M., Chidambaram Gunanathan, Alexey Potapov, Irena Efremenko, Jan M. L. Martin, David Milstein, and Daniella Goldfarb. 2007. "Gd3+ complexes as potential spin labels for high field pulsed EPR distance measurements." *Journal of the American Chemical Society* (ACS Publications) 129: 14138–14139.

Raitsimring, Arnold, and Petr Borbat. 1996. "Electron spin-echo modulation for a '1+ 2'pulse train in a weak hyperfine interaction limit." *Chemical physics letters* (Elsevier) 262: 8–16.

Redfield, Alfred G. 1957. "On the theory of relaxation processes." *IBM Journal of Research and Development* (IBM) 1: 19–31.

Salikhov, K. M., S.-A Dzuba, and A.N.D.A. M. Raitsimring. 1981. "The theory of electron spin-echo signal decay resulting from dipole-dipole interactions between paramagnetic centers in solids." *Journal of Magnetic Resonance (1969)* (Elsevier) 42: 255–276.

Saxena, Sunil, and Jack H. Freed. 1996. "Double quantum two-dimensional Fourier transform electron spin resonance: Distance measurements." *Chemical physics letters* (Elsevier) 251: 102–110.

Saxena, Sunil, and Jack H. Freed. 1997. "Theory of double quantum two-dimensional electron spin resonance with application to distance measurements." *The Journal of chemical physics* (American Institute of Physics) 107: 1317–1340.

Schwartz, Leslie J., Arthur E. Stillman, and Jack H. Freed. 1982. "Analysis of electron spin echoes by spectral representation of the stochastic Liouville equation." *The Journal of Chemical Physics* (American Institute of Physics) 77: 5410–5425.

Schweiger, A. and G. Jeschke. 2001. *Principles of pulse electron paramagnetic resonance.*

Schweiger, Arthur, and Gunnar Jeschke. 2001. *Principles of pulse electron paramagnetic resonance.* Oxford University Press on Demand.

Slichter, Charles P. 2013. *Principles of magnetic resonance.* Vol. 1. Springer Science & Business Media.

Stein, Natalia, Laxman Mainali, James S. Hyde, and Witold K. Subczynski. 2019. "Characterization of the Distribution of Spin–Lattice Relaxation Rates of Lipid Spin Labels in Fiber Cell Plasma Membranes of Eye Lenses with a Stretched Exponential Function." *Applied magnetic resonance* (Springer) 50: 903–918.

Stoll, Stefan, and Arthur Schweiger. 2006. "EasySpin, a comprehensive software package for spectral simulation and analysis in EPR." *Journal of magnetic resonance* (Elsevier) 178: 42–55.

Stoll, Stefan, and R. David Britt. 2009. "General and efficient simulation of pulse EPR spectra." *Physical Chemistry Chemical Physics* (Royal Society of Chemistry) 11: 6614–6625.

Yagi, Hiromasa, Debamalya Banerjee, Bim Graham, Thomas Huber, Daniella Goldfarb, and Gottfried Otting. 2011. "Gadolinium tagging for high-precision measurements of 6 nm distances in protein assemblies by EPR." *Journal of the American Chemical Society* (ACS Publications) 133: 10418–10421.

Appendices

Appendix A. Spin Hamiltonian for nitroxide biradical

In this appendix, the coefficients C, A and B of the spin Hamiltonian of a nitroxide are defined. The coupled- nitroxide static Hamiltonian, used in Eq. (3.2), can be expressed in terms of the irreducible spherical tensor operators (ISTO) as (Saxena and Freed 1997, Misra $et. al.$ 2009)

$$H_{0k} = \sum_{\mu_k, L, M} F_{\mu_k, l}^{L, M^*} A_{\mu_k, l}^{L, M} \ k \ (=1,2) \tag{A.1}$$

where μ_k determines type of the interaction and takes two values: g_k or A_k for Zeeman and Hyperfine interactions, respectively, k (=1,2) specifies the two nitroxides, L is the rank of the tensor, and M takes integer values between $-L$ and $+L$. Here l stands for the *laboratory* frame, defined to be such that the z-axis is parallel to the static magnetic field. In Eq. (A.1), $F_{\mu_k, l}^{L, M^*}$ are the standard ISTO components of the magnetic tensors of μ_k kind in the laboratory reference frame. These $F_{\mu_k, l}^{L, M^*}$s are conveniently defined in the magnetic g-frame of a nitroxide ($F_{\mu_k, g}^{L, M^*}$) and then transformed to the laboratory frame by two successive transformations: first, from the g-frame to the dipolar frame defined by its z-axis along the vector connecting the magnetic dipoles of the two nitroxides and then to the laboratory frame. The various components of $A_{\mu_k, l}^{L, M}$ and $F_{\mu_k, g}^{L, M}$ are listed in (Freed 1976). Note that in the high-field limit, the contribution of the non-secular terms of $A_{\mu_k, l}^{L, M}$ (i.e., $S_\pm, S_\pm I_z, S_\pm I_\pm, S_\pm I_\mp$) is negligible. Using the Wigner D-matrices $D_{m, m'}^L$, the transformed $F_{\mu_k, l}^{L, M^*}$ can then be expressed as

$$F_{\mu_k, l}^{L, M^*} = \sum_{m', m''} D_{m, m'}^L (\eta) D_{m', m''}^L (\lambda_k) F_{\mu_k, g}^{L, m''} \tag{A.2}$$

where $\eta = (\alpha, \beta, \gamma)$ and $\lambda_k = (0, \theta, \varphi)$ are the Euler angles defining the two transformations from g-frame to the dipolar frame and from the dipolar frame to the laboratory frame, respectively. Inserting Eq. (A.2) into Eq. (A.1), the static Hamiltonian of two coupled nitroxides in the laboratory frame in the secular approximation, i.e., neglecting the non-secular terms, is

$$H_0 = \sum_{k=1,2} H_{0k} = \sum_{k=1,2} S_{zk} [C_k + A_k I_{zk} + B_k I_{+k} + B_k^* I_{-k}] \tag{A.3}$$

where the coefficients C_k, A_k, B_k are defined in the rotating frame as

$$C_k = \sqrt{\frac{2}{3}} \sum_{m'} D_{0, m'}^2 (\eta_k) K_{g_k, m'} (\lambda_k) \tag{A.4}$$

$$A_k = \sqrt{\frac{2}{3}} \sum_{m'} D_{0, m'}^2 (\eta_k) K_{A_k, m'} (\lambda_k) + \frac{g_e \beta_e}{3\hbar} (A_{xx} + A_{yy} + A_{zz}) \tag{A.5}$$

$$B_k = \frac{1}{2} \sum_{m'} D_{1, m'}^2 (\eta_k) K_{A_k, m'} (\lambda_k) \tag{A.6}$$

It is noted that the isotropic part of the Zeeman term is put equal to zero in the rotating frame and the Zeeman term, as given by Eq. (A.4), is the resonant offset term as calculated here

quantitively. The $K_{\mu_i,m'}$ terms in Eqs. (A.4) -(A.6), which contain the transformation from the magnetic frame to the dipolar frame, are defined as

$$K_{\mu_i,m'}(\lambda_i) = \left[D^2_{m',2}(\lambda_i) + D^2_{m',-2}(\lambda_i)\right]F^{2,2}_{\mu_i,g} + D^2_{m',0}(\lambda_i)F^{2,0}_{\mu_i,g} \qquad (A.7)$$

Appendix B. Projection operators for the various coherence pathways

The Projection operators for the various coherence pathways, which project the density matrix of coupled nitroxide system on to the coherence pathway of interest after the application of a pulse, are listed in this Appendix for the coherence pathways $p = 0$, $p = \pm1$ and $p = \pm2$. After the application of a projection operator, only those 9×9 blocks of the density matrix which correspond to the non-zero elements of the projection operator are retained, using Hadamard product, putting all the other elements of the density matrix equal to zero.

Coherence pathway	Matrix elements to be retained by Hadamard product
$p = +1$	$\begin{pmatrix} 0 & 1 & 1 & 0 \\ 0 & 0 & 0 & 1 \\ 0 & 0 & 0 & 1 \\ 0 & 0 & 0 & 0 \end{pmatrix}$
$p = -1$	$\begin{pmatrix} 0 & 0 & 0 & 0 \\ 1 & 0 & 0 & 0 \\ 1 & 0 & 0 & 0 \\ 0 & 1 & 1 & 0 \end{pmatrix}$
$p = +2$	$\begin{pmatrix} 0 & 0 & 0 & 1 \\ 0 & 0 & 0 & 0 \\ 0 & 0 & 0 & 0 \\ 0 & 0 & 0 & 0 \end{pmatrix}$
$p = -2$	$\begin{pmatrix} 0 & 0 & 0 & 0 \\ 0 & 0 & 0 & 0 \\ 0 & 0 & 0 & 0 \\ 1 & 0 & 0 & 0 \end{pmatrix}$
$p = 0$	$\begin{pmatrix} 1 & 0 & 0 & 0 \\ 0 & 1 & 1 & 0 \\ 0 & 1 & 1 & 0 \\ 0 & 0 & 0 & 1 \end{pmatrix}$

Appendix C. Flowchart for the calculation of the multi-pulse signals
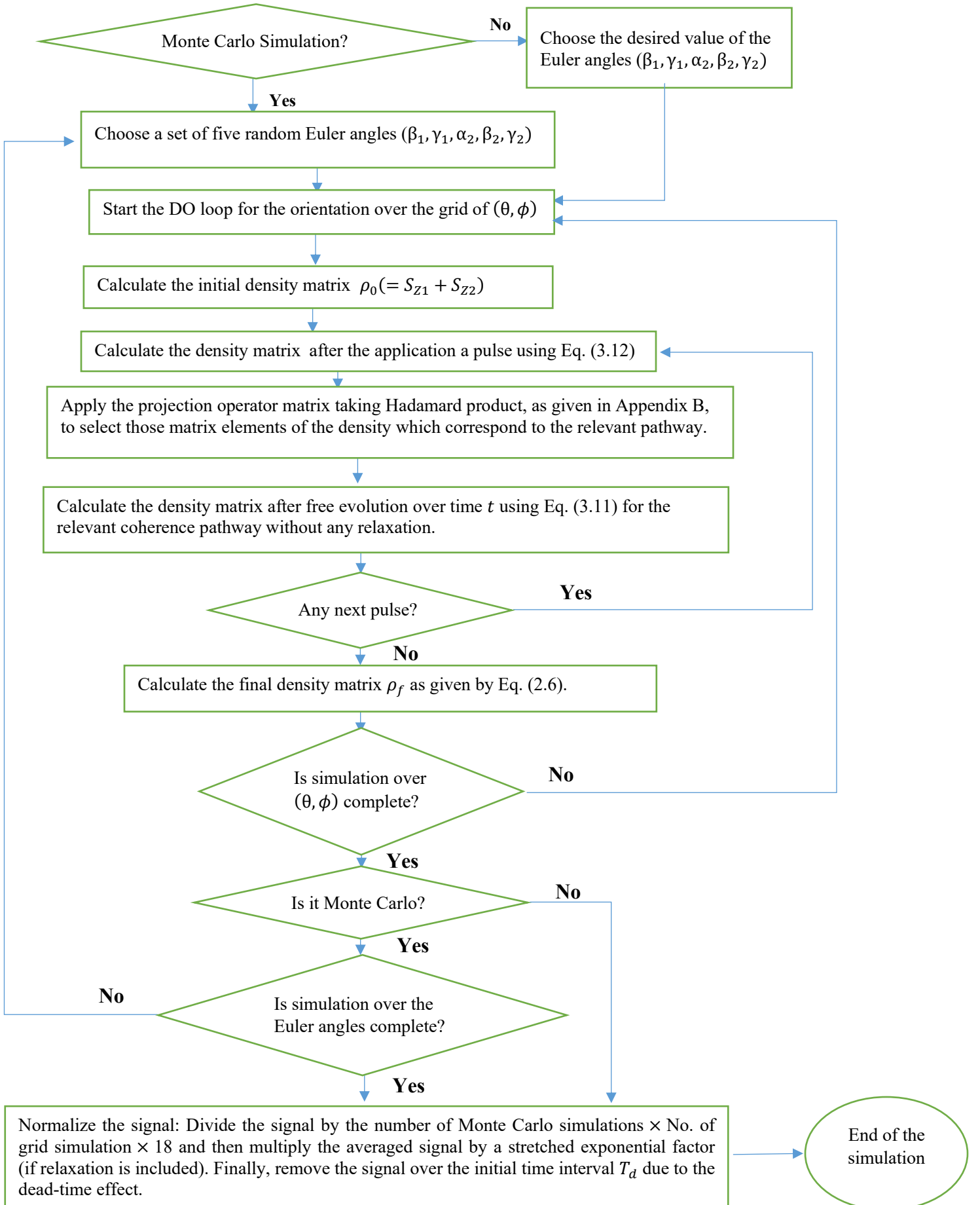
Appendix D. An analytical expression for modulation depth

In this Appendix, the analytical expression of $S'(t)$, found by integrating Eq. (3.18) for an isotropic modulation depth, i.e., $\delta_m(\eta, \lambda_1, \lambda_2) = \Delta$, along with the analytical expression of its Fourier transform are provided. The analytical expression as calculated using *Mathematica is*.

$$S'(t) = S'_0 \left(\frac{\Delta \left(C(q_1)\cos(td) + S(q_1)\sin(td) \right)}{q_1} + (1 - \Delta) \right)$$

(D.1)

where $q_1 = \sqrt{\frac{6}{\pi}t}\, d$ and $C(x)$ and $S(x)$ are FresnelC and FresnelS functions, respectively, which are defined as

$$C(x) = \int_0^x \cos(t^2)dt$$
$$S(x) = \int_0^x \sin(t^2)dt$$

(D.2)

As time $t \to 0$, the first term in bracket in Eq. (C.1) becomes equal to Δ, the second term approaches 0, so that $S'(t \to 0) = S'_0$. Equation (D.1) thus describes a time domain signal that has its maximum value S'_0 at time $t = 0$, then it drops as time increases and undergoes decaying oscillations, because of $\sqrt{t}$ in q_1 in the denominator, around the equilibrium value S'_{eq}, as follows.

$$S'(t) = S'_{eq} + S'_0 \left(\frac{\Delta \left(C(q_1)\cos(td) + S(q_1)\sin(td) \right)}{q_1} \right)$$

(D.3)

where,

$$S'_{eq} = S'_0(1 - \Delta),$$

(D.4)

Therefore, by measuring S'_0 and S'_{eq} from the time-domain signal, the modulation depth can be calculated as $\Delta = \left(S'_0 - S'_{eq} \right)/S'_0$. The Fourier transform of $S'(t)$ with respect to the variable t, is found to be, using *Mathematica*:

$$S''(\omega) = \int_{-\infty}^{\infty} S'(t)\, e^{-i\omega t} dt = 4\sqrt{2}\pi^{\frac{3}{2}} S'_0 [(1 - \Delta)\delta(\omega)$$

$$-\frac{\Delta}{4\sqrt{3d}} \left(\frac{\Theta(d+\omega)[\Theta\{\frac{1}{9}-\frac{d^2}{(d+\omega)^2}\}-1]}{(d+\omega)^{1/2}} + \frac{\Theta(d-\omega)[\Theta\{\frac{1}{9}-\left|\frac{d^2}{(d-\omega)^2}\right|\}-1]}{(d-\omega)^{1/2}} \right)]$$

(D.5)

where $\delta(\omega)$ is the Dirac delta function and $\Theta(x)$ is the Heaviside function which is defined as

$$\Theta(x) = \begin{cases} 1, & x > 0 \\ 0, & x < 0 \end{cases}$$

(D.6)

It is seen that the peaks of $S''(\omega)$ as given by Eq. (D.5) occur at $\pm\omega$. The plots of $S'(t)$ and $S''(\omega)$ for two values of Δ, $\Delta = 0.4$ and $\Delta = 0.7$, are shown in Fig. 8.

Appendix E. Matrix Representation, eigenvalues and eigenvectors
of the static Hamiltonian

The magnetic basis, defined in the direct product of the electron spin basis eigenvectors $M_S = |+\rangle$ and $|-\rangle$ and the nuclear spin basis eigenvectors, $m_I = |-1\rangle, |0\rangle$ and $|1\rangle$, are used here for matrix representation of the static Hamiltonian. The matrix for Eq. (A.3), for example, for one of the nitroxide biradicals, can be expressed in this basis as

$$H_{01} = \begin{pmatrix} \frac{1}{2}(A_1 + C_1) & \frac{B_1}{\sqrt{2}} & 0 & 0 & 0 & 0 \\ \frac{B_1}{\sqrt{2}} & \frac{C_1}{2} & \frac{B_1}{\sqrt{2}} & 0 & 0 & 0 \\ 0 & \frac{B_1}{\sqrt{2}} & \frac{1}{2}(C_1 - A_1) & 0 & 0 & 0 \\ 0 & 0 & 0 & \frac{-1}{2}(A_1 + C_1) & -\frac{B_1}{\sqrt{2}} & 0 \\ 0 & 0 & 0 & -\frac{B_1}{\sqrt{2}} & -\frac{C_1}{2} & -\frac{B_1}{\sqrt{2}} \\ 0 & 0 & 0 & 0 & -\frac{B_1}{\sqrt{2}} & \frac{1}{2}(A_1 - C_1) \end{pmatrix} \quad \text{(E.1)}$$

The matrix in Eq. (E.1) is diagonalized by a unitary transformation as $E_1 = T^{(1)\dagger} H_{01} T^{(1)}$, where $T^{(1)}$ is

$$T^{(1)} = \begin{pmatrix} T_\alpha^{(1)} & 0 \\ 0 & T_\alpha^{(1)} \end{pmatrix} \quad \text{(E.2)}$$

where $T_\alpha^{(1)}$ is a 3×3 matrix, using the basis vectors $\left(|\psi_{-1}^{(1)}\rangle, |\psi_0^{(1)}\rangle, \psi_1^{(1)}\rangle\right)$, as follows:

$$T_\alpha^{(1)} == \begin{pmatrix} \dfrac{A_1(A_1 + \omega) + 2|B_1|^2}{\omega_+} & -\dfrac{|B_1|}{\sqrt{2}\omega} & \dfrac{-A_1\omega + A_1^2 + 2|B_1|^2}{\omega_-} \\[3ex] \dfrac{\sqrt{2}(A_1 + \omega)|B_1|}{\omega_+} & \dfrac{A_1}{\omega} & \dfrac{\sqrt{2}(A_1 - \omega)|B_1|}{\omega_-} \\[3ex] \dfrac{2|B_1|^2}{\omega_+} & \dfrac{|B_1|}{\sqrt{2}\omega} & \dfrac{2|B_1|^2}{\omega_-} \end{pmatrix} \qquad (E.3)$$

where,

$$\omega = \sqrt{A_1^2 + 4|B_1|^2}$$
(E.3a)

$$\omega_+ = \sqrt{2(A_1 + \omega)(3A_1 + \omega)|B_1|^2 + A_1^2(A_1 + \omega)^2 + 8|B_1|^4}$$

$$\omega_- = \sqrt{2(\omega - A_1)(\omega - 3A_1)|B_1|^2 + A_1^2(\omega - A_1)^2 + 8|B_1|^4}$$

Similar results for H_{02} for the second nitroxide can be obtained by $A_1 \to A_2$ and $B_1 \to B_2$.

For the coupled nitroxides system, the spin Hamiltonian in Eq. (A.3) has the dimension in the Hilbert space: $(2S_1 + 1)(2S_2 + 1)(2I_1 + 1)(2I_2 + 1) = 36$, which can be split into sixteen 9×9 blocks, of which only six blocks have non-zero elements, as shown in the matrix (E.5) below. The non-zero blocks are: (1,1), (2,2), (2,3), (3,2), (3,3) and (4,4). Each block of this block is diagonalized by the unitary transformation $U^\dagger H_{ij} U$, where U is constructed from the direct product of the eigenvectors in the spin basis of the two coupled nuclei as

$$T_\alpha^{(1)} \otimes T_\alpha^{(2)} = |\psi_j^{(1)}; \psi_k^{(2)}\rangle \qquad (E.4)$$

where $j, k = -1, 0, 1$. Using the eigenvectors of Eq (E.4), the matrix of the static Hamiltonian of the coupled nitroxides system can be expressed as

$$H_0 = \begin{pmatrix} [[H_{11}]] & [[0]] & [[0]] & [[0]] \\ [[0]] & [[H_{22}]] & [[H_{23}]] & [[0]] \\ [[0]] & [[H_{32}]] & [[H_{33}]] & [[0]] \\ [[0]] & [[0]] & [[0]] & [[H_{44}]] \end{pmatrix} \qquad (E.5)$$

In (E.5), the double square bracket [[]] are used to indicate a diagonal matrix in the hyperfine space. In Eq. (E.5), the blocks $H_{23} = H_{32}$, with real elements, are non-zero due to the dipolar interaction between the two nitroxide radicals. Each matrix element in Eq. (E.5) is a 9×9

diagonal matrix, corresponding to different indices l, m in the direct-product space, which are combinations of $j, k, j', k' = -1, 0, 1$, as follows: $l = 3j + k + 5, m = 3j' + k' + 5$, so that l, m=1, 2, ….,9. These are given by

$$(H_{11})_{lm} = \{\frac{1}{2}[C_1 + C_2 + (A_1^2 + 4|B_1|^2 j)^{1/2} j + (A_2^2 + 4|B_2|^2 k)^{1/2} k] + \frac{d}{4}(3\cos^2\theta - 1)\}\delta_{lm},$$

$$(H_{22})_{lm} = \{\frac{1}{2}[C_1 - C_2 + (A_1^2 + 4|B_1|^2 j)^{1/2} j - (A_2^2 + 4|B_2|^2 k)^{1/2} k]$$
$$- \frac{d}{4}(3\cos^2\theta - 1)\}\delta_{lm},$$

$$(H_{23})_{lm} = (H_{32})_{lm} = -\frac{d}{4}(3\cos^2\theta - 1)\delta_{lm},$$

$$(H_{33})_{lm} = \{\frac{1}{2}[-C_1 + C_2 - (A_1^2 + 4|B_1|^2 j)^{1/2} j + (A_2^2 + 4|B_2|^2 k)^{1/2} k]$$
$$- \frac{d}{4}(3\cos^2\theta - 1)\}\delta_{lm},$$

$$(H_{44})_{lm} = \{-\frac{1}{2}[C_1 + C_2 + (A_1^2 + 4|B_1|^2 j)^{1/2} j + (A_2^2 + 4|B_2|^2 j)^{1/2} k]$$

(E.6)

$$+ \frac{d}{4}(3\cos^2\theta - 1)\}\delta_{lm}$$

The static Hamiltonian H_0 in Eq. (E.5) is diagonalized by a unitary transformation $E = S^\dagger H_0 S$ where S is

$$S = \begin{pmatrix} [[1]] & [[0]] & [[0]] & [[0]] \\ [[0]] & [[\xi]] & [[\zeta]] & [0]] \\ [[0]] & [[-\zeta]] & [[\xi]] & [0]] \\ [[0]] & [[0]] & [[0]] & [[1]] \end{pmatrix},$$

(E.7)

In (E.7), $[[\xi]]$ and $[[\zeta]]$ are 9×9 diagonal matrices whose ith diagonal elements are $\xi_{ii} = \cos(\Xi_i)$ and $\zeta_{ii} = \sin(\Xi_i)$, respectively with

(E.8)

$$\tan(2\Xi_i) = \frac{2(H_{23})_{ii}}{(H_{33})_{ii} - (H_{22})_{ii}}.$$

In Eq. (E.7), $i = 1, 2, \ldots, 9$ specifies the matrix element in the hyperfine nuclear space. The eigenvalue matrix of the coupled-nitroxides system is expressed as

$$E = \begin{pmatrix} [[E_1]] & [[0]] & [[0]] & [[0]] \\ [[0]] & [[E_2]] & [[0]] & [[0]] \\ [[0]] & [[0]] & [[E_3]] & [[0]] \\ [[0]] & [[0]] & [[0]] & [[E_4]] \end{pmatrix} \qquad (E.9)$$

where the lth ($l = 1, \dots, 9$) diagonal elements of the various $[[E_n]]$, ($n = 1,2,3,4$) are

$$[[E_1]]_{ll} = (H_{11})_{ll},$$

$$[[E_2]]_{ll} = \{-\frac{d}{4}(3cos^2\theta - 1) - [(\frac{d}{4}(3cos^2\theta - 1))^2$$

$$+ \frac{1}{4}(C_1 - C_2 + (A_1^2 + 4|B_1|^2 j)^{1/2} j - (A_2^2 + 4|B_2|^2 k)^{1/2} k^2)^2]\}$$

$$[[E_3]]_{ll} = \{-\frac{d}{4}(3cos^2\theta - 1) + [(\frac{d}{4}(3cos^2\theta - 1))^2$$

$$+ \frac{1}{4}(C_1 - C_2 + (A_1^2 + 4|B_1|^2 j)^{1/2} j - (A_2^2 + 4|B_2|^2 k)^{1/2} k^2)^2]\}$$

$$[[E_4]]_{ll} = (H_{44})_{ll} \qquad (E.10)$$

In Eq. (E.10), $l = 3j + k + 5$ with $j, k = -1,0,1$.

To calculate the density matrix during the free evolution, one needs to calculate $e^{-iH_0 t}$, as follows transformation S as

$$e^{-iH_0 t} = S\, e^{-iEt} S^\dagger$$

$$= \begin{pmatrix} [[e^{-iE_1 t}]] & [[0]] & [[0]] & [[0]] \\ [[0]] & e^{-i[[E_2]]t}[[\xi^2]] + e^{-i[[E_3]]t}[[\zeta^2]] & [[\zeta]]\,[[\xi]]\,(e^{-i[[E_2]]t} - e^{-i[[E_3]]t}) & [[0]] \\ [[0]] & [[\zeta]]\,[[\xi]]\,(e^{-i[[E_2]]t} - e^{-i[[E_3]]t}) & e^{-i[[E_2]]t}[[\xi^2]] + e^{-i[[E_3]]t}[[\zeta^2]] & [[0]] \\ [[0]] & [[0]] & [[0]] & [[e^{-iE_4 t}]] \end{pmatrix}$$

$$\qquad (E.11)$$

Appendix F

The ZFS tensor and its transformation from the eigenframe of the ZFS tensor to the laboratory frame

The ZFS term of the spin Hamiltonian for the Gd^{3+} ions and their transformations from the principal axes systems of the ZFS to the dipolar frame of the coupled Gd^{3+} ions, thereafter from the dipolar frame to the laboratory frame, is described in this appendix. No subscripts are used in the following discussion as the same analysis applies to any one of the two Gd^{3+} ions.

In general, for any one of the two $S = 7/2$ Gd^{3+} ions, the ZFS of the spin Hamiltonian, in the principal axis system (x, y, z) of the ZFS tensor, is described as follows [1]

$$H_{ZFS} = \sum_{L,M} B_L^M Y_L^M(\boldsymbol{S}) \, ; L = 2,4,6 \text{ with } M = -L, -(L-2), \dots, (L-2), L, \quad (F.1)$$

where the $Y_L^M(\boldsymbol{S})$ are spin operators that transform as the spherical harmonics $Y_L^M(\theta, \phi)$. For orthorhombic symmetry, keeping only the second-order terms, one has

$$H_{ZFS} = B_2^0 Y_2^0(\boldsymbol{S}) + B_2^2 Y_2^2(\boldsymbol{S}) + B_2^{-2} Y_2^{-2}(\boldsymbol{S}). \quad (F.2)$$

Assuming $B_2^2 = B_2^{-2}$, i.e., they are real, one obtains

$$H_{ZFS} = \frac{D}{3}[3S_z^2 - S(S+1)] + E[S_x^2 - S_y^2], \quad (F.3)$$

in the commonly used CW (continuous wave) EPR notation, where $D = 3B_2^0$ and $E = B_2^2$.

The transformation to the laboratory frame (X, Y, Z) where the Z-axis is chosen parallel to the external magnetic field, $\boldsymbol{B_0}$, via the dipolar frame, following the sequence ZFS $\rightarrow$ dipolar frame $\rightarrow$ laboratory frame, is given by (Saxena and Freed 1997)

$$B_L^{M*} = \sum_{m',m''} D_{Mm'}^L(\eta) D_{m'm''}^L(\lambda) B_L^{m''} \quad (F.4)$$

where $\eta = (\theta, \phi)$ are the orientation of the dipolar axis with respect to the laboratory axis $(\vec{B}||Z)$ and $\lambda = (\alpha, \beta, \gamma)$ are the Euler angles of the principal axes of the ZFS tensor with respect to the dipolar frame, whose z axis chosen parallel to the line joining the two Gd^{3+} ions, as shown in Figure 4.7, for the two Gd^{3+} ions. In Eq. (F.4) the $D_{mm'}^L$ are the Wigner coefficients.

Appendix G

All the publications related to this thesis are listed in this appendix.

1-S. K. Misra and H. R. Salahi *Calculation of pulsed EPR DEER signal for two coupled Gd^{3+} ions by dipolar interaction using rotating frames*, *Physica B: Condensed Matter*, 637 2022

2-S. K. Misra and H. R. Salahi *Estimation of distance-distribution probabilities from pulsed electron paramagnetic resonance (EPR) data of two dipolar interaction coupled nitroxide spin labels using doubly rotating frames and least-squares fitting*, *EPJD*, 76(89) 2022

3-S. K. Misra and H. R. Salahi *Calculation of DEER spectrum by the use of doubly rotating frames: Three-pulse and four-pulse nitroxide biradical DEER signals*, *Physica B: Condensed Matter*, 625, pp. 413511, 2022

4-S. K. Misra and H. R. Salahi *Two-Pulse EPR COSY (Correlation Spectroscopy) Sequence: Feasibility for Distance Measurements in Biological Systems*, *Appl. Magn. Reson.*, 53(2), 2022

5-S. K. Misra and H. R. Salahi *Two-pulse double quantum and five-pulse double-quantum modulation sequences in EPR: Coherence transfer and distance measurements*, *MRSej*, 23 paper #21203, 2021

6- S. K. Misra and H. R. Salahi *Simulation of four-, five-, and six-pulse Double Quantum Coherence signals for nitroxide biradicals: Distance measurement in biological systems*, *MRSej*, 23 paper #21101, 2021

7-S. K. Misra and H. R. Salahi *Spin relaxation in six-pulse double-quantum coherence (DQC) signal: stretched exponential approach for a polycrystalline average*, *Eur. Phys. J. Plus*, 136(3) pp. 1–17, 2021

8-S. K. Misra and H. R. Salahi *Relaxation in Pulsed EPR: Thermal Fluctuation of Spin-Hamiltonian Parameters of an Electron-Nuclear Spin-Coupled System in a Malonic Acid Single Crystal in a Strong Harmonic-Oscillator Restoring Potential*, *Appl. Magn. Reson.*, 52(3) pp. 247–261, 2021

9-S. K. Misra and H. R. Salahi *Relaxation due to thermal vibrations in pulsed EPR: Cylindrical fluctuation model of perturbation of g- and A-matrices of an electron-nuclear spin-coupled system in a malonic-acid single crystal*, *MRSej*, 22 paper #20101, 2020

10-S. K. Misra, H. R. Salahi and L. Li *Calculation of single crystal and polycrystalline pulsed EPR signals including relaxation by phonon modulation of hyperfine and g matrices by solving Liouville-von Neumann equation*, *MRSej*, 21 paper #19505, 2019

11-S. K. Misra and H. R. Salahi, *A Rigorous Calculation of Pulsed EPR SECSY and Echo-ELDOR Signals: Inclusion of Static Hamiltonian and Relaxation during Pulses*, *J. Theor. Appl. Phys.*, 3(2): 9–48, 2019